Predictions to the Plasma Environment of Comet 67P/Churyumov-Gerasimenko

Von der Fakultät für Elektrotechnik, Informationstechnik, Physik
der Technischen Universität Carolo-Wilhelmina zu Braunschweig

zur Erlangung des Grades eines Doktors
der Naturwissenschaften (Dr. rer. nat.)

genehmigte Dissertation

von Christoph Wilhelm Arnold Koenders

aus Bocholt

eingereicht am 5.2.2015

Disputation am 29.4.2015

1. Referent: Prof. Dr. Karl-Heinz Glaßmeier
2. Referent: Prof. Dr. Uwe Motschmann

Druckjahr: 2015

Vorveröffentlichungen der Dissertation

Teilergebnisse aus dieser Arbeit wurden mit Genehmigung der Fakultät für Elektrotechnik, Informationstechnik, Physik, vertreten durch den Mentor der Arbeit, in folgenden Beiträgen vorab veröffentlicht:

Publikationen

- Wiehle, S., Motschmann, U., Gortsas, N., Glassmeier, K.-H., Müller, J., **Koenders, C.**, 2011a, Simulation of cometary jets in interaction with the solar wind, Advances in Space Research, 48, 1108–1113, ISSN 02731177
- Eastwood, J. P., Schwartz, S. J., Horbury, T. S., Carr, C. M., Glassmeier, K.-H., Richter, I., **Koenders, C.**, Plaschke, F., Wild, J. A., 2011, Transient Pc3 wave activity generated by a hot flow anomaly: Cluster, Rosetta, and ground-based observations, Journal of Geophysical Research, 116, A08 224, ISSN 0148-0227
- Richter, I., **Koenders, C.**, Glassmeier, K.-H., Tsurutani, B. T., Goldstein, R., 2011, Deep Space 1 at comet 19P/Borrelly: Magnetic field and plasma observations, Planetary and Space Science, 59, 691–698, ISSN 00320633
- Richter, I., Auster, H. U., Glassmeier, K.-H., **Koenders, C.**, Carr, C., Motschmann, U., Müller, J., McKenna-Lawlor, S., 2012, Magnetic field measurements during the ROSETTA flyby at asteroid (21)Lutetia, Planetary and Space Science, 66, 155–164, ISSN 00320633
- Tsurutani, B. T., Echer, E., Richter, I., **Koenders, C.**, Glassmeier, K.-H., 2013, SLAMS at comet 19P/Borrelly: DS1 observations, Planetary and Space Science, 75, 17–27, ISSN 00320633
- **Koenders, C.**, Glassmeier, K.-H., Richter, I., Motschmann, U., Rubin, M., 2013, Revisiting cometary bow shock positions, Planetary and Space Science, 87, 85–95, ISSN 00320633
- Volwerk, M., **Koenders, C.**, Delva, M., Richter, I., Schwingenschuh, K., Bentley, M. S., Glassmeier, K.-H., 2013, Ion cyclotron waves during the Rosetta approach phase: a magnetic estimate of cometary outgassing, Annales Geophysicae, 31, 2201–2206, ISSN 1432-0576
- Rubin, M., **Koenders**, C., Altwegg, K., Combi, M., Glassmeier, K.-H., Gombosi, T., Hansen, K., Motschmann, U., Richter, I., Tenishev, V., Tóth, G., 2014b, Plasma environment of a weak comet – Predictions for Comet 67P/Churyumov-Gerasimenko from multifluid-MHD and Hybrid models, Icarus, 242, 38–49, ISSN 00191035

- Volwerk, M., Glassmeier, K.-H., Delva, M., Schmid, D., **Koenders, C.**, Richter, I., Szegö, K., 2014, A comparison between VEGA 1, 2 and Giotto flybys of comet 1P/Halley: implications for Rosetta, Annales Geophysicae, 32, 1441–1453, ISSN 1432-0576
- **Koenders, C.**, Glassmeier, K.-H., Richter, I., Ranocha, H., Motschmann, U., 2015, Dynamical Features and Spatial Structures of the Plasma Interaction Region of 67P/Churyumov-Gerasimenko and the Solar Wind, Planetary and Space Science, 105, 101–116, ISSN 00320633
- Nilsson, H., Stenberg Wieser, G., Behar, E., Wedlund, C. S., Gunell, H., Yamauchi, M., Lundin, R., Barabash, S., Wieser, M., Carr, C., Cupido, E., Burch, J. L., Fedorov, A., Sauvaud, J.-A., Koskinen, H., Kallio, E., Lebreton, J.-P., Eriksson, A., Edberg, N., Goldstein, R., Henri, P., **Koenders, C.**, Mokashi, P., Nemeth, Z., Richter, I., Szego, K., Volwerk, M., Vallat, C., Rubin, M., 2015, Birth of a comet magnetosphere: A spring of water ions, Science, 347, ISSN 0036-8075

Tagungsbeiträge

- Koenders, C., Overview of Structures and Boundaries in the Interaction Region of Comets, RPC Teammeeting 2010, Braunschweig, 6. September 2010, (Vortrag)
- Koenders, C., Status Report on Hybrid Plasma Simulations, WG-X Meeting, Darmstadt, 6. Dezember 2010, (Vortrag)
- Koenders, C., Hybrid Simulations of the Interaction between comet Churyumov-Gerasimenko and the Solar Wind, IMPRS S3 Seminar, Lindau, 2. Februar 2011, (Vortrag)
- Koenders, C., Simulations of the Cometary Plasma Environment, Magnetometer Meeting, Sigüenza, 19. Juli 2011, (Vortrag)
- Koenders, C., Modelling of Plasma Boundaries for the RPC, WG-X Meeting, Noordwijk , 15. November 2011, (Vortrag)
- Koenders, C., Prognosen für die Rosetta-Mission, Oberseminar des Institut für Geophysik und Meteorologie, Köln, 20. Januar 2012, (eingeladener Vortrag)
- Koenders, C., The Massloading Process and the Cometary Bow Shock Position, IMPRS S3 Seminar, Lindau, 15. Februar 2012, (Vortrag)
- Koenders, C., Glassmeier, K.-H., Nabert, C. und Richter, I., Revisiting Cometary Bow Shock Positions, EGU General Assembly 2012, Wien, 22. – 27. April 2012, p. 5491, (Poster)
- Koenders, C., Modelling the Cometary Environment in Hybrid Plasma Simulations, ISSI Meeting, Bern, 21. November 2012, (Vortrag)
- Koenders, C., Revisiting Cometary Bow Shock Position, IMPRS S3 Seminar, Lindau, 20. Februar 2013, (Vortrag)

- Koenders, C., Hybrid Simulations of the Plasma Environment of Comet 67P/Churyumov-Gerasimenko, Seminar, Uppsala, 18. August 2013, (eingeladener Vortrag)
- Koenders, C., Glassmeier, K.-H., Richter, I., Motschmann, U. und Rubin, M., Revisiting Cometary Bow Shock Position, European Planetary Science Congress 2013, London, 13. September 2013, (Vortrag)
- Koenders, C., Hybrid Plasma Simulations of the Cometary Environment, ISSI Meeting, Bern, 22. Januar 2014, (Vortrag)
- Koenders, C., RPC Measurements at Comet Churyumov-Gerasimenko, ISSI Meeting, Bern, 23. Januar 2014, (Vortrag)
- Koenders, C., Predictions for MTP 16, RPC-Teammeeting 2014, Paris, 8. März 2014, (Vortrag)
- Koenders, C., Richter, I., Motschmann, U. und Glassmeier, K.-H., Hybrid Plasma Simulations of 67P/Churyumov-Gerasimenko, EGU General Assembly 2014, Wien, 27. April – 2. Mai 2014, id. 12421, (Poster)
- Koenders, C., Richter, I., Heinisch, P., Auster, H.-U. , Glassmeier, K.-H., Tsurutani, B. und Volwerk, M., Combined Measurements of the Magnetic Field in the Plasma Environment of 67P/Churyumov-Gerasimenko, EGU General Assembly 2014, Wien, 27. April – 2. Mai 2014, id. 12597, (Poster)
- Koenders, C., Rubin, M., Altwegg, K., Combi, M. R., Glassmeier, K.-H., Gombosi, T. I., Hansen, K. C., Motschmann, U., Richter, I., Tenishev, V. M. und Toth, G., Plasma environment of a weak comet - Predictions for Comet 67P/Churyumov-Gerasimenko from multifluid-MHD and Hybrid models, WG-X Meeting, Madrid, 10. Juni 2014, (Vortrag)
- Koenders, C., Plasma around the Comet - Predictions for MTP 16 HAC by 3D Global Hybrid Simulation, SWT Meeting, Madrid, 11. Juni 2014, (Vortrag)
- Koenders, C., Glassmeier, K.-H., Richter, I. und Motschmann, U., Hybrid Plasma Simulations at 67P/Churyumov-Gerasimenko - Predictions for the High Activity Phase, 6th Alfven Conference, London, 7. July 2014, (Vortrag)
- Koenders, C., Carr, C., Burch, J., Eriksson, A., Glassmeier, K.-H., Lebreton, J.-P., Nilsson, H., Vallat, C. , Cupido, E.,Goldstein, R.,Henri, P. und Richter, I., A Walk Around a Comet with the Rosetta Plasma Consortium, 6th Alfven Conference, London, 7. July 2014, (eingeladener Vortrag)
- Koenders, C., A Walk around the Comet, RPC-Teammeeting, London, 24. July 2014, (Vortrag)
- Koenders, C., Glassmeier, K.-H., Richter, I. und Motschmann, U., Hybrid Plasma Simulations of 67P/Churyumov-Gerasimenko, European Planetary Science Congress 2014, Estoril, EPSC2014-239, (Poster)

- Koenders, C., The Plasma Environment at CG Close to the Perihelion, ISSI Meeting, Bern, 1. Oktober 2014, (Vortrag)
- Koenders, C., First RPC-MAG Observation at 67P, ISSI Meeting, Bern, 1. Oktober 2014, (Vortrag)
- Koenders, C., Glassmeier, K.-H., Richter, I., Goetz, C., Carr, C., Cupido, E., Vallat, C., Motschmann, U., Burch, J., Eriksson, A., Goldstein, R., Henri, P., Lebreton, J.-P., Nilsson, H., Structures and Dynamics of the Interaction Region at Comet 67P/Churyumov-Gerasimenko: Comparing Numerical Simulations and RPC Magnetic Field Observations, AGU Fall Meeting 2014, San Francisco, 14996, (Poster)

Contents

.

Abstract

In summer 2014 the European Rosetta mission arrived at comet 67P/Churyumov-Gerasimenko and will stay close to the comet during its orbit around the Sun. Comets are kilometre-sized objects consisting of dust and ices. As the comet approaches the Sun solar insolation leads to the sublimation of these ices and an cometary atmosphere is formed which interacts with the impinging solar wind. The Rosetta Plasma Consortium (RPC), a suite of plasma instruments onboard Rosetta, will study this interaction and the evolution of the plasma environment at different cometary activity levels from close by. Various structures and boundaries within this environment such as the bow shock or the diamagnetic cavity will be the point of interest for RPC. For successful measurements a careful preparation of Rosetta's trajectory is required. The aim of this thesis is to make predictions about the location of the various plasma structures and boundaries to support the mission and to ensure its scientific success.

These predictions are obtained by means of analytical models and numerical simulations, i.e. the A.I.K.E.F. (Adaptive Ion Kinetic Electron Fluid) code. In parallel the processes which lead to the plasma interaction and the structures in the cometary plasma environment are analysed.

Since Rosetta's arrival at 67P/Churyumov-Gerasimenko the comet is weakly active due to a faint insolation. A first study shows that at this activity level the interaction is dominated by the cometary pick-up ion tail which is populated with cometary ions performing a cycloidal motion. Furthermore, it is found that along this tail a repetitive Mach cone is triggered.

In a second study the close vicinity of the comet is analysed. There the cometary pick-up ion tail and the footpoint of a Mach cone is found. In addition, this work investigates a low frequency wave pattern which is analysed and a first preliminary comparison to the RPC magnetometer data is conducted, in which a similarity to the waves in the hybrid simulations is observed.

Close to the perihelion, the cometary activity will reach its maximum and the Mach cone will be transformed into a bow shock. In a third study the position of this bow shock is analysed by means of various models. A comparison reveals a major difference between the fluid models and the hybrid model concerning the instantaneous pick-up of the cometary ions. Due to the more realistic description of the pick-up in the hybrid model, the bow shock is much closer to the comet than expected before. In addition, a strong dependency of the bow shock position on the solar wind parameters is found.

In the fourth study the innermost coma is analysed. For the first time ever, a global hybrid simulation is able to resolve this region sufficiently to allow for an investigation of the plasma boundaries in that region, i.e. the diamagnetic cavity and the cometary ionopause. A shift of the entire interaction region as well as of all related structures and boundaries therein away from the Sun-comet line is found. In addition, this study predicts the presence of three distinct cometary ion populations at the innermost boundaries.

Kurzzusammenfassung

Im Sommer 2014 ist die europäische Raumsonde Rosetta am Kometen 67P/Churyumov-Gerasimenko angekommen und wird ihn bei seinem Umlauf um die Sonne begleiten. Kometen sind kilometergroße Himmelskörper, welche aus Staub und Eis bestehen. Wenn sie sich der Sonne nähern sublimiert das Eis durch Sonneneinstrahlung, und es bildet sich eine Atmosphäre aus. Diese wechselwirkt mit dem anströmenden Sonnenwind. Das Rosetta Plasma Consortium (RPC), ein Verbund von Plasmainstrumenten an Bord von Rosetta, wird diese Wechselwirkung und deren Entwicklung aus nächster Nähe untersuchen. Dabei werden auch die verschiedenen Strukturen die durch diese Wechselwirkung entstehen, wie zum Beispiel die Bugstoßwelle oder die diamagnetiche Kavität, für RPC von Interesse sein. Erfolgreiche Messungen dieser Strukturen verlangen jedoch eine sorgfältige Vorbereitung. Das Ziel dieser Arbeit ist die Vorhersage der Positionen der verschiedenen Strukturen und deren Eigenschaften um die Rosetta Mission vorzubereiten und somit den wissenschaftlichen Erfolg zu ermöglichen.

Diese Vorhersagen werden in der vorliegenden Arbeit mit Hilfe verschiedener Modelle, hauptsächlich aber mit numerischen Simulationen mit dem A.I.K.E.F. Programm (Adaptive Ion Kinetic Electron Fluid), erstellt. Gleichzeitig werden auch die Prozesse untersucht, die zu der Plasmawechselwirkung führen, um so ein möglichst detailliertes Verständnis über den Kometen zu gewinnen.

Seit Rosettas Ankunft hat der Komet auf Grund der geringen Sonneneinstrahlung nur eine geringe Aktivität. Die daraus resultierende Wechselwirkung wurde in einer ersten Studie untersucht, und es zeigt sich, dass die Wechselwirkung vom kometaren Ionenschweif dominiert wird. In diesem bewegen sich die Ionen auf einer Zykloidenbahn. Entlang dieser Bahnen werden wiederholt Machkegel angeregt.

In einer zweiten Studie wurde dann die nähere Umgebung bei dieser schwachen Aktivität erforscht. Dort findet man neben dem Anfang des kometaren Ionenschweifes und des Machkegels auch ein Wellenmuster, welches detailliert untersucht wird. In einem ersten Vergleich mit den Daten des RPC-Magnetometers zeigen sich ähnliche Wellen.

In der Nähe des Perihels wird die Aktivität des Kometen ihr Maximum erreichen und der Machkegel wird in eine Bugstoßwelle übergehen. Die Position dieser Struktur wird in einer dritten Studie untersucht. Ein Vergleich zeigte einen deutlichen Unterschied zwischen den Flüssigkeitsmodellen und dem Hybridmodell im Bezug auf die Beschleunigung der kometaren Ionen. Auf Grund der realistischeren Beschreibung im Hybridmodell ist die Bugstoßwelle deutlich näher am Kometen. Zudem zeigten die Hybridsimulationen, dass die Position der Bugstoßwelle sehr stark von den Sonnenwindbedingungen abhängt.

In einer vierten Studie wird zum ersten Mal eine globale Hybridsimulation vorgestellt, die die innere Region so gut auflösen kann, dass eine Analyse der Plasmagrenzschichten in dieser Region möglich wird. Dabei zeigt sich, dass die komplette Wechelwirkungsregion eine Asymmetrie zur Sonnen-Kometen Linie aufweist. Zudem werden in den innersten Grenzschichten drei verschiedene Gruppen an kometaren Ionen identifiziert.

1 Introduction

An Ariane flight lifted off on 2^{nd} March 2004 carrying with it the Rosetta spacecraft on the start of its 10 year journey to comet Churyumov-Gerasimenko, which is a small, kilometre-sized, object in the Solar System consisting of dust and ice. At large distances to the Sun comets are inactive and hardly visible from the Earth, but when such a comet approaches the Sun, solar radiation leads to the sublimation of the ice and the comet becomes active. The gas, consisting mainly of water molecules emanating from the nucleus, forms an extended neutral cometary atmosphere, the coma. In addition, the fast streaming gas transports dust particles away from the nucleus into the coma. These processes describe active comets which are sometimes visible from the Earth to the unaided eye and have been fascinating mankind since thousands of years. A famous example is the Bayeux Tapestry, which tells the story of the conquest of England by William the Conqueror in 1066. It shows a comet at the firmament on the eve of to the crucial battle of Hastings.

Nowadays, scientists study comets in order to understand the formation of planets and the source of water on Earth because it is believed that comets are the least processed objects in the Solar System. The European Rosetta spacecraft mission will try to answer these important questions by observing comet 67P/Churyumov-Gerasimenko at close range. Thereby Rosetta enters uncharted territory: for the first time ever the spacecraft has delivered a lander (Philae) onto the surface of a nucleus, the central part of a comet. This was the first smooth landing performed on a nucleus, subsequently the lander has been studying the surface of the comet and its interior. The other main goal of the mission is the escort of the comet during its journey around the Sun. Consequently, the Rosetta mission allows us to study the evolution of the comet from the inactive stages far away from the Sun towards the active stages near the Sun. This is a great achievement in contrast to all previous cometary spacecraft missions, which only performed flybys and took snapshots of the comets and their environment.

The different aspects of the comet and its cometary atmosphere will be studied by several instruments. Among these is the Rosetta Plasma Consortium (RPC), which is a group of five plasma instruments, studying the coma and its interaction with the solar wind, as will be discussed in great detail in this work. The interaction is triggered by the ionisation of the neutral cometary gas within the coma, mainly by solar UV radiation, and the impinging solar wind, a constant stream of charged particles from the Sun. The newborn cometary ions are picked up by the solar wind and structures and boundaries are formed in the plasma environment of the comet, e.g. the plasma tail. Figure (1.1) shows a picture of comet Hale-Bopp and its plasma tail. The actual body of the comet, the small nucleus, is not visible on this picture, however, the extended coma, the white dust, and the blue plasma tail are clearly visible. Besides the plasma tail, several other structures and boundaries will occur in the cometary plasma environment. They allow us to study

Figure 1.1: A picture of the comet Hale-Bopp (C/1995 O1) taken on 4th April 1997, by E. Kolmhofer and H. Raab from Johannes-Kepler-Observatory in Linz, Austria. The coma and the dust tail are white whereas the plasma tail, which is orientated anti-sunward, is blue. The image is published under the Creative Commons Attribution-Share Alike 3.0 Unported license.

the interaction of the solar wind with the comet, and following this, to investigate some of the properties of the comet and its activity. Consequently, RPC intends to contribute to the success of the Rosetta mission.

Based on the limited knowledge of the cometary plasma environment prior to Rosetta, such a mission and the measurements of the instruments, especially those of RPC, need careful preparation. Since RPC is only able to observe the plasma properties in-situ, the measurement of a plasma boundary is only feasible if Rosetta's trajectory passes this region of interest, the instruments are in a certain mode, and a sufficient data rate is available. Hence, predictions of the positions of the plasma structures and boundaries and their behaviour have to be made in advance. Because former cometary flyby missions only visited stongly active comets, the interaction at inactive or weakly active comets has never been observed before. Furthermore, the data obtained at the previous missions revealed a large variety of positions of boundaries and structures as the properties of the comets differ. This is why theoretical considerations and numerical models have to be taken into account for the mission planning.

Consequently, the aim of this thesis is to study the behaviour of the plasma interaction during the mission and the positions and behaviour of individual structures and boundaries therein and to provide reliable predictions for interesting effects to be observed during the Rosetta mission. These predictions allow the RPC to negotiate the trajectory and the attitude of the spacecraft at the comet and the data rate with the other instrument teams. By this, observations of a certain structure or boundary with appropriate pointing and a sufficient data rate becomes possible. Hence, proper predictions are one of the key elements for the scientific success of the RPC instruments.

The introduction focuses on general aspects of cometary science. Among others, the formation of comets and their evolution as known so far is discussed. In addition, a short summary of plasma measurements performed by spacecraft that have visited comets so far is given, as well as a portrait of the Rosetta mission, its target comet 67P/Churyumov-Gerasimenko and its instrumentation. Finally, the planning process of the Rosetta mission is described briefly.

The purpose of the second chapter is to give a detailed description of the processes which have an impact on the plasma interaction. Furthermore, different plasma models that are used at various places in this work are presented. Among these, one can find a description of the A.I.K.E.F. code, a three dimensional hybrid plasma simulation model. Because the A.I.K.E.F. code is the means of choice for the study of the cometary plasma interaction, a very detailed description of the implementation of the cometary processes is given. A justification for the advantages of the A.I.K.E.F. code in modelling the cometary plasma interaction is given in the next two chapters, where various stages of the interaction are discussed in great detail.

The third chapter discusses the initial interaction, i.e. the pick-up of the cometary ions, due to which the solar wind is decelerated and the formation of structures becomes possible. This pick-up process and the implications on the solar wind on very large scales and on small scales in the direct vicinity of the comet for the very early stages of the mission are discussed.

With an increasing activity of the comet, the comet triggers the formation of plasma boundaries. Initially, a Mach cone forms behind the comet, which then transfers into a bow shock when the gas production rate increases. The position and the behaviour of the bow shock, the most sunward boundary in the cometary environment, are discussed in this fourth chapter. Besides the bow shock, a diamagnetic cavity is expected close to perihelion. This is a small magnetic field free space close to the nucleus triggered by the cometary activity. The hybrid simulations presented in this chapter are the first global hybrid plasma simulations which resolve this region. The details of this region and their formation will be discussed in this chapter, as well as the surrounding cometary plasma environment of the inner coma. This is especially important, since the Rosetta spacecraft stays within this region most of time.

The fifth chapter focusses on the RPC science planning and describes how the RPC measurements are planned with the help of hybrid simulations. Finally, a summary of this work will be presented in the last chapter.

1.1 Comets

In general comets are kilometre-sized objects which consist of ice, organic and non-volatile materials. It is assumed that these *dirty snowballs* are formed in the early phase of the Solar System and orbit the Sun since those days (Whipple 1950). However, nowadays the phrase *dirty snowballs* is criticized since water is probably not the dominant component in the comet. This is why the phrase *icy dirtball* is used instead (Küppers et al. 2005). Currently, different models on comet formations are controversially discussed, e.g. gravitational instability and mass transfer scenario. Since the comet formation is not the focus of this work, but might have an impact on the observed activity of comets, only the most promising model according to Blum et al. (2014) is briefly summarised.

It is assumed that the formation of comets happened in parallel to the formation of planets, which took place about 4.5 to 4.6 billion years ago. In those days a protoplanetary disc orbited the early Sun (Morbidelli et al. 2012). In the beginning it consisted of gas, which partially condensed to solid grains. The gas can condense to ice if the partial pressure of the particular gas species exceeds the saturation pressure (Festou et al. 2004). Thus, depending on the temperature distribution in the protoplanetary disc the elementary abundances vary. In the inner part, atoms and molecules with higher condensation temperatures can be found, e.g. calcium-aluminium inclusions or silicates, whereas water and other more volatile materials can early be found beyond the snowline. In the early Solar System the snowline for water was probably between a heliocentric distance of 1.6 AU to 2.7 AU[1] (Lecar et al. 2006).

Induced by sticking collisions between the icy grains and dust grains, the size of the agglomerates increases up to centimetre-size (Güttler et al. 2010), or decimetre-size for ice (Gundlach 2013). At this size, a *bouncing barrier* prevents the further growth of the agglomerates (Zsom et al. 2010). In order to allow a further growth of the agglomerates, the relative velocities between the grains must decrease. This can be achieved by in a two-step process (Johansen and Youdin 2007): Kelvin-Helmholtz instability or a streaming instability, and a gravitational instability. At first, depending on the local properties and the heliocentric distance, either a Kelvin-Helmholtz instability or a streaming instability, or both, are triggered in the protoplanetary disc (Johansen and Youdin 2007). Both instabilities are mainly caused by the different speeds in the protoplanetary disc. Gas orbits the Sun at a sub-Keplerian speed, whereas the agglomerates can either move with sub-Kepler or Kepler speed. The first case is applicable as long as the agglomerates are small and coupled to the gas. The latter case is true if the larger agglomerate are not coupled to the gas any more. Thus, the larger agglomerates rotate faster than the gas which triggers the instabilities. As a consequence, volumes with higher densities of agglomerates are formed (Youdin and Goodman 2005). Due to the higher densities, the gravitational instability is triggered and kilometre-sized or bigger objects are formed (Johansen and Youdin 2007). However, as the gravitational forces are small, no compaction of the material takes places. This is at least true for comets. As a consequence of this model, the object is built as an agglomerate of dezimetre-sized ice grains and centimetre-sized dust grains. Furthermore, the tensile strength of the surface layer which has to be exceeded by the gas pressure to remove grains from the comet is only about 1 Pa (Blum et al. 2014). This is in contrast to other models, such as the *mass transfer* model, which compacts the agglomerates and leads to tensile strengths of about 1 kPa (Skorov and Blum 2012).

After the formation of comets and planets, a major change in the Solar System structure occurred. Walsh et al. (2011) showed that Jupiter and Saturn can undergo a substantial orbit change during 500 kyr. As a consequence, smaller objects, such as comets are scattered. Nowadays, two major reservoirs for comets in the Solar System are known. The first reservoir is the Oort cloud (Oort 1950). Observations of the orbital motion of Oort cloud comets showed that these objects can have stable orbits with semimajor axes larger than 10 000 AU and an eccentricity close to one. In addition, any inclination is found for

---

[1] Astronomical Unit: 1 AU = 149 597 870 691 m

those comets. Based on this result, Oort (1950) suggested a large reservoir of cometary nuclei at large heliocentric distances, the Oort cloud. The shape of that cloud is a spherical shell with a minimum radius of 5000 AU (Stern 2003). Comets in the Oort cloud might start their journey back into the inner Solar System, when a passing star or tidal effects of the galaxy act on the nuclei (Festou et al. 2004). These comets are the source of long-period comets, which have orbital periods of more than 200 years (cf. Dones et al. 2005, Prialnik et al. 2008).

The second reservoir is the Kuiper belt (Festou et al. 2004). The objects in this belt are about 30 AU to 1000 AU away from the Sun. As known so far, the transition from the Kuiper belt to the Oort cloud is fluent. However, in contrast to the Oort cloud, the belt has the shape of a scattered disc (Stern 2003). It is supposed that the region contains the debris of the planetary formation. It is further assumed that the average size of Kuiper belt objects is above 50 km. Due to collisions between those Kuiper belt objects, which have a much higher probability then collisions between comets in the Oort cloud, Kuiper belt comets are formed (Stern 2003). Typically those comets have orbital periods below 200 years and are named as short period comets. It is most likely that these comets constitute the majority of the Jupiter family comets, a class of comets captured by planet Jupiter during one of their approaches to the Sun (cf. Festou et al. 2004).

It is generally believed that cometary nuclei contain the least processed material in the inner regions of the Solar System. The Kuiper belt objects or comets in the Oort cloud may contain more unprocessed material, but they are not reachable by modern spacecraft and hardly visible from Earth. The main changes of the cometary material might occur in the early evolution and when the comets pass the inner regions of the Solar System. In the early phase, the cometary nuclei or Kuiper belt objects could be heated by radioactive decay (Prialnik et al. 2008). One important source for this process is ^{26}Al, which is a short-lived radioactive material with a half-life period of about $7 \cdot 10^5$ years. The heating leads to the melting of the initially amorphous water ice in the interior. Afterwards, the interior cools down and crystalline water ice is formed. Prialnik et al. (2008) conclude that the process only affects the comet, when the accretion timescale is comparable to that of the radioactive decay. Thus, by an investigation of the interior of a comet, a timescale of the comet formation can be estimated. Other processes which affect the cometary material are collisions, at least in the Kuiper belt, where collisions between Kuiper belt objects are more likely than in the Oort cloud. This changes the properties of the material: A compression of material will affect the activity of the collision region, when the comet enters the inner Solar System (Vincent et al. 2013b). In addition, also UV radiation or space weathering can restructure the surface of the comet (Stern 2003).

The next important phase in the life of a comet is the passage of the comet through the inner Solar System. While the distance to the Sun is decreasing, insolation heats the the cometary surface. As reported by various authors, e.g. Keller et al. (1986) or A'Hearn et al. (2011), the albedo of the comet nuclei is very low due to a surface of porous dust. Lamy et al. (2008) measured the albedo of about 50 short period comets and found a mean albedo of about 0.04[2]. Hence, cometary nuclei are the darkest objects in the Solar System and the absorption of light is very efficient. This triggers a heat wave propagating from

---

[2] The surface albedo of comets entering the inner region for the first time might be higher, but such a comet and its albedo has never been observed. In addition, during the first approach to the Sun the water-ice from the surface will evaporate and a dust layer will remain.

the surface of the nucleus to the cold interior through the dust layer at the surface (Prialnik et al. 2008). During the sublimation of ice or the crystallisation of amorphous ice, gases are released (Prialnik et al. 2008). The depth of the heat wave propagation depends, among others on the properties of the rotation axis of the nucleus[3]. Consequently, there are diurnal and also seasonal changes. For example, Prialnik et al. (2008) discussed for comet 9P/Tempel 1 that although the maximum surface temperature is reached next to noon, the flux of water gas molecules at the equator reached its maximum on the dusk side.

Another parameter of the heat wave propagation which has an impact on the local activity is the thickness of the dust layer atop the surface. The released gas produces a pressure beneath the dust layer. This pressure can detach dust agglomerates from the dust layer if the gas pressure exceeds the tensile strength in the dust agglomerates. In case the gas pressure is below the tensile strength, the thickness of the dust layer grows and the cometary activity shrinks. However, the tensile strength depends on the size of the agglomerates as found by Skorov and Blum (2012). This is why a minimum size of dust agglomerates exists at which they can be lifted by the gas pressure at a certain heliocentric distance (Blum et al. 2014).

The activity of a comet is detectable from Earth at distances closer than 5 AU (cf. Festou et al. 2004). However, even further out, the cometary activity is not zero. For example, at 5 AU comet Hale-Bopp, shown in Figure (1.1), already had a gas production rate of about $Q \approx 10^{28}\,\mathrm{s}^{-1}$ (cf. Kührt 1999). At these large heliocentric distances the activity is not driven by water but by more volatile gases, i.e. CO. Only at a distance of about 2.5 AU and closer the water molecules can become the main driver for the activity. The actual gas production rate, the main indicator for the comet's activity, increases with a decreasing heliocentric distance and differs between comets. The emanating gas forms a coma, the extended neutral gas cometary atmosphere. Further details will be presented in Section (2.3) because the coma, its structuring, and transient effects such as jet-like features are important parameters for plasma models.

1.2 Cometary Spacecraft Missions and Observations of the Plasma Environment

The first cometary spacecraft mission was carried out almost 30 years ago. At that time, the International Cometary Explorer (ICE) visited comet 21P/Giacobini-Zinner (Smith et al. 1986a). About a year later, the up to now, most famous comet 1P/Halley revisited the inner solar system. As predicted by Edmund Halley, this comet orbits the Sun with an orbital period of 73.3 years [4]. Its aphelion distance is at about 35 AU away from the Sun. Therefore, this comet is not a member of the Jupiter family comets. In addition, the activity of the comet by far exceeds those of other comets, which have been visited by spacecraft yet. Hence, an armada of spacecraft seized the rare opportunity to study this comet in great detail. Particularly the ESA mission Giotto was able to broaden the knowledge about comets substantially.

---

[3] Other factors are the heat conductivity, heat capacity and porosity of the surface.

[4] See JPL Small-Body Database: http://ssd.jpl.nasa.gov/sbdb.cgi?sstr=1P

Due to the retrograde orbit of comet 1P/Halley, the flyby speed of the Giotto spacecraft was large (about $68\,\mathrm{km\,s^{-1}}$). The angle of the trajectory to the Sun-comet line was about 107° and the distance of closest approach was about 596 km (Reinhard 1986, Curdt et al. 1988). Hence, the trajectory was close to the terminator plane. During the days of the encounter the heliocentric distance of the comet was about 0.9 AU and the comet had a gas production rate of $Q = 6.9 \times 10^{29}\,\mathrm{s^{-1}}$(Reinhard 1986). Among other remarkable results, the Halley Multicolor Camera, for example, took the first picture of a cometary nucleus in history. On these pictures, the nucleus reveals as a solid and irregularly shaped body. Its surface was covered by non-volatile material, its albedo was below 0.04 and only minor parts of the surface were active (Keller et al. 1986).

In addition, several plasma instruments were onboard the spacecraft to study the plasma interaction between the comet and the solar wind (cf. Neubauer et al. 1986, Balsiger et al. 1986, Johnstone et al. 1986, Rème et al. 1986, McKenna-Lawlor et al. 1986). On the basis of these measurements, the plasma environment at 1P/Halley is described briefly in this chapter, whereas detailed explanations are given later on.

In comparison to planetary atmospheres, cometary atmospheres are much larger due to the low gravity of the nucleus. Hence, the neutral gas envelopes expands to several million kilometres. The solar wind can enter the thin part of the neutral cometary atmosphere. In the uncharged state of the gas molecules, the interaction of the solar wind and the neutral gas is negligible as long as the collision frequencies are small, i.e. the densities are low. Nevertheless, solar UV-radiation leads to ionisation of the cometary neutral molecules and the interaction emerges. The cometary ions are accelerated by the convective electric field and incorporated in the solar wind (Section 3.1).

Because of the vast neutral coma the cometary plasma environment is extended to large distances as well. Johnstone et al. (1986) and McKenna-Lawlor et al. (1986) reported the detection of the first pick-up ions at a distance of about 7 million kilometres to the nucleus. These ions differ from the solar wind ions in their energy and phase space distributions. Correspondingly, upstream waves were measured at a distance of about 2 million kilometres to the nucleus (Neubauer et al. 1986).

Shortly after the first detection on cometary activity, at about 19:30 on the 13th of March 1986, the instruments observed a bow shock. Here the magnetic field strength jumps to about 18 nT (Figure 1.2) (Neubauer et al. 1986). The bow shock is triggered by the ongoing pick-up of the cometary ions, and observing the laws of conservation of momentum and energy the acceleration of the cometary ions leads to a deceleration of the solar wind. In the undisturbed solar wind, the flow speed is super-magnetosonic, i.e. faster than the magnetosonic speed. At the bow shock, the deceleration reduces the solar wind speed to subsonic speeds. Besides the jump in the magnetic field, a weak jump also occurs in the density, the velocity and the temperature, as reported by Balsiger et al. (1986). The JPA (Johnstone Plasma Analyser) instrument observed a number of sharp transitions with changes in the distribution of the ions in the vicinity of the bow shock (Johnstone et al. 1986). The position and behaviour of the cometary bow shock will be discussed in detail in Section (4.1).

After the bow shock crossing, the experiments onboard detected a region of intensive wave activity (Neubauer et al. 1986, Rème et al. 1986). Further inward, along the trajectory between 5×10^5 km and 1.4×10^5 km distance, the electron electrostatic analyser (Rème et al. 1986) identified a transition to an isotropic distribution of electrons, which

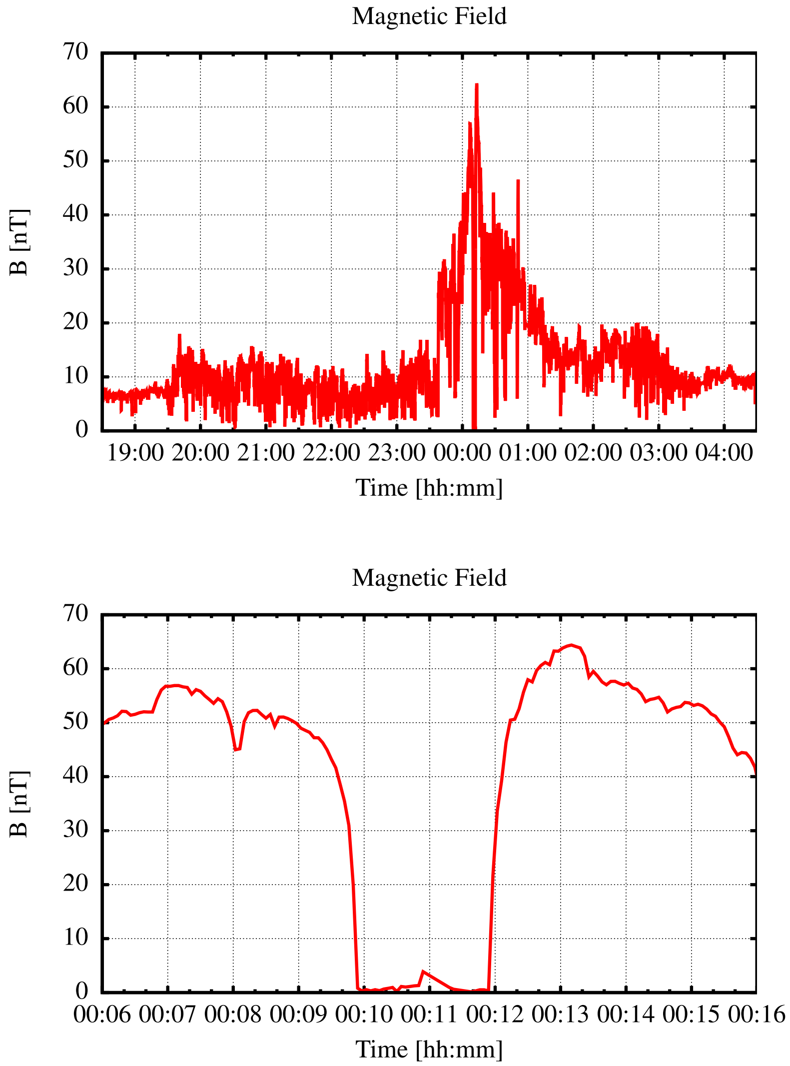

Figure 1.2: The magnetic field magnitude of the magnetometer experiment on board the Giotto spacecraft during the flyby at comet Halley on 13th and 14th March 1986 (Neubauer et al. 1986). Magnetic field vectors are averaged over 4 seconds. The time on the x-axis is given in hours and minutes. The upper panel shows the field strength of the bow shock crossing on the inbound path to the bow shock on the outbound path, whereas the lower panel only presents the data around the point of closest approach at 00:10:57 (GRT - Ground Received Time) on 14th March 1986. The timeformat is GRT.

is caused by collisions between charged particles and the neutral gas. Although cometary neutrals are ubiquitous in the coma, the collisions become dominant as soon as the frequency of collisions is high in comparison to characteristic scales of the particle motion. This transition is called collisionopause.

At a distance of about 1.3×10^5 km to the nucleus, the magnetic field strength jumps to values above 30 nT indicating the crossing of the so called magnetic pile-up boundary. Afterwards the spacecraft was located in the magnetic pile-up region, which is characterised by an increased magnetic field strength value. A maximum field strength of about

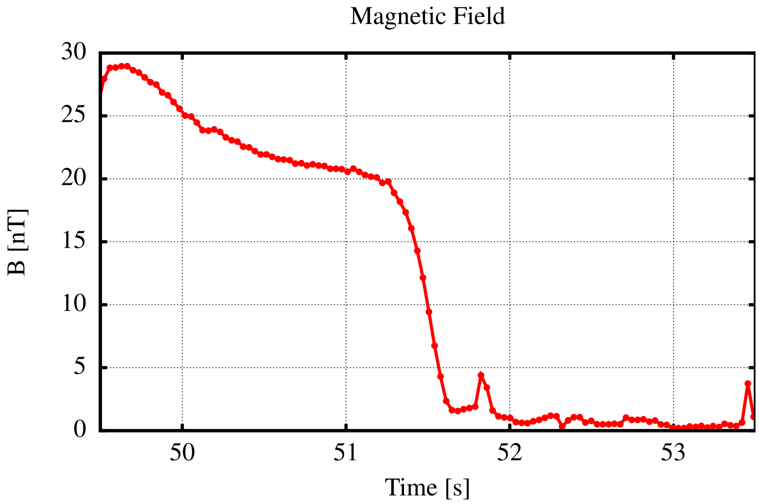

Figure 1.3: High resolution data from the Giotto magnetometer experiment at the cometary ionopause on the inbound path (Neubauer et al. 1986). The sampling rate of the dataset is 28.235 Hz and the spin is not removed from the data. The time on the *x*-axis is given in seconds of the 9th minute after midnight on 14th March 1986. The time-format is GRT (Ground Recieved Time). The closest approach to the comet was on the 14th March 1986 at 00:10:57 (GRT), which corresponds to 00:03 (UTC).

57 nT was reached at a distance of about 15 000 km to the nucleus (Figure 1.2). Immediately afterwards, when the spacecraft was at a distance of about 10 000 km, the HIS (high intensity spectrometer) data indicate the presence of a region of enhanced ion density (Balsiger et al. 1986). Additionally, the authors report that the plasma was nearly stagnant.

At a distance of about 4500 km, the spacecraft enters the diamagnetic cavity[5]. This is a region with a magnetic field strength of zero as theoretically predicted (cf. Wallis and Dryer 1976). The transition from the magnetic pile-up region to this region is called cometary ionopause[6] and is characterised by a remarkable decrease of the magnetic field strength. Within 25 km the magnitude drops by 20 nT to relatively small values, see Figure (1.3) (Neubauer 1988). In addition, the HIS experiment detected a sharp decrease in the ion temperature and the radial velocity of the ions increases to a value of about 1 km s^{-1}. Furthermore, Goldstein et al. (1989) found a peak of the density at the same location. The formation of this boundary is discussed in great detail in Section (4.2).

The diamagnetic cavity is the innermost plasma region which has been observed by spacecraft so far. On the outbound path the Giotto spacecraft passed again the cometary ionopause, the magnetic pile-up region and the bow shock, before Giotto entered the interplanetary space again (Figure 1.4).

The Giotto spacecraft was reactivated in 1992 to perform a second cometary flyby at comet 26P/Grigg-Skellerup (Neubauer et al. 1993). For this flyby the distance at the point of the closest approach was reduced to 330 km on the nightside. Nevertheless, a diamagnetic cavity could not be observed during this flyby nor at any other cometary spacecraft

---

[5] This region is also called cavity.

[6] The use of the terms diamagnetic cavity boundary surface, ionopause, contact surface, cavity surface or tangential discontinuity is controversially discussed.

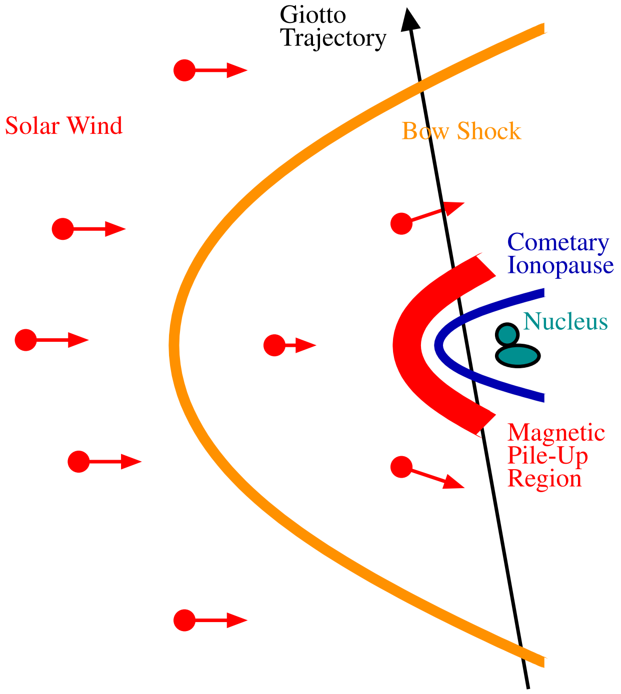

Figure 1.4: Sketch of the cometary plasma environment at comet 1P/Halley as observed by the European Giotto mission. The black arrow shows the trajectory of the Giotto spacecraft, which was tilted by 107° to the solar wind flow. The spacecraft crossed the bow shock (orange) at a distance of about 10^6 km. The size of the nucleus of 1P/Halley is only 15 km. The sketch is not true to scale.

mission. Table (1.1) lists information on all cometary flybys by spacecraft which were equipped with plasma instruments. Unfortunately, the recent missions Stardust, Deep Impact, and EPOXI did not carry instruments to measure plasma activities. In general, the existing observations are similar to each other but, caused by the different solar wind and comet parameters, trajectories and available data, many questions on the various boundaries and their properties remain open. For example, caused by the unique observation of the diamagnetic cavity at 1P/Halley by Giotto, it is unclear how the diamagnetic cavity behaves at different gas production rates or solar wind parameters. It is unclear as well if the surface of this region is stable and if it always prevents the magnetic field to penetrate the diamagnetic cavity. Observations of an akin region at Venus showed that magnetic flux ropes can penetrate through the Venus ionopause (Russell et al. 1980). It is also unclear, how the diamagnetic cavity develops when the comet approaches the Sun from large distances, since the solar wind and the scales of the plasma characteristics change as well. These are only a few questions regarding the cometary ionopause. A similar set of questions could be compiled for each other boundary in the cometary plasma interaction. Hence, they are the basis for the science objectives of the plasma instruments onboard the Rosetta spacecraft.

Table 1.1: The table lists the spacecraft flybys at comets in the past years. References: Richter et al. (2011), Tsurutani et al. (2013), Smith et al. (1986a), Reinhard (1986), Cravens and Gombosi (2004) and Coates and Jones (2009).

Comet	21P/Giacobini-Zinner	1P/Halley	26P/Grigg-Skjellerup	19P/Borrelly
Missions	International Cometary Explorer	Vega1, Susei, Vega2, Giotto	Giotto	Deep Space 1
Flyby date(s)	11.09.1985	6/8/9/14.03.1986	10.7.1992	22.09.2001
Closest approach distance [km]	7800	610	330	2171
Spacecraft velocity [km s^{-1}]	21	68.4	14	16.6
Heliocentric distance [AU]	1.03	0.89	1.01	1.36
Gas production rate [s^{-1}]	2.5×10^{28}	6.9×10^{29}	7×10^{27}	3.5×10^{28}
Bow shock distance along trajectory [km]	1.1×10^{5}	1.2×10^{6}	2.5×10^{4}	1.47×10^{5}
Observed peak in magnetic field [nT] (in-/out-bound)	58/57	57/65	88.7	83

1.3 The Rosetta Mission

The Rosetta mission is a Planetary Cornerstone Mission of the Horizon 2000 program of the European Space Agency (ESA) launched in March 2004. The mission schedule was influenced by the wish to study the evolution of the comet during its journey around the Sun. Thus, the spacecraft arrived at the comet close to its aphelion and the spacecraft has been escorting it during its journey since then. Rosetta also delivered the surface science package, the lander Philae. Philae landed on the nucleus and performed in-situ measurements on the surface.[7] Meanwhile, the Rosetta spacecraft stays close to the comet and performs in-situ measurements of the coma and remote measurements of the nucleus until the end of 2015. Those measurements will characterise the global properties of the comet, the dynamic properties, and the surface morphology. In addition, detailed studies on the chemical and isotopic composition will be performed. The interrelation between the volatiles and the refractories are a focus of the measurements as well. Finally, the Rosetta mission will investigate the evolution of the activity, the dust-gas interaction and the interaction between the solar wind and the cometary gas.

---

[7] See ESA Rosetta blog website: http://blogs.esa.int/rosetta/

1.3.1 A Portrait of Comet Churyumov-Gerasimenko

The comet 46P/Wirtanen had been selected as the initial target of the Rosetta mission. However, a delay of the launch combined with a short launch window (Verdant and Schwehm 1998) required the search for a new target comet. To achieve the scientific goals, an ordinary Jupiter family comet with adequate orbit was required. The new selected target then was comet 67P/Churyumov-Gerasimenko, which was the most suitable one.

67P/Churyumov-Gerasimenko was discovered by Klim Ivanovich Churyumov and Svetlana Ivanovna Gerasimenko in September 1969. A detailed report of the discovery is given by Lamy et al. (2007). Krolikowska (2003) studied the orbital evolution of the comet in the last 500 and the next 500 years. Their calculations reveal that the perihelion distance of the comet was between 2.5 and 2.9 AU in the 19th and 20th century. In addition, the calculations show that a dramatic change occurred in the year 1959 when the comet encountered planet Jupiter, where it was redirected to an orbit closer to the Sun by the planet's gravity. The perihelion distance of the new orbit is about 1.3 AU, whereas the previous perihelion distance was at about 2.7 AU (Hanner et al. 1985, Lamy et al. 2007). These authors inferred that this major event increased the activity of the comet, due to restructuring of the cometary surface and, based on that, the discovery was possible at the second perihelion after this event. In addition, Lamy et al. (2007) reported that the orbital period changed from 8.97 to 6.55 years. The calculations by Krolikowska (2003) show that the behaviour of the orbit is chaotic and the orbits are only well defined between the years 1700 and 2200. In 2200 another close encounter with Jupiter will again change the orbit of the comet.

At the current orbit, the orbit of the Rosetta encounter, the aphelion distance to the Sun was about 5.7 AU. The perihelion will be passed at a heliocentric distance of 1.24 AU on 13th August 2015. The semi-major axis of the orbit is about 3.46 AU and the eccentricity ε is 0.64. The orbital plane is tilted by about 7 degrees to the ecliptic plane.[8] More parameters are listed in Table (1.2). Based on these orbital properties this comet is a member of the Jupiter family (Lamy et al. 2007).

Lamy et al. (2007) and Lowry et al. (2012) studied the shape of the nucleus during the inactive phase close to the aphelion by using remote observations. The effective radius of the nucleus is about $r_{\mathrm{nuc}} = 1.93\,\mathrm{km}$ to $2.03\,\mathrm{km}$ (Lamy et al. 2008). It is defined by the radius of a sphere with the same volume of the actual nucleus. The axial ratios of the nucleus are $b/a = 1.239$ and $c/a = 0.819$. Based on this, it was rather expected to see a more rounded shape in the camera images, like that of 9P/Temple 1, than a *bi-lobed* shape, like that of 103P/Hartley. Contrarily, the first camera images obtained in July 2014 revealed that the nucleus is bi-lobed, and consists of a small lobe, a large lobe and a connection.[9]

The rotation axis of the nucleus was determined by Lowry et al. (2012) and Vincent et al. (2013a). They showed that 67P/Churyumov-Gerasimenko rotates with a sidereal period of about 12.76 hours. Based on their conclusions, the equinox on the nucleus is 50 days before the perihelion passage. Furthermore Vincent et al. (2013a) summarised, that the comet has a stable state of rotation, at least for the last two apparitions. However,

---

[8] See SPICE and JPL Small Body Database: http://ssd.jpl.nasa.gov

[9] See ESA Rosetta blog website: http://blogs.esa.int/rosetta/

Table 1.2: A collection of properties of comet 67P/Churyumov-Gerasimenko. The orbital elements are relevant for the forthcoming apparition of the comet.

Parameter	Value	Reference
Effective Radius	$r_{\mathrm{nuc}} = 1.93 - 2.03\,\mathrm{km}$	Lamy et al. (2008)
Rotation Period in 2009	$T_{\mathrm{rot}} = 12.76\,\mathrm{h}$	Lowry et al. (2012)
Rotation Period in 2014	$T_{\mathrm{rot}} = 12.40\,\mathrm{h}$	Mottola et al. (2014)
Aphelion Distance	$r_{\mathrm{h,max}} = 5.685\,\mathrm{AU}$	SPICE (Acton 1996)
Perihelion Distance	$r_{\mathrm{h,min}} = 1.243\,\mathrm{AU}$	SPICE (Acton 1996)
Semi-Major Axis	$r_{\mathrm{h,sma}} = 3.46\,\mathrm{AU}$	JPL Small Body Database
Inclination	$i = 7.04°$	JPL Small Body Database
Bulk Density	$\rho_{\mathrm{nuc}} = 370\,\mathrm{kg\,m^{-3}}$	Lamy et al. (2007)
Mass	$m_{\mathrm{nuc}} = 2.1 \times 10^{12} - 1.1 \times 10^{13}\,\mathrm{kg}$	Lamy et al. (2007)

new measurements obtained by Mottola et al. (2014) reveal that the rotation period today is only 12.40 hours.

As reported by Lamy et al. (2008), the albedo of the nucleus is between 0.039 and 0.043. This is similar to the mean albedo value of other comets. Besides this, the size of the nucleus is comparable to other nuclei. Lamy et al. (2014) studied the sizes of 65 elliptical cometary nuclei and found radii between 0.2 and 15 km. Moreover, most of them are below 5 km. Thus, the comet is probably a quite ordinary comet for a Jupiter family comet if there is an *ordinary comet* at all.

The gas production rate of 67P/Churyumov-Gerasimenko has been observed by various authors, e.g. Hanner et al. (1985), Schulz et al. (2004), and Schleicher (2006). Based on those measurements, Lamy et al. (2007) fitted a power law and obtained the total gas production rate versus the heliocentric distance, as shown in Figure (1.5). However, only very few remote measurements are available for larger heliocentric distances, which leads to a large uncertainty in the gas production rate at these distances. With the arrival of the Rosetta spacecraft at the comet, various instruments started their measurements to obtain a value for the gas production rate. Nevertheless, in order to plan the mission an estimation on the gas production rate and its evolution during the mission was and is needed far in advance. This is why the scientists of the instruments onboard Rosetta, the Science Working Team (SWT), agreed on two extreme scenarios: The high activity case (HAC) is a prediction of the highest possible gas production rate of the comet, and the low activity case (LAC) for a minimum activity, both shown in Figure (1.5) (Biele and Herfort 2012, Biele and Ulamec 2013). These values, which are listed in Table (1.3), are not obtained by a model, but rather derived from a simple extrapolation between various existing observations.

Recently, Snodgrass et al. (2013) reported that, based on an increased flux in photo-

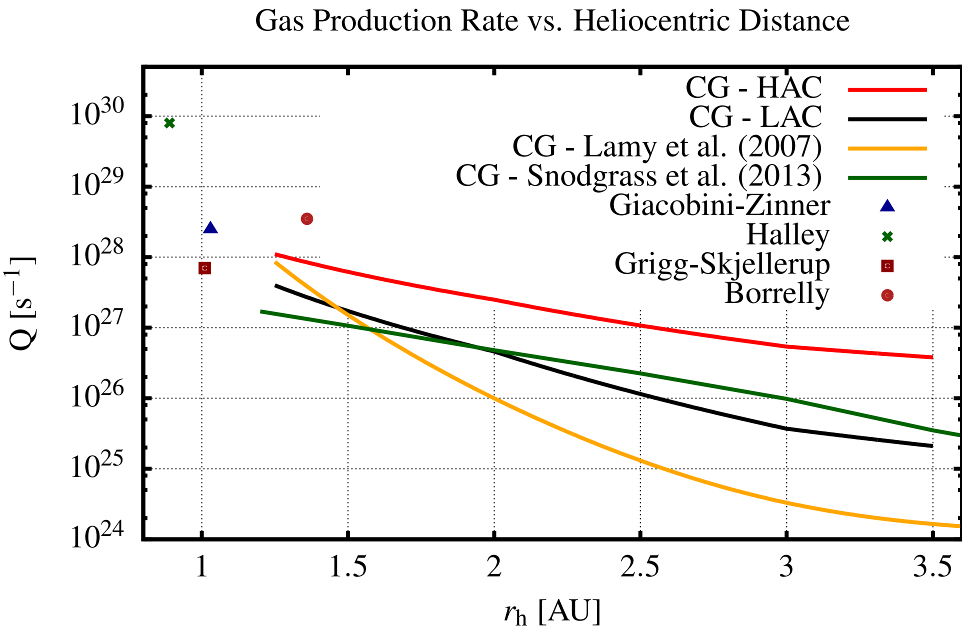

Figure 1.5: The gas production rates of various comets versus the heliocentric distance are shown. Close to 1 AU the gas production rate of comets which were targeted by a spacecraft mission, so far, are displayed. In addition, the figure shows predictions of the gas production rate of comet 67P/Churyumov-Gerasimenko during the Rosetta mission phase.

metric measurements, the activity of comet 67P/Churyumov-Gerasimenko already starts at a heliocentric distance of 4.3 AU. In contrast, former measurements detected the first signs of activity at a heliocentric distance of about 3.4 AU. However, the measurements by Snodgrass et al. (2013) only observed the dust activity, i.e. the reflection of sunlight from the dust particles but not the gas activity via emission lines, as done by Schulz et al. (2004) and Schleicher (2006). Snodgrass et al. (2013) used a model of the sublimation process reproduce the observed brightness of the comet. The resulting gas production rate of this ice sublimation model is shown in Figure (1.5) as well. The authors found that an active area of about 1.4% of the nucleus' surface is needed to reproduce the observed brightness with their model. However, close to perihelion an active area of about 4% is needed. The enhanced activity is confirmed by various observations gathered by the gas production model by Lamy et al. (2007).

In addition, the gas production rate of the comets visited by spacecraft, which are equipped with plasma instruments, are plotted there as well. It is obvious that the plasma interaction between 67P/Churyumov-Gerasimenko and the solar wind, which is triggered by the outgassing of neutral gas from the comet, will differ to a large extend from the observations made so far.

The activity of the comet will reach its maximum shortly after the perihelion passage, as it was observed during the past perihelion passages (Snodgrass et al. 2013). This is in agreement with measurements of the water production rate by Schleicher (2006) and the coma morphology by Vincent et al. (2013a). The maximum will occur about one month after perihelion. This might be caused by a heat wave propagating into the nucleus and reaching greater depths. Therefore, it triggers more sublimation of ice. Due to the

Table 1.3: The minimum and maximum gas production rates from the comet reference model during the Rosetta mission phase (Biele and Herfort 2012).

r_h [AU]		Q_{min} [s^{-1}]	Q_{max} [s^{-1}]
1.24	H_2O	$4 \cdot 10^{27}$	$1 \cdot 10^{28}$
	CO	$4 \cdot 10^{25}$	$5 \cdot 10^{26}$
	CO_2	$1 \cdot 10^{26}$	$8 \cdot 10^{26}$
	Total	$4.14 \cdot 10^{27}$	$1.13 \cdot 10^{28}$
2	H_2O	$4 \cdot 10^{26}$	$2 \cdot 10^{27}$
	CO	$2 \cdot 10^{25}$	$2 \cdot 10^{26}$
	CO_2	$4 \cdot 10^{25}$	$3 \cdot 10^{26}$
	Total	$4.60 \cdot 10^{26}$	$2.50 \cdot 10^{27}$
3	H_2O	$1 \cdot 10^{25}$	$3 \cdot 10^{26}$
	CO	$7 \cdot 10^{24}$	$9 \cdot 10^{25}$
	CO_2	$2 \cdot 10^{25}$	$1.5 \cdot 10^{26}$
	Total	$3.70 \cdot 10^{25}$	$5.40 \cdot 10^{26}$
3.5	H_2O	$1 \cdot 10^{24}$	$2 \cdot 10^{26}$
	CO	$6 \cdot 10^{24}$	$7 \cdot 10^{25}$
	CO_2	$1.4 \cdot 10^{25}$	$1.10 \cdot 10^{26}$
	Total	$2.10 \cdot 10^{25}$	$3.80 \cdot 10^{26}$

retardation of the heat wave, the maximum activity occurs after the insolation maximum. Such a delay of the daily activity has also been discussed by Prialnik et al. (2008). A second hypothesis which could explain the behaviour of the activity assumes that large grains are lifted and fragmented afterwards. This could also cause a delay but only of about 2 – 3 days (cf. Snodgrass et al. 2013). Alternatively, seasonal effects might cause the maximum activity after the perihelion passage. As reported by Vincent et al. (2013a) and Lowry et al. (2012), equinox is about 50 days prior to perihelion. Hence regions that were previously shadowed are exposed to sunlight and might cause an enhancement in sublimation.

1.3.2 The Spacecraft and Instruments

The design of a spacecraft which can achieve the scientific objectives of the Rosetta mission was challenging. Verdant and Schwehm (1998) summarised the objectives: firstly, the spacecraft needed to stay in deep space for more than 10 years prior to the start of its main mission phase. Secondly, during the mission the spacecraft experiences large variations of the heliocentric distance. Nevertheless, full scientific operations are required when the spacecraft arrives at the comet close to its aphelion.

Because of the decision to use only a photovoltaic system, the spacecraft needs large solar panels. Hence, two solar panels, each 14 metres long and 32 square metres large, have been mounted on the sides of the central frame of the spacecraft. This frame has a dimension of $2.8\,\mathrm{m} \times 2.1\,\mathrm{m} \times 2.0\,\mathrm{m}$ (Glassmeier et al. 2007a). The spacecraft communicates with the operation centre on Earth via a high gain antenna with a steerable dish with a diameter of 2.2 m. The signals received from Earth are delayed (up to 40 minutes) which is caused by the large distance between the spacecraft and Earth. Due to the fact that the spacecraft stays close to the comet, a highly autonomous spacecraft is required. This is also important for the lander Philae, which finally performed an autonomous landing.

The lander Philae is equipped with ten instruments in order to investigate the local surface and subsurface properties of the nucleus in-situ and the orbiter is armed with eleven instruments to address the main scientific questions in the coma, on the entire surface of the nucleus, and the internal structure of the primordial object. The orbiter instruments are listed in Table (1.4). A list of the lander instruments is given in Glassmeier et al. (2007a).

The main plasma experiment onboard the orbiter is the Rosetta Plasma Consortium (RPC). It is a group of five individual instruments plus a central data and communication unit, the plasma interface unit (PIU) (Carr et al. 2007). The consortium approach allows a coordination of operation, measurements as well as scientific activities. The main scientific objective of RPC is the study of the evolution of the interaction between the comet and the solar wind. Based on that, RPC wants to study the formation of the structures and boundaries which have been observed during various cometary spacecraft missions. This will give information on the cometary activity, one of the major goals of the mission. In addition, in cooperation with the ROMAP (Rosetta Magnetometer and Plasma Monitor) instrument the RPC instruments search for a remanent magnetisation of the nucleus and will estimate the conductivity of the nucleus.

The Ion Composition Analyser, ICA (Nilsson et al. 2006), and the Ion and Electron Sensor, IES (Burch et al. 2006), are able to measure the distribution functions of the ions. The ICA sensor can resolve the masses of the solar wind and various cometary ion species. The energy range of the sensor is between 25 eV and 40 keV. However, the mass-resolution is only sufficient to distinguish between the major ion groups. For example, the ions O^+, N^+, and H_2O^+ are not distinguishable by the sensor.

In contrast to ICA, IES is not able to separate the ions into mass groups. Nevertheless it can measure the electron distribution functions on a second sensor and has a finer spatial resolution. The energy range of these sensors is between 1 eV and 22 keV with an energy resolution of $\Delta E/E = 0.04$. Both instruments have the same field of view of $90^\circ \times 360^\circ$. However, caused by the fact that the instruments are mounted on different places on the spacecraft and have a different orientation the actual field of view of the instruments differ. Both instruments use an electrostatic analyser which deflects the charged particles onto microchannel plates according to their energy. In the ICA experiment the charged particles pass a mass analyser, which deflects the ions by using a cylindrical magnetic field, before the ions are detected via microchannel plates. Based on the measured distribution function the instruments are able to determine the density, velocities, and temperatures of the various plasma species. However, it has to be ensured that the distribution function

Table 1.4: The instruments onboard the Rosetta spacecraft.

Instrument	Described by	Main Scientific Objectives
ALICE UV spectroscopy λ =70 nm to 205 nm	Stern et al. (2006)	- characterisation of the coma - coupling of the nucleus and the coma
CONSERT radio waves	Kofman et al. (2007)	- internal structure of the nucleus
COSIMA secondary ion mass spectrometry	Kissel et al. (2007)	- cometary dust environment - composition of grains
GIADA mass/size and velocity dust measurements	Colangeli et al. (2007)	- cometary dust environment - dust flux evolution
MIDAS atomic force microscope	Riedler et al. (2006)	- cometary dust environment - structure of nm to µm dust grains
MIRO microwave spectroscopy λ = 0.5 mm and 1.3 mm	Gulkis et al. (2006)	- evolution of gas production rate - thermal emission
OSIRIS narrow and wide angle camera λ =250 nm to 700 nm	Keller et al. (2007)	- properties of the nucleus - activity of the nucleus
ROSINA neutral gas and ion mass spectroscopy m =1 amu to 300 amu neutral gas pressure	Balsiger et al. (2007)	- evolution of the coma - elemental and isotopic abundances - extended sources
RPC ion composition ion and electron sensor Langmuir probe fluxgate magnetometer mutual impedance probe	Carr et al. (2007)	- evolution of the coma - solar wind interaction - plasma processes in the inner coma - conductivity of the nucleus
RSI radio sounding	Pätzold et al. (2007)	-mass and bulk density of the nucleus - size and shape of the nucleus - plasma in the coma
SREM standard radiation environment monitor		
VIRTIS infrared spectrometry λ = 0.25 µm to 5 µm	Coradini et al. (2007)	- characterisation of outgassing material - thermal evolution

is sufficiently covered by the measurements, i.e. the impact of the spacecraft orientation and the blocked field of view have to be considered.

Another way to determine the density and the temperature of the plasma species, especially of the electrons, is the Langmuir probe instrument, LAP (Eriksson et al. 2006). It consists of a pair of Langmuir probes mounted on two booms, about 1.6 and 2.2 m long. The probes themselves are spheres with a diameter of 5 cm covered by titanium nitride. The instrument is able to switch between various modes. In the basic mode a voltage is applied to the probes and the current towards the probes is measured. More information is obtained by a bias sweep, which varies the potential of the probes and records the current collected by the probes. By using theoretical models, some plasma parameters can be determined. The experiment is also able to determine fluctuations of the electric field up to 8 kHz but only in one direction since only two probes are mounted to the spacecraft.

One of the Langmuir probes can also be used by the Mutual Impedance Probe, MIP (Trotignon et al. 2006). In this case, the experiments operate in Long Debye Length mode and can measure Debye lengths λ_D between 10 and 200 cm. Furthermore, MIP uses its own antennas and measures Debye lengths between 0.5 and 20 cm, which will be used in the dense and cold inner coma. The principle idea of the instrument is the emission of a radio signal with a frequency range containing the plasma frequency, and to measure a difference in voltage between two receiving electrodes. This allows to calculate the mutual impedance which depends on the properties of the surrounding plasma. In the obtained spectra the plasma frequencies and other waves, is the plasma permits a transmission, can be determined. By comparison to models information on the electron density and temperature can be deduced.

Finally, the suite of plasma instruments is completed by a magnetometer experiment, MAG (Glassmeier et al. 2007b). Two triaxial fluxgate magnetometers are mounted on a spacecraft boom at a distance of about 1.5 m to the central frame of the spacecraft. In order to identify disturbance from the spacecraft, the second sensor is located 15 cm closer to the central spacecraft frame. The instrument can measure magnetic field up to about 16000 nT, which is far above the maximum magnetic field strength observed at the flyby at comet 1P/Halley, but which is sufficient for the study of the magnetic field present during Earth slingshot manoeuvres. In the highest data rate the instrument generates magnetic field vectors with a frequency of 20 Hz. Hence, waves with frequencies up to 10 Hz can be analysed. The resolution of the instrument is 31 pT. However, magnetic disturbances by the spacecraft and its instruments are in the order of a few nT. In addition, the determination of the instrument offsets and the remaining spacecraft field is challenging because they change with temperatures, over time, and are closely connected to the instrument states of the other instruments onboard.

Besides the RPC experiments, the ROMAP (Rosetta Magnetometer and Plasma Monitor) experiment (Auster et al. 2007) is able to determine plasma parameters as well. Onboard the lander Philae this experiment measures the magnetic field with a fluxgate magnetometer, as well as ions and electrons. The latter ones are detected by an electrostatic analyser and a Faraday cup. Due to the location of the instrument, i.e. on the surface of the nucleus, the particle detector will be able to measure the density close to the surface. The main scientific objective of ROMAP is the determination of the magnetisation of the nucleus. Furthermore, this experiment will also help to understand physics in the coma since it allows synchronous measurements at two different locations.

The prime objective of the ROSINA (Rosetta Orbiter Spectrometer for Ion and Neutral Analysis) experiment (Balsiger et al. 2007), which is located on board the orbiter, is the analysis of the neutral gas coma. This will be done with a remarkably high resolution of up to $m/\Delta m = 3000$ at 1% peak height. ROSINA is also able to analyse low energetic cometary ions, i.e. ions shortly after their ionisation or in the diamagnetic cavity, where the plasma is cooled by collision with the neutral gas.

Finally, the Radio Science Investigations, RSI (Pätzold et al. 2007), is able to contribute to the plasma measurements. By sending a radio signal to Earth through the cometary coma, the signal is modified in speed and phase. Those differences can be used to determine the number of electrons between the spacecraft and Earth. However, von Oertzen (2003) found that the expected plasma densities in the coma will be quite low, even close to perihelion, which will make a survey on the electron density via the RSI instrument unlikely. If any measurements will be conducted, they will take place only close to the perihelion, where the gas production rate is the highest.

1.3.3 The Mission and its Planning

On 2^{nd} March 2004 the Rosetta spacecraft was launched by an Ariane-5G+ rocket from the Guiana Space Center in Kourou, French Guiana. The extensive cruise phase lasted 10 years until May 2014. In order to reach 67P/Churyumov-Gerasimenko, Rosetta performed a series of gravity assists, see Figure (1.6) (Glassmeier et al. 2007a, Edberg et al. 2009, Eastwood et al. 2011). In addition, the spacecraft passed two asteroids, the asteroid 2867 Steins, and the asteroid 21 Lutetia, where the scientific instruments determined various properties. Among others the magnetometer estimated the remanent magnetisation of the asteroids. For Lutetia Richter et al. (2012) found a maximum global magnetisation below $2.1 \times 10^{-3}\,\mathrm{A\,m^{-1}}$.

Finally, at the end of May 2014 the spacecraft performed a last big manoeuvre to reach the comet (Glassmeier et al. 2007a). The distance to the comet was reduced stepwise, thereby the spacecraft approached the comet from the dayside. After the determination of the comet's gravity potential as well as its shape and surface morphology, which is used for the navigation of the spacecraft, the distance to the comet is reduced to 30 km and later on 10 km but only for a very short time. In November 2014 Philae was separated from the spacecraft and descended slowly to the surface. During the first operation phase of the lander Rosetta stayed close to the nucleus. Afterwards, the extended monitoring phase has started in which different types of orbits and trajectory segments will be flown.

Close to the comet, the neutral cometary atmosphere affects the attitude and the trajectory of the spacecraft. A drag force from the neutral gas acts on the spacecraft, especially on the large solar panels. Since the panels are always oriented towards the Sun, the drag force is most efficient to disturb the orbit when the spacecraft is in a subsolar position. The force is minimal when the spacecraft is at the terminator plane, where the solarpanels are parallel to the expected neutral gas flow. However, an anisotropic outgassing leads to the modification of the neutral gas flow and a different force acting on the spacecraft. Other error sources are the unknown and maybe asymmetric gravity potential and the solar radiation pressure force.

Because of the drag force, *classical* bound orbits are not possible all the time. Instead, either far or close flybys can be flown by the spacecraft. A far flyby is characterised by

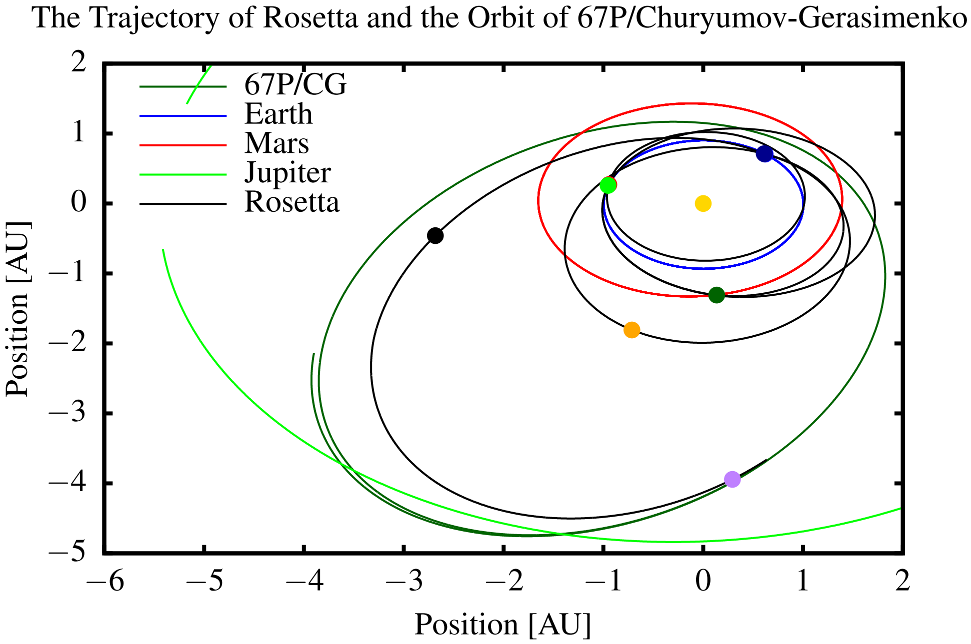

Figure 1.6: The journey of the Rosetta spacecraft and the orbit of 67P/Churyumov-Gerasimenko. The coloured bullets are major events of the mission, such as the launch, the Earth flybys, the asteroid flybys or the last rendezvous manoeuvre. The red bullet, covered by the light green bullet, marks the position of the first gravity assist by Earth. A gravity assist at Mars follows (dark green bullet) and a second assists at Earth (light green bullet). In September 2008, Rosetta flew by the asteroid 2867 Steins (orange bullet) before a last gravity assist manoeuvre was performed at Earth (dark blue). The second asteroid flyby at asteroid 21 Lutetia is marked by a black bullet. The last big manoeuvre before the arrival in May 2014 is highlighted by a violet bullet. The yellow bullet is the Sun. The orbit of Earth is marked in blue, the orbit of Mars in red, and the orbit of comet 67P/Churyumov-Gerasimenko is shown for its apparitions in 2015 in dark green.

a closest approach distance of about 50 km or even larger, depending on the gas production rate of the comet, and a spacecraft relative speed to the comet of about $0.5\,\mathrm{m\,s^{-1}}$ to $1\,\mathrm{m\,s^{-1}}$. At a close flyby Rosetta passes the comet at a much closer distance, i.e. 8 km to 30 km. Therefore, a higher spacecraft velocity is required. After closest approach, the spacecraft moves to large cometocentric distances as a consequence of the navigation constraints (Companys 2012).

According to RSGS-Team (2013), the entire extended mission phase is split into two-week segments which are allocated to four different disciplinary groups (DG), each of them linked to a specific scientific objective of the mission, e.g. the study of the nucleus, the gas and dust composition, or the activity. During the skeleton planning phase, the first phase in the mission planning, the DGs suggest certain measurements during those segments and propose a trajectory design. The discussion in the DGs are ongoing until the 21st week before the execution of the first short term planning (STP) segment of a long term planning (LTP) segment. A STP segment lasts a week. Four STPs roughly cover a month, and these are grouped as medium term planning (MTP) cycles. Then again four

MTP segments build a long term planning, LTP, segment. The entire time of the mission is structured in this way.

Figure (1.7) shows a simplified version of the planning process. During the weeks 20 to 17, before the execution, the LTP cycle continues and the Science Working Team (SWT) finally decides on a trajectory for the entire LTP segment. A trajectory request has to be sent to the mission operations centre (MOC) at the end of week -17. To give an example: The first segment of LTP 5 will be executed in mid-March, but the last possible date for change of the trajectory is already in mid-November. The MOC checks the trajectory during the weeks 16 to 13 prior to the first execution and the instrument teams and the science ground segment (SGS) can start their MTP activities of the first MTP block in the LTP in week -12. At the end of week -9, an attitude request will be sent to MOC, which will perform checks during the weeks -8 till -5. Four weeks before the first execution, the approved pointing and resource envelopes arrive at the SGS and the instrument teams. They can finalise their command series and send them to the MOC a week before the execution. The MOC performs a last validation of the payload and the spacecraft operations. In the following week the commands will be executed on the spacecraft (S/C). Because the mission lasts for about one and a half years, several planning stages for different segments have to run in parallel most of the time.

Based on this, the following main constraints on the mission planning are given. Firstly, the trajectory has to be fixed four months before the execution of the first command, therefore, the trajectory planning requires a proper prediction of the gas production rate. However, the development of the gas production rate of the comet is unknown. Therefore, the mission uses two different gas production rate estimations. The preferred activity case (PREF), a modified LAC, is the best possible estimation of the gas production rate of the comet, which is available four months in advance. In a first attempt, the spacecraft tries to fly the trajectory of this preferred case. However, if the actual gas production rate exceeds the preferred case, the spacecraft trajectory will be changed and the HAC trajectory will be flown. This is why all planning stages, except for the STP, have to be done for a high activity case and for the preferred activity case. Consequently, the spacecraft can hardly react on new findings, e.g. an new jet-like feature. Their detection by in-situ instruments is thereby only by chance. Or if their properties, the orientation, remain constant for about 4 months.

Secondly, the attitude of the spacecraft has to be fixed two months prior to the execution. And finally, the envelopes of the resources also have to be defined two months in advance. This means that the upper limits on power and data rate are fixed as well. For the plasma instruments onboard the latter constraints restrict the instruments to react on solar events like a coronal mass ejection or the crossing of a heliospheric current sheet.

In addition, the resources are already allocated to the instruments during the skeleton planning phase in the DG meetings and in the LTP stage only a fine tuning takes place. This keeps the workload manageable and the discussions short in the LTP stage. Consequently, at the planning stage of the disciplinary groups each instrument team should already have a detailed concept of their measurements.

RPC should be aware of the fact that the measurements can only be performed successfully if the spacecraft is in an appropriate position, e.g. at the bow shock or in the diamagnetic cavity, and if the instruments are in an appropriate mode, which requires a suitable data rate. Besides this, the particle instruments, IES and ICA, request a pointing

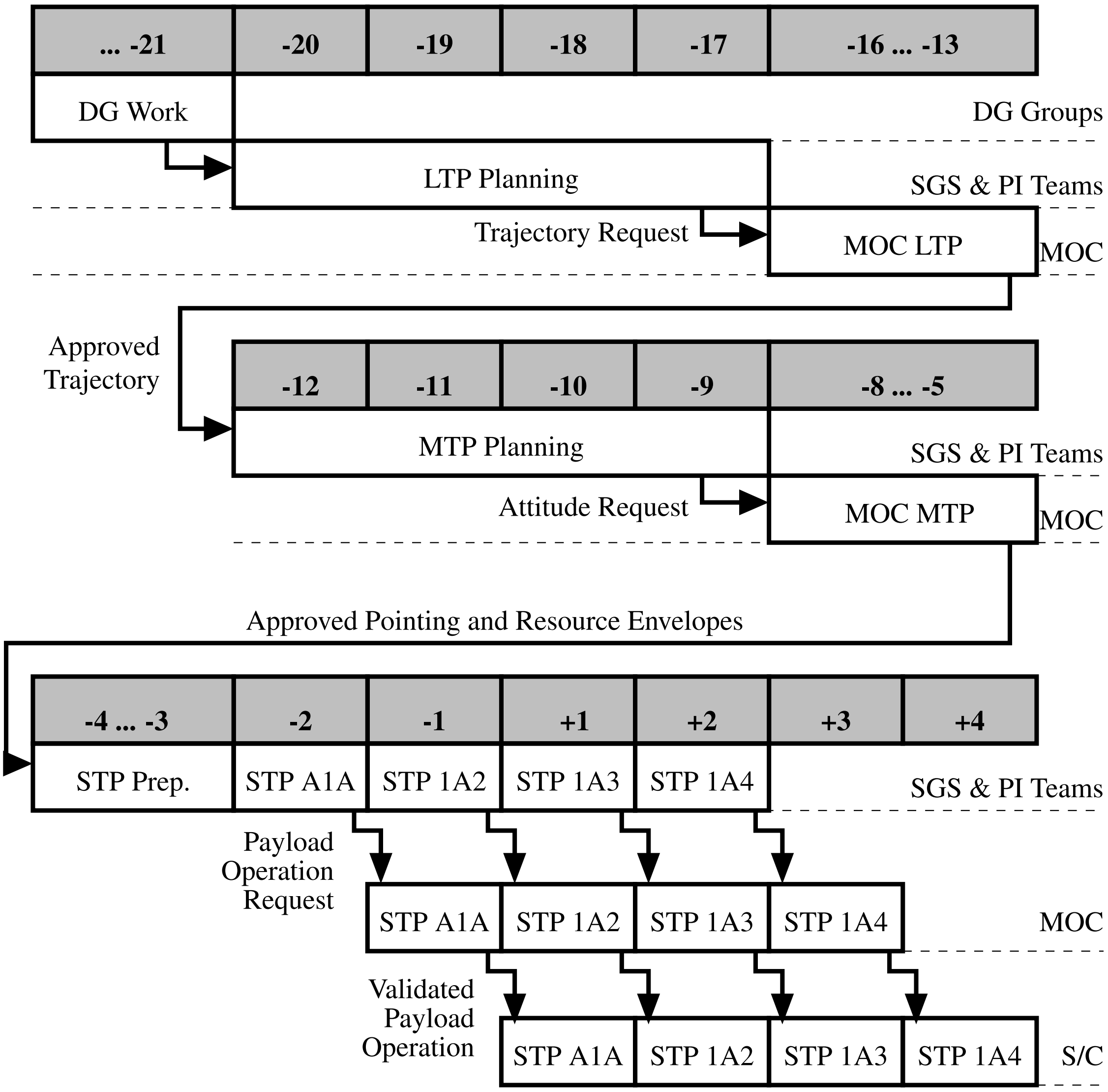

Figure 1.7: The planning cycles of the planning process in the Rosetta mission, according to Almeida (2013). S/C denotes spacecraft.

for some of the measurements. Overall RPC has about 40 different measurement objectives, which are defined by the data rate, a pointing request and a description of the requested region. By using these definitions the so-called Windows of Opportunities have to be calculated. These windows indicate if a certain measurement is possible at a certain time, see Figure (1.8).

In summary, it can be emphasised that the key element for the scientific success for the RPC instruments, and by this to some extend of the Rosetta mission as well, is the detailed planning of the mission. It defines if an observation of a certain structure or boundary in the plasma interaction is possible or not. This means, that only if the spacecraft is at an appropriate position at a certain time, the measurements can be conducted. However, in order to plan the RPC measurements, extensive modelling of the plasma interaction has to be done in advance.

One of the aims of this thesis is to use various plasma models which are capable to

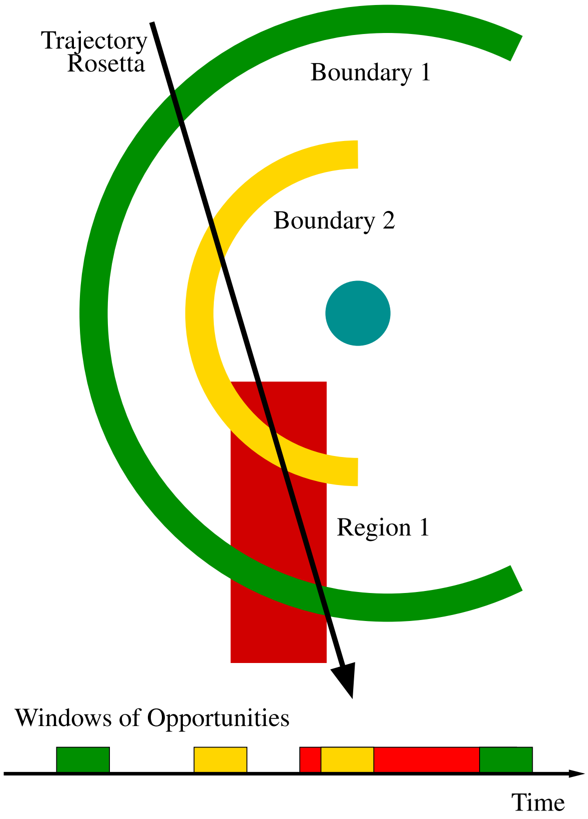

Figure 1.8: A sketch of the cometary plasma environment, which reveals two boundaries, e.g. the bow shock and the ionopause, and a region, e.g. the location of a jet. Besides that the trajectory of spacecraft is shown. Whenever the spacecraft crosses a certain region or boundary a Window of Opportunity opens on the timeline, in the bottom part of the sketch. The nucleus is shown by the cyan circle.

describe the processes in the cometary environment. In a first step, a model which is able to describe the plasma interaction from the very weak stages to the very active stages of comet 67P/Churyumov-Gerasimenko has to be developed, configured, and validated. In the second and major step then is the investigation of the structures and boundaries in the cometary plasma environment at the different stages by the means of this model. Thereby comparisons to former studies have to been carried out in order to proof the model and its capabilities.

The final aim of this thesis is to make the best possible predictions of the cometary plasma interaction usable for the Rosetta mission. Hence, the model results should be transformed into the Windows of Opportunities, which are required by the mission planning to schedule the measurements. Only by doing so, the scientific success of the RPC instruments can be guaranteed and maximised.

2 Modelling of the Cometary Plasma Environment

The pioneering work by Biermann et al. (1967) was the first attempt to model the cometary plasma environment. The authors investigated the deceleration of the solar wind flow due to massloading by means of a stationary, one-dimensional fluid model. The ionisation of the cometary neutral molecules, which initiates the interaction, is described in this approach by a mass source which adds mass into the plasma flow. Since the newborn ions are nearly resting with respect to the solar wind, they are accelerated by the flow. Consequently, the velocity of the flow decreases, which is the main aspect for the solar wind interaction with the comet.

Since these early days of modelling the cometary plasma environment, the knowledge of the properties of the comet and its cometary atmosphere as well as about the processes taking place in this environment increased significantly. This became possible due to more complex modelling techniques and several spacecraft missions to comets in the past years. The main purpose of this chapter is to give a detailed description of the important properties and processes in the cometary environment which have an impact on the plasma. Hereby, the focus is mainly on comet 67P/Churyumov-Gerasimenko and the Rosetta mission. The different modelling techniques for the plasma environment are presented in this chapter as well. These techniques are the foundations for the investigations of the plasma environment at weakly active stages and strongly active stages, which are discussed in the following Chapters (3) and (4).

This work discusses and uses various modelling approaches. The models depend on each other and each of the models describes the comet in a slightly different way. Therefore, this chapter is structured as follows. At the beginning, the properties of the incoming plasma, the solar wind, are presented in Section (2.1). Afterwards the alleged obstacle, the nucleus, is discussed. It follows in Section (2.3) a description of the properties of the neutral gas coma and the processes therein, which have an impact to the plasma. The different possibilities to describe the cometary plasma environment are presented, afterwards. Among them one can find the hybrid model. Its numerics and the modelling of the discussed processes in the hybrid framework are finally presented in Section (2.5).

2.1 Properties of the Solar Wind

While the comet is approaching the Sun, the properties of the supersonic solar wind as well as the interplanetary magnetic field change significantly, spatially and temporarily. Unfortunately, it is not possible to forecast these changes on time scales, which would

Table 2.1: Characteristic parameters of the solar wind at a heliocentric distance of $r_0 = 1\,\mathrm{AU}$ (Hansen et al. 2007).

Quantity	**Value**
solar wind number density $n_{\mathrm{SW},0}$	$10\,\mathrm{cm}^{-3}$
solar wind velocity $u_{\mathrm{SW},0}$	$400\,\mathrm{km\,s}^{-1}$
solar wind ion temperature $T_{\mathrm{SW,i},0}$	$5 \times 10^4\,\mathrm{K}$
solar wind electron temperature $T_{\mathrm{SW,e},0}$	$1 \times 10^5\,\mathrm{K}$
strength of interplanetary magnetic field $B_{\mathrm{IMF},0}$	$7\,\mathrm{nT}$
Parker angle θ_0	$45°$

be required for the instruments to request a modified pointing or a different data rate in the Rosetta mission planning. Thus, for the planning of the mission nominal values of the solar wind are used. In Table (2.1) nominal parameters of the solar wind at 1 AU according to Hansen et al. (2007) are listed.

Since the comet orbits the Sun on its Keplerian orbit between 1.24 AU and 5.17 AU and close to the ecliptic plane, the solar wind parameters are extrapolated to these distances by applying the model by Parker (1958). The model predicts that the solar wind speed is approximately constant between those distances, which has been verified by measurements onboard the Voyager 2 and IMP 8 spacecraft (Richardson et al. 1995). Musmann et al. (1977) studied the solar wind magnetic field between 0.3 AU and 1.0 AU and found that the measured magnetic field profile is in agreement with the simple solar wind model by Parker (1958). As a consequence of the continuity equation, the density of the flow is described by

$$n_{\mathrm{SW}}\left(r_{\mathrm{h}}\right) = n_{\mathrm{SW},0}\left(\frac{r_0}{r_{\mathrm{h}}}\right)^2 , \tag{2.1}$$

where $n_{\mathrm{SW},0}$ denotes the solar wind density at a reference distance r_0. According to the model by Parker (1958), the interplanetary magnetic field can be obtained by

$$B_{\mathrm{IMF,r}}\left(r_{\mathrm{h}}\right) = B_{\mathrm{IMF},0}\frac{r_0^2}{r_{\mathrm{h}}^2} \tag{2.2}$$

$$B_{\mathrm{IMF},\theta}\left(r_{\mathrm{h}}\right) = 0 \tag{2.3}$$

$$B_{\mathrm{IMF},\phi}\left(r_{\mathrm{h}}\right) = B_{\mathrm{IMF,r}}\left(r_{\mathrm{h}}\right)\frac{\omega}{u_{\mathrm{SW}}}\left(r_{\mathrm{h}} - r_0\right)\sin\theta , \tag{2.4}$$

where $B_{\mathrm{IMF},0}$ is the strength of the interplanetary magnetic field at a reference distance of r_0 to the Sun. The rotation frequency of the Sun is $\omega = 2.6 \times 10^{-6}\,\mathrm{rad\,s}^{-1}$ and u_{SW} denotes the solar wind speed (Kivelson and Russell 1995).

More sophisticated solar wind models, e.g. Zieger and Hansen (2008), try to propagate fluctuations of the solar wind to larger heliocentric distances by using real time data from other satellites in the solar system or solar observations. However, Zieger and Hansen (2008) applied a one-dimensional magnetohydrodynamic (MHD) approach. This model can propagate the velocity of the solar wind or the density, but it is not able to propagate the magnetic field orientation to larger distances correctly, which will be important for the data analysis afterwards.

2.2 The Nucleus

The nucleus initially causes the entire interaction since neutral gas emanates from its surface. However, as long as the neutral gas coma is modelled separately, the actual nucleus only plays a minor part in the interaction. The neutral gas coma is intensively discussed in the next section, whereas this section focusses on the remaining possibilities which could have an impact on the plasma environment. A sketch of the various processes taking place at the nucleus is shown in Figure (2.1).

Besides the thermal gas production, an additional mechanism to generate a gaseous envelope around the nucleus is the sputtering of ions from the nucleus' surface. This mechanism is most productive when the nucleus is exposed to the solar wind and protons interact directly with the bleak nucleus' surface. In contrast, if the solar wind is excluded from the innermost region, like in case of 1P/Halley during the Giotto flyby, the amount of sputtered ions is zero. At very large heliocentric distances 67P/Churyumov-Gerasimenko only has a very low gas production rate and the solar wind can reach the surface. In this case sputtering of the nucleus surface material into free space by solar wind particles occurs. The sputtering yield of water ice was measured by Shi et al. (1995). They reported that the yield is below 100 molecules per impacting ion at target temperatures of about 120 K, which is roughly the temperature of an inactive nucleus (Prialnik et al. 2008). The flux of ions which impact on the nucleus' surface can be calculated by the solar wind density, the velocity and the area of the illuminated surface of the nucleus. When using solar wind parameters at 3.5 AU, corresponding to the comet's location at Rosetta's arrival in August 2014, a flux of $3.2 \times 10^{11}\,\mathrm{m^{-2}\,s^{-1}}$ hits the surface. Estimating the exposed surface by a circle with a radius of 1.7 km, a maximum number of $3 \times 10^{18}\,\mathrm{s^{-1}}$ molecules may trigger the sputtering of molecules and, based on the results of Shi et al. (1995), up to $3 \times 10^{20}\,\mathrm{s^{-1}}$ molecules escape from the nucleus and form a small exosphere. However, this gas production rate is about five magnitudes below the gas production rate of the ice sublimation even in the lowest predicted gas production rate of model comet 67P/-Churyumov-Gerasimenko at 3.5 AU (Lamy et al. 2007). Therefore, the impact of the sputtering is only of minor importance for the entire plasma interaction.

Due to absorption of solar wind particles on the nucleus surface, a wake structure is triggered on the nightside of the nucleus. In case of an inactive comet the density in this wake is reduced. Thus, the cometary wake is comparable to the wake of the Moon or of asteroids. As known from various simulations and measurements of the Moon's wake, e.g. Trávníček (2005) and Wiehle et al. (2011b), it is a source of various waves, for example fast and whistler waves. The length of the wake is estimated to about 10 radii of the obstacle[1] (Coates 1997), i.e. in case of 67P/Churyumov-Gerasimenko about 17 km. However, due to the small size of the nucleus, the kinetic effects of the ions as well as of the electrons need to be taken into account because the electron gyroradius is about $r_{\mathrm{gyr,e}} \approx 3\,\mathrm{km}$, for solar wind conditions at 3.5 AU, which is as big as the nucleus itself.

---

[1] This depends on various parameters, e.g. the temperature of the plasma.

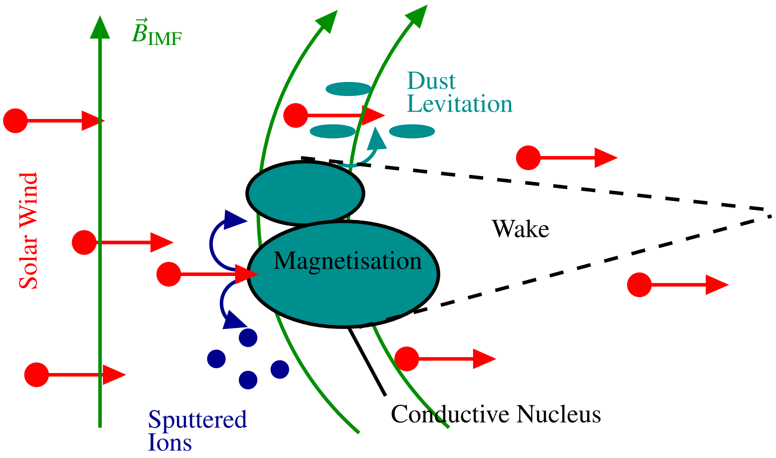

Figure 2.1: Sketch of the interaction between the inactive nucleus and the solar wind, adopted from Coates (1997). The incoming plasma leads to sputtering of surface material and a possible charging of the nucleus. Based on that also dust may levitation. The wake behind the nucleus is triggered by the absorption of the solar wind.

Nevertheless, the effects of the wake on the global plasma interaction are expected to be negligible because the wake is very small in comparison to other structures.

Another effect caused by the nucleus, and not directly connected to its thermal activity, is the surface charging. The impact of the solar wind ions onto the surface and subsequent sputtering lead to a surface charging on the dayside. This result in electric fields at the terminator (cf. Zimmerman et al. 2014), which lead to the levitation of additional dust particles (Szego et al. 2014). The electric fields are only present close to the nucleus. Therefore, their impact on the plasma environment is only of minor importance.

The electrical conductivity of the material in the cometary nucleus varies eminently as listed in Constantinescu et al. (2012). However, the small size of the nucleus of 67P/-Churyumov-Gerasimenko leads to a diffusion time of the magnetic field of only a few milliseconds in case of an ice sphere with a conductivity of $10^{-2}\,\mathrm{S\,m^{-1}}$. This would lead to a displacement of a magnetic field line by only a few hundred meters over a length of 4 km at a solar wind speed of $u_{\mathrm{sw}} = 400\,\mathrm{km\,s^{-1}}$. Thus, a detectable draping of the magnetic field caused by the bleak nucleus is not expected.

In case of a remanent magnetisation of the nucleus (Nübold 2000, Nübold et al. 2003, Auster et al. 2007, Fu and Weiss 2012) a small signature of the nucleus in the magnetic field data is expected. In case of an inactive nucleus this would be the same type of interaction as triggered by an asteroid. This interaction is discussed in detail in Section (3.3). One can anticipate that the effect onto the global plasma environment caused by the nucleus itself is a very minor one.

2.3 The Coma - the Cometary Atmosphere - and Processes Therein

In general, an atmosphere is the gaseous envelope around an object, e.g. a planet, which has a sufficient gravitation to keep the gas at the object. In the topmost layer of an atmosphere, its exosphere, the number density of molecules is low and the mean free paths are large. For that reasons collisions are unlikely. In addition, the velocity of the gas is above the escape velocity so that the molecules can escape into free space (Raith 1997). In this respect, the coma, the gaseous envelope around the nucleus, is not an atmosphere because the gas is not held at the nucleus due to gravitation. Since the mean velocity of the neutral gas at a comet is in the order of $1\,\mathrm{km\,s^{-1}}$, this velocity is above the escape velocity. Consequently, all neutral molecules can escape into free space. However, close to the nucleus collisions between the neutral molecules are important, as well as chemical reactions. Based on that, the term of an exosphere is not appropriate for the gaseous envelope. Thus, in this work the terms coma and cometary atmosphere are used interchangeably for the gaseous envelope around the comet.

Apart of the effects of the low gravity, the coma is similar to an ordinary planetary atmosphere in the Solar System in many aspects. Thus, various processes, such as ionisation, binary collisions, charge exchange of various molecules, atoms, ions and electrons, and recombination of ions and electrons take place (cf. Bhardwaj and Haider 2002, Schunk and Nagy 2009, Bhardwaj and Raghuram 2012). However, based on the fact that the cometary nucleus has a very low mass, the atmospheric profile differs from its planetary counterpart. Furthermore, the approach of the comet to the Sun leads to large variations in the sublimation rate and thereby to vast changes in the coma structure. The formation of the coma is discussed in the first subsection. In the following subsections a simple chemical model with reduced complexity in comparison to reality and its different processes is presented.

2.3.1 The Coma - the Neutral Cometary Atmosphere

As mentioned above, the source of the cometary activity is the sublimation of ice. A first theoretical description of the neutral cometary atmosphere was given by Haser (1957). The author argued that the number of molecules within a spherical shell around the nucleus is constant for different radial distances as long as the loss of molecules due to photoionisation is neglected.

A different deduction is presented here. First of all, it is assumed that the nucleus is a sphere with radius r_{nuc}. The neutral molecules emanate radially from this sphere with an initial velocity u_{CN}. Hereby it is assumed that the movement of the neutral gas molecules can be described as a fluid. Due to the low mass of the nucleus, the gravitational force onto the emanating gas can be neglected. Therefore, the speed of the gas is constant. For the sake of simplicity it can be assumed that the whole process is stationary. Thus, the continuity equation in spherical coordinates reads

$$\frac{1}{r^2}\partial_r\left(r^2\cdot n_{\mathrm{CN}}\left(r\right)\right)u_{\mathrm{CN}}=\frac{Q\delta\left(r-r_{\mathrm{nuc}}\right)}{4\pi r_{\mathrm{nuc}}^2}-\nu_{\mathrm{ion}}n_{\mathrm{CN}}\left(r\right)\;, \tag{2.5}$$

where r is the radial distance to the centre of the nucleus and $n_{\mathrm{CN}}\left(r\right)$ denotes the neutral density.

The source of neutral molecules is modelled by the first term on the right-hand side of the equation. Each second a number of Q neutral molecules emanates from a sphere with the radius r_{nuc}. Since the molecules only emanate homogeneously from the surface, the source term is multiplied by the Dirac delta function and divided by the surface of

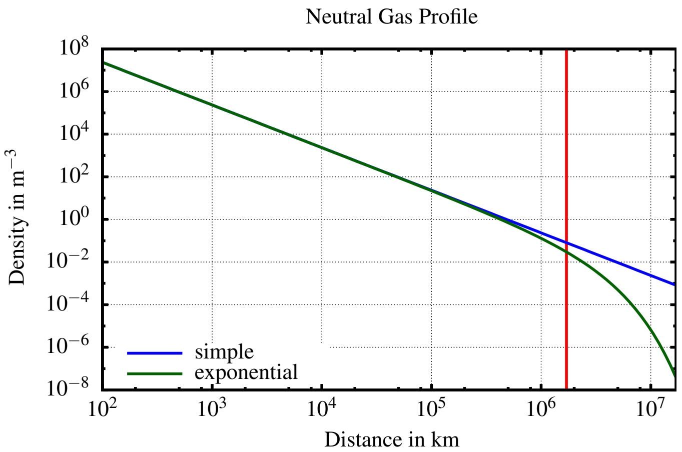

Figure 2.2: The density of the cometary exosphere as a function of distance. The figure shows the density of the model by Haser (1957) and a simplification for weakly outgassing comets. In addition, the red vertical line displays the position of $\lambda = u_{\mathrm{cn}}/\nu_{\mathrm{ion}}$, the ionisation scale length.

the sphere. A volume integral over this source term is equal to Q. The loss of neutral molecules is caused by the ionisation of the neutrals. This can be modelled by the second term on the right-hand side, where ν_{ion} is the ionisation frequency. By using the boundary condition $n_{\mathrm{CN}}(0) = 0$ and considering only distances larger than the radius of the nucleus, the solution of the continuity equation is

$$n_{\mathrm{CN}}(r) = \frac{Q}{4\pi u_{\mathrm{CN}} r^2} \exp\left(-\frac{\nu_{\mathrm{ion}}(r - r_{\mathrm{nuc}})}{u_{\mathrm{CN}}}\right) , \tag{2.6}$$

which is the same result as derived by Haser (1957).

In comparison to a planetary atmosphere, the velocity of the cometary gas is relatively high. An often used value is $u_{\mathrm{CN}} = 1\,\mathrm{km\,s^{-1}}$, which originates from the surface temperature. For this value a total gas production rate of $Q = 5 \times 10^{27}\,\mathrm{s^{-1}}$ and an ionisation frequency of $\nu = 5.88 \times 10^{-7}\,\mathrm{s^{-1}}$, which are characteristic parameters of 67P/Churyumov-Gerasimenko at 1.3 AU, the density profile is shown in Figure (2.2). The figure also shows a simplification which can be used to model the plasma environment of weakly outgassing comets. In this simplified case the main interaction takes place close to the nucleus, within the characteristic length of $\lambda = u_{\mathrm{CN}}/\nu_{\mathrm{ion}}$, and the exponential term is equal to unity:

$$n(r) = \frac{Q}{4\pi u_{\mathrm{CN}} r^2} . \tag{2.7}$$

In the advent of the Rosetta arrival at its target comet the modelling of the coma has been improved to a large extend. Mainly the various assumptions made by the model by Haser (1957) have been critically discussed. More sophisticated models were presented. For example, close to the surface, the real cometary gas is not in thermal equilibrium since neutral molecules which move towards the nucleus are absorbed by the surface. Hence, the velocity distribution function strongly deviates from a Maxwellian distribution. There a Knudsen layer is formed (Davidsson 2008). In order to investigate this, the Direct Simulation Monte Carlo (DSMC) technique is used to study the outgassing (Crifo 2002, Crifo et al. 2003, Tenishev et al. 2008).

Moreover the bulk velocity of the cometary gas is not constant. Within a radius of 10 km the gas is accelerated to its terminal velocity. And far away from the nucleus the fast molecules dominate, since it is more likely that the slower molecules are ionised (Tenishev et al. 2008, Finklenburg and Thomas 2014).

Haser (1957), among others, assumed a spherical symmetry to simplify the problem. However, the outgassing is closely connected to the nucleus' surface, which in real is not a sphere. Surface structures as well as the day-nightside differences modify the gas atmosphere. Enhancements in the gas density or the dust density are called jet-like features. Those have been observed at 1P/Halley, where these structures are restricted to the dayside hemisphere (Keller et al. 1986). Vincent et al. (2013b) studied the formation on a jet by a rim on 9P/Temple 1. Even at 67P/Churyumov-Gerasimenko Vincent et al. (2013a) found jet-like features with Earth-based observations. Young et al. (2004) also detected an asymmetry in the density profile of comet 19P/Borelly. Thus, an isotropic coma is very simplified description. Besides those arguments, since the comet rotates around its axis the assumption of a stationary situation is attacked as well.

Although the simple model by Haser (1957) can be criticised in many aspects, the model characterises the emanating gas in an appropriate way at larger distances to the nucleus. Thus, this model is used as a base line in the simulations to model the neutral coma.

2.3.2 The Processes in the Cometary Environment

As known from ground-based observations and former cometary spacecraft missions, the abundances of the various chemical elements and molecules vary in time as well as in space. For example, during the approach of 67P/Churyumov-Gerasimenko towards the Sun the ratio of the mother molecules CO and H_2O changes because of different sublimation temperatures. Close to the perihelion passage the water becomes the dominant species. Another example is the ratio of the water group ions within the cometary ions. On the one hand, H_2O^+ is significantly more abundant than H_3O^+ at larger distances to the nucleus, as found by Ogilvie et al. (1986) with ICE measurements at 21P/Giacobini-Zinner or by Balsiger et al. (1986) with measurements onboard Giotto at comet 1P/Halley. On the other hand, in case of the Giotto measurements, the abundance of H_3O^+ becomes dominant in the inner coma (Balsiger et al. 1986). This change is caused by collisions of the H_2O^+ ions with neutral water molecules:

$$H_2O^+ + H_2O \longrightarrow H_3O^+ + OH\,. \tag{2.8}$$

Another example is the ion pile-up region: At comet 1P/Halley, the ion detectors registered a sudden enhancement of the ion density (Balsiger et al. 1986). This is caused by a significant change in the reaction rate (Haeberli et al. 1995, Eberhardt and Krankowsky 1995).

These different observations have been discussed by various complex chemical reaction models (cf. Bhardwaj and Raghuram 2012, Vigren and Galand 2013). However, the reactions rates depend to some extend on the properties of the plasma environment. A summary of the different processes taking place in planetary and cometary atmospheres is given by Schunk and Nagy (2009).

For the purpose of the current work, the modelling of the cometary plasma environment, most of the cometary species have a quite similar impact on the interaction or their abundances are too low to have a significant impact on the global properties of the plasma environment. Hence, the modelling of the chemical processes only focusses on the major species: The most important neutral gas species in the cometary atmosphere are the water group molecules with masses close to 18 amu[2], carbon-monoxide (28 amu) and carbon-dioxide with a mass of about 44 amu. Their reactions are discussed in this section. However, in most of the time, water is by far the dominant species.

Changes of the neutral background, caused for example by recombination, are not considered in our plasma simulations. This can be justified by the fact that the neutral density exceeds the cometary ion density by several orders of magnitude in most of the regions.

2.3.2.1 Photoionisation

The interaction between the comet and the solar wind is caused by the ionisation of the neutral molecules in the coma. Most dominant among the different ionisation processes is the ionisation by solar UV radiation. A photon with an energy of $h\nu^{\mathrm{ph}}$ ionises a neutral molecule M and creates a new ion I^+ and a new electron e^-,

$$\mathrm{M} + \mathrm{h}\nu^{\mathrm{ph}} \rightarrow \mathrm{I}^+ + \mathrm{e}^- \,. \tag{2.9}$$

This only occurs if the energy of the photon exceeds the ionisation energy of the molecule E_{ion}. For example, water has an ionisation energy of $E_{\mathrm{ion,H_2O}} = 12.62\,\mathrm{eV}$ (Schunk and Nagy 2009).

The energy of the new electron, called photoelectron, is given by the difference of the photon energy and the ionisation energy $E_{\mathrm{e,ph}} = h\nu^{\mathrm{ph}} - E_{\mathrm{ion}}$. Thus, the energy of the photoelectrons varies with the wavelength of the UV radiation (Schunk and Nagy 2009). This energy spectrum is considered in some electron models, e.g. the electron models of Cravens et al. (1987) or Gan and Cravens (1990), but it can also be approximated by using a mean energy input to the photoelectrons.

Based on the fact that the energy of the photon is absorbed by the electron, the ions do not experience a change in velocity or temperature, which can be explained by the heavier mass of the ion. Hence, the initial velocity of a newborn ion is equal to the velocity of the former neutral molecule.

By neglecting the complex energy spectrum of the solar UV radiation (cf. Schunk and Nagy 2009) the production rate of new ions can be simplified to

$$I_\alpha^{\mathrm{ph}} = \eta\,\sigma_{\mathrm{ion,ph}} n_{\mathrm{CN}} I \,, \tag{2.10}$$

where η is the probability of a photon absorption, $\sigma_{\mathrm{ion,ph}}$ the absorption cross section and I the solar flux of UV radiation. The index α denotes the plasma species, e.g. the solar wind protons (SW), cometary ions (CI) or electrons (e). This expression assumes that the process can be described by a fluid model. In case of planetary atmospheres, this expression leads to a Chapman production function (cf. Baumjohann and Treumann 1996) with a clear maximum above the surface of the planet due to absorption of the

---

[2] Atomic Mass Unit: 1 amu = $1.660\,538\,86 \times 10^{-27}$ kg

Table 2.2: The photoionisation frequencies of different molecules in the coma for conditions at a distance of 1 AU to the Sun. The parameters are given for the conditions at the solar minimum and the solar maximum (Schunk and Nagy 2009).

	Solar Minimum	**Solar Maximum**
H_2O	$4.286 \times 10^{-7}\,\mathrm{s}^{-1}$	$1.184 \times 10^{-6}\,\mathrm{s}^{-1}$
CO_2	$6.696 \times 10^{-7}\,\mathrm{s}^{-1}$	$1.695 \times 10^{-6}\,\mathrm{s}^{-1}$
CO	$4.245 \times 10^{-7}\,\mathrm{s}^{-1}$	$1.127 \times 10^{-6}\,\mathrm{s}^{-1}$

UV radiation by the neutrals along their ray trace. For the cometary environment this absorption can be estimated by solving the equation

$$dI = \sigma_{\mathrm{ion,ph}} n_{\mathrm{CN}} I dr \; . \tag{2.11}$$

The equation describes the change of the flux due to absorption of photons by the neutral cometary atmosphere along the Sun-comet line. In order to estimate an upper limit for the absorption, the density profile of Equation (2.7) can be used. Thus, the solar flux is expressed by

$$I = I_\infty \exp\left(-\frac{\sigma_{\mathrm{ion,ph}} Q}{4\pi u_{\mathrm{CN}} r}\right) \; . \tag{2.12}$$

The actual cross section of water $\sigma_{\mathrm{ion,ph}}$ varies with the wavelength of the radiation (an overview can be found in Schunk and Nagy (2009)) but no value exceeds $\sigma_{\mathrm{ion,ph,max}} = 25 \times 10^{-18}\,\mathrm{cm}^2$. The maximum activity of 67P/Churyumov-Gerasimenko is present close to the perihelion, i.e. at about 1.3 AU, where a gas production rate of $Q = 5 \times 10^{27}\,\mathrm{s}^{-1}$ and a typical velocity of the neutral gas of $u_{\mathrm{CN}} = 1\,\mathrm{km\,s}^{-1}$ can be used. For these parameters, the solar flux is absorbed by more than 50 % as long as the a radial distance of $r \leq 1.4\,\mathrm{km}$ to the nucleus. Based on that, the absorption of the solar flux can generally be neglected in the coma, at least on the sunward side, and Equation (2.10) can be simplified to

$$I_\alpha^{\mathrm{ph}} = \nu_\alpha^{\mathrm{ph}} n_{\mathrm{CN}} \; . \tag{2.13}$$

The values for the ionisation frequency vary with the activity of the Sun. Close to the solar minimum, the ionisation frequency of water is $\nu_{\mathrm{ion,ph,0,min}} \approx 4.3 \times 10^{-7}\,\mathrm{s}^{-1}$ at a heliocentric distance of 1 AU from the Sun, whereas, at the solar maximum this value increases to $\nu_{\mathrm{ion,ph,0,max}} \approx 1.2 \times 10^{-6}\,\mathrm{s}^{-1}$ (Huebner et al. 1992, Schunk and Nagy 2009). Table (2.2) lists the ionisation frequencies of the major molecules in the cometary environment at a heliocentric distance of 1 AU. Since the values are quite similar to each other and the exact conditions during the escort phase are unknown, a default photoionisation rate of $\nu_{\mathrm{ion,ph,0}} = 1.0 \times 10^{-6}\,\mathrm{s}^{-1}$ is used (Hansen et al. 2007).

Because of the fact that the distance between the comet and the Sun changes during the mission the ionisation frequencies vary as well. The ionisation frequency at a given distance to the Sun r_{h} is given by

$$\nu_{\mathrm{ion,ph}}(r_{\mathrm{h}}) = \frac{\nu_{\mathrm{ion,ph,0}} r_0^2}{r_{\mathrm{h}}^2} \; , \tag{2.14}$$

where $\nu_{\mathrm{ion,ph,0}}$ is the ionisation frequency at the reference distance. This change is caused by the reduction of the intensity of the solar radiation when moving to larger distances.

2.3.2.2 Collisions and Charge Exchange

In addition to the ionisation processes, collisions between charged particles and the neutral molecules are quite important in general ionospheric plasma environments. This also applies to the cometary environment, because collisions lead to the formation of the diamagnetic cavity (Section 4.2). These collision processes are important as long as the ion densities as well as the neutral densities are high. Because several processes are involved, this section focuses on the most important ones. A detailed description and the deduction of the reaction rates of all these processes is given by Schunk and Nagy (2009).

The most important class of processes are elastic collisions between ions and neutral molecules. These collisions are most prominent whenever the neutral gas density is high. However, they are not a source of new particles but rather a source or loss of momentum. Based on the fact that these collisions are mainly elastic, the kinetic energy of the ions after the collision is determined by the mass ratio and the velocity of the neutral molecules before the collision. Schunk and Nagy (2009) expressed the change of momentum of the plasma species α, $\frac{\delta p_\alpha^{\mathrm{coll}}}{\delta t}$, due to these collisions for Maxwellian molecules by

$$\frac{\delta p_\alpha^{\mathrm{coll}}}{\delta t} = \sum_{\mathrm{n}} k_{\alpha,\mathrm{n}}^{\mathrm{coll}} n_{\mathrm{n}} n_\alpha m_\alpha \left(\vec{u}_{\mathrm{n}} - \vec{u}_\alpha\right) , \tag{2.15}$$

where n_{n} and $\vec{u}_{\mathrm{n}}$ denote the density and the velocity of a specific neutral gas species, respectively. The mass, the density and the velocity of the plasma species α is labelled by m_α, n_α, and $\vec{u}_\alpha$. It follows that the collisions act like a force on the plasma, which accelerates or decelerates the plasma species depending on the velocity $\vec{u}_\alpha$. For the common cometary molecules the collision rates $k_{\alpha,\mathrm{n}}^{\mathrm{coll}}$ are listed in Table (2.3).

Besides elastic collisions, the charge exchange process plays an important role in the cometary environment. Mainly, solar wind protons enter the neutral coma and collide with neutral gas molecules. Hereby, an ion I^+ reacts with a neutral molecule M

$$\mathrm{M} + \mathrm{I}^+ \rightarrow \mathrm{I}^+ + \mathrm{M} , \tag{2.16}$$

to a neutral and newborn ion. In the case of the resonant charge exchange, the momentum and the kinetic energy of each of the reactants is constant. Although this process leads to the loss of solar wind protons and evokes cometary ions, it is not related to a change of the net charge of the plasma, because only single charged ions are taken into consideration for this study. Hence, the charge exchange process is a source or a loss of momentum and mass for the plasma depending on the parameters. The rates of the charge exchange processes depend on the particle velocity and the cross-section of the particles. In a first order, the cross-section is inverse to the particle velocity, hence, for the sake of simplicity, the charge exchange rate can be assumed as constant (Kriegel 2013). Typical reaction rates are stated in Table (2.3).

In addition to the ion-neutral processes discussed so far, the electron-neutral collisions are also quite important, among those the elastic collisions between electrons and neutral

Table 2.3: The table lists the most important reaction rates of the collision, the charge-exchange and the recombination processes as used in our simulations. It should be noted that in reality some of these rates depend on the velocity (Nakai et al. 1987, Gombosi et al. 1996, Schunk and Nagy 2009, Kriegel 2013).

Reaction	**Rate in** $\mathrm{cm^3\,s^{-1}}$
$H_3O^+ + H_2O \rightarrow H_3O^+ + H_2O$	1.7×10^{-9}
$H^+ + H_2O \rightarrow H_3O^+$	$1. \times 10^{-8}$
$CO^+ + CO \rightarrow CO + CO^+$	9.8×10^{-10}
${CO_2}^+ + CO_2 \rightarrow CO_2 + {CO_2}^+$	8.8×10^{-10}
$H_2O^+/H_3O^+ + e^-$	$1.57 \times 10^{-5}\,(T_e)^{-0.569}$ for $T_e < 800\,\mathrm{K}$
	$4.73 \times 10^{-5}\,(T_e)^{-0.74}$ for $800\,\mathrm{K} < T_e < 4000\,\mathrm{K}$
	$1.03 \times 10^{-3}\,(T_e)^{-1.111}$ for $T_e > 4000\,\mathrm{K}$
${CO_2}^+ + e^-$	$4.2 \times 10^{-7}\left(\frac{300\,\mathrm{K}}{T_e}\right)^{0.75}$

molecules. The reaction rate coefficient is given by $k_{\mathrm{en,elastic}} = \sigma v_e$, where v_e is the velocity of the electrons. Here it is assumed that this velocity can simply be expressed by the thermal velocity

$$\frac{1}{2} m_e v_e^2 = \frac{f_e}{2} k_B T_e \; ,$$

where f_e, k_B, and T_e denote the number of degrees of freedom for the electrons, the Boltzmann constant, and the electron temperature. This is reasonable since the thermal velocity of the electrons by far exceeds the bulk velocity in every region. The momentum transfer cross section σ of the electron collision with water are obtained by the review of Itikawa (2005). The resulting reaction rate coefficients are shown in Figure (2.3). Since they are relatively close to each other, a constant reaction rate coefficient of $k_{\mathrm{en,elastic,fit}} = 1.1 \times 10^{-7}\,\mathrm{cm^3\,s^{-1}}$ is used in this work.

Besides elastic collisions, also inelastic collisions in the inner coma have to be considered. As discussed below, they allow the electron fluid to be cooled in the inner coma. Gan and Cravens (1990) stated that the electrons excite the water molecules in their electron model of comet Halley. The most dominant states are rotation, vibrational and electronic excitations. In the review by Itikawa (2005), the rotational excitation is agreed by several measurements, whereas the measurements of the cross section of the electronic excitation of the water molecules of the different authors contradict each other and will be addressed by the Rosetta measurements. Here, the values suggested by Gan and Cravens (1990) are used. The energy transfer to the water molecules is expressed by

$$\ln E^{\mathrm{ex}}_{\mathrm{H_2O}} = -188.4701 + 33.2547 \ln(T_e) - 2.0729 \ln(T_e)^2 + 0.0425 \log(T_e)^3 \; . \qquad (2.17)$$

In combination with the rotational and vibrational excitations, this process is a very efficient process in cooling the electrons, as will be discussed in Section (2.5.3.6). The total

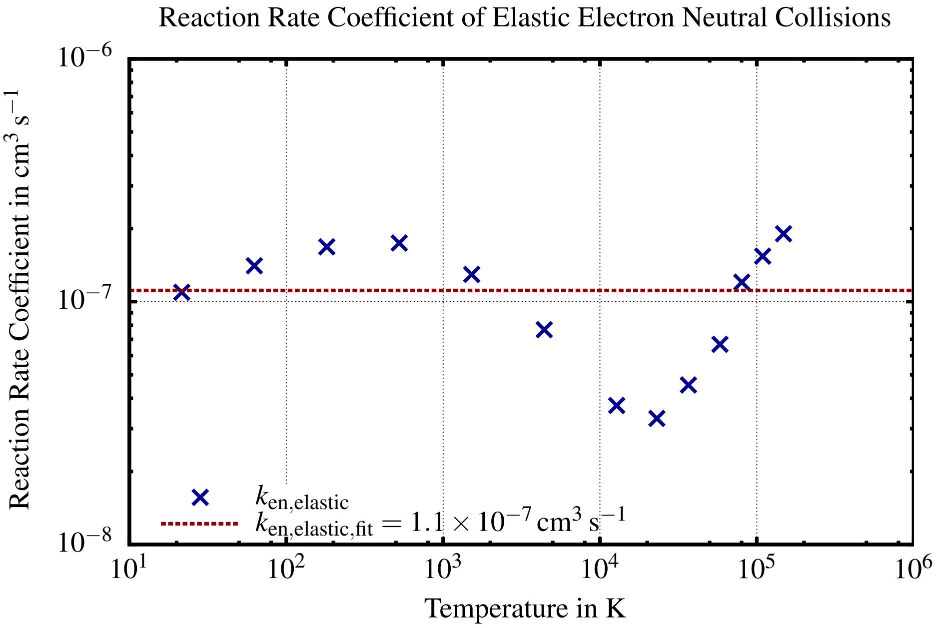

Figure 2.3: The reaction rate coefficient of the elastic electron neutral collision is shown. The coefficient is calculated by using the recommended momentum transfer cross sections σ from Itikawa (2005) and the velocity of the electrons by assuming $E_{\mathrm{kin,e}} = E_{\mathrm{therm,e}}$. In addition, the figure shows the constant $k_{\mathrm{en,elastic,fit}}$, which is a fit to the reaction rate coefficient within the temperature range from 10 K to 10^5 K.

energy loss due to the excitation of the water molecules is shown in Figure (2.4). The electronic excitation dominates the loss at high energies, whereas the rotational loss dominates the at lower temperatures. If the electrons are cooler than the neutrals, the electrons are heated by the collisions. However, this cooling of the electrons will be extensively investigated on the basis of the RPC measurements in future studies.

2.3.2.3 Recombination

A loss of plasma is the recombination process which plays an important role in regions with a low electron temperature. During this process, an ion I^+ and an electron e^- recombine to a neutral molecule and a photon. In case of molecular ions, dissociative recombinations occur and two neutral molecules are produced

$$\mathrm{I}^+ + \mathrm{e}^- \rightarrow \mathrm{M}_1 + \mathrm{M}_2 \,. \tag{2.18}$$

In ionospheric plasmas dissociative recombination is more frequent (Schunk and Nagy 2009). The loss within a plasma species α, R_α, can be modelled in a fluid description by

$$R_\alpha = \alpha(T_\mathrm{e}) n_\mathrm{e} n_\alpha \,, \tag{2.19}$$

where $\alpha(T_\mathrm{e})$ denotes the recombination rate. This rate strongly depends on the electron temperature and is large for low temperatures, see Figure (2.5) (Schunk and Nagy 2009). Table (2.3) lists the recombination rates of common cometary ions.

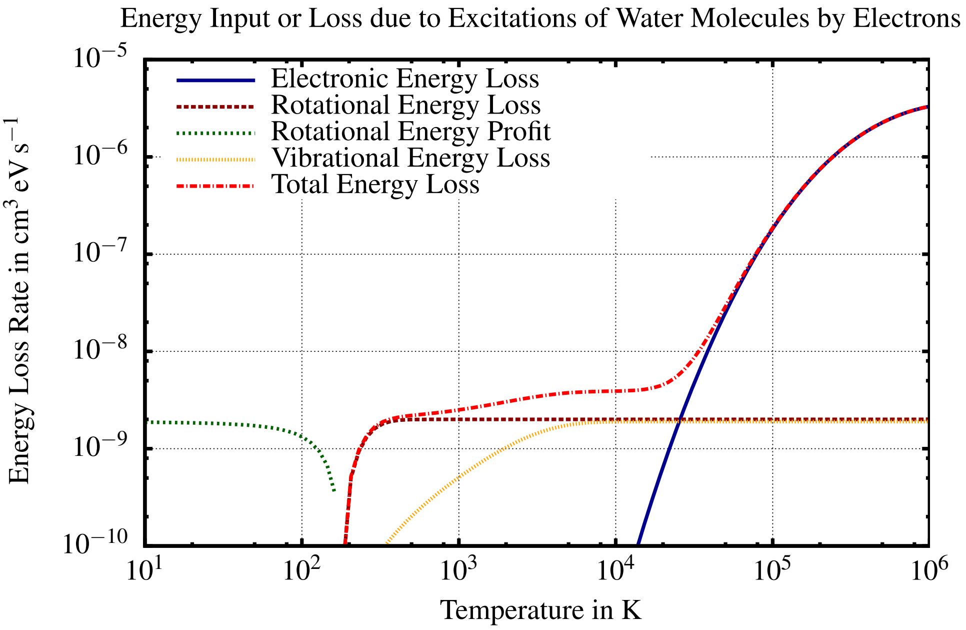

Figure 2.4: The energy profit and loss due to rotational and electronic excitation of water molecules by electrons, constructed by using values of Gan and Cravens (1990). The temperature of the water molecules is assumed to be 180 K.

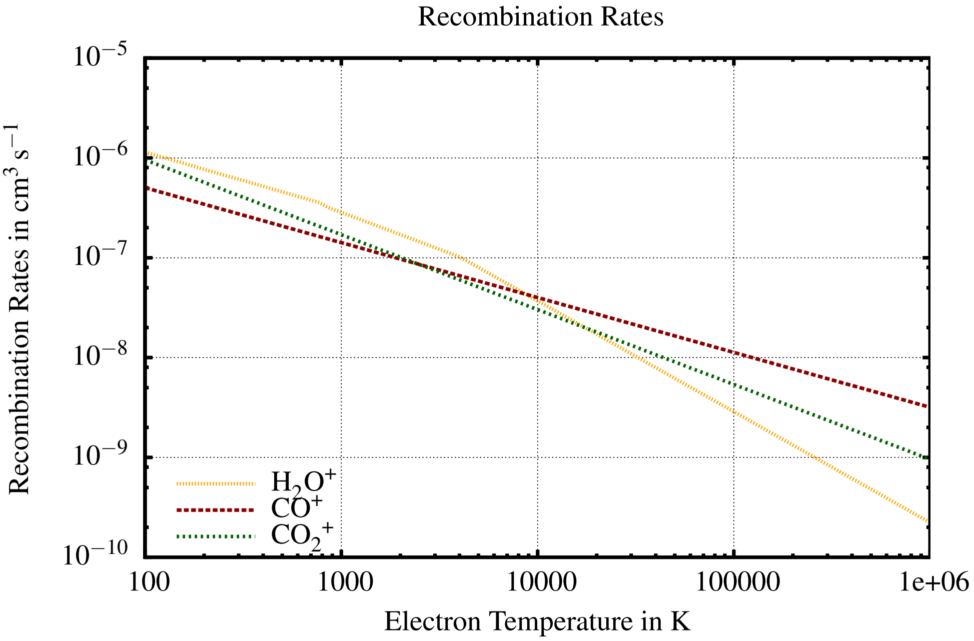

Figure 2.5: The recombination rates for the major species as a function of the electron temperature (Schunk and Nagy 2009).

2.3.3 Dust Particles and Further Uncertainties at the Comet

Besides the gas molecules, dust particles can be found in the coma of a comet. From the plasma perspective dust consists of solid particles with sizes between nanometres and a few hundred micrometres. Since those particles are exposed to the plasma, the grains collect electrons and ions in their environment depending on the grain size, the plasma density and the plasma velocities.

In general, this leads to negatively charged dust grains. In cases of a sufficient solar radiation photoionisation removes electrons from the dust grains and results in less negative or even positive grain charge. A similar effect is triggered by the electron impact ionisation.

Due to the large masses, the charge per mass ratio is orders of magnitude smaller than for the ordinary ions. Because of that, the dust particles have other gyrofrequencies and very low frequency dust ion waves can be excited in the plasma. Recent observations by the Cassini spacecraft at Saturn's moon Enceladus showed that dust particles have a significant impact on the plasma interaction of the moon with Saturn's magnetosphere (cf. Kriegel 2013).

In case of Enceladus the grains are negatively charged. Around comet 67P/Churyumov-Gerasimenko this might be different because of the smaller distance to the Sun, photoionisation is more important. However, a detailed analysis of the effects of dust grains at comet 67P/Churyumov-Gerasimenko is very complicated since the size distribution as produced by the comet, the charge as controlled by the plasma environment, the amount of dust grains produced by the comet, and further properties are unknown. An examination of those effects must be subject of a future study.

2.4 General Plasma Description

A general description of a multi-species plasma is possible using the Boltzmann equation for each plasma species α

$$\partial_t F_\alpha + \vec{v}\partial_{\vec{x}} F_\alpha + \frac{q_\alpha e}{m_\alpha}\left(\vec{E} + \vec{v} \times \vec{B}\right)\partial_{\vec{v}} F_\alpha = \frac{\delta F_\alpha}{\delta t} \tag{2.20}$$

and the Maxwell equations

$$\partial_{\vec{x}} \cdot \vec{E} = \frac{\rho_\mathrm{c}}{\varepsilon_0} \tag{2.21}$$

$$\partial_{\vec{x}} \cdot \vec{B} = 0 \tag{2.22}$$

$$\partial_{\vec{x}} \times \vec{E} = -\partial_t \vec{B} \tag{2.23}$$

$$\partial_{\vec{x}} \times \vec{B} = \frac{1}{c^2}\partial_t \vec{E} + \mu_0 \vec{j}\,. \tag{2.24}$$

Hereby $F_\alpha = F_\alpha(\vec{x}, \vec{v}, t)$, $q_\alpha e$ and m_α are the phase space distribution function, the charge and the mass of species α, respectively. $\vec{v}$ denotes the velocity, and $\delta F_\alpha / \delta t$ allows modelling of ionisation, collisions and loss processes. The electromagnetic fields are labelled by $\vec{E}$ and $\vec{B}$. The constants c, ε_0 and μ_0 are the speed of light, the vacuum permittivity and the vacuum permeability, respectively. The charge density

$$\rho_\mathrm{c}(\vec{x},t) = \sum_\alpha q_\alpha e \int F_\alpha d^3v\,, \tag{2.25}$$

and the current density

$$\vec{j}_\mathrm{c}(\vec{x},t) = \sum_\alpha q_\alpha e \int \vec{v} F_\alpha d^3v\,, \tag{2.26}$$

and the electromagnetic fields couple the equations.

In order to describe the dynamics of the entire plasma in the environment, one could solve the non-linear set of equations or use different approximation levels, which allow an easier, faster and more appropriate way to investigate the global plasma environment of a comet. In the following subsections some of these different approaches are shortly presented, because the hybrid model (Section 2.5) used for this thesis is partly based on the other approaches. In addition, the simpler fluid model is used to investigate the ongoing processes at various places in this work. A detailed deduction of the different fluid plasma models can be found for example in Motschmann (2009).

2.4.1 The Multifluid Magnetohydrodynamic Model

A first approximation of the set of Equations (2.20) to (2.24) is the multifluid approach. In this approach, the effects of individual particles are neglected and the different species of the plasma particles are described by fluids. Hereby, the model uses moments of the distribution function F_α to describe the plasma. By using an endless number of moments, the complete distribution function can be reconstructed and all effects of the plasma are included. However, the system becomes simpler by using a limited number of moments only. In this work only the first four moments are taken into consideration, namely the number density n_α, the mean velocity $\vec{u}_\alpha$, the internal energy ε_α and the pressure tensor $\underline{\underline{\Pi}}_\alpha$:

$$n_\alpha(\vec{x},t) = \int F_\alpha d^3v \tag{2.27}$$

$$\vec{u}_\alpha(\vec{x},t) = \frac{1}{n_\alpha}\int \vec{v} F_\alpha d^3v \tag{2.28}$$

$$\varepsilon_\alpha(\vec{x},t) = \frac{m_\alpha}{2}\int (\vec{v}-\vec{u}_\alpha)^2 F_\alpha d^3v \tag{2.29}$$

$$\underline{\underline{\Pi}}_\alpha(\vec{x},t) = m_\alpha \int (\vec{v}-\vec{u}_\alpha)\circ(\vec{v}-\vec{u}_\alpha) F_\alpha d^3v\,. \tag{2.30}$$

It is generally assumed that moments of higher order, such as the heat flux density, can be neglected, as long as the dynamics of the entire plasma are investigated. However, some models use the heat flux to model specific effects, for example, the electron model by Gan and Cravens (1990). In contrast to this basic assumption of the fluid model, the hybrid model, which describes the ions as particles allows the description of higher order moments by construction.

A first equation to govern the moments and, based on that, the dynamics of the plasma can be obtained by integrating the Boltzmann equation (2.20) over the velocity space. The resulting equation is the continuity equation:

$$\partial_t n_\alpha + \partial_{\vec{x}} (n_\alpha \vec{u}_\alpha) = \int \frac{\delta F_\alpha}{\delta t} d^3 v =: \frac{\delta n_\alpha}{\delta t} \, . \tag{2.31}$$

Multiplying the Boltzmann equation with $m_\alpha \vec{v}$ before the integration is done and assuming an isotropic pressure p_α yields the momentum conservation

$$\begin{aligned} &\partial_t \left(n_\alpha m_\alpha \vec{u}_\alpha\right) + \partial_{\vec{x}} \left(n_\alpha m_\alpha \vec{u}_\alpha \circ \vec{u}_\alpha\right) + \\ &\quad + \partial_{\vec{x}} p_\alpha - n_\alpha q_\alpha e \left(\vec{E} + \vec{u}_\alpha \times \vec{B}\right) = \int m_\alpha \vec{v} \frac{\delta F_\alpha}{\delta t} d^3 v \, . \end{aligned} \tag{2.32}$$

Using the continuity equation, Equation (2.31), the expression can be converted into

$$\begin{aligned} &n_\alpha m_\alpha \left(\partial_t \vec{u}_\alpha + \left(\vec{u}_\alpha \partial_{\vec{x}}\right) \vec{u}_\alpha\right) + \\ &\partial_{\vec{x}} p_\alpha - n_\alpha q_\alpha e \left(\vec{E} + \vec{u}_\alpha \times \vec{B}\right) = \int \frac{\delta F_\alpha}{\delta t} m_\alpha \left(\vec{v} - \vec{u}_\alpha\right) d^3 v =: \frac{\delta p_\alpha}{\delta t} \, . \end{aligned} \tag{2.33}$$

The energy equation can be obtained by multiplying the Boltzmann equation with $m_\alpha \vec{v}^2/2$ and integrating it afterwards. In addition, it is assumed that $\varepsilon_\alpha = f_\alpha n_\alpha k_\mathrm{B} T_\alpha / 2$ and $p_\alpha = n_\alpha k_\mathrm{B} T_\alpha$. k_B are the Boltzmann constant and f_α expresses the number of degrees of freedom. It follows that the energy equation is given by

$$\begin{aligned} &\partial_t \left(\frac{1}{2} n_\alpha m_\alpha \vec{u}_\alpha^2 + \frac{f_\alpha}{2} p_\alpha\right) + \\ &+ \partial_{\vec{x}} \left(\frac{1}{2} n_\alpha m_\alpha \vec{u}_\alpha^2 \vec{u}_\alpha + \frac{f_\alpha + 2}{2} p_\alpha \vec{u}_\alpha\right) - \\ &\qquad - \partial_{\vec{x}} \vec{q}_\alpha - n_\alpha q_\alpha e \vec{u}_\alpha \vec{E} = \int \frac{1}{2} m_\alpha \vec{v}^2 \frac{\delta F_\alpha}{\delta t} d^3 v \, . \end{aligned} \tag{2.34}$$

The application of Equation (2.33) leads to the pressure equation:

$$\frac{f_\alpha}{2} \left(\partial_t + \vec{u}_\alpha \partial_{\vec{x}}\right) p_\alpha + \frac{f_\alpha + 2}{2} p_\alpha \partial_{\vec{x}} \vec{u}_\alpha + \partial_{\vec{x}} \vec{q}_\alpha = \int \frac{1}{2} m_\alpha \left(\vec{v} - \vec{u}_\alpha\right)^2 \frac{\delta F_\alpha}{\delta t} d^3 v =: \frac{\delta \varepsilon_\alpha}{\delta t} \, . \tag{2.35}$$

Solving the continuity equations, Equations (2.31), (2.33) and (2.35) and Maxwell's equations, the behaviour of the fluids can be described. However, in order to model the obstacle, the right-hand sides of the Equations (2.31), (2.33) and (2.35), the sources and losses of the plasma density, of the velocity and energy need to be modelled. Theses sources and losses correspond to the different physical processes, which have been discussed in the first part of this chapter. Because of the fact that neither the description by Ranocha (2013) nor Rubin et al. (2014a) are complete and appropriate for the purpose of this work, the sources and losses in the equations are deduced in this work using parts of Motschmann (2009), Ranocha (2013) and Rubin et al. (2014a). Concerning the continuity equation, a source of density is caused by photo-ionisation I_α^ph, and charge exchange C_α^s, but charge exchange is also a loss of density to another species C_α^l. Furthermore, the recombination loss of ions and electrons R_α reduces the density. In contrast, elastic and inelastic collisions do not yield to a change in the continuity equation. Thus, the continuity equation can be expressed by

$$\begin{aligned}\partial_t n_\alpha + \partial_{\vec{x}}(n_\alpha \vec{u}_\alpha) =& I_\alpha^{\mathrm{ph}} + C_\alpha^{\mathrm{s}} - C_\alpha^{\mathrm{l}} - R_\alpha \\ =& \sum_n I_{\alpha,\mathrm{n}}^{\mathrm{ph}} + \sum_n C_{\alpha,\mathrm{n}}^{\mathrm{s}} - \sum_n C_{\alpha,\mathrm{n}}^{\mathrm{l}} - R_\alpha \\ =& \sum_n \nu_\alpha^{\mathrm{ph}} n_\mathrm{n} + \sum_n C_{\alpha,\mathrm{n}}^{\mathrm{s}} - \sum_n C_{\alpha,\mathrm{n}}^{\mathrm{l}} - \alpha(T_\mathrm{e}) n_\mathrm{e} n_\alpha \,. \end{aligned} \tag{2.36}$$

Since several neutral gas species can be involved in the sources and sinks, the sum over all neutral gas species n is considered. Collisions between ions and neutral molecules do not cause sources or sinks for the continuity equation, but are important in the momentum equation because they provide a change in velocity. Reference is made to Schunk and Nagy (2009), Ranocha (2013) and Rubin et al. (2014a) for a detailed deduction of the appropriate source terms. As already discussed the change due to elastic binary collisions of molecules is given by

$$\frac{\delta p_\alpha^{\mathrm{coll}}}{\delta t} = \sum_{\mathrm{n}} k_{\alpha,\mathrm{n}}^{\mathrm{coll}} n_\mathrm{n} n_\alpha m_\alpha (\vec{u}_\mathrm{n} - \vec{u}_\alpha) \,. \tag{2.37}$$

The sources and losses because of ionisation, charge exchange and recombination are given by

$$\begin{aligned}\frac{\delta p_\alpha^{\mathrm{prod}}}{\delta t} &= \int m_\alpha (\vec{v} - \vec{u}_\alpha) \frac{\delta F_\alpha^{\mathrm{prod}}}{\delta t} d^3 v \\ &= \sum_n I_{\alpha,\mathrm{n}}^{\mathrm{ph}} m_\alpha \vec{u}_\mathrm{n} + \sum_n C_{\alpha,\mathrm{n}}^{\mathrm{s}} m_\alpha \vec{u}_\mathrm{n} \\ &\quad - \sum_n C_{\alpha,\mathrm{n}}^{\mathrm{l}} m_\alpha \vec{u}_\alpha - R_\alpha m_\alpha \vec{u}_\alpha \\ &\quad - m_\alpha \vec{u}_\alpha \left(\sum_n I_{\alpha,\mathrm{n}}^{\mathrm{ph}} + \sum_n C_{\alpha,\mathrm{n}}^{\mathrm{s}} - \sum_n C_{\alpha,\mathrm{n}}^{\mathrm{l}} - R_\alpha \right) \\ &= \sum_n I_{\alpha,\mathrm{n}}^{\mathrm{ph}} m_\alpha (\vec{u}_\mathrm{n} - \vec{u}_\alpha) + \sum_n C_{\alpha,\mathrm{n}}^{\mathrm{s}} m_\alpha (\vec{u}_\mathrm{n} - \vec{u}_\alpha) \,. \end{aligned} \tag{2.38}$$

It should be noted that the losses by recombination and charge exchange do not occur in the final expression of the momentum change. This can be explained by the fact that the losses take place in the plasma at the velocity $\vec{u}_\alpha$ of the plasma fluid. Thus, the momentum loss due to those processes is only caused by a change in the density, but this is already considered in the continuity equation. A similar consideration appears in case of equal plasma and neutral velocities. Then, the change of momentum is already considered by the continuity equation and the source terms in the momentum equation vanish.

Finally, the complete momentum equation for the fluid of species α is given by

$$\begin{aligned} n_\alpha m_\alpha (\partial_t \vec{u}_\alpha + (\vec{u}_\alpha \partial_{\vec{x}}) \vec{u}_\alpha) + \partial_{\vec{x}} p_\alpha - n_\alpha q_\alpha e \left(\vec{E} + \vec{u}_\alpha \times \vec{B} \right) = \frac{\delta p_\alpha^{\mathrm{prod}}}{\delta t} + \frac{\delta p_\alpha^{\mathrm{coll}}}{\delta t} \\ = \sum_n I_{\alpha,\mathrm{n}}^{\mathrm{ph}} m_\alpha (\vec{u}_\mathrm{n} - \vec{u}_\alpha) + \sum_n C_{\alpha,\mathrm{n}}^{\mathrm{s}} m_\alpha (\vec{u}_\mathrm{n} - \vec{u}_\alpha) + \sum_{\mathrm{n}} k_{\alpha,\mathrm{n}}^{\mathrm{coll}} n_\mathrm{n} n_\alpha m_\alpha (\vec{u}_\mathrm{n} - \vec{u}_\alpha) \,. \end{aligned} \tag{2.39}$$

For modelling the input of energy into the plasma, right hand side of Equation (2.35), the calculations done for the momentum and continuity equation are useful. It is (Ranocha 2013)

$$\begin{aligned}\frac{\delta \varepsilon_\alpha}{\delta t} &= \int \frac{1}{2} m_\alpha \left(\vec{v} - \vec{u}_\alpha\right)^2 \frac{\delta F_\alpha}{\delta t} d^3 v \\ &= \int \frac{1}{2} m_\alpha \vec{v}^2 \frac{\delta F_\alpha}{\delta t} d^3 v - \vec{u}_\alpha \int \frac{1}{2} m_\alpha \vec{v} \frac{\delta F_\alpha}{\delta t} d^3 v + \frac{1}{2} m_\alpha \vec{u}_\alpha^2 \int \frac{\delta F_\alpha}{\delta t} d^3 v \\ &= \int \frac{1}{2} m_\alpha \vec{v}^2 \frac{\delta F_\alpha}{\delta t} d^3 v - \vec{u}_\alpha \frac{\delta p_\alpha}{\delta t} + \frac{1}{2} m_\alpha \vec{u}_\alpha^2 \frac{\delta n_\alpha}{\delta t} \,. \end{aligned} \tag{2.40}$$

Based on this equation, the calculation can again be separated into the energy input of the collisions and that of the production and loss processes.

$$\frac{\delta \varepsilon_\alpha}{\delta t} = \frac{\delta \varepsilon_\alpha^{\mathrm{prod}}}{\delta t} + \frac{\delta \varepsilon_\alpha^{\mathrm{coll}}}{\delta t} \,. \tag{2.41}$$

However, the behaviour of the ions and electrons in the reactions becomes different at this stage. As described in Section (2.3) there are no changes of the ion temperature due to ionisation and charge exchange. Therefore, the sources and sinks for the ions caused by ionisation, charge exchange and recombination can be modelled by

$$\begin{aligned}\frac{\delta \varepsilon_\alpha^{\mathrm{prod}}}{\delta t} = &\sum_n I_{\alpha,\mathrm{n}}^{\mathrm{ph}} \frac{m_\alpha}{2} \vec{u}_\mathrm{n}^2 - \sum_n I_{\alpha,\mathrm{n}}^{\mathrm{ph}} m_\alpha \vec{u}_\mathrm{n} \left(\vec{u}_\mathrm{n} - \vec{u}_\alpha\right) - \sum_n I_{\alpha,\mathrm{n}}^{\mathrm{ph}} \frac{1}{2} m_\alpha \vec{u}_\alpha \\ &+ \sum_n C_{\alpha,\mathrm{n}}^{\mathrm{s}} \frac{m_\alpha}{2} \vec{u}_\mathrm{n}^2 - \sum_n C_{\alpha,\mathrm{n}}^{\mathrm{s}} m_\alpha \vec{u}_\mathrm{n} \left(\vec{u}_\mathrm{n} - \vec{u}_\alpha\right) - \sum_n C_{\alpha,\mathrm{n}}^{\mathrm{s}} \frac{1}{2} m_\alpha \vec{u}_\alpha \\ &- \sum_n C_{\alpha,\mathrm{n}}^{\mathrm{l}} \frac{f_\alpha p_\alpha}{2 n_\alpha} - R_\alpha \frac{f_\alpha p_\alpha}{2 n_\alpha} \,. \end{aligned} \tag{2.42}$$

In contrast to the ions, the electrons experience a change in temperature. The photoionisation produces new electrons of a mean energy $E_\mathrm{n}^{\mathrm{ph}}$. Furthermore, since only single charged ions are considered, their charge exchange does not change the electron pressure. Thus, the change of the electron pressure can be expressed by

$$\begin{aligned}\frac{\delta \varepsilon_\mathrm{e}^{\mathrm{prod}}}{\delta t} = &\sum_n I_{\mathrm{e,n}}^{\mathrm{ph}} \left(\frac{m_\mathrm{e}}{2} \vec{u}_\mathrm{n}^2 + \frac{f_\mathrm{e}}{2} k_\mathrm{B} T_\mathrm{n}^{\mathrm{ph}}\right) - \sum_n I_{\mathrm{e,n}}^{\mathrm{ph}} m_\mathrm{e} \vec{u}_\mathrm{n} \left(\vec{u}_\mathrm{n} - \vec{u}_\mathrm{e}\right) \\ &- \sum_n I_{\mathrm{e,n}}^{\mathrm{ph}} \frac{1}{2} m_\mathrm{e} \vec{u}_\mathrm{e} - R_\mathrm{e} \frac{f_\mathrm{e} p_\mathrm{e}}{2 n_\mathrm{e}} \,. \end{aligned} \tag{2.43}$$

Because of the various processes in the cometary environment, the electron distribution function is not a simple Maxwellian distribution. Therefore, the electron model by Gan and Cravens (1990) distinguishes between thermal and superthermal electrons. In the multifluid approach, which is presented here, the electrons are only considered as a single fluid. Consequently, some problems occur: For example, the electron fluid is cooled by recombination, but a heating might be more appropriate in reality, because the recombination rate is higher for cold electrons. Thus, cold electrons are removed from the electron ensemble and the warmer electrons remain. Hence, the electron fluid temperature increases. However, as discussed in Section (2.5.3.6), the cooling of the electrons is negligibly small.

Following Ranocha (2013) the energy transfer due to elastic collisions is given by

$$\frac{\delta \varepsilon_\alpha^{\text{coll}}}{\delta t} = \sum_n \frac{n_\alpha m_\alpha}{m_\alpha + m_\text{n}} k_{\alpha,\text{n}}^{\text{coll}} n_\text{n} \left(\frac{f_\text{n} p_\text{n}}{n_\text{n}} - \frac{f_\alpha p_\alpha}{n_\alpha} + m_\text{n} \left(\vec{u}_\alpha - \vec{u}_\text{n} \right)^2 \right) . \tag{2.44}$$

According to Rubin et al. (2014a), the loss due to inelastic electron water collisions can be expressed by

$$\frac{\delta \varepsilon_\text{e}^{\text{in.coll}}}{\delta t} = - \frac{2}{3} n_\text{e} n_{\text{H}_2\text{O}} \left(R_{\text{H}_2\text{O}}^{\text{ex}} + V_{\text{H}_2\text{O}}^{\text{ex}} + E_{\text{H}_2\text{O}}^{\text{ex}} \right) . \tag{2.45}$$

Finally, the pressure equation of a fluid of ions can be written as

$$\frac{f_\alpha}{2} \left(\partial_t + \vec{u}_\alpha \partial_{\vec{x}} \right) p_\alpha + \frac{f_\alpha + 2}{2} p_\alpha \partial_{\vec{x}} \vec{u}_\alpha + \partial_{\vec{x}} \vec{q}_\alpha = \frac{\delta \varepsilon_\alpha^{\text{prod}}}{\delta t} + \frac{\delta \varepsilon_\alpha^{\text{coll}}}{\delta t} . \tag{2.46}$$

If the fluid describes electrons, the energy equation is given by

$$\frac{f_\text{e}}{2} \left(\partial_t + \vec{u}_\text{e} \partial_{\vec{x}} \right) p_\text{e} + \frac{f_\text{e} + 2}{2} p_\text{e} \partial_{\vec{x}} \vec{u}_\text{e} + \partial_{\vec{x}} \vec{q}_\text{e} = \frac{\delta \varepsilon_\text{e}^{\text{prod}}}{\delta t} + \frac{\delta \varepsilon_\text{e}^{\text{coll}}}{\delta t} + \frac{\delta \varepsilon_\text{e}^{\text{in.coll}}}{\delta t} . \tag{2.47}$$

Equations (2.36), (2.39), (2.46) and (2.47) represent the multifluid MHD model, which considers the major processes in the cometary interaction. A detailed discussion of the advantages and disadvantages of multifluid models with respect to the plasma interaction of 67P/Churyumov-Gerasimenko with the solar wind is discussed in Section (3.2). There, the latest available multifluid model, developed by Rubin et al. (2014a), is compared with the hybrid model.

2.4.2 The Single Fluid Magnetohydrodynamic Model

The multifluid model presented in the previous Section (2.4.1) can be simplified by assuming that the different species have the same behaviour, i.e. that the velocities are comparable to each other:

$$\vec{u}_{\text{SW}} \approx \vec{u}_{\text{CI}} \approx \vec{u}_\text{e} \approx \vec{u} . \tag{2.48}$$

In this case, the different fluids can merge to a single fluid description. For example, the mass density ρ can be defined by

$$\rho = \sum_\alpha m_\alpha n_\alpha . \tag{2.49}$$

In consequence, a single fluid model is not able to describe fast processes and the model requires scales much larger than the gyroradius. The procedure of deducing the equations is described by several standard textbooks (cf. Motschmann 2009). The resulting equations are:

$$\partial_t \rho + \partial_{\vec{x}} \left(\rho \vec{u} \right) = M_{\text{src}} \tag{2.50}$$

$$\partial_t \left(\rho \vec{u} \right) + \partial_{\vec{x}} \left(\rho \vec{u} \circ \vec{u} \right) + \partial_{\vec{x}} p = \vec{j} \times \vec{B} + \vec{I}_{\text{src}} \tag{2.51}$$

$$\partial_t \left(\frac{1}{2} \rho \vec{u}^2 + \varepsilon \right) + \partial_{\vec{x}} \left(\frac{1}{2} \rho \vec{u}^2 \vec{u} + \varepsilon \vec{u} + p \vec{u} + \vec{q} \right) = \vec{j} \cdot \vec{E} + E_{\text{src}} \tag{2.52}$$

$$\partial_{\vec{x}} \times \vec{E} = - \partial_t \vec{B} + \vec{F}_{\text{src}} . \tag{2.53}$$

The mass density, the velocity, and the pressure of the fluid are denoted as ρ, $\vec{u}$ and p, respectively. $\vec{q}$ is the heat flux and ε the internal energy. M_{src}, $\vec{I}_{\mathrm{src}}$, E_{src}, and $\vec{F}_{\mathrm{src}}$ denote the source and loss terms for mass, momentum, energy and diffusion. A general deduction of these from the expressions gained in the last section is omitted because of the limited used of the model in this work. The interaction between a comet and the solar wind within this fluid framework has been discussed by various authors, (cf. Schmidt and Wegmann 1982, Gombosi et al. 1996, Kartalev 1998, Hansen et al. 2007, Jia et al. 2007, Rubin et al. 2012).

2.4.2.1 The 1D Single Fluid Magnetohydrodynamic Model

In order to prepare the presentation of the extended upstream boundary model in Section (2.5.3.1), which is used in the hybrid plasma simulations to model the cometary environment upstream of the simulation box, a generalised one dimensional MHD model is deduced here. In addition, this 1D MHD model is extensively used for the study of the bow shock position in Section (4.1). A similar model has been proposed by Flammer and Mendis (1991) and by Schmidt et al. (1993). And, by reducing the complexity, the simple fluid model used by Biermann et al. (1967) can be derived from this model.

The purpose of the model is the simple description of the cometary interaction, in which the flow is modelled within a single dimension. This model is not appropriate for the entire cometary plasma environment but usable, for example, for some aspects in the upstream region, where the flow mainly moves away from the Sun and towards the comet. This is the one dimension to be considered (labelled with x). Furthermore, the model assumes a stationary state. Hence, effects caused by fluctuations in the solar wind cannot be investigated in this model. Moreover, the model neglects the heat flux and assumes an isotropic pressure. Based on these assumptions, the set of equations (2.50),(2.51),(2.52) and (2.53) can be simplified to (cf. Biermann et al. 1967, Flammer and Mendis 1991, Schmidt et al. 1993):

$$\partial_x (\rho u_x) = M_{\mathrm{src}} \tag{2.54}$$

$$\partial_x \left(\rho u_x^2 + p_{\mathrm{t}} + \frac{B_y^2}{2\mu_0} \right) = I_{\mathrm{src}} \tag{2.55}$$

$$\partial_x \left(\frac{1}{2}\rho u_x^3 + \frac{f+2}{2} p_{\mathrm{t}} u_x + \frac{B_y^2}{\mu_0} \right) = E_{\mathrm{src}} \tag{2.56}$$

$$\partial_x (u_x B_y) = F_{\mathrm{src}} \; . \tag{2.57}$$

The number of degrees of freedom of the flow is denoted by f. A discussion regarding the number of degrees of freedom is given in Section (4.1). For this simplification it is also assumed that the magnetic field is orientated in y-direction and the strength of the field is given by B_y. Thus, the magnetic field is perpendicular to the solar wind velocity. The integration of these equations from $-\infty$ to a position x allows us to resolve the following expressions for the magnetic field

$$B_y = \frac{1}{u_x} \left(\int_{-\infty}^{x} F_{\mathrm{src}} dx' + u_\infty B_\infty \right) \; , \tag{2.58}$$

for the mass density

$$\rho = \frac{1}{u_x}\left(\int_{-\infty}^{x} M_{\mathrm{src}} dx' + \rho_\infty u_\infty\right) , \tag{2.59}$$

and for the pressure

$$p_{\mathrm{t}} = \int_{-\infty}^{x} I_{\mathrm{src}} dx' + P_\infty - \rho u_x^2 - \frac{B_y^2}{2\mu_0} . \tag{2.60}$$

The entities with index ∞ represent values in the undisturbed solar wind. The total pressure in the undisturbed solar wind is given by the sum of the ram pressure, the thermal pressure and the magnetic pressure

$$\begin{aligned} P_\infty =& p_{\mathrm{r},\infty} + p_{\mathrm{t},\infty} + p_{\mathrm{m},\infty} \\ =& \rho_\infty u_\infty^2 + p_{\mathrm{t},\infty} + \frac{B_\infty^2}{2\mu_0} . \end{aligned} \tag{2.61}$$

In a similar way, the energy density can also be expressed by

$$E_\infty = \frac{1}{2}\rho_\infty u_\infty^2 + \frac{f+2}{2} p_{t,\infty} + \frac{B_\infty^2}{\mu_0} . \tag{2.62}$$

The fourth equation which remains from the integration is a cubic equation for the velocity of the plasma:

$$\begin{aligned} 0 =& \frac{1}{2}(f+1)\left(\int_{-\infty}^{x} M_{\mathrm{src}} dx' + \rho_\infty u_\infty\right) u_x^3 \\ &- \frac{1}{2}(f+2)\left(\int_{-\infty}^{x} I_{\mathrm{src}} dx' + P_\infty\right) u_x^2 \\ &+ \left(\int_{-\infty}^{x} E_{\mathrm{src}} dx' + E_\infty u_\infty\right) u_x \\ &+ \frac{1}{2}(f-2)\frac{1}{2\mu_0}\left(\int_{-\infty}^{x} F_{\mathrm{src}} dx' + u_\infty B_\infty\right)^2 . \end{aligned} \tag{2.63}$$

Using this general 1D single magnetohydrodynamic model, the basic effects of the mass-loading of the solar wind can be investigated. A similar investigation has been carried out by Biermann et al. (1967). They neglected the magnetic field and the thermal pressure in the undisturbed solar wind. Furthermore, they argued that the photo-ionisation of the neutral cometary gas far upstream of the comet leads to a change in the mass density. This is why the authors only used the mass density source M_{src} to model the interaction. All other sources are neglected. Regarding the momentum and energy sources, this can easily be justified by a comparison of the velocities: the velocity of the newly inserted cometary ions is about $1\,\mathrm{km\,s^{-1}}$, whereas the solar wind velocity is about $400\,\mathrm{km\,s^{-1}}$. Assuming that only the mass source M_{src} is relevant, Equation (2.63) simplifies to

$$\begin{aligned} 0 =& (f+1)\left(\int_{-\infty}^{x} M_{\mathrm{src}} dx' + \rho_\infty u_\infty\right) u_x^2 \\ &- (f+2)\,\rho_\infty u_\infty^2 u_x \\ &+ \rho_\infty u_\infty^3 . \end{aligned} \tag{2.64}$$

This can be solved:

$$\begin{aligned} u_{x_{1,2}} =& \frac{1}{2\,(f+1)\left(\int_{-\infty}^{x} M_{\mathrm{src}} dx' + \rho_\infty u_\infty\right)} \cdot \Bigg[(f+2)\,\rho_\infty u_\infty^2 \\ & \pm \sqrt{(f+2)^2\,\rho_\infty^2 u_\infty^4 - 4\,(f+1)\left(\int_{-\infty}^{x} M_{\mathrm{src}} dx' + \rho_\infty u_\infty\right)\rho_\infty u_\infty^3}\,\Bigg] \,. \end{aligned} \tag{2.65}$$

The injected mass in the undisturbed solar wind is zero. Therefore, the two solutions for the velocity in this case reduce to

$$u_{x_1}(x=-\infty) = u_\infty \qquad\qquad u_{x_2}(x=-\infty) = u_\infty \frac{1}{(f+1)} \,. \tag{2.66}$$

The solution u_{x_1} represents the cometary scenario. Based on that, the Mach number of the flow in the undisturbed solar wind can be calculated by

$$M_{\mathrm{s}} = \frac{u_x}{c_{\mathrm{s}}} = \sqrt{\frac{f\rho u_x^2}{(f+2)\,p}} \,, \tag{2.67}$$

where $c_{\mathrm{s}} = \sqrt{(f+2)p/(f\rho)}$ denotes the sonic speed. Within this framework, close to the undisturbed solar wind the velocity is close to u_∞ and the density close to ρ_∞. However, for large distances the pressure (see Equation 2.60) decreases towards zero because the thermal pressure in the undisturbed solar wind is neglected. Hence, the flow of solution u_{x_1} is supersonic at large distances. As a consequence, the supersonic solution is given by the "+" in Equation (2.65).

In the supersonic case the flow decelerates when mass is inserted into the flow. The more mass is inserted, the more the flow decelerates. In the cometary context this means that cometary ions are injected into the solar wind. Since the momentum source is neglected in the approach by Biermann et al. (1967), the new ions are resting in comparison to the solar wind flow. Consequently, the mass which needs to be transported by the flow is increased by this process. The conservation of energy and momentum requires a reduction of the flow speed. The remaining equations for the mass density and the pressure increase the more mass is inserted into the flow. Figure (2.6) shows the behaviour of the different quantities for the situation of comet 67P/Churyumov-Gerasimenko at 1.3 AU, which is discussed in detail Chapter (4).

2.5 The Hybrid Model

In contrast to the aforementioned fluid models, hybrid models try to solve the Boltzmann equation (2.20) for the ion species by a statistical approach. Hence, the ions in the plasma are described as individual particles and not as fluids. In contrast the electrons in the hybrid model are described as a fluid. In a fluid, the state at a given time and position is only characterised by the moments which are mean values. Furthermore, most fluid models only calculate the first three moments, as shown above, and, based on that, they are not able to reproduce complex distribution functions. In the hybrid approach each particle

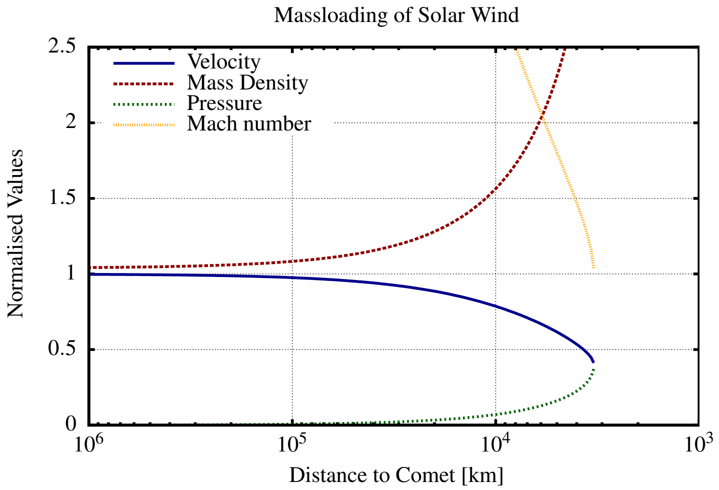

Figure 2.6: The effects of the massloading process on the solar wind are shown for comet 67P/Churyumov-Gerasimenko at a heliocentric distance of 1.3 AU, which will be discussed in Chapter (4), normalised to background values. For the calculation the fluid model by Biermann et al. (1967) is used with $f = 3$ and the neutral density according to Equation (2.6). While the solar wind flow approaches the comet, cometary ions are injected and the mass density increases. Simultaneously, the flow speed decreases. In addition, an increase in the pressure can be observed during the approach. At about 3300 km the sonic Mach number becomes equal to 1. At this point the solutions for the flow quantities also become complex.

can have an arbitrary position and a different velocity, wherefore arbitrary ion distribution functions can be modelled. This is especially important for the cometary environment in the weakly active phase of 67P/Churyumov-Gerasimenko, where the ring distribution of the cometary ions in the phase-space (see Section 3.1) and the decay of this distribution has a major impact and triggers many effects, such as ion-cyclotron waves. Also in case of a strongly active comet, the distribution function differs from a Maxwellian distribution at several places.

Within the hybrid framework the relative movement of ions to each other can be described due to the construction of the hybrid model, this can neither be done in multifluid models, except they use many fluids to describe a single species, nor in single-fluid models.

Especially, whenever the characteristic scales of the motion of the ions are comparable to the scale of the obstacle, the usage of hybrid models are strongly preferred. In contrast to the heavy solar wind protons and cometary ions, the characteristic scales of the electron motion are much smaller. Hence, the electrons in the hybrid model are described as a fluid.

Due to the fact that the hybrid approach is a common technique in plasma physics, several authors have used the hybrid model to study the cometary plasma interaction or similar interactions: Omidi and Winske (1987) investigated the massloading of the solar wind by using a one-dimensional hybrid model. The interaction of the solar wind with a cloud of charged dust has been investigated by Motschmann et al. (1992). Furthermore, based on the study of the cometary ionopause by Cravens (1989), Puhl-Quinn and Cravens (1995) simulated the ionopause of comet 1P/Halley in a one-dimensional hybrid simulation. Delamere (2006) used a three-dimensional hybrid model, which is combined with a fluid model, to study the asymmetry measured by Young et al. (2004) in the interaction region of comet 19P/Borrelly. What is more, Bagdonat and Motschmann (2002), Gortsas (2010) and Wiehle et al. (2011a) studied the evolution of a comet at various places and the impact of anisotropic outgassing. These authors used a code named *Braunschweig Code*, which is the predecessor of the A.I.K.E.F. code. The latter is used in this work and will be presented in detail now.

2.5.1 The Hybrid Model within the A.I.K.E.F. Code

The A.I.K.E.F. (Adaptive Ion Kinetic Electron Fluid) code is an implementation of the hybrid model and has initially been developed by Müller (2012). It is the successor of the *Braunschweig Code*, which has been developed by Bagdonat (2004). The purpose of the development was the study of the plasma interaction at weakly active comets, like comet 67P/Churyumov-Gerasimenko or comet 47P/Wirtanen. This code and its successor have been successfully applied to various different interaction scenarios, like Asteroids (e.g. Simon et al. 2006), Mars (e.g. Boesswetter et al. 2009), Titan (e.g. Müller et al. 2010) and particularly to Enceladus (e.g. Kriegel 2013).

In the hybrid model the equation of motion of each individual ion reads:

$$\frac{d}{dt}\vec{x}_\mathrm{i} = \vec{v}_\mathrm{i} \tag{2.68}$$

$$\frac{d}{dt}\vec{v}_\mathrm{i} = \frac{q_\mathrm{i}}{m_\mathrm{i}}\left(\vec{E} + \vec{v}_\mathrm{i} \times \vec{B}\right) + \frac{1}{n_\mathrm{i} m_\mathrm{i}}\vec{f}_\mathrm{cx} \,. \tag{2.69}$$

$\vec{x}_\mathrm{i}$ and $\vec{v}_\mathrm{i}$ denote the position and the velocity of an ion i, respectively. The charge and the mass of the ions of this species are given by q_i and m_i. In combination with the electric field $\vec{E}$ and the magnetic field $\vec{B}$, the Lorentz force acts on the charged particles. $\vec{f}_\mathrm{cx}$ represents additional forces acting on the ions.

For the description of the electron fluid, it is assumed that the plasma is quasi-neutral

$$0 = \sum_\alpha \rho_{\mathrm{c},\alpha} = \rho_\mathrm{c,i} + \rho_{c,e}$$

within the A.I.K.E.F. code. $\rho_{\mathrm{c},\alpha} = e q_\alpha n_\alpha$ denotes the charge density of plasma species α and $\rho_\mathrm{c,i}$ and $\rho_\mathrm{c,e}$ represent the charge densities of the ions and the electrons, respectively. Based on this assumption it is not necessary to derive the electron density by solving the continuity equation for the electron fluid as long as the density of the ions is known. The momentum equation for the electrons, see Equation (2.39), can be simplified by assuming zero mass for the electrons. Thereby, the equation can be transformed into an expression for the electric field (Bagdonat 2004)

$$\vec{E} = -\vec{u}_\mathrm{e} \times \vec{B} + \frac{\partial_{\vec{x}} p_\mathrm{e}}{\rho_\mathrm{e}} + \eta \vec{j} \,. \tag{2.70}$$

Since the electron mass is neglected in this equation, the sources and sinks on the right-hand side of Equation (2.39), e.g. the collision term, are negligible. However, as suggested by Bagdonat (2004), a resistivity η and the current density $\vec{j}$ are introduced in order to describe the *anomalous resistivity* due to high frequency wave-particle scattering. By using the definition of the current density

$$\vec{j} = \sum_{\alpha} \rho_{c,\alpha}\vec{u}_\alpha = \rho_{c,i}\vec{u}_\mathrm{i} + \rho_{c,e}\vec{u}_\mathrm{e} \,, \tag{2.71}$$

where $\rho_{c,i}\vec{u}_\mathrm{i}$ denotes the current density based on the ion movement and the quasi-neutrality, the expression for the electric field can be reformulated to

$$\vec{E} = -\vec{u}_\mathrm{i} \times \vec{B} + \frac{\vec{j} \times \vec{B}}{\rho_\mathrm{c,i}} - \frac{\partial_{\vec{x}} p_\mathrm{e}}{\rho_\mathrm{i}} + \eta \vec{j} \,. \tag{2.72}$$

The main purpose of the A.I.K.E.F. simulations are investigations of large-scale and low-frequency plasma phenomena. Therefore, it is suitable to neglect the displacement current. Based on that, the current density can be expressed by Ampère's Law

$$\vec{j} = \frac{1}{\mu_0} \partial_{\vec{x}} \times \vec{B} \,, \tag{2.73}$$

and the equation of the electric field can finally be reformulated into

$$\vec{E} = -\vec{u}_\mathrm{i} \times \vec{B} + \frac{\left(\partial_{\vec{x}} \times \vec{B}\right) \times \vec{B}}{\mu_0 \rho_\mathrm{c,i}} - \frac{\partial_{\vec{x}} p_\mathrm{e}}{\rho_\mathrm{i}} + \frac{\eta}{\mu_0} \partial_{\vec{x}} \times \vec{B} \,. \tag{2.74}$$

Regarding the pressure of the electrons, two different approaches are used within this thesis. In the first approach, proposed by Bagdonat (2004), the state equation for the electron fluid can be described by an adiabatic law

$$p_\mathrm{e} = p_\mathrm{e,0} \left(\frac{\rho_\mathrm{c,e}}{\rho_\mathrm{c,0}} \right)^{\gamma} \,, \tag{2.75}$$

where $p_\mathrm{e,0}$ and $\rho_\mathrm{c,0}$ denote the electron pressure and the charge density in the undisturbed solar wind, respectively. The adiabatic index is set to $\gamma = 2$ according to Bagdonat (2004). However, the cooling processes discussed in Section (2.3.2.2), and the resulting low temperature of the electrons in close vicinity of the nucleus cannot be described by an adiabatic law. Bagdonat (2004) suggested to split the electron pressure into two parts by using Dalton's law

$$p_\mathrm{e} = p_\mathrm{e,SW} + p_\mathrm{e,CI} \,. \tag{2.76}$$

Here the pressure of the hot solar wind electrons is given by $p_\mathrm{e,SW}$ and that of the 'cold' photoelectrons from the cometary environment by $p_\mathrm{e,CI}$ and both partial pressures are assumed to be adiabatic. As claimed by Bagdonat (2004), this simple model of the electron pressure is correct in the two extreme regions of the interaction, the undisturbed solar wind and in the close vicinity, where both plasmas are not mixed. However, in the regions in between, this simple model is not able to produce a correct electron temperature and causes a major shift of important plasma boundaries in case of strongly active comets, as discussed in Section (4.2.2).

The second approach to determine the electron pressure directly results from the pressure equation, Equation (2.47), which is similar to the multifluid approach described above. By modelling of all source and loss terms and by solving the resulting electron pressure equation

$$\frac{f_\mathrm{e}}{2}\left(\partial_t + \vec{u}_\mathrm{e}\partial_{\vec{x}}\right) p_\mathrm{e} + \frac{f_\mathrm{e}+2}{2} p_\mathrm{e}\partial_{\vec{x}}\vec{u}_\mathrm{e} + \partial_{\vec{x}}\vec{q}_\mathrm{e} = \frac{\delta\varepsilon_\mathrm{e}^\mathrm{prod}}{\delta t} + \frac{\delta\varepsilon_\mathrm{e}^\mathrm{coll}}{\delta t} + \frac{\delta\varepsilon_\mathrm{e}^\mathrm{in.coll}}{\delta t}\,, \tag{2.77}$$

the electron pressure can be derived in a more self-consistent fashion. This approach has been introduced to A.I.K.E.F. by Ranocha (2013). In comparison to the first approach, the sources and loss terms in this approach need to be adjusted carefully.

Faraday's law is used to derive an equation for the magnetic field

$$\begin{aligned}\partial_t\vec{B} &= -\partial_{\vec{x}} \times \vec{E} \qquad (2.78)\\ &= \partial_{\vec{x}} \times \left(\vec{u}_\mathrm{i} \times \vec{B}\right) - \partial_{\vec{x}} \times \left(\frac{\left(\partial_{\vec{x}} \times \vec{B}\right) \times \vec{B}}{\mu_0\rho_\mathrm{c,i}}\right) - \partial_{\vec{x}} \times \left(\frac{\partial_{\vec{x}} p_\mathrm{e}}{\rho_\mathrm{i}}\right) + \partial_{\vec{x}} \times \left(\frac{\eta}{\mu_0}\partial_{\vec{x}} \times \vec{B}\right)\,.\end{aligned}$$

It should be noted that in the case of an adiabatic electron pressure, the term with the electron pressure p_e vanishes from the magnetic field equation, as shown by Simon (2007). In case of a non-adiabatic electron pressure this term remains.

2.5.2 General Numerics of the A.I.K.E.F. Code

In this section, a brief overview of the numerical aspects and the used methods is given. For a more detailed description the author refers to Bagdonat (2004) and Müller (2012). Additional details about the electron pressure can be found in Ranocha (2013).

The A.I.K.E.F. code uses the Particle-In-Cell method. This means that individual particles can basically move to every position within a certain volume, whereas the moments and the electromagnetic fields are stored and computed on the nodes of a numerical mesh. These fields are transported to the particle position for the advancement of the new velocities and positions by an interpolation scheme.

In contrast to the former hybrid code by Bagdonat (2004), the A.I.K.E.F. code only uses a Cartesian mesh. One of the advantages of the A.I.K.E.F. code in comparison to its predecessor is based on this numerical mesh: it can use the *Hybrid Block Adaptive Mesh Refinement* (AMR) technique, which splits the entire simulation volume into blocks. Each block consists of eight octants, which can be overlayed by a new block of a higher refinement level. This allows, if needed, to adjust the resolution of the mesh locally, which is doubled by each level of refinement. The refinement can be static (hierarchical) or dynamically adjusted to the structures during run time (adaptive).

Another advantage of the A.I.K.E.F. code is the use of the *Message Passing Interface* (MPI), which allows us to split the computation to several processors on different nodes. An attempt is being made to impose an equal workload of the CPUs, therefore the blocks can be shifted among the participating CPUs.

However, it is obvious that it is not possible to describe every individual ion within the cometary plasma environment with the computational resources which are available nowadays. Therefore the ions are gathered to macro-particles in the A.I.K.E.F. code and are sometimes also named superparticles. Each macro-particle in the simulation represents a certain amount of ions, the so-called weight, which is not necessarily constant in the A.I.K.E.F. code. Nevertheless, each macro-particle has the same charge per mass ratio as the real ions. This is why the Equations (2.68) and (2.69) remain valid and have to be solved during each time step. The size of each time step has to fulfil the *Courant-Friedrichs-Lewy*-criterion, which demands that no macro-particle travels distances larger than the smallest mesh size within a single time step. Otherwise the simulation becomes numerically unstable. The same is true if the number of macro-particles within a cell is too low. This becomes important, when the size of the cell changes due to the mesh refinement. However, this can be avoided if the number of macro-particles is increased before the plasma enters a region of finer mesh size. It can be done by splitting the macro-particle into two, which are again separated perpendicular to the particle velocity from the original particle position by random distances. The momentum and the energy are conserved in this process, but the centre of mass is not conserved exactly. Nevertheless, due to the splitting of thousands of macro-particles, the error is statistically reduced (Müller 2012).

As a next step in the time integration scheme, the moments are gathered on the node of the mesh. Therefore, the weight and the velocity of the macro-particle within the cells are gathered according to their distance to the node. This technique is called the *Could-In-Cell* technique and the A.I.K.E.F. code uses a first order implementation, where the macro-particle only influences the moments of the neighbouring nodes of the mesh, but not the next nodes. The inverse scheme is used to extrapolate the electromagnetic field from the nodes towards the particle position. The *Current Advance Method* (Matthews 1994) is applied to calculate the electric field. And the *Cycling Leapfrog* integration scheme is used to advance the magnetic field in time. At the same time the electron pressure equation has to be solved. In order to avoid numerical fluctuations, i.e. local strong gradients, and to increase the stability of the simulation, a simple smoothing mechanism for the electromagnetic fields and the electron pressure has to be applied. The smoothed field value $F^{\mathrm{sm}}_{[i,j,k]}$ at a mesh node $[i,j,k]$ is given by

$$F^{\mathrm{sm}}_{[i,j,k]} = (1-\eta_{\mathrm{sm}})\,F_{[i,j,k]} + \eta_{\mathrm{sm}}\overline{F_{[i,j,k]}}\ , \tag{2.79}$$

where $\eta_{\mathrm{sm}} \in [0,1]$ denotes the smooting factor and

$$\overline{F_{[i,j,k]}} = \sum_{a,b,c=-1}^{1} \frac{2^{-\left(a^2+b^2+c^2\right)}}{8} F_{[i+a,j+b,k+c]} \tag{2.80}$$

represents the values of the neighbouring mesh nodes weighted by the distance.

An alternative option for the reduction of these fluctuations would be the use of a global resistivity η in the simulations. A detailed comparison of both methods can be found in Kriegel (2013). However, in case of simulations of the cometary interaction, the latter option is not successful: the diffusion value, which leads to a stable simulation, blurs all significant structures. Therefore only the former option is used.

As given by the construction of the numerical mesh, it is not ensured that the divergence of the magnetic field vanishes. This is especially true in case of highly refined numerical meshes. Müller (2007) introduced an additional *divergence cleaning* scheme to the A.I.K.E.F. code to reduce the divergence of the magnetic field. After each calculation of the magnetic field, a divergence free solution of the field is obtained by

$$\vec{B}_{\mathrm{div}=0} = \vec{B} + \partial_{\vec{x}}\phi\ , \tag{2.81}$$

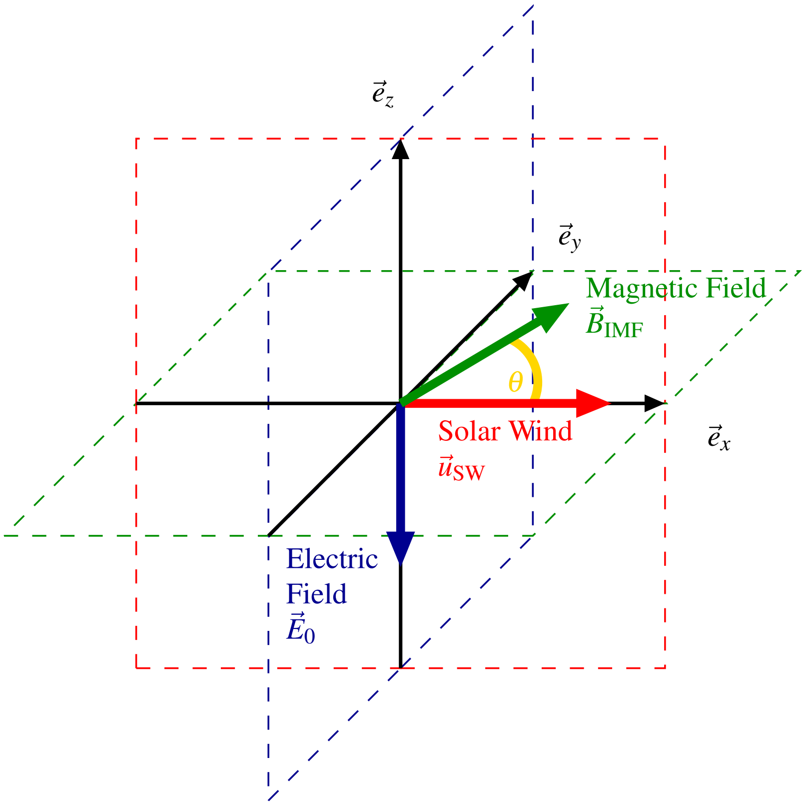

Figure 2.7: The orientation of the simulation box used throughout this work. The undisturbed solar wind enters the box at the $-x$-boundary and moves into positive x-direction. The xy-plane, marked in green, contains the interplanetary magnetic field. The Parker angle θ is the angle between the magnetic field and the solar wind velocity vector. Based on this orientation, the convective electric field of the undisturbed solar wind points anti-parallel to $\vec{e}_z$.

where ϕ is the solution of a Poisson equation

$$\partial_{\vec{x}}^2 \phi = -\partial_{\vec{x}} \cdot \vec{B} \,. \tag{2.82}$$

2.5.3 The Modelling of the Comet in the A.I.K.E.F. Code

In general, the simulation boxes in the A.I.K.E.F. code are cubes or cuboids with varying edge lengths LX, LY and LZ. The positions in the box are described by a Cartesian coordinate system. In this work, the undisturbed solar wind is directed in x-direction, and the motion of the comet during a simulation is neglected. This can be justified by the small orbital velocity of the comet in comparison to the fast solar wind speed. The xy-plane contains the interplanetary magnetic field. The actual angle between the solar wind velocity and the interplanetary magnetic field is θ and varies with heliocentric distance, as discussed in Section 2.1. The origin of the system is at the nucleus, respectively the centre of the neutral gas cloud. The orientation of the described setup is shown in Figure (2.7).

Based on the simulation geometry, the solar wind enters the simulation box at the $-x$-

boundary. Here *inflow* conditions for particles and fields are used. This means that the particles, which are located in the cells at the boundaries, are removed and refilled according to the undisturbed solar wind density value at each time step. The fields are constant on these nodes at the boundaries. On the opposite side of the simulation box,*outflow* conditions are used. Here, the particles are removed and the derivative of the field in normal direction to the boundary is set to zero.

The applied boundary conditions on the remaining boundaries depend on the specific scenario: In case of a weakly active comet, a warm solar wind and boundaries far away from the nucleus, *inflow*-boundaries can be used at all remaining boundaries. In case of a cold solar wind and *inflow*-boundary conditions, a void in the solar wind density is generated. This artefact is caused by the injection of cometary ions which trigger a motion of the solar wind particles in $+z$-direction in the box. The physics behind this motion are explained in detail in Section (3.1). However, the solar wind particles in the boundary cells have in contrast to the other ions only a constant velocity into x-direction plus a small temperature velocity component perpendicular to the boundary and cannot refill the void caused by the solar wind particles moving upward. This is why it has to be ensured that the boundary is far away from the nucleus and the resulting artefact is not interacting with the structures or boundaries of interest. In case of an active comet, a bow shock is formed. This bow shock extends to large distances in y- and z-direction and intersects with the boundaries of the simulation box. Because of the solar wind deflection towards $+z$-direction, a reflection of the bow shock can occur at the $+z$-boundary when *inflow*-conditions are used. In case of *outflow*-conditions this reflection vanishes, as shown in Figure (2.8).

2.5.3.1 The Extended Upstream Boundary Model

One of the most significant facts of the cometary environment is the vast size of the interaction region. As mentioned at the beginning of this chapter, the coma extends to distances of several million kilometres away from the comet. At these large distances the initial interaction takes place and the first cometary neutral molecule becomes ionised by solar radiation. However, the main interaction takes place closer to the nucleus, where different boundaries and structures can be observed. Based on limited numerical resources, the large demand by the A.I.K.E.F. code, the description of ions as particles and the need of resolving the boundaries with a sufficient mesh resolution, a negotiation process on the simulation box size and the highest mesh resolution is required.

As know from the flyby of the Giotto spacecraft at comet 1P/Halley, the thinnest boundary is the cometary ionopause with a thickness of 25 km (Neubauer 1988). Within this boundary the magnetic field strength drops by 20 nT. In order to resolve such thin structures and large gradients with a numerical mesh, its size has to be much smaller than this length scale. However, the A.I.K.E.F. code is only able to handle five mesh refinement levels. At each refinement level the resolution is doubled, the number of macro-particles is increased to ensure sufficient statistics. This is why each refinement level requests a huge amount of additional computational resources. If using a minimum span of about 2 km between the mesh nodes at the highest refinement level, the minimum resolution is about 70 km. Such a mesh configuration would require several tens of thousand mesh nodes in each direction to model the entire simulation box and each of these cells would be filled

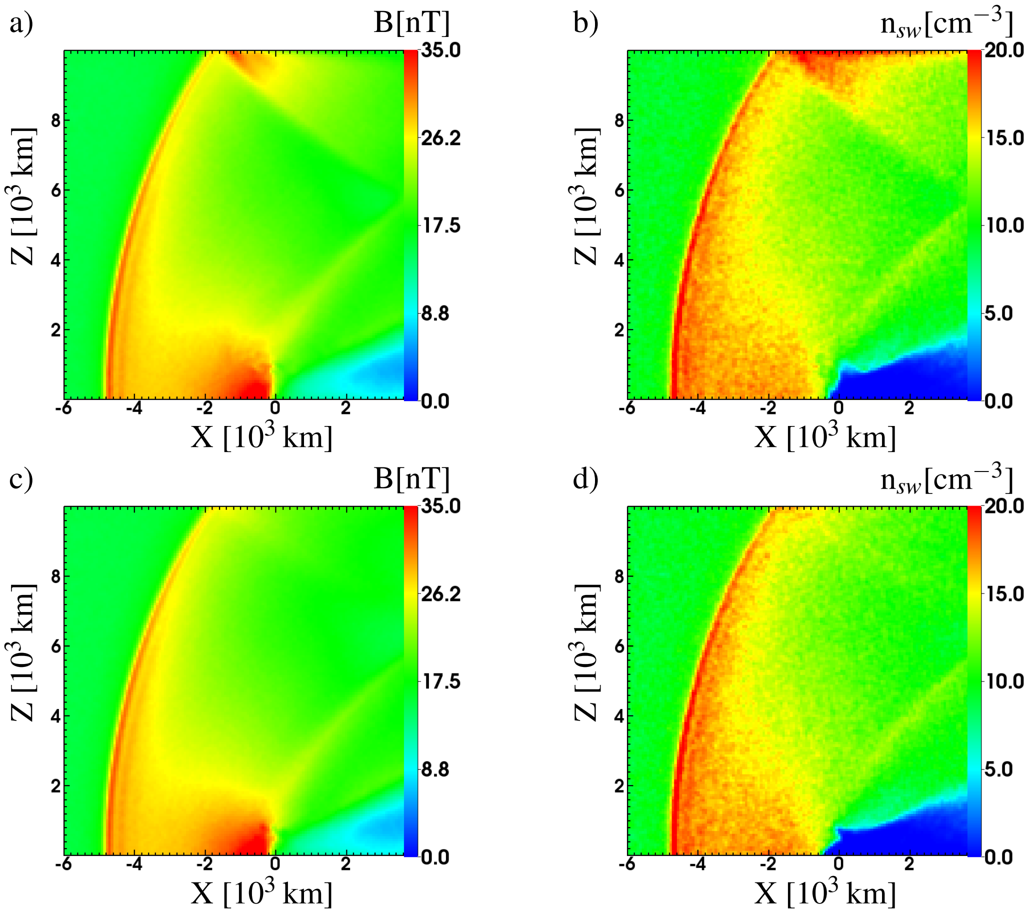

Figure 2.8: The upper hemisphere of the xz-cross-section for two simulations with different boundary conditions are presented. a) and b) show the solar wind density and the magnetic field strength of a simulation with *inflow*-boundary conditions at the $+z$-boundary, whereas c) and d) present the same fields for simulations with *outflow*-conditions. The scenario is a strongly active comet, which is discussed in detail in Chapter (4). In these figures a bow shock is visible, which has a stand-off distance of about 5000 km and which is characterised by a jump in the magnetic field and the density. In case of *inflow*-conditions, a strong reflection of the bow shock occurs at the upper boundary. This reflection is not present in case *outflow*-conditions are used.

with hundreds of macro-particles. Additionally, the each mesh refinement level requires a reduction of the time step by a factor of 2, in order to fulfil the *Courant-Friedrichs-Lewy* condition. Such a simulation setup is not feasible with modern computers. Moreover, it is not important to model the interaction at large distances in such great detail because the changes appear on much larger scales. This is why a maximum simulation box size of several thousand kilometres is sufficient for comet 67P/Churyumov-Gerasimenko. Nevertheless, the massloading of the solar wind upstream of the simulation cannot be neglected.

The modifications of the solar wind flow due to the interaction upstream of the simulation box can be modelled by using a semi-kinetic approach. The model assumes that it is sufficient to describe the flow in one-dimension because the scales of the ion motion perpendicular to the flow direction are much smaller than the length of the interaction region upstream of the simulation box. Hence, the changes in y- and z-direction are neglected. The semi-kinetic model furthermore assumes a stationary situation. This model has been developed as part of this thesis and is based on the model by Galeev et al. (1985) and Flammer and Mendis (1991). The basic equations of this semi-kinetic model are based on the single fluid approach, which is described in Section (2.4.2.1), plus an additional equation to describe the cometary ion density:

$$\partial_x \left(\rho_{\mathrm{CI}} u_x f\left(u_x, \mu\right)\right) = M_{\mathrm{src}} \cdot \delta\left(\mu - \frac{m_{\mathrm{CI}} u_x^2}{2 B_y}\right) \tag{2.83}$$

$$\partial_x \left(\rho u_x\right) = M_{\mathrm{src}} \tag{2.84}$$

$$\partial_x \left(\rho u_x^2 + p_{\mathrm{t}} + \frac{B_y^2}{2\mu_0}\right) = I_{\mathrm{src}} \tag{2.85}$$

$$\partial_x \left(\frac{1}{2}\rho u_x^3 + \frac{f+2}{2} p_{\mathrm{t}} u_x + \frac{B_y^2}{\mu_0}\right) = E_{\mathrm{src}} \tag{2.86}$$

$$\partial_x \left(u_x B_y\right) = F_{\mathrm{src}} \; . \tag{2.87}$$

The distribution function of the cometary ions is denoted by $f_{\mathrm{CI}}\left(u_x, \mu\right)$ and depends on the flow velocity and the magnetic moment $\mu = m_{\mathrm{CI}} v_{\perp}^2 / 2B_y$ of the cometary ions. The magnetic moment is a constant of motion for slow variations. Hence, the magnetic moment remains constant over time intervals larger than the gyroperiod. In contrast to the general deduction, the source terms for momentum and energy and the diffusion of the magnetic field are neglected. As shown above, the single fluid equations can be used to derive an equation for the velocity. The general expression is given by Equation (2.63). By neglecting the source terms, and by replacing $\left(\int M_{\mathrm{src}} dx + \rho_\infty u_\infty\right)$ with ρu_x, which is a statement from the continuity equation, the following equation for the mass density flux can be deduced:

$$\rho u_x = \frac{1}{u_\infty} \left(\frac{(f+2)}{(f+1)} P_\infty \frac{u_\infty}{u_x} - \frac{2}{(f+1)} E_\infty \frac{u_\infty^2}{u_x^2} - \frac{(f-2)}{(f+1)} p_{\mathrm{m},\infty} \frac{u_\infty^3}{u_x^3} \right) . \tag{2.88}$$

In the limit of the model by Biermann et al. (1967) this expression can be simplified to Equation (6) from Galeev et al. (1985).

As stated by Galeev et al. (1985) the solution of the continuity equation for the cometary

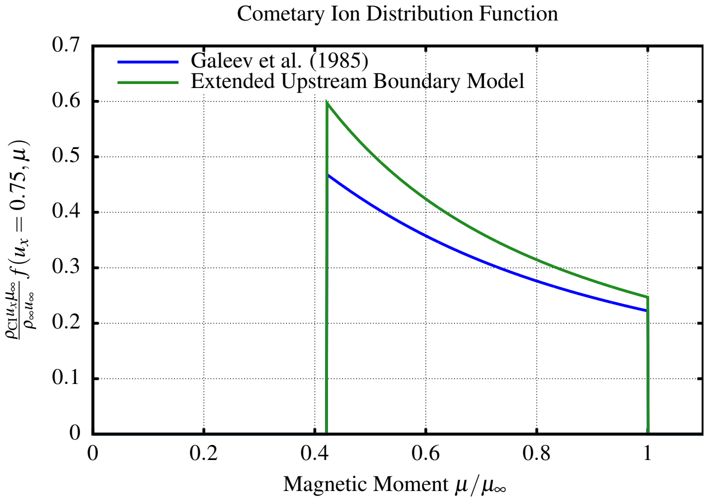

Figure 2.9: The cometary ion distribution functions in the unshocked solar wind for comet 67P/-Churyumov-Gerasimenko at 1.3 AU based on the *extend upstream boundary model* and the model by Galeev et al. (1985). The distribution functions are shown for a solar wind speed reduction to 0.75 of the undisturbed solar wind speed. The first cometary ions which are picked up by the solar wind have a magnetic moment of μ_∞, whereas cometary ions which are picked-up close to the nucleus have a smaller magnetic moment, but are more prominent in the distribution function. In comparison to the original model by Galeev et al. (1985), which uses $f = 2$ and no magnetic field or thermal pressure, the distribution function of the new model, which uses $f = 3$, increases faster to smaller magnetic moments.

ions is given by

$$\rho_{\mathrm{CI}} u_x f(u_x, \mu) = \int_{u_\infty}^{u} \frac{d(\rho' u')}{du'} \delta \left(\mu - \frac{m_{\mathrm{CI}} u_x'^2}{2B_y'} \right) du' \,. \tag{2.89}$$

The deviation $d(\rho' u')/du'$ can be calculated by using Equation (2.88) and the magnetic field can be replaced by $B_y' = u_\infty B_\infty / u_x$, see Equation (2.58). With an additional conversion of the argument of the delta distribution, the cometary mass flux density in the new extended approach is given by

$$\begin{aligned} \rho_{\mathrm{CI}} u_x f(u_x, \mu) = & \frac{1}{u_\infty} \left(\frac{(f+2)}{(f+1)} P_\infty \mu^{*-\frac{2}{3}} - \frac{4}{(f+1)} E_\infty \mu^{*-1} - \frac{(f-2)}{(f+1)} p_{\mathrm{m},\infty} \mu^{*-\frac{4}{3}} \right) \\ & \cdot \quad \Theta(1-\mu^*) \Theta\left(\mu^* - \frac{u_x}{u_\infty} \right) \cdot 1 / \left(3 \mu_\infty^{\frac{1}{3}} \mu^{\frac{2}{3}} \right) \,. \end{aligned} \tag{2.90}$$

Θ is the Heaviside step function and μ^* denotes the magnetic moment normalised to the undisturbed solar wind.

In Figure (2.9) the cometary ion distribution functions for this new model and for the original model by Galeev et al. (1985) are shown for a situation where the solar wind speed is reduced to 300 km s^{-1} from initially 400 km s^{-1}, i.e. close to the bow shock. At large distances to the comet, the magnetic moment of the cometary ions is equal to the moment in the undisturbed solar wind. It should be noted that the model by Galeev et al. (1985) uses $f = 2$, whereas the new extended upstream boundary model uses $f = 3$. A

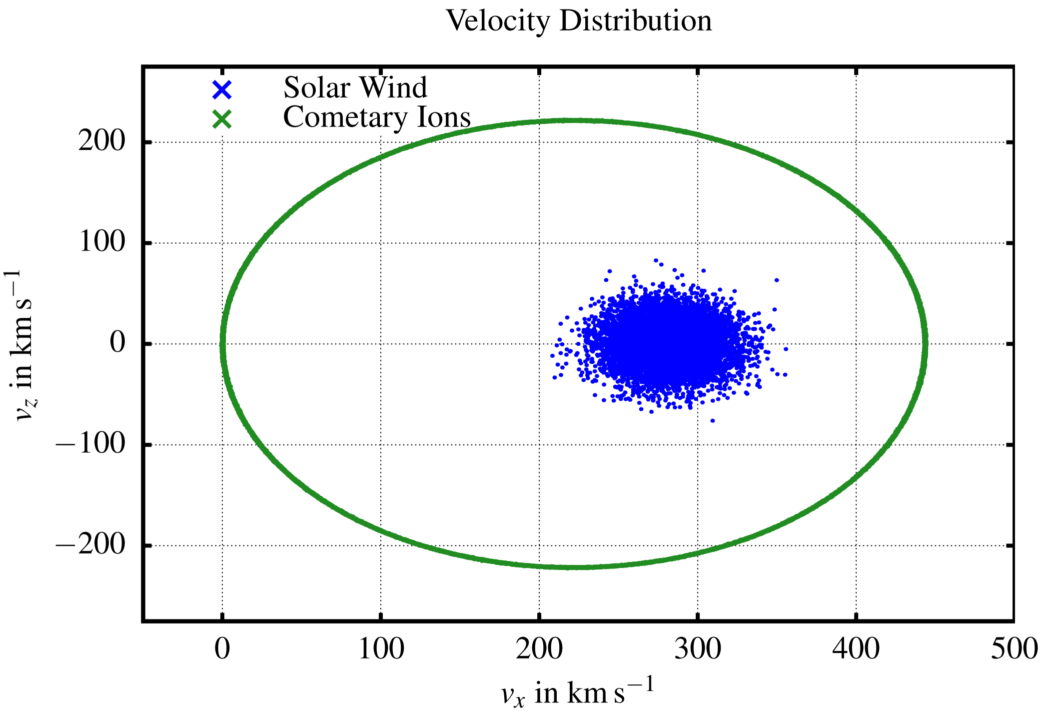

Figure 2.10: The distribution of solar wind and cometary ions in the velocity space as inserted into the simulation box. The blue dots represent the velocities of the solar wind and the green dots stand for the cometary ions. Because of the good statistics the green dots are joint to a single circle. The angle between the magnetic field and the solar wind flow is 52°. The solar wind particles have a bulk velocity according to the extended upstream boundary model and a thermal velocity. The cometary ions are inserted into the simulation box with the same bulk velocity plus a gyromotion.

discussion of the number of degrees of freedom is provided in Section (4.1). In contrast to Galeev et al. (1985), the extended upstream boundary model considers a magnetic field and a thermal pressure. The more the flow approaches the comet, the more the velocity of the flow is reduced, and the more the magnetic moment of new picked up cometary ions decrease. However, in the construction of this model, the scattering of cometary ions from a ring distribution towards a shell distribution is not possible. However, as known from observation, the initial ring distribution remains for a few periods (Coates et al. 1993, Coates 2010).

The total cometary ion flux density in the flow can be determined by an integration over all magnetic moments:

$$\begin{aligned}\rho_{\mathrm{CI}} u_x = \frac{1}{3\,(f+1)\,u_\infty} \cdot \Bigg(& -3\,(f+2)\,P_\infty \left(1-\frac{u_\infty}{u_x}\right) \\ & +6E_\infty \left(1-\frac{u_\infty^2}{u_x^2}\right) + 3\,(f-2)\,p_{\mathrm{m},\infty} \left(1-\frac{u_\infty^3}{u_x^3}\right)\Bigg)\ .\end{aligned} \tag{2.91}$$

Since the extended upstream boundary model based on the 1D single fluid model, which was presented in Section (2.4.2.1), the flow speed can be determined by solving Equation (2.63), and the expression for the total mass density in Equation (2.59). Subsequently, the cometary number density and the solar wind number density can be calculated. In the model the mean velocity of the cometary ions is equal to that of the solar wind protons. The velocity of the cometary ions is superimposed by a gyromotion. Figure (2.10) shows an example of the initial distribution of the particles in the phase space on the $v_x v_z$-plane as modelled in A.I.K.E.F. code, which finally follows from the extended upstream boundary model. The solar wind particles are distributed around their bulk velocity according their temperature, whereas the cometary ions reveal a large ring distribution in case of a magnetic field orientated to the solar wind velocity with an angle of 52°. In addition, the magnetic field and the pressure of the entire plasma can also be determined by this model. As discussed by Galeev et al. (1985), the pressure is only provided by the presence of the cometary ions. Consequently, the thermal pressure of the solar wind remains constant.

By using the extended upstream boundary model, the plasma parameters at the position of the upstream boundary in the simulation box can be calculated. The variation of the massloading due to the different radial distances to the Sun-comet line is taken into account by using different integration paths. This is especially important for simulation boxes with a large extension in y- and z-direction (Figure 2.11). The figure shows the initial state of a simulation of comet 67P/Churyumov-Gerasimenko at 1.3 AU. At the first time step, the values calculated for the upstream boundary are also applied to the entire simulation box, which can be seen in Figure (2.11 b).

It is clearly visible in Figure (2.11) that the solar wind plasma is modified upstream of the simulation box . For example, the velocity of the solar wind is reduced from $400\,\mathrm{km\,s^{-1}}$ to about $280\,\mathrm{km\,s^{-1}}$ on the Sun-comet line at a distance of 6000 km upstream of the nucleus for the selected scenario. A simplification is carried out by the injection of cometary ions into the simulation box at the upstream boundary. Instead of using the complex velocity distribution, as shown in Figure (2.9), it is assumed that all cometary ions have an equal magnetic moment, which is determined by the flow quantities at the upstream boundary. Hence, the distribution of the cometary ions is a single ring distribution, see Figure (2.10). This simplification is justified by the fact that even the usage of a Maxwellian distribution for the injected ions does not effect the bow shock position.

Further effects like the draping of the magnetic field due to the velocity shear with different radial distances to the Sun-comet line are neglected. It should also be clear that the model collapses at a certain point, because the variations in y- and z-direction are no longer negligible. This can be seen in Figure (2.12), where the stand-off positions of the cometary bow shock are shown for different simulation box sizes. The bow shock distances in simulations without the extended upstream boundary model are labelled in green. They show a clear increase in the bow shock position, when the modelled upstream region is increased. This is obvious because the larger the modelled region, the more cometary ions can modify the flow. The result indicates that the hybrid plasma simulations of the global interaction region, as performed by Bagdonat (2004) and Gortsas (2010), can only show the qualitatively behaviour. However, quantitative results should be treated with caution, since the simulation box size influences the position of the major boundaries. A detailed discussion of the position of the cometary bow shock is given in Section (4.1).

However, the figure demonstrates the capabilities of the extended upstream boundary model. The bow shock stand-off distance in simulations which use the extended upstream boundary model (red) is constant as long as the distance between the nucleus and the upstream boundary of the simulation is large enough. This length is estimated to be three

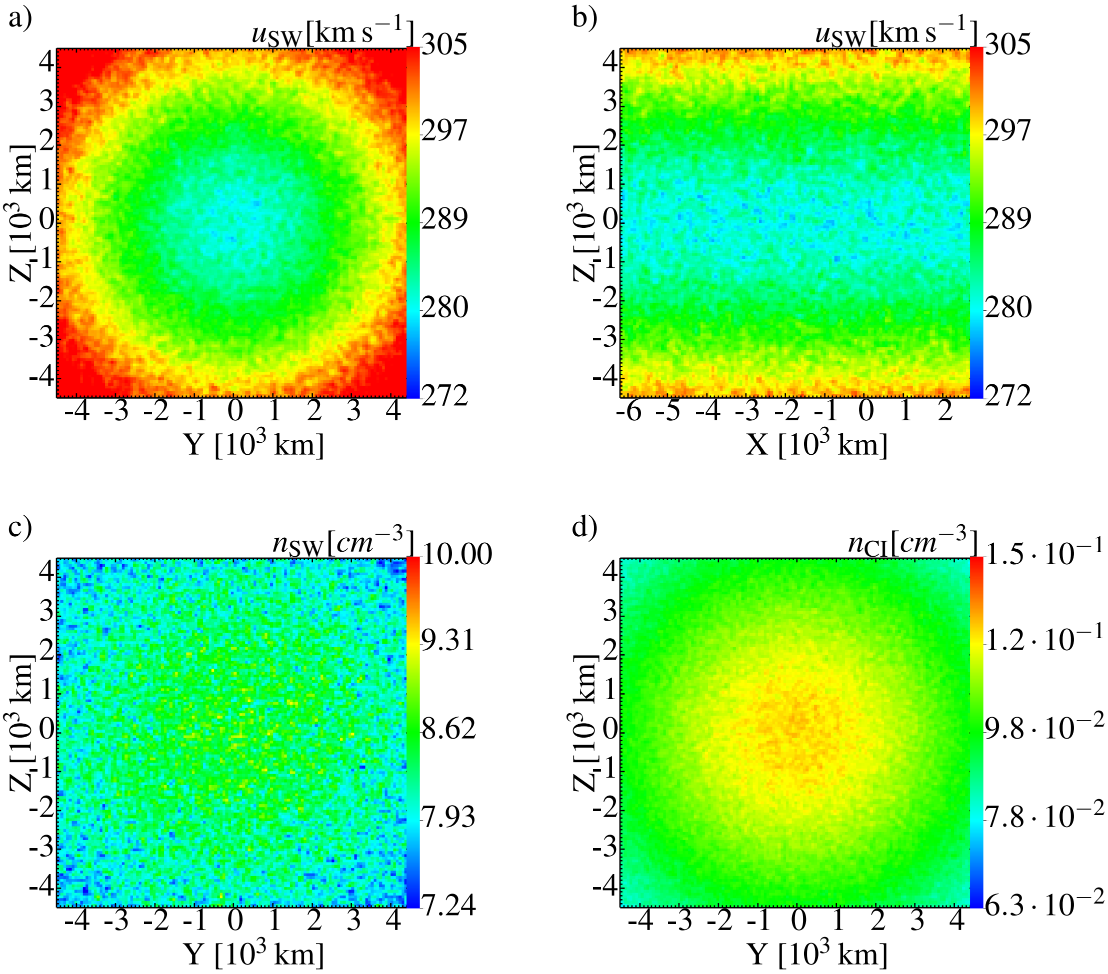

Figure 2.11: The initial state (TL = 0) of a simulation of comet 67P/Churyumov-Gerasimenko at 1.3 AU, which uses the extended upstream boundary conditions. The panels a) and b) show the solar wind speed in the x=0-cross-section and the y=0-cross-section. The panels c) and d) present the densities of the solar wind protons and the cometary ions on the x-cross-section. The plasma close to the Sun-comet line is slower than the plasma at larger distances. A contrary character can be observed in the density profiles.

times the bow shock distance. At the bow shock, the entire extended upstream boundary model collapses as well as all other one-dimensional models of the upstream region, since a deflection of the flow towards y- and z-direction occurs. In the setup shown in the figure, the stand-off distance of the bow shock distance is at about 2200 km. Thus, the minimum distance between the nucleus and the upstream boundary in the A.I.K.E.F. code simulation is at about 6600 km, which is again a compromise regarding the computational time of the simulations. At a distance of 5000 km, the deviation of the bow shock is less than 5% of the other bow shock stand-off distances, i.e. about 100 km.

This demonstration shows that hybrid plasma simulations of the global plasma interaction request a model of the physics upstream of the limited simulation box. Otherwise,

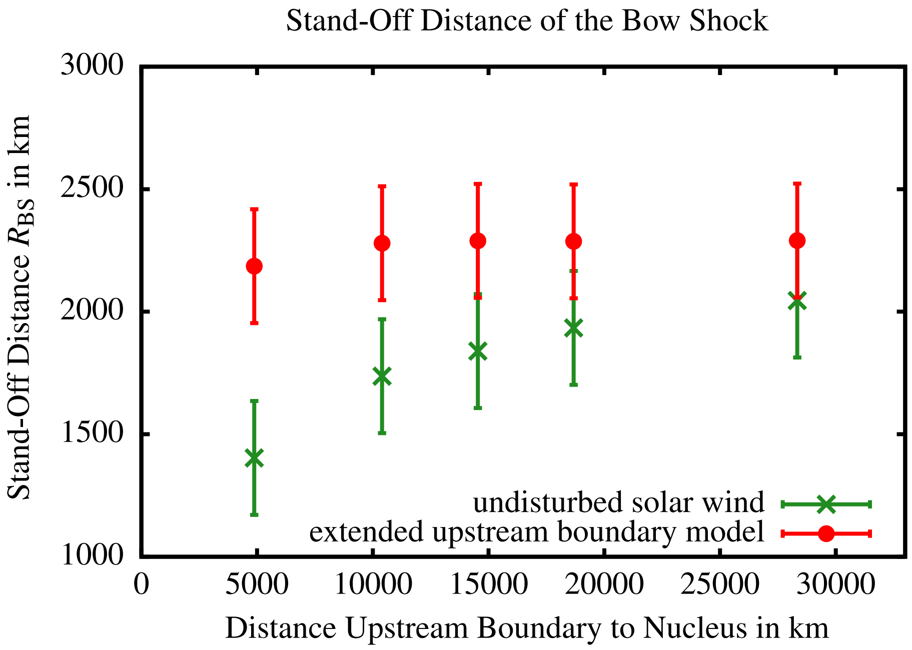

Figure 2.12: The stand-off distance of the cometary bow shock for different simulation box configurations by using two different boundary conditions. The green crosses label the distances for the bow shock in case the undisturbed solar wind enters the simulation box on the upstream boundary. As one can see, the more of the upstream region is modelled by the A.I.K.E.F. code simulation, the more the bow shock moves towards the Sun. In contrast, the bow shock position remains nearly constant in the simulations with the newly extended upstream boundary model. Reprinted from Koenders et al. (2013) with permission from Elsevier.

the size of the simulation box has an impact on the position of major boundaries.

2.5.3.2 The Nucleus

The radius of the nucleus of 67P/Churyumov-Gerasimenko, which is about 2 km, is at best comparable to the resolution of the numerical mesh. This is set by the limited numerical resources and the vast increase of computational time by any additional mesh refinement levels. Hence, in the best case, the nucleus can be modelled by three mesh nodes in each direction. For reasons of numerically stability, the gradients caused by a small nucleus cannot be modelled on three data points.

Moreover, as discussed above, the actual obstacle for the solar wind is the cometary atmosphere rather than the nucleus, which only triggers minor effects. Therefore the nucleus is neglected in hybrid plasma simulations. Furthermore, effects like the sputtering of ions, absorption of the solar wind particles and the triggering of the wake are not modelled either.

In order to avoid problems at the origin in simulations with a strongly outgassing comet, i.e. the generation of magnetic field caused by too strong density variations at the origin, the neutral gas density is limited to the value reached at a distance of $r_{\text{min}} = \sqrt{3}\Delta x_{\text{max}}$, where Δx_{max} denotes the maximum spatial resolution of the numerical mesh. In addition, in a sphere with a radius of $5\Delta x_{\text{max}}$ the electron pressure is kept constant to the mean pressure on a shell with a radius of $6\Delta x_{\text{max}}$, which proved to be a suitable value.

2.5.3.3 Neutral Species

The obstacles for the incoming solar wind are the cometary atmosphere and the reactions triggered by this extended region. Thus, the cometary atmosphere is a key feature for the cometary interaction. However, calculations of the properties of this atmosphere are not performed with the A.I.K.E.F. code. Within the code, the neutral gas is considered as a fluid in the background. In contrast to former simulations of the cometary interaction, the properties, the density, the velocity and the pressure are stored on the nodes of the numerical mesh. Consequently, the values of these moments have to be interpolated between mesh nodes. This approach reduces the resolution. In comparison, an analytical expression could produce finer gradients, but the resolution of the simulation is limited to the mesh size. The advantage of the chosen approach is that results of external modelling or experimental groups can easily be included in future. Furthermore, this approach saves computational resources.

In the standard configuration of this thesis, the isotropic model by Haser (1957) is applied to the respective situations. Thus, the density of the neutral fluid is set according to Equation (2.6) and the magnitude of the velocity is set to a constant value u_{CN}.

2.5.3.4 Ionisation

As discussed in Section (2.3.2.1), ionisation is the most dominant process in the plasma interaction. This is why the modelling of this process has to be taken with care and the application of the usually used method has to be discussed in case of applied adaptive mesh refinements. The fashion, in which the ionisation process is modelled in the hybrid simulations of Bagdonat (2004) and various others of the *Braunschweig Code* and its successor, is based on the *accept-rejection method*, which is described in detail by Bagdonat (2004). At each time step dt, this common technique is used to generate a fixed number N of random positions within a given volume according to a distribution, which is in this case defined by the ionisation profile. At each position new macro-particles are inserted into the volume. Thus, all macro-particles have the same weight, and, thus, represent the same number of ions. In a cometary environment, the simplest case is given by a neutral density profile, according to Haser (1957), and a uniform ionisation frequency. This ionisation profile is given by Equation (2.13) and the volume V is a spherical shell with an inner radius equal to the radius of the nucleus r_{nuc} and an outer radius r_{out}. Thus, the weight of the new macro-particles w has to be determined by

$$w = \frac{dt}{N} \iiint_{\text{V}} \nu_{\text{ion,ph}} n_{\text{CN}}(x) \, dV \; . \tag{2.92}$$

As a consequence of the equal weight for all new macro-particles, this technique inserts more macro-particles into regions where the ionisation $\nu_{\text{ion,ph}} n_{\text{CN}}$ rate is higher. However, in highly refined numerical simulations of the cometary environment this technique is only suitable to a limited extend: the amount of new produced macro-particles increases faster than the mesh resolution. Thus, the cells close to the nucleus contain much more macro-particles than the cells further away from it. The cells which contains too many macro-particles can be avoided by reducing the number of new macro-particles N. However, in order to reach sufficient statistics for the cometary ions at large distances to the nucleus, the number of macro-particles N has to be large. In case of a simulation box with an edge length of 10^5 km, five refinement levels, and a maximum resolution of 2 km, about 10^5 macro-particles are inserted into the box at each time step to yield a sufficient statistic at the cells at large cometocentric distances. Thus, in order to maintain the amount of macro-particles in the inner region a merging of the newly inserted macro-particles could help. This, however, would increase the computation time. In order to fill all cells of the simulation box, in particular the cells at the corners of the box, the volume V has to be larger than the box. Thus, random numbers have to be generated without any use. Therefore this technique increases the amount of computational time again.

In a different approach, which is more suitable for ionisation profiles with strong peaks, the macro-particles are inserted more homogeneously. Consequently, the weight of the new macro-particles cannot be constant. This approach checks for each cell at each time step if a new macro-particle has to be inserted. This is given by a fixed probability $k \leq 1$. Afterwards, a new macro-particle is inserted at a random position within the cell. The weight of this macro-particle is defined by

$$w = k\nu_{\mathrm{ion,ph}} n_{\mathrm{CN}}(x)\,dt\ . \tag{2.93}$$

The main advantage of this technique is that the number of newly inserted macro-particles in all cells is similar. Thus, a balanced workload for the cells can easily be reached. This saves valuable computational resources. Furthermore, this technique allows us to easily use arbitrary neutral densities, i.e. none-analytical density profiles such as results from other models.

The different approaches are compared in a series of test-simulations. For this purpose, two different simulation boxes were configured: one box does not use a mesh refinement and has a mesh size of about 75 km, whereas the second configuration uses this technique and reaches a maximum resolution of 2 km. The simulation boxes were empty at the initial time step and the movement of the ions was suppressed during the simulation and the splitting, and the merging of macro-particles was disabled. Each of the configurations is used with both ionisation methods. The resulting quantities along the Sun-comet line are shown in Figure (2.13). The densities are shown in a) and are in agreement with the analytical solution which was obtained by integrating the ionisation profile $\nu_{\mathrm{ion,ph}} n_{\mathrm{CN}}$. The density only differs from the analytically expected value at distances comparable to the mesh resolution. This difference has been implemented to avoid vast massive macro-particles that seriously disturb the numerical stability. In this test the initial velocity of the new cometary ions is set to 1 km plus a thermal component (Figure 2.13 b), but the movement was suppressed. Finally, the number of macro-particles is shown in (Figure 2.13 c). When using the second method, the number of macro-particles remains constant, except for spikes due to ghost cells in the high refined simulation[3]. In contrast, the simulation which uses the *accept-rejection method* shows a strong variation and unacceptable high

---

[3] Ghost cells are cells at the boundaries of a block in the A.I.K.E.F. code, which are used for the communication between neighbouring blocks (Müller 2012).

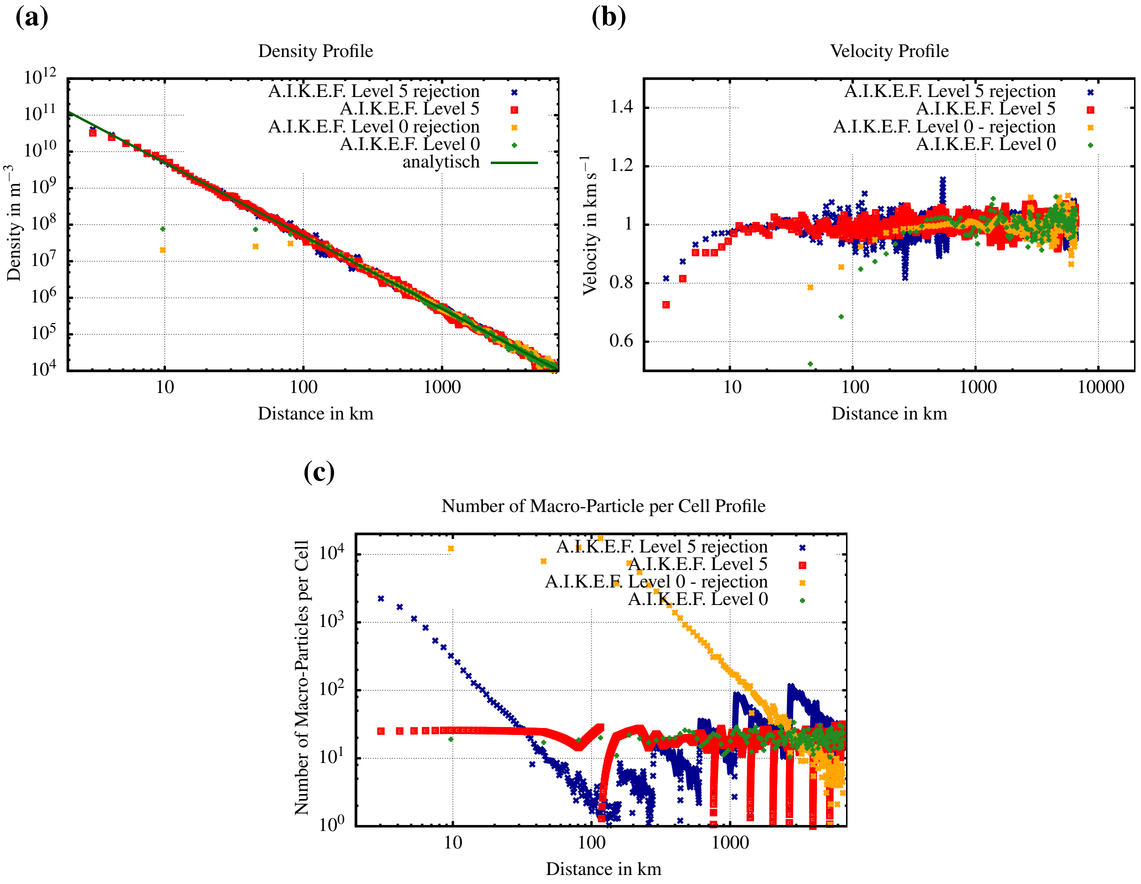

Figure 2.13: A series of test-simulations which check the modelling of the ionisation process. The panels show the density, the velocity of the cometary ions and the number of macro-particles per cell after $\Delta t = 1000$ time-steps $= 2.13\,\mathrm{s}$ along the x-axis. The series shows the differences between the *accept-rejection method* and the other method. For each method two simulations were performed, one with a uniform mesh ($\Delta x \approx 75\,\mathrm{km}$) and one with a hierarchical mesh with 5 refinement levels and a minimum mesh size of ($\Delta x \approx 2\,\mathrm{km}$). In all simulations the movement and the acceleration of the cometary ions, the splitting and merging of the macro-particles and other chemical processes were disabled. As one can see in a), both methods reproduce the theoretically predicted density as long the distance is larger than the mesh size. The velocity is shown in b). The initial radial velocity is about $v_{\mathrm{CI,init}} = 1\,\mathrm{km\,s^{-1}}$ plus a randomly distribute thermal velocity corresponding to 180 K. In c) the number of macro-particles per cell is shown. The number of macro-particles inserted per time step is similar in simulations with the same mesh.

values, i.e. up to 10^5 macroparticle per cell, are reached close to the nucleus, although the number of macro-particles inserted into the simulation box are similar newly inserted macro-particles to smooth their distribution in the simulation box. Consequently, the second technique is favoured for the modelling since numerical resources are saved and can it easily be adopted to new ionisation profiles.

2.5.3.5 Ion-Neutral Collisions, Charge Exchange and Recombination

Besides the ionisation, the modelling of collision processes is important for an adequate modelling of the cometary plasma interaction in the A.I.K.E.F. code. This is especially true in the innermost coma, where the neutral gas density is high. For the collisions between ions and neutral molecules two different approaches are used in this thesis: A former fluid-like friction force, and a more general collision model based on a statistical approach.

In the former approach, suggested by Bagdonat (2004), the collisions are modelled by an external friction force f_{cx} which acts on the motion of each particle, see Equation (2.68). This force

$$\vec{f}_{\mathrm{cx}} = -\sum_{\mathrm{n}} k^{\mathrm{coll}}_{\alpha,\mathrm{n}} n_{\mathrm{n}} n_{\mathrm{i}} m_{\mathrm{i}} \left(\vec{v}_{\mathrm{i}} - \vec{u}_{\mathrm{n}}\right) \tag{2.94}$$

is assumed to be similar to the momentum change of a fluid due to collisions between the ion, i, and the neutral fluid, see Equation (2.37). However, in contrast to the second method, this friction force cannot model the reactions as described at the beginning of this chapter since no ion is removed from the plasma or transferred to another species.

A more general approach was suggested by Kriegel (2013). This approach is based on a statistical description of the collisional processes and as shown by the author the friction force can be deduced from the statistical approach by simplifications. As part of this work, this new approach was revised to consider also the important recombination process and, furthermore, the entire A.I.K.E.F. part was reprogrammed, generalised and optimised. In the statistical approach, the simulation checks for all macro-particles at each time step whether a reaction, i.e. a collision, a charge exchange process or a recombination takes place. In doing so, it is assumed that a macro-particle can only react once or not at all during each time step. This requires a short numerical time step. But, this is also demanded by the *Courant-Friedrichs-Lewy*-criteria, in simulations with an high numerical resolution. Furthermore, the reaction rate is constant during a time step. Thus, the probability for a reaction increases if the time step is increased. Finally, it can be assumed that the reactions are independent from each other. This is why the probability, w, that an ion undergoes a reaction within a time step is given by

$$wdt = \frac{d}{dt}\left(1 - \exp\left(-\frac{t}{\tau}\right)\right)\bigg|_{t=0} dt = \frac{dt}{\tau} = \left(\sum_{\mathrm{n}} k^{\mathrm{coll}}_{\alpha,\mathrm{n}} n_{\mathrm{n}} + \alpha\left(T_{\mathrm{e}}\right) n_{\mathrm{e}}\right) dt\ , \tag{2.95}$$

where τ is the average time between two reactions, which can be expressed by the process rate discussed at the beginning of the chapter. Since this approximation is only valid for small time intervals, it has to be ensured that wdt is much smaller than 1. By comparing a random number $r \in [0;1]$ with the probability, it can be checked whether a reaction occurs or not. In case of $pdt > r$, a macro-particle reacts with one of the considered reactions, which are determined by a second random number $s \in [0;1]$. This interval is separated according to the ratios of the process rates and the total reaction rate $\sum_{\mathrm{n}} \nu_{\mathrm{i,n}} + \alpha\left(T_{\mathrm{e}}\right) n_{\mathrm{e}}$.

In case this second random process decides that a collision or a charge exchange takes place, the macro-particle is removed and a new macro-particle with the same weight and the properties of the other reactant is inserted. Thus, a cometary ion which hits a cometary neutral gets a new velocity, i.e. moves away from the nucleus with a speed of u_{CN}. If a recombination process takes place, the macro-particle is simply removed.

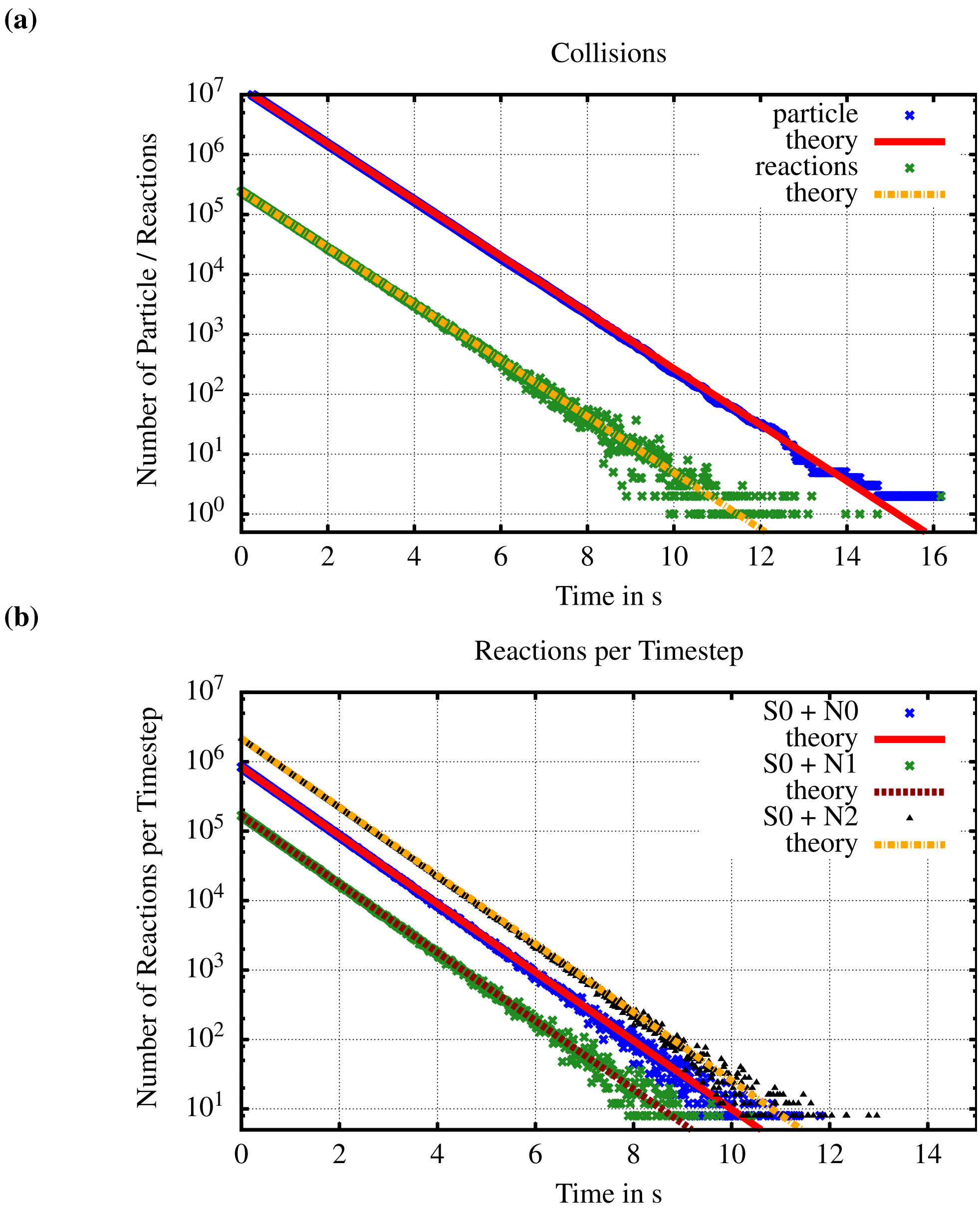

Figure 2.14: The results of two tests of the newly programmed reaction module of the A.I.K.E.F. code. In panel a) the number of macro-particles in a simulation box is shown over time by blue crosses. These macro-particle can react with a neutral gas species in the background, and in this case the macro-particle is removed from the simulation. The green crosses show the number of reactions which occur during a time step. The corresponding theory is shown by the orange and the red line. In panel b) the result of a simulation is shown, where one ion species can react with three neutral gas species (N0, N1, N2) with different probabilities. After a reaction, the ion is removed from the simulation. The numbers of a certain reaction are presented in blue, green and black and the lines show the corresponding analytical model.

For the purpose of demonstration of this approach, a series of test-simulations has been performed. In a first test a simulation box is filled homogeneously with an ion species which can react with a constant neutral gas background. The movement, the acceleration, the splitting, the merging and the ionisation are switched off, only collisions are allowed. In the case that a collision occurs, the macro-particle is removed from the simulation box. In Figure (2.14 a) the number of macro-particles in the simulation over time and the number of reactions per time step is shown. The change of the density or the numbers of macro-particles, which are equal weighted in theses simulations, can be described by a simple exponential decay

$$N(t) = N_0 \exp\left(-k_{\mathrm{coll}} n_{\mathrm{CN}} t\right) \ , \tag{2.96}$$

since the reaction rate is constant, where N_0 is the number of macro-particles at the initial time step and k_{coll} denotes the reaction rate. Hence, also the number of reactions per time step is given by the an exponential law. This is shown in the figure by the red and orange lines. These analytical lines match perfectly with the simulation results.

A second test is performed, in which an ion species (S0) in the simulation box can react with three different neutral gas species (N0, N1 and N2) with different reaction rates. Again, the ion is removed from the simulation box in case a reaction occurs. The number of reactions with a certain neutral gas species is logged and shown in Figure (2.14 b). Since the ion is removed afterwards and the reaction rates are constant due to the constant neutral gas background, an exponential decay is expected. The number of reactions per reactant $\Delta N_{\mathrm{reac,i}}(t)$ is given by

$$\Delta N_{\mathrm{reac,i}}(t) = k_{\mathrm{coll,i}} n_{\mathrm{CN}} N_0 \exp\left(-\Sigma_n k_{\mathrm{coll,n}} n_{\mathrm{CN}} t\right) \ , \tag{2.97}$$

where $k_{\mathrm{coll,i}}$, $\Sigma_n k_{\mathrm{coll,n}}$ denote the reaction rate of the ion species with neutral gas species i and the sum of all reaction rates. Those analytically obtained curves fit the simulated distribution of reaction quite well as long as the number of macro-particle is sufficiently large.

In the next test series the recombination is examined. For this purpose, a simulation box is homogeneously filled with a resting plasma. The movement, acceleration, splitting, merging of the macro-particle and the ionisation are switched off and only recombination is enabled. For the sake of simplicity, the electron temperature is set to a constant value. As presented in Figure (2.15) the number density in the simulation box drops. Because of the fact that the recombination rate increases with lower temperatures (Section 2.3.2.2), the density drops faster in the simulation with a colder electron fluid than in the simulation with an temperature of $T_{\mathrm{e}} = 5000\,\mathrm{K}$. An analytical expression can be obtained from the continuity equation. Under the given assumptions this simplifies to

$$\partial_t n = -\alpha\left(T_{\mathrm{e}}\right) n_{\mathrm{e}} n \ . \tag{2.98}$$

By using the assumption of the quasi-neutrality, the electron density n_{e} can be replaced by the ion density n. The solution of this differential equation is

$$n\left(t\right) = \frac{n_0}{1 + \alpha\left(T_{\mathrm{e}}\right) n_0 t} \ . \tag{2.99}$$

The results obtained by using this expression are shown in the Figure (2.15) with the used electron temperatures. These lines match the hybrid result for both cases perfectly.

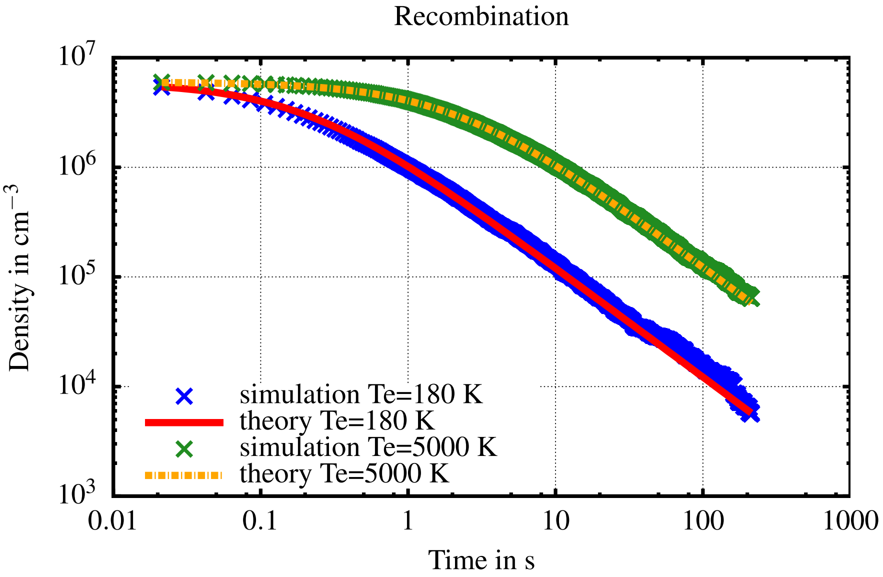

Figure 2.15: The ion density is shown for two different simulations which models the recombination with different constant electron temperatures. The blue and green data points represent the simulations with electron temperatures of 180 K and 5000 K. In addition, the analytical solutions for the decay with the corresponding recombination rates are shown for both cases.

A final test checks if the version of the A.I.K.E.F. code developed as part of this work can reproduce the photochemical equilibrium. In the cometary interaction region this equilibrium occurs in regions where the plasma is at rest and the situation is stationary, e.g. at the stagnation point. There, the ionisation processes, mainly the photoionisation, and the loss processes are balanced. Hence, the left hand side of the continuity equation

$$\partial_t \rho + \partial_{\vec{x}} \cdot (\rho \vec{u}) = I_{\mathrm{CI}}^{\mathrm{ph}} - R_{\mathrm{CI}} \tag{2.100}$$

can be set to zero. By using the Equations (2.7), (2.13) and (2.19), the ion source $I_{\mathrm{CI}}^{\mathrm{ph}}$ and the loss term R_{CI} can be replaced. It is assumed that the electron temperature and the recombination rate remain constant. Thus, the equilibrium density can be expressed by

$$n_{\mathrm{i}} = \sqrt{\frac{\nu Q}{4\pi u_{\mathrm{CN}} \alpha(T_{\mathrm{e}}) r^2}} \, . \tag{2.101}$$

As one can see, the density in the photochemical equilibrium sinks as the distance to the nucleus increases. Furthermore, by dropping the assumption of a stationary situation and set of an empty box at the beginning, $n_{\mathrm{i}}(0) = 0$, the evolution of the density is given by

$$n_{\mathrm{i}}(t) = \sqrt{\frac{\nu Q}{4\pi u_{\mathrm{CN}} \alpha(T_{\mathrm{e}}) r^2}} \tanh\left(\sqrt{\frac{\nu Q \alpha(T_{\mathrm{e}})}{4\pi u_{\mathrm{CN}}}} \frac{t}{r} \right) . \tag{2.102}$$

At the beginning, the density of the ion is low, therefore, the recombination rate is small and the ionisation dominates. The higher the density the more the recombination becomes important and reduces the density grows. Finally the ionisation and recombination

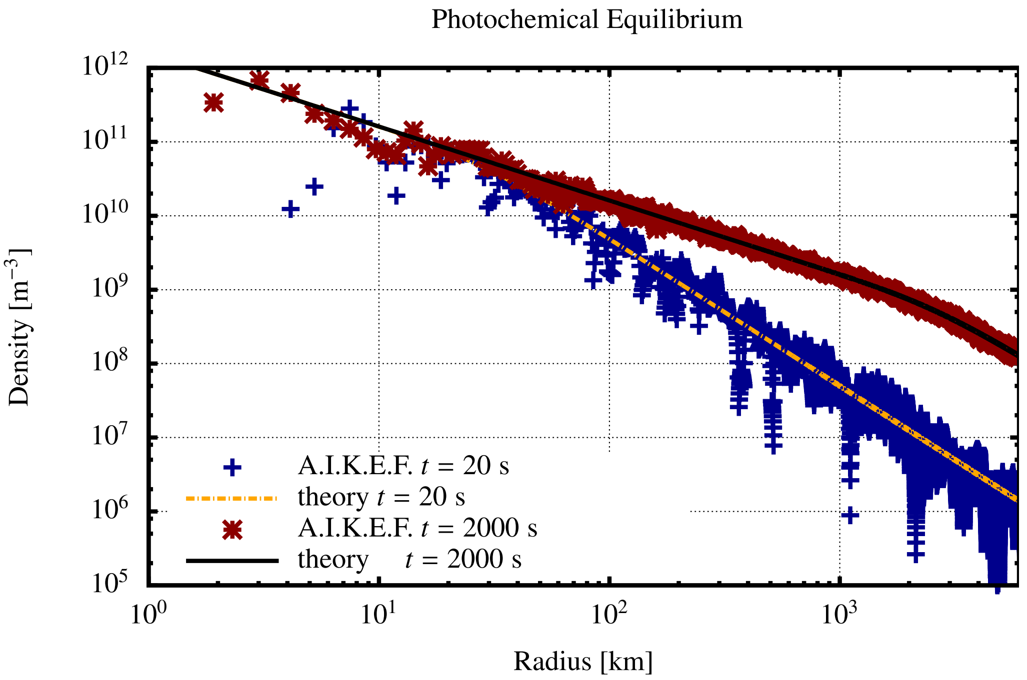

Figure 2.16: The cometary ion densities along the x-axis of a simulation at different time levels. The simulations only consider ionisation and recombination of cometary ions with a constant electron temperature. As one can see, the ion density increases with time. The initial state was an empty simulation box. However, at a certain time, the density reaches a maximum, then ionisation and recombination balance each other. At larger distances, the time increases until this photochemical equilibrium is reached. In addition to the densities of the simulation, the solution of the analytical expression is shown for the same time levels. Reprinted from Koenders et al. (2015) with permission from Elsevier.

balances each other at the equilibrium. This equilibrium is reached later the larger the distance to the comet.

In Figure (2.16) the density profiles along the x-axis of a test simulation at different time levels are shown. In this test simulation, the movement of the ions is suppressed, the electron temperature is constant and the box was empty at time level zero. As one can see, the density profiles of the simulations fit to the analytical solution for the corresponding time. However, the simulation shows some fluctuations which are based on the limited amount of macro-particles in the cells. In addition, it is visible that the equilibrium density is reached later at larger distances.

2.5.3.6 Modelling the Electron Source Terms

As discussed by Bagdonat (2004), the adiabatic equation of state for the electron fluid only needs to be modelled by two plasma betas, i.e. two temperatures, in the undisturbed solar wind and in the cold innermost coma in order to describe the electron temperatures observed in the cometary environment. In this approach, no sources or loss terms have to be considered.

Compared to this simple model, modelling of the source and loss terms is much more complicated when using the pressure equation for the electrons. The current model takes ionisation, elastic collisions, inelastic collisions, and recombination into consideration as described in the first part of this chapter. The effects of these different source and loss terms are discussed here and the results are compared to the A.I.K.E.F. results. For this purpose, a resting plasma is studied, i.e. $\vec{u}_{\mathrm{e}} = 0$. In addition, the neutral gas is also at rest: $\vec{u}_{\mathrm{CN}} = 0$. With these simplifications the pressure equation for the electron fluid, see Equation (2.47), is given by

$$\frac{f_{\mathrm{e}}}{2}\partial_t p_{\mathrm{e}} = \frac{\delta \varepsilon_{\mathrm{e}}^{\mathrm{prod}}}{\delta t} + \frac{\delta \varepsilon_{\mathrm{e}}^{\mathrm{coll}}}{\delta t} + \frac{\delta \varepsilon_{\mathrm{e}}^{\mathrm{in.coll}}}{\delta t} \; . \tag{2.103}$$

As a first step, only elastic collisions between the neutral gas and the electron fluid are considered. The corresponding source term, Equation (2.44), is simplified to

$$\frac{\delta \varepsilon_{\alpha}^{\mathrm{coll}}}{\delta t} = \sum_n \frac{n_\alpha m_\alpha}{m_\alpha + m_{\mathrm{n}}} k_{\alpha,\mathrm{n}}^{\mathrm{coll}} n_{\mathrm{n}} \left(\frac{f_{\mathrm{n}} p_{\mathrm{n}}}{n_{\mathrm{n}}} - \frac{f_\alpha p_\alpha}{n_\alpha} \right)^2 \; . \tag{2.104}$$

Hence, the energy profit or loss is determined by a temperature difference. In the testscenario, the neutral gas and the water gas have a temperature of 180 K, whereas the initial temperature of the electrons is about 5×10^4 K. The expected decrease of the electron temperature is shown in Figure (2.17) with the dark-red curve. The solution of the same differential equation has also been obtained with the computer algebra program *Mathematica*[4], in order to validate the A.I.K.E.F. code results. The corresponding dark-green dotted line fits the A.I.K.E.F. result quite well. Since changes of the neutral gas background are not considered in the A.I.K.E.F. code, the heating of the neutral gas is neglected. Moreover, this is reasonable because the plasma density, especially in the inner coma, is orders of magnitude below the neutral gas density.

In a second step photoionisation is considered. This process heats the electron fluid because high energetic photoelectrons are introduced into the plasma. The corresponding source term is given by Equation (2.43) and can be simplified to

$$\frac{\delta \varepsilon_{\mathrm{e}}^{\mathrm{prod}}}{\delta t} = \sum_n I_{\mathrm{e,n}}^{\mathrm{ph}} \frac{f_{\mathrm{e}}}{2} k_{\mathrm{B}} T_{\mathrm{n}}^{\mathrm{ph}} \; . \tag{2.105}$$

The dashed-dotted blue curve in Figure (2.17) shows the result of an A.I.K.E.F. simulation which only takes the ionisation into account. The fast heating is clearly visible.

By taking additional elastic collisions into consideration, the plasma is heated by ionisation, and at about 30 s the heating is balanced by the cooling of the elastic collisions. However, the photoionisation clearly dominates the situation and by only taking the cooling process into account, the electron temperature cannot reach values comparable to the neutral gas temperature, as observed in the inner coma of comet 1P/Halley (Eberhardt and Krankowsky 1995).

A possible candidate for this cooling process is the excitation of water molecules by inelastic electron collisions. As stated by Gan and Cravens (1990) the loss or source for

---

[4] http://www.wolfram.com/mathematica/

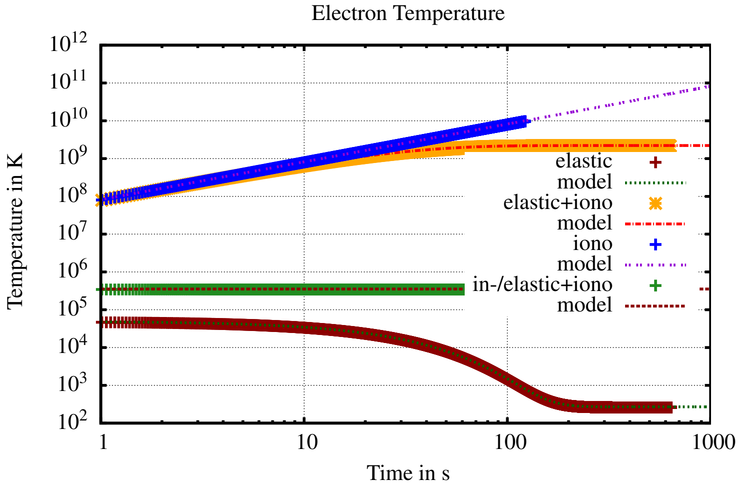

Figure 2.17: The result of different test run in A.I.K.E.F. which demonstrates the effect of the different source terms on the electron temperature. The dark red crosses represent the electron temperature in a simulation which considers elastic collisions (*elastic*). The dark-green line, which is denoted by *model*, shows the result of the calculation obtained with *Mathematica*. The yellow stars, the blue crosses, and the green crosses show the results of a simulation with elastic collisions and ionisation (*elastic + iono*), ionisation (*iono*), and elastic and inelastic collisions and ionisation (*in-/elastic + iono*), respectively. The corresponding line show the result obtained by *Mathematica*. A detailed description is given in the text.

the electrons is given by Equation (2.45)

$$\frac{\delta \varepsilon_{\mathrm{e}}^{\mathrm{in.coll}}}{\delta t} = -\frac{2}{3} n_{\mathrm{e}} n_{\mathrm{H_2O}} \left(R_{\mathrm{H_2O}}^{\mathrm{ex}} + V_{\mathrm{H_2O}}^{\mathrm{ex}} + E_{\mathrm{H_2O}}^{\mathrm{ex}} \right) . \tag{2.106}$$

As one can see from Figure (2.17), the green dashed-dotted line, the temperature of the electron fluid, is balanced within the first advancement of the electron pressure by considering ionisation, elastic and inelastic collisions. This is possible since the advancement of the electron pressure is divided into 11 steps during each time step. However, the temperature remains constant in the testscenario at about $2 \times 10^5\,\mathrm{K}$. This can be explained by the used parameters for this test. The electron density was $n_{\mathrm{e}} = 6\,\mathrm{cm}^{-3}$, which corresponds to an undisturbed solar wind at 1.3 AU, whereas the neutral density was set to $n_{\mathrm{e}} = 6 \times 10^9\,\mathrm{cm}^{-3}$, which is a typical value close to an active comet. In contrast to the photoionisation, the excitation of the water molecules also depends on the electron density. Thus, it is not sufficient to cool the plasma to temperatures comparable to the neutral gas temperature in this scenario. However, in regions of a dense plasma, the excitation of the water molecules can cool the electron fluid to neutral gas temperatures. It will be investigated by the RPC team if this excitation of water molecules is indeed that efficient.

2.6 Summary

The pioneering work by Biermann et al. (1967) defined the onset of a series of intensive discussions on the cometary plasma environment. Most of those studies are motivated by the Giotto flyby at comet 1P/Halley, thus, many focus on strongly active comets. Hence, most authors used single fluid models, such as the MHD-model, to describe the processes in the cometary environment. This changed in the advent of the Rosetta launch because the target comet will be less active. In this case, the scales of the ion motion are comparable or smaller than the size of the main interaction region, which requires a different modelling approach: the hybrid model.

Since the aim of this thesis is to make predictions of the plasma environment at comet 67P/Churyumov-Gerasimenko on the basis of this hybrid model, it has to be ensured that the comet is modelled correctly in this framework. This is why this chapter starts with a description of the involved participants of the interaction; the impinging solar wind which changes over the mission time and the properties of the cometary atmosphere. Hereby, the most important processes from the plasma perspective are presented: the ionisation by solar UV radiation, collisions between ions and neutral gas molecules, which lead to momentum exchange or charge-exchange, and the recombination process, which removes ions from the plasma. Moreover, the impact of those processes on the electrons and the excitation of water molecules is discussed.

Because of the fact that the hybrid model relies on some fundamentals of the multifluid approach and the single fluid model, a short description on those models and their modelling of the comet is given. Furthermore, the source and losses caused by the important processes are deduced as part of this work for the framework of the multifluid approach in order to prepare the setup of A.I.K.E.F. for the cometary scenario. These basics will be used in the next chapters to evaluate the hybrid model and allow a discussion of the differences in the various approaches. Finally, the hybrid model and the A.I.K.E.F. code are presented. Besides the basic equations, the implementation of the comet into the simulation code is intensively discussed. Among those one finds the extended upstream boundary model which models the region upstream of the simulation box and which is absolutely necessary to obtain quantitative estimations on the position of the boundaries in the cometary environment by a hybrid model. This is requested by the RPC science planning, since valuable predictions of positions of boundaries and structures have to been made. The extended upstream boundary model was developed in this work. In addition, in this work the various processes, i.e. ionisation and collisions, have been revised extensively, and a module to consider the recombination process was developed for the A.I.K.E.F. code. As a consequence, the A.I.K.E.F. code is now able to describe all those processes on a statistical approach, which allows for a better description of the important processes and their impact on the plasma environment.

3 The Weakly Active Phase - Approach and Early Escort Phase

During the first months Rosetta stays at the comet, the instruments of the RPC will explore a type of cometary plasma interaction, which has never been observed by spacecraft before. In this scenario the gas production rate of the comet is too low to trigger sharp boundaries, such as a bow shock or a diamagnetic cavity, as observed at comet 1P/Halley. Instead, in this weakly active scenario, the cometary ions are picked-up by the solar wind and perform a cycloidal motion, which is firstly orientated perpendicular to the solar wind flow (Bagdonat and Motschmann 2002).

Some of the models, which have been presented in the previous chapter in detail, are used to study this initial cometary plasma environment. This is worthwhile because the solar wind is only weakly disturbed in the early stage. Hence, besides the understanding of the plasma effects, a verification of the hybrid model seems reasonable. Therefore, the hybrid results are compared to an analytical single-particle-motion model and to a new multifluid MHD model. At the beginning of this chapter, the motion of the cometary ions is calculated by the analytical model. Afterwards, the more complex models, the multifluid MHD model and the hybrid model, are consulted. These models can also describe the perturbation of the solar wind and the interplanetary magnetic field. Besides the large spatial structures related to the cometary ion tail, also small spatial and time varying structures in the vicinity of the comet are discussed. In both cases, differences and extensions to previous studies are expected due to the use of the improved A.I.K.E.F. code.

3.1 The Pick-Up Process

The initial interaction between the solar wind and a comet is caused by the ionisation of a cometary neutral molecule in the undisturbed solar wind, i.e. close to a weakly active comet or far upstream of an active comet. Since the ion densities and neutral densities are low, collisions between ions and neutrals or other ions can be neglected. Thus, the motion of the newborn ions is controlled by the Lorentz force

$$\frac{d}{dt}\vec{v}_{\mathrm{CI}} = \frac{q_{\mathrm{CI}}}{m_{\mathrm{CI}}} \left(\vec{E} + \vec{v}_{\mathrm{CI}} \times \vec{B} \right) . \tag{3.1}$$

$\vec{v}_{\mathrm{CI}}$, q_{CI} and m_{CI} denote the velocity of an individual cometary ion, its charge and its mass, respectively. In the framework of the single-particle-motion model, the presence of a single cometary ion in the solar wind does not change the solar wind. Hence, the magnetic field $\vec{B}$ is equal to the interplanetary magnetic field. As the orientation of the interplanetary magnetic field will change during the mission, the orientation is expressed by the Parker angle θ

$$\vec{B} = B_0 \left(\cos\theta \vec{e}_x + \sin\theta \vec{e}_y\right) \ , \tag{3.2}$$

where $\vec{e}_x$ and $\vec{e}_y$ are the unit vectors in x- and y-direction. Without losing generality the z-component of the magnetic field can be set to zero. The electric field in the undisturbed solar wind can be expressed by

$$\vec{E} = -\vec{u}_{\mathrm{i}} \times \vec{B} \, , \tag{3.3}$$

which is a simplified version of Equation (2.74), where $\vec{u}_{\mathrm{i}}$ denotes the mean velocity of all ions. This can be assumed because the curvature of the magnetic field and the gradient of the electron pressure can be neglected. The mean velocity of the ions is denoted by $\vec{u}_{\mathrm{i}}$, which is equal to the undisturbed and constant solar wind velocity $\vec{u}_{\mathrm{SW}} = u_{\mathrm{SW}} \vec{e}_x$ in this model. Thus, the following equation has to be solved to determine the velocity of the newborn cometary ions

$$\frac{d}{dt} \vec{v}_{\mathrm{CI}} = \frac{q_{\mathrm{CI}}}{m_{\mathrm{CI}}} \left(\vec{v}_{\mathrm{CI}} - \vec{u}_{\mathrm{SW}}\right) \times \vec{B} \, . \tag{3.4}$$

It should be clear, in case of a parallel orientation ($\theta = 0°$) the Lorentz force vanishes. By neglecting the initial velocity of the cometary ion $\vec{v}_{\mathrm{CI}}(t=0) = 0$ the following solution for the velocity can be obtained

$$\vec{v}_{\mathrm{CI}} = \begin{pmatrix} u_{\mathrm{SW}} \sin^2\theta \left(1 - \cos\left(\Omega_{\mathrm{CI}} t\right)\right) \\ -u_{\mathrm{SW}} \sin\theta \cos\theta \left(1 - \cos\left(\Omega_{\mathrm{CI}} t\right)\right) \\ -u_{\mathrm{SW}} \sin\theta \sin\left(\Omega_{\mathrm{CI}} t\right) \end{pmatrix} \ , \tag{3.5}$$

where the gyrofrequency of the cometary ion is represented by

$$\Omega_{\mathrm{CI}} = \frac{q_{\mathrm{CI}} B}{m_{\mathrm{CI}}} \, . \tag{3.6}$$

Using $\vec{x}_{\mathrm{CI}}(t=0) = 0$ as the position of the ionisation, the trajectory of the cometary ions can be described by

$$\vec{x}_{\mathrm{CI}} = \begin{pmatrix} r_{\mathrm{gyr,CI}} \sin^2\theta \left(\Omega_{\mathrm{CI}} t - \sin\left(\Omega_{\mathrm{CI}} t\right)\right) \\ r_{\mathrm{gyr,CI}} \sin\theta \cos\theta \left(\cos\left(\Omega_{\mathrm{CI}} t\right) - \Omega_{\mathrm{CI}} t\right) \\ r_{\mathrm{gyr,CI}} \sin\theta \left(\cos\left(\Omega_{CI} t\right) - 1\right) \end{pmatrix} \, . \tag{3.7}$$

This trajectory is a cycloid which is equal to a gyromotion superimposed by an $\vec{E} \times \vec{B}$-drift. It follows that the pick-up ion performs its cycloidal motion in a plane constructed by $\vec{E}$ and $\vec{E} \times \vec{B}$. The dimensions of such a single cycloidal arc are determined by the gyroradius of the cometary ions: The width of the cycloid from one cusp to another is

$$w = 2\pi r_{\mathrm{gyr,CI}} \sin^2\theta = 2\pi \frac{m_{\mathrm{CI}} u_{\mathrm{SW}}}{\mid q_{\mathrm{CI}} \mid B} \sin^2\theta \tag{3.8}$$

and its height

$$h = 2 \, r_{\mathrm{gyr,CI}} \sin\theta = 2 \frac{m_{\mathrm{CI}} u_{\mathrm{SW}}}{\mid q_{\mathrm{CI}} \mid B} \sin\theta \, . \tag{3.9}$$

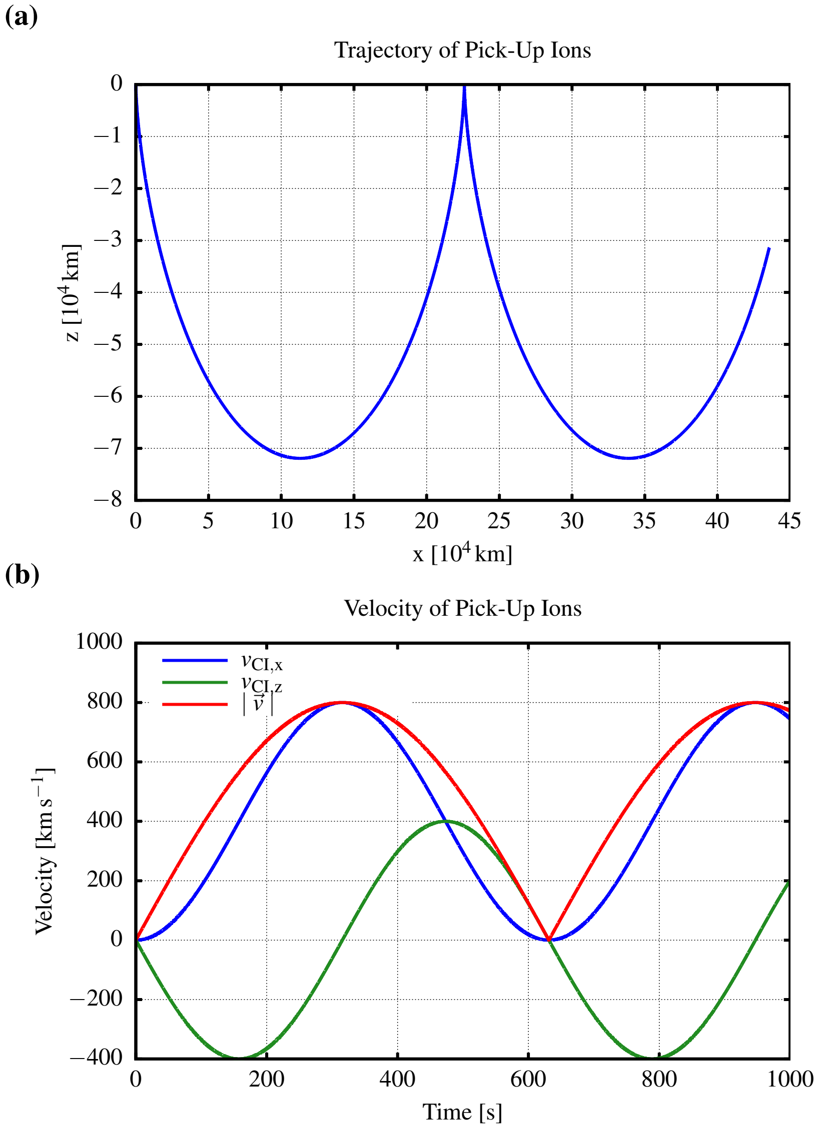

Figure 3.1: The motion of newborn cometary ions in the undisturbed solar wind is shown in the comet frame. The cometary ion has a mass of $m_{\mathrm{CI}} = 17\,\mathrm{amu}$ and a charge of $q_{\mathrm{CI}} = 1\,\mathrm{e}$. The constant solar wind is characterised by a velocity of $u_{\mathrm{SW}} = 400\,\mathrm{km\,s^{-1}}$ in x-direction and the magnetic field is orientated in y-direction with a magnitude of $1.96\,\mathrm{nT}$. It follows that the convective electric field points towards $-z$. The cometary ions perform a motion along cycloidal arcs within the xz-plane. The height and width of these arcs are $w = 2\pi r_{\mathrm{gyr,CI}} = 2.25\times 10^5\,\mathrm{km}$ and $h = 2r_{\mathrm{gyr,CI}} = 7.2\times 10^4\,\mathrm{km}$. Their velocities in x- and z-direction oscillate between $-u_{\mathrm{SW}}$ and $+u_{\mathrm{SW}}$. In addition, the velocity in x-direction is superimposed by a constant velocity of u_{SW}. And the magnitude of the velocity is drawn by a red line.

At the time $t_{\mathrm{cusp}} = 2\pi n/\Omega$, where $n \in \mathbb{N}$, the pick-up ion reaches the cusps. h is equal to the diameter of the gyromotion multiplied with the sine of the Parker angle.

The trajectory of a pick-up ion for a perpendicular orientation of the magnetic field to the solar wind velocity is shown in Figure (3.1 a). Here, the ion performs its motion within the xz-plane. In this special case there is no motion in y-direction. In addition, the dimensions of the motion are as large as possible. The ion reaches maximum speeds in x-direction of exactly twice the solar wind speed (Figure 3.1 b). In z-direction the ion only performs the gyration, therefore, the z-component of the velocity oscillates between $+u_{\mathrm{SW}}$ and $-u_{\mathrm{SW}}$.

If more than a single cometary ion is injected into the solar wind, the ionisation profile has a major impact on the resulting velocity space configuration and, consequently on the resulting plasma interaction. A first case considers a weak but homogeneously distributed ion source, which is true far upstream of an active comet. Each newborn cometary ion is picked up and starts performing a cycloidal motion, as long as the solar wind and the interplanetary magnetic field are not parallel. Since the new ions are homogeneously distributed in space, no density fluctuations are present initially. In contrast, the velocity space distribution is not homogeneously populated; in case of a perpendicular orientation of the magnetic field, the cometary ions populate a ring distribution. As an example consider, a ring distribution of the cometary ions was observed at comet 26P/Grigg-Skjellerup by Coates et al. (1993). In case of a parallel configuration, a cold beam distribution is formed and in case of an oblique magnetic field configuration, a mixture between these two configurations, a ring-beam distribution, is present in the velocity space.

Each of these distributions are susceptible to several instabilities since the large relative speed between the cometary ions and the solar wind acts as a reservoir of free energy (Wu and Davidson 1972, Gary 1991). The energy of a cometary ion due to its gyration is given by (Coates and Jones 2009)

$$E_{\mathrm{pick-up}} = \frac{1}{2} m_{\mathrm{CI}} u_{\mathrm{SW}}^2 \sin\theta \ . \tag{3.10}$$

Thus, the total energy density of a ring distribution can be estimated by (Volwerk et al. 2013)

$$E_{\mathrm{ring}} = \frac{1}{2} n_{\mathrm{CI}} m_{\mathrm{CI}} u_{\mathrm{SW}}^2 \sin\theta \tag{3.11}$$

plus the additional energy parallel to the magnetic field. This energy, which originates from the relative movement of the cometary ions to the solarwind, can be transferred into wave energy. For example, in case of an oblique orientation of $\vec{B}$ and $\vec{u}_{\mathrm{SW}}$ an instability is triggered by the presence of cometary ions, which can be resonant if the following condition in the solar wind frame is met:

$$\omega_{(\mathrm{sw})} = k u_{\parallel} \pm \Omega_{\mathrm{gyr,CI}} \ , \tag{3.12}$$

where k is the wave vector and $u_{\parallel}$ denotes the relative velocity of the cometary ions to the resting solar wind (cf. Wu and Davidson 1972, Tsurutani and Smith 1986). Tsurutani and Smith (1986) found that the Doppler shift into the spacecraft frame cancels the first term on the right-hand side in case of a wave propagation parallel to the magnetic field and the low frequency waves. Hence, the pick-up of the cometary ions excites ion cycloids waves, which have frequencies near to the cometary ion gyrofrequency. These can be detected by a magnetometer, like RPC-MAG.

Ion cyclotron waves have been observed during the previous cometary spacecraft mission (Tsurutani and Smith 1986, Glassmeier et al. 1989). Volwerk et al. (2013) predicted the ion cyclotron wave amplitude in the upstream region of comet 67P/Churyumov-Gerasimenko for the approach phase in summer 2014. It was found that the wave amplitude depends on the gas production rate of the comet and the solar wind properties. Both define the energy of the cometary ions in the ring. For $Q \geq 3.5 \times 10^{25}\,\mathrm{s}^{-1}$, ion cyclotron waves with an amplitude above 0.1 nT were expected within a distance of 3.5×10^{5} km to the nucleus. Because of the low ambient magnetic field strength during the approach phase, the long wave periods are in the orders of hours and they will have very low amplitudes, which makes a wave detection challenging for RPC-MAG.

3.2 Large Scale Structures

The aim of this section is to study the pick-up process in the framework of a hybrid model. The construction of this model allows us to study the effects triggered in the solar wind and the interplanetary magnetic field by a localised and inhomogeneous ionisation profile. Such a profile may be given by an analytical model, e.g. the Haser model, in which the neutral gas density increases rapidly at close distances to the comet. Because of the fact that this type of profile triggers effects on very different scales, this section focusses on the large scales, i.e. on scales of several thousands of kilometres or several ion inertia lengths. The interaction in the direct vicinity to the comet will be discussed in Section (3.3).

In addition, the results of the hybrid simulation in this section will be compared with those of a multifluid MHD model used by Rubin et al. (2014a) to check the consistency of the models. A similar comparison between a single-fluid MHD model, the predecessor of the multifluid model by Rubin et al. (2014a), and a hybrid model, the predecessor of the A.I.K.E.F. code, has been conducted by Hansen et al. (2007) for a weakly active comet. These authors showed that the gyromotion of the ions has a significant impact on the plasma environment in this weakly active stage, which cannot be described by the single-fluid model.

3.2.1 Setup

In the selected scenario the comet 67P/Churyumov-Gerasimenko is at a heliocentric distance of 2.7 AU. The gas production rate was set to $Q = 8 \times 10^{25}\,\mathrm{s}^{-1}$, which corresponds to the LAC of the mission at that heliospheric distance. This gas is distributed with the Haser model (Section 2.3.1). The constant velocity and the temperatures of the neutral gas are in agreement to the simulations of the neutral gas coma by Tenishev et al. (2008). The properties of the impinging solar wind are calculated with the Parker model and the values as discussed in Section (2.1). For the sake of simplicity the interplanetary magnetic field in this scenario is only oriented into y-direction. A complete list of the physical parameters of the comet and the solar wind used in the simulation is shown in Table (3.1).

In this comparison the involved models are restricted to only two ion species, the

Table 3.1: The parameters used for the study of the large scale structure, solar wind conditions at a heliocentric distance of $r_{\mathrm{h}} = 2.7\,\mathrm{AU}$ and a common value of the gas production rate. For the purpose of comparability the Parker angle is set to $\theta = 90°$.

Quantity	**Value**
gas production rate Q	$8 \times 10^{25}\,\mathrm{s}^{-1}$
neutral gas outflow velocity u_{CN}	$800\,\mathrm{m\,s}^{-1}$
neutral water temperature T_{CN}	$50\,\mathrm{K}$
solar wind number density $n_{\mathrm{SW},0}$	$1.37\,\mathrm{cm}^{-3}$
solar wind velocity $u_{\mathrm{SW},0}$	$400\,\mathrm{km\,s}^{-1}$
solar wind ion temperature $T_{\mathrm{SW,i},0}$	$4.6 \times 10^{4}\,\mathrm{K}$
solar wind electron temperature $T_{\mathrm{SW,e},0}$	$9.4 \times 10^{4}\,\mathrm{K}$
strength of interplanetary magnetic field $B_{\mathrm{IMF},0}$	$1.96\,\mathrm{nT}$
Parker angle θ_0	$90°$

cometary water group ions with a mass of 17 amu and the solar wind protons. While the multifluid MHD model considers various processes, such as photoionisation, electron-impact ionisation, ion-neutral collisions, charge-exchange, and ion-ion collisions, the hybrid model only describes the ionisation process and the ion-neutral collisions. The latter process is modelled by the force term, as described in Section (2.5.3.5) but not by the statistical procedure. Additionally, only the adiabatic pressure equation of the electron fluid is used in the hybrid simulation, whereas the multifluid model solves the pressure equation for the electron fluid. The exact details of the multifluid model and the description of the source terms are given in Rubin et al. (2014b). Nevertheless, both models are brought up to par as much as possible.

As mentioned above, the focus of the comparison in this section is on the motion of the cometary ion motion and the large scale structures triggered by them. In order to study those, a simulation box longer than one single cycloidal arc is required. Consequently, the hybrid simulation box is a cuboid with an edge length of about $4.28 \times 10^{5}\,\mathrm{km}$ in x-direction, $3.8 \times 10^{4}\,\mathrm{km}$ in y-direction, and $2.1 \times 10^{5}\,\mathrm{km}$ in z-direction. The length in x-direction is equal to $2000\,\mathrm{x}_0$. The centre of the cometary ion profile, the nucleus, which is not resolved in this simulation, is located at a distance of $5 \times 10^{4}\,\mathrm{km}$ downstream of the sunward boundary, the $-x$-boundary, 19456 km from the $-y$-boundary, and $1.5 \times 10^{5}\,\mathrm{km}$ from the $-z$-boundary. This simulation does not use a hierarchical mesh. The size of a cell is about 700 km in each direction. Thus, the simulation box contains approximately 10^{7} cells. For stability reasons, each of these cells contains at least 300 macro-particles which only represent the solar wind ions. If a cell contains cometary ions, the number of macro-particles can be higher, namely up to 450 macro-particles. However, not every cell in this simulation contains cometary ions. Based on the large simulation box and the weak activity of the comet, cometary ions are only inserted within a sphere with a radius of about $5 \times 10^{4}\,\mathrm{km}$. At that distance, the cometary ion production rate is about

$4 \times 10^{-7}\,\mathrm{cm}^{-3}\,\mathrm{s}^{-1}$. This production rate is negligible in comparison to the solar wind density. In total, about 3.3×10^{9} macro-particles are inside the large simulation box. In addition, the extended upstream boundary model is not used in this large simulation box, since the changes in the undisturbed solar wind are negligible at the upstream boundary of the simulation box.

By design the multifluid model needs much less computational resources than the hybrid model because only the moments have to be stored and not the particle informations. Moreover, the refinement of the numerical mesh needs less computational power since the particle splitting and merging is not required. Thus, the multifluid model uses a total box size of about $32 \times 10^{6}\,\mathrm{km}$ in x-direction and about $16 \times 10^{6}\,\mathrm{km}$ in y- and z-direction. The entire simulation box is split into 3×10^{6} cells, where the smallest cells are cubes with 200 m edge length. The nucleus is modelled by a sphere of 2 km radius, which allows a flow inward, but the radial outward flow is artificially set to zero. In order to solve the multifluid equations, the MHD code uses the Block Adaptive-Tree Solar wind Roe-type Upwind Scheme (BATS-R-US) code by Powell et al. (1999). More details in the numerical setup of the multifluid simulation are given by Rubin et al. (2014b).

Both simulations were run until the quasi-stationary state has been reached. This was the case after 535 s in the hybrid simulation. During this time the undisturbed solar wind could pass the simulation box twice.

3.2.2 Results

In the vicinity of the comet new cometary ions are produced and picked-up by the solar wind and the interplanetary magnetic field. The resulting cometary ion density on the y=0-cross-section, which is the plane perpendicular to the magnetic field, of both simulations is shown in Figure (3.2). The bulk velocities of the cometary ions are also shown by streamlines in this figure.

In the figure the cometary ions are distributed along cycloids in the hybrid simulation, which is shown in the lower panel. In addition, also the streamlines of the bulk cometary ion velocity coincide with the cycloid. The main cometary ion tail of the hybrid simulation, which is characterised by the highest density, has a height of $h \approx 6.9 \times 10^{4}\,\mathrm{km}$. The first cusp of the ion tail in the hybrid simulation is located at $x \approx 2.28 \times 10^{5}\,\mathrm{km}$, which corresponds to the width w of the cycloid. These values only differ slightly from the ion movement in the single-particle-motion model, as discussed in Section (3.1). There, an ion move along a cycloidal arc with a width of $w = 2\pi r_{\mathrm{gyr,CI}} = 2.25 \times 10^{5}\,\mathrm{km}$ and a height of $h = 2r_{\mathrm{gyr,CI}} = 7.2 \times 10^{4}\,\mathrm{km}$. Thus, the deviation in the width between the hybrid model and the analytical description is less then 3000 km. this is why it can be deduced that the solar wind is only weakly disturbed, otherwise, a much larger deviation should be present.

It is noteworthy to highlight the higher cometary ion density at the first cusp, in comparison to the ion density around the comet. This can be explained by the fact that the first cusp contains particles which enter and leave the region. In contrast, the region around the comet is only populated by ions which leave the region. Hence, a higher ion density is expected at this point.

In addtion to the ion density, the cometary ion velocity of the hybrid simulations, as shown in Figure (3.3), reveals a large similarity to the analytical description. The maximum speed of the cometary ions in the hybrid simulation is about $800\,\mathrm{km\,s}^{-1}$ which is

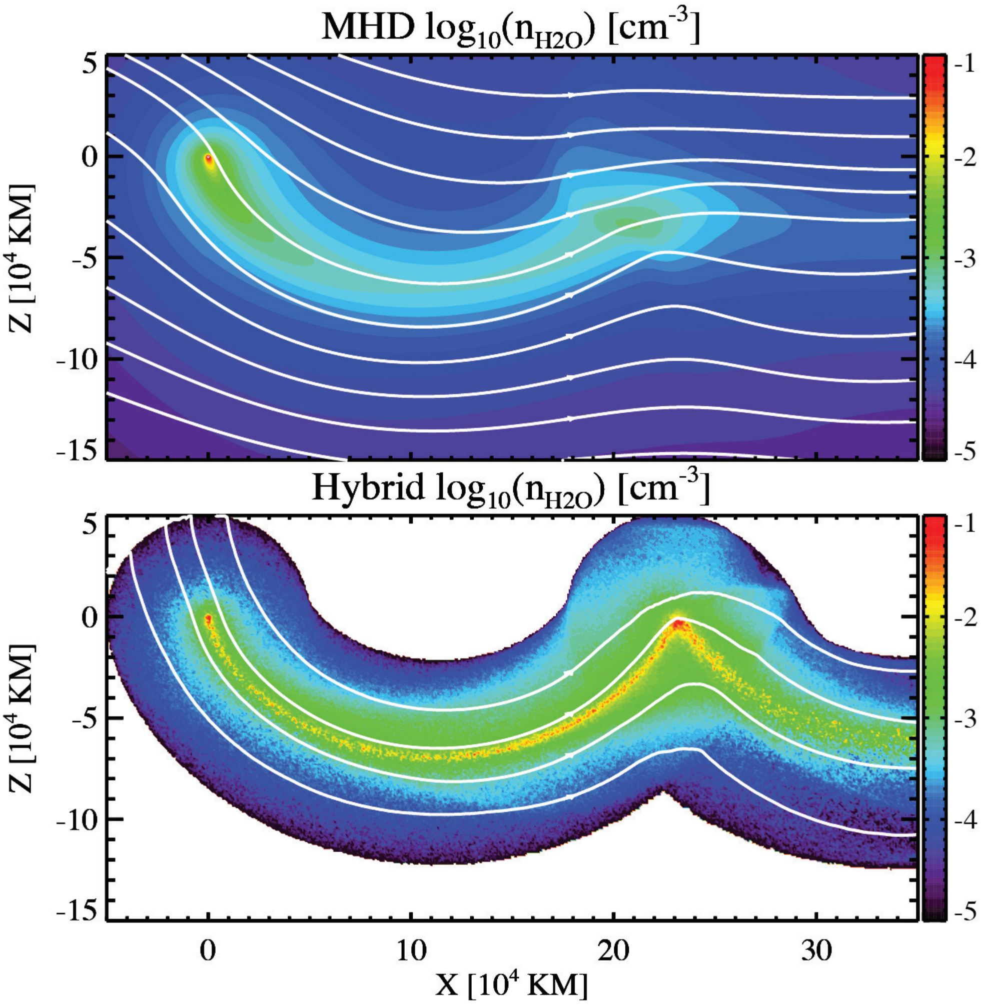

Figure 3.2: The cometary ion density on the y=0-cross-section. The result of the multifluid model is shown in the upper panel and the hybrid simulation result is presented in the lower panel. In addition streamlines of the bulk velocity of the cometary ions are shown by white lines in both figures. Reprinted from Rubin et al. (2014b) with permission from Elsevier.

the doubled solar wind speed, as theoretically predicted by the analytical solution. At the cusp, the velocity is the smallest, i.e. close to zero. As already mentioned, in order to save computational resources of the A.I.K.E.F. code, new macro-particles, which represents cometary ions, are only inserted into the simulation box within a sphere with a radius of about 5×10^4 km. Hence, there are regions without any cometary ions, which are marked by a blank area in the figures.

A similar result was obtained by the hybrid simulations of Bagdonat (2004). However, such a result cannot be obtained from a single-fluid MHD model, as shown among others by Hansen et al. (2007). In contrast to the single-fluid MHD model, the multifluid MHD model is capable to describe some of the effects of the gyration, which is caused by the Lorentz force and by fluids moving relative to each other. So the model can reproduce a part of the first cycloid of the cometary ion tail. This can be explained by the fact that

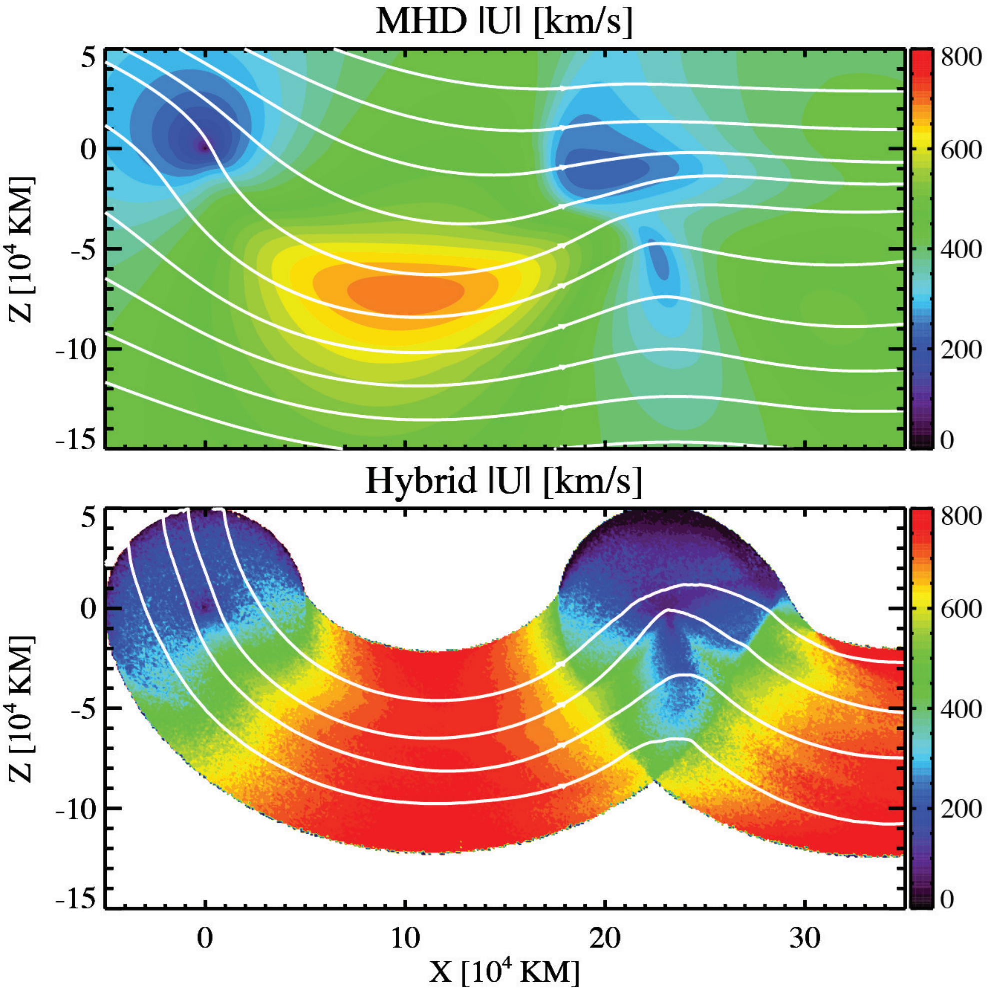

Figure 3.3: The bulk velocity of the cometary ions on the y=0-cross-section. The result of the multifluid simulation is shown in the upper part and the hybrid simulation result is presented in the lower panel. In addition streamlines of the cometary ions, by using the bulk velocity of the cometary ions, are shown by white lines in both figures. Reprinted from Rubin et al. (2014b) with permission from Elsevier.

close to the comet many ions are ionised and dominate the local phase space distribution function. All of these new ions perform a similar motion, which can partially be described by the multifluid model, see Figure (3.2). Within the first cycloid all cometary ions have nearly the same trajectory. However, the model collapse as soon as particles within the fluid moves in different directions. This happens at the first cusp in this scenario, where particles move in and out of the region. This is also the reason why the density at the first cusp is much lower than in the hybrid model.

A difference between both models caused by the limitations of the hybrid model is the maximum speed of the cometary ions. From the analytical description a maximum speed of $800\,\mathrm{km\,s^{-1}}$ is expected for a single cometary ion. This is observable in the hybrid simulation result. However, in reality cometary ions might be inserted over a wide volume, and this is why the plasma always contains cometary ions originating from different locations and based on that not all of them reach their maximum velocity at the same position. Thus, in in reality, a velocity below the doubled solar wind speed is expected. This is shown by the multifluid MHD which only reaches a maximum speed of $700\,\mathrm{km\,s^{-1}}$.

Figure (3.4) shows the z-component of the solar wind ion velocity on the y=0-cross-sections of both simulation boxes. As one can see in the hybrid result, the solar wind reveals a positive velocity z-component in the region around the comet and around the cusp. This means that the solar wind is deflected upwards. In constrast, the solar wind moves towards the $-z$-direction along the long edge of the cycloid of the cometary ion tail.

In the framework of the hybrid model this behaviour can be explained by studying the Lorentz force, which acts on a solar wind proton. Initially, it can be assumed that a proton which enters a region has a velocity equal to the undisturbed solar wind $\vec{v}_\mathrm{i} = \vec{u}_\mathrm{SW}$. Furthermore, the mean ion velocity in the hybrid model can be expressed by

$$\vec{u}_\mathrm{i} = \frac{\rho_\mathrm{c,SW}\vec{u}_\mathrm{SW} + \rho_\mathrm{c,CI}\vec{u}_\mathrm{CI}}{\rho_\mathrm{c}} \,. \tag{3.13}$$

Employing this and assuming a frozen-in magnetic field, the initial force on a solar wind particle can be expressed by

$$\vec{F}_\mathrm{L,SW,0} = \frac{q_\mathrm{SW}\rho_\mathrm{c,CI}}{\rho_\mathrm{c}} \left(\vec{u}_\mathrm{SW} - \vec{u}_\mathrm{CI}\right) \times \vec{B}_\mathrm{IMF} \,. \tag{3.14}$$

In regions without any cometary ions, the initial force vanishes, $\rho_\mathrm{c,CI} = 0$, and the velocity of the ions in z-direction remains constant. Close to the comet, cometary ions are present. However, their velocity is small in comparison to the solar wind speed, and can be neglected. Based on that, the solar wind particle is pushed toward $+z$-direction, as long as the magnetic field is constant in y-direction. The same is true at the first cusp, but due to the higher cometary ion density the deflection of the solar wind particles is stronger.

An opposite effect can be observed along the long edge of the cycloid of the cometary ion tail. At this position, the cometary ions have a velocity of twice the solar wind speed. Due to this, the sign of the force term changes and the solar wind is deflected towards $-z$-direction.

Both models reproduce this expected behaviour. However, the magnitude of the disturbances in the solar wind velocity is about a factor of ten stronger in the hybrid model than in the multifluid model.

Equation (3.14) can also be used to explain the resulting velocity distribution in the x-component of the solar wind. The lowest panel of Figure (3.5) is the unsaturated hybrid simulation result. Here, the area between the comet, the first cusp and the first long edge of the cometary ion tail reveals a reduced x-component of the solar wind velocity. In contrast, an enhanced x-velocity component is present in the area between the first and second long edge and the first cusp. The strength of the variation is about $3\,\%$ to the background velocity. However, these areas are not filled homogeneously with an enhanced or reduced velocity. Instead, the velocity approaches the background velocity at the downstream part of the regions in the hybrid simulations. In the multifluid simulation result, the first reduction is clearly visible, but again, the strength of the perturbation is only a tenth of

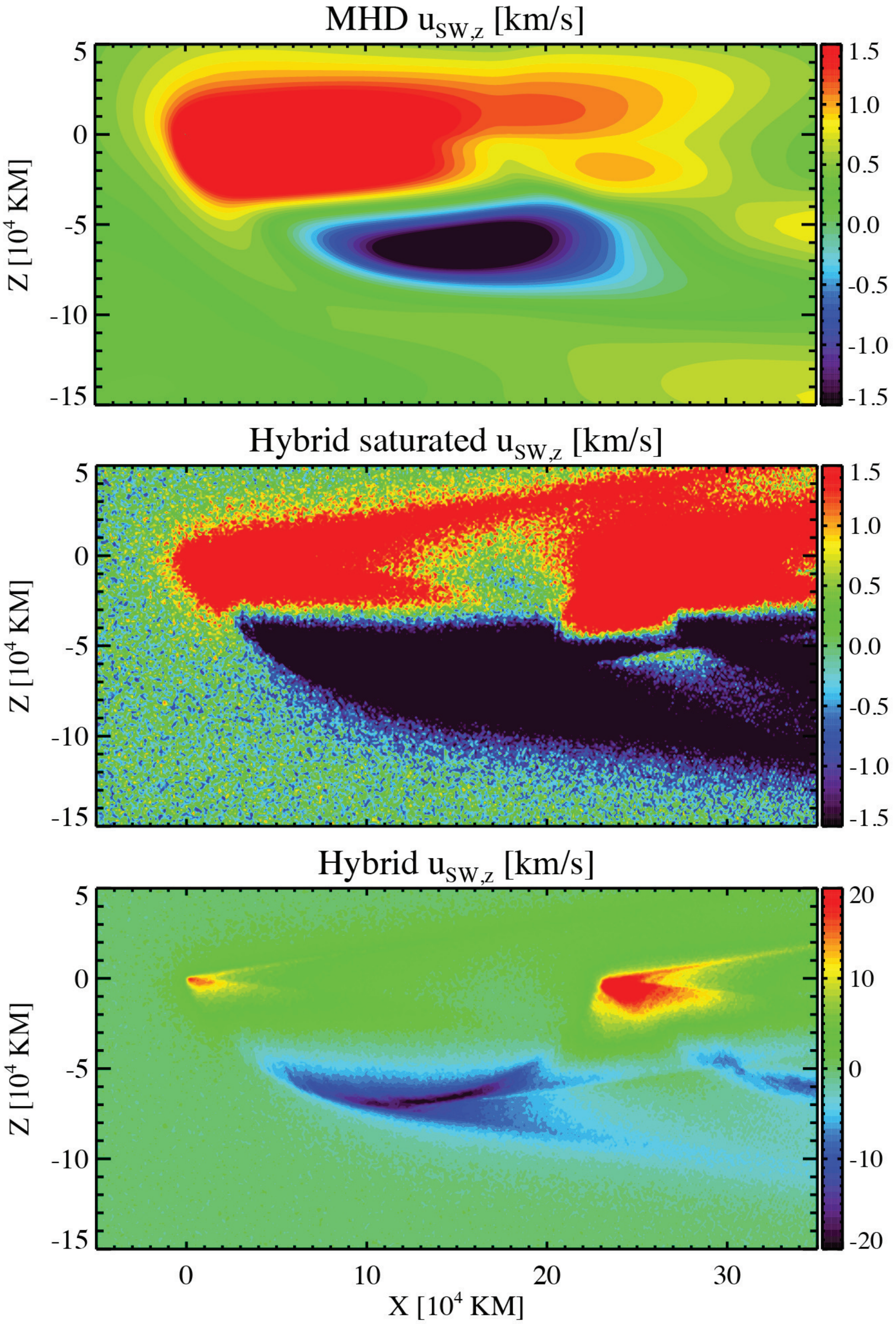

Figure 3.4: The bulk velocity component in *z*-direction of the solar wind protons on the *y*=0-cross-section. The result of the multifluid simulation is shown in the upper part and the hybrid simulation result is presented in the central and lower panels. The central panel shows the result with a saturated colourcode to allow for a better comparison to the multifluid model results. Reprinted from Rubin et al. (2014b) with permission from Elsevier.

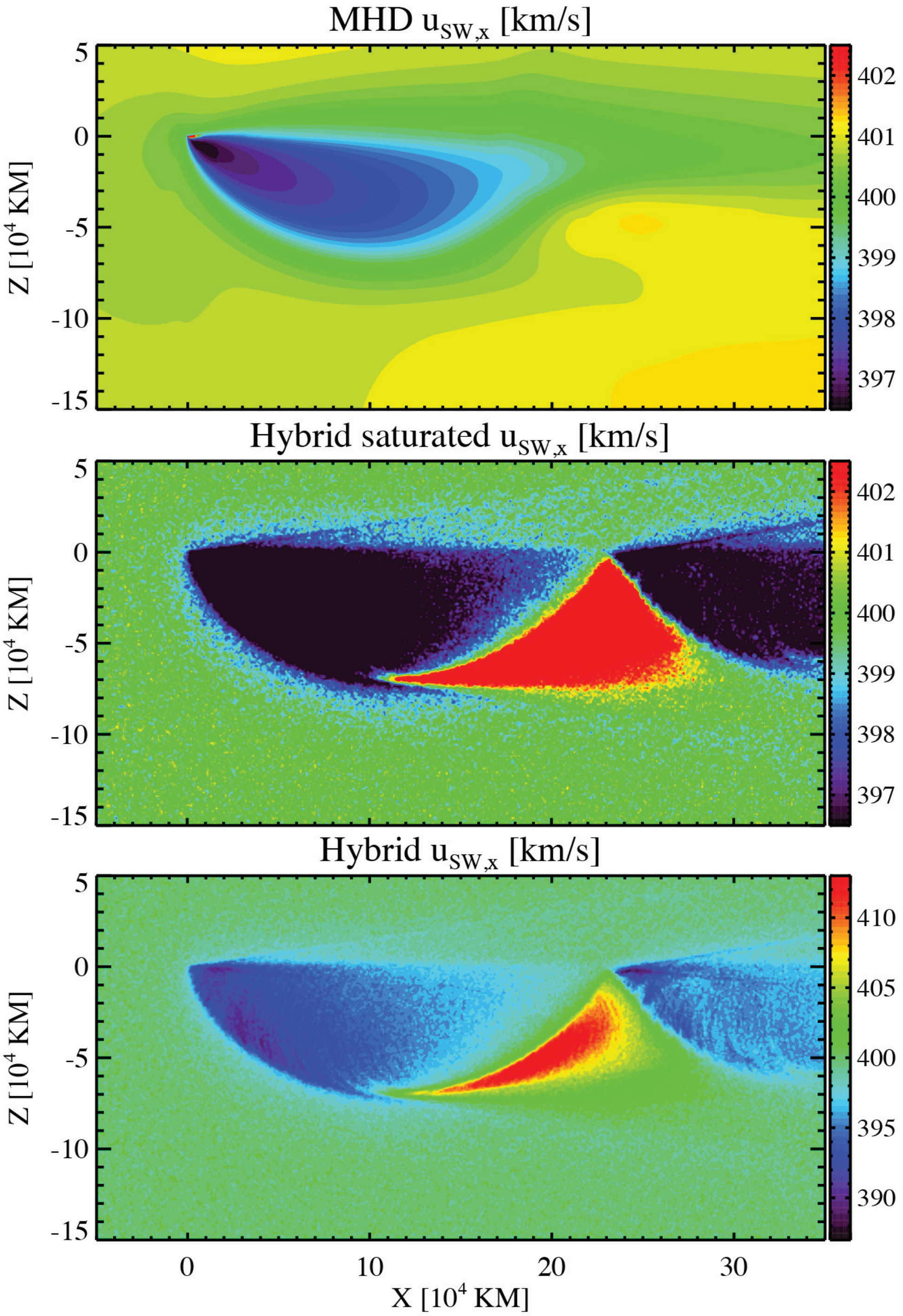

Figure 3.5: The bulk velocity component in *x*-direction of the solar wind protons on the *y*=0-cross-section. The result of the multifluid simulation is shown in the upper part and the hybrid simulation result is presented in the central and lower panel. The central panel shows the result with a saturated colourcode to allow for a better comparison to the multifluid model results. Reprinted from Rubin et al. (2014b) with permission from Elsevier.

the perturbation in the hybrid simulation and the enhancement in the solar wind velocity at the first cusp can only be guessed.

In the first part of the cycloid, the cometary ions have a velocity component into $-z$-direction. By applying this to Equation (3.14) one finds that the solar wind protons are affected by a force towards $-x$-direction. Consequently, a reduction in the solar wind speed in x-direction is present after the solar wind has passed the cometary ion tail for the first time. The reverse effect is initiated in the region where the cometary ions move upward, i.e. towards $+z$-direction. There, the solar wind is accelerated and the solar wind is faster in x-direction. Because of the fact that the solar wind has a finite temperature, the perturbation is reduced towards the next cometary ion tail crossing.

Due to the changes in the solar wind speed in x- and z-direction, it is expected that the solar wind density changes as well. The resulting solar wind density of the simulation models is presented in Figure (3.6) on the y=0-cross-section from both models. Density enhancements are visible as thin lines in the bottom panel of the figure, starting at the places where the solar wind velocity has its maximum or minimum in z-direction, i.e. at the comet, the cusp and the long edge. Furthermore, depletions of the density occur behind those regions.

A similar structuring of the interaction region can be observed in the magnetic field (Figure 3.7) because the magnetic field is frozen into the plasma flow. Noticeable is the positive correlation between the magnetic field and the solar wind density in regions with enhanced density. In addition, the opening angle, the angle between the thin lines and the x-direction, is measured to $\alpha = 8^\circ$. A similar angle can be obtained, if a fast magnetosonic wave is assumed to be triggered at the locations of the disturbance with maxima in z-component of the solar wind velocity (i.e. Bagdonat 2004).

$$\alpha = \arcsin \frac{c_{\mathrm{MS}} \cdot t}{u_{\mathrm{SW}} \cdot t} = \arcsin \frac{1}{M_{\mathrm{MS}}} = 8.2^\circ \,, \tag{3.15}$$

where $c_{\mathrm{MS}} = 56.8\,\mathrm{km\,s^{-1}}$ is the propagation speed of the fast magnetosonic wave. The solarwind speed normalised to the fast mode propagation speed is the magnetosonic Mach number which is $M_{\mathrm{MS}} = 7.0$ in this scenario. Thus, the cones are a signature of a standing fast magneotsonic wave, a Mach cone, which is triggered due to the presence of cometary ions.

Since the Mach cones are triggered at every location where the relative motion between the cometary ions and the solar wind protons has a maximum, a repetitive pattern of Mach cones is visible in the hybrid simulations. As long as a relative motion between the ions occurs, waves are triggered to reduce the differences. This has not been resolved by the hybrid simulations of a weakly active comet by Bagdonat (2004). In addition, due to the limitations of the multifluid MHD model in describing the pick-up ion tail, only traces of the repetitive Mach cones and the disturbances in the solar wind velocity are visible.

Due to the ongoing modifications of the solar wind along the pick-up ion tail, a transfer of momentum and energy via the excitation of waves is established. This reduces the relative speed; the cometary ions accelerate, and the size of the cycloids decreases. Using the same hybrid model, Götz (2014) investigated the decay of this pick-up ion tail. In the simulations the pick-up ion tail is modified by two processes: Firstly, a scattering process, which is observed by an expansion of the ion tail in y-direction, which has not been investigated in this work. Secondly, a reduction of the relative speed, which is visible

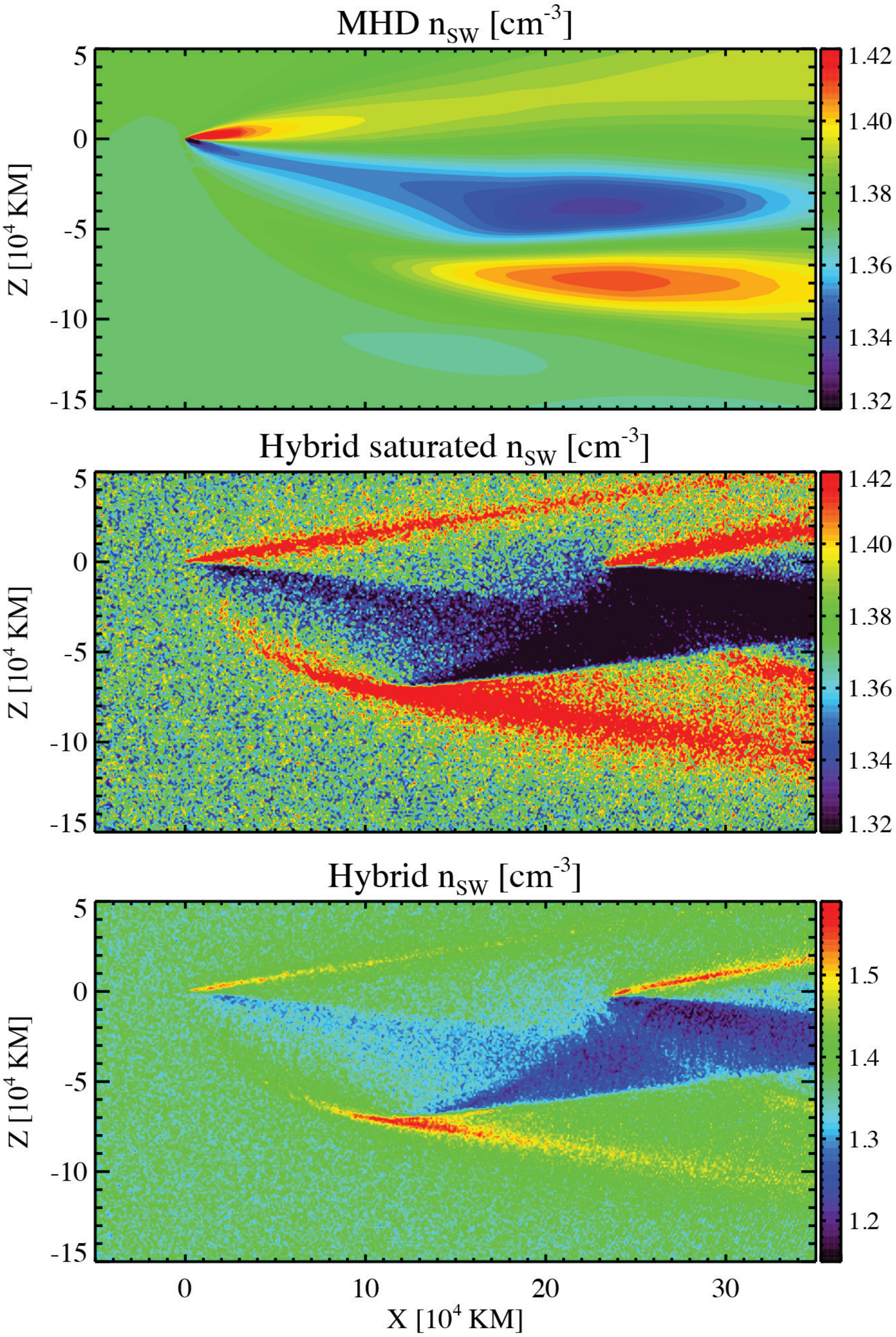

Figure 3.6: The density of the solar wind protons on the *y*=0-cross-section. The result of the multifluid simulation is shown in the upper part and the hybrid simulation result is presented in the central and lower panel. The central panel shows the result with a saturated colourcode to allow for a better comparison to the multifluid model results. Reprinted from Rubin et al. (2014b) with permission from Elsevier.

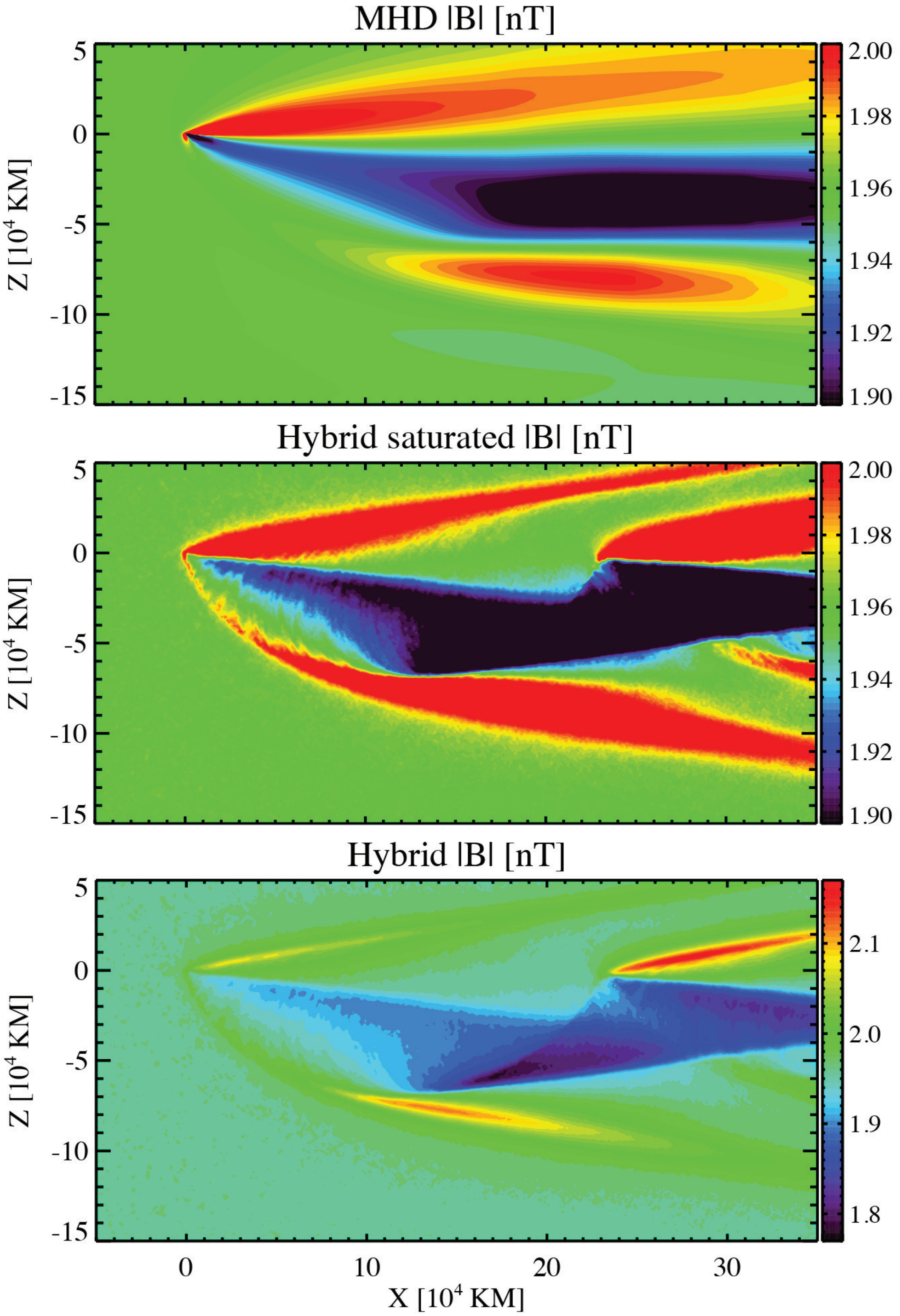

Figure 3.7: The strength of the magnetic field on the *y*=0-cross-section. The result of the multifluid simulation is shown in the upper part and the hybrid simulation result is presented in the central and lower panel. The central panel shows the result with a saturated colourcode to allow for a better comparison to the multifluid model results. Reprinted from Rubin et al. (2014b) with permission from Elsevier.

in the width of the ion tail, which decreases in her simulations. However, in this scenario, the cometary ions do not populate a ring in the velocity phase space but rather an unstable non-gyrotropic ion distribution (cf. Motschmann and Glassmeier 1993, 1998).

3.3 Small Scale Structures at Weakly Active Comets

Although the large scales are interesting, a direct observation will not be possible with the Rosetta spacecraft because the spacecraft will stay close to the nucleus, i.e. within 1500 km, in the nominal mission. Thus, for the mission planning the interaction close the nucleus is most interesting. Here, Rosetta will be able to observe the formation of these structures. Hence, the same scenario, i.e. a weakly active comet with a gas production rate of $8 \times 10^{25}\,\mathrm{s}^{-1}$ at 2.7 AU, as described in Section (3.2.1), is investigated in a series of hybrid simulations with a much smaller box and a much higher spatial resolution of the numerical mesh to resolve all relevant structures. The results of the first simulation are shown in Rubin et al. (2014b) and compared to the multifluid simulation. These results are very similar to the results of a second simulation, named *Simulation B*, which are shown in Figure (3.8). In this simulation the initial temperatures of the solar wind protons, the solar wind electrons, and the cometary electrons are set to zero, in order to simplify the scenario. In addition, the simulation box of *Simulation B* is slightly smaller in comparison to the simulation presented in Rubin et al. (2014b) in order to save computational resources. The simulation box extends from about $-1167\,\mathrm{km} < x < 583\,\mathrm{km}$ and from -1167 km to 1167 km in y- and z-direction. At the lowest refinement level a mesh resolution of $\Delta x_{\mathrm{L0}} = 16.2\,\mathrm{km}$ is set. An additional refinement level is defined by a cube with $-1167\,\mathrm{km} < x < 583\,\mathrm{km}$ and -778 km to 778 km in y- and z-direction, reaching a resolution of $\Delta x_{\mathrm{L1}} = 8.1\,\mathrm{km}$. Due to this configuration, no splitting of macro-particles directly ahead of the main interaction region takes place, which assures that the splitting of macro-particles does not trigger obvious numerical artefacts. The time step in this simulation is $\Delta t = 2.66 \times 10^{-3}$ s, which easily satisfies the *Courant-Friedrichs-Lewy*-criterion. The simulation uses the extended upstream boundary model and, uses inflow boundary conditions at all boundaries except for the $+x$ boundary. In order to guarantee good statistics each cell in the simulation is filled with at least 75 macro-particles of each species. The macro-particles which represent cometary ions are injected everywhere in the simulation box.

3.3.1 Numerical Observations

In Figure (3.8) the quasi-stationary state of *Simulation B* is presented. However, as will be discussed later in detail, the simulation is not stationary. The newborn cometary ions are picked-up, as discussed above, and in the beginning move towards $-z$-direction (Figure 3.8 e). Later, the cometary ions would also move in x-direction if the simulation box was larger (Section 3.2). On the z=0-cross-section the cometary ion density is confined to a small but nonetheless dense, cometary ion tail, which is oriented anti-sunward and extends to about 500 km. The solar wind is only weakly disturbed due to the presence of the comet.

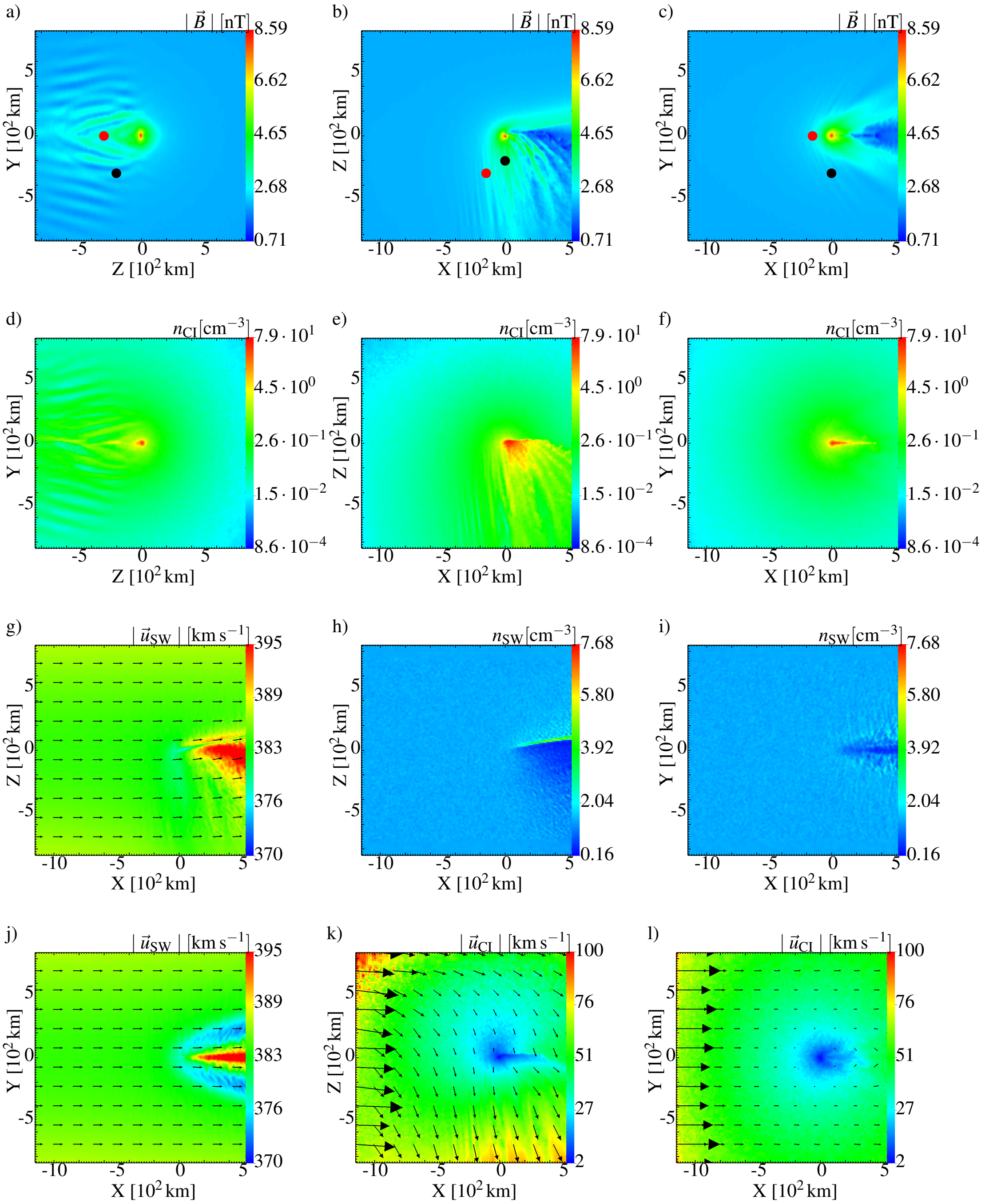

Figure 3.8: The results of *Simulation B*. The panels a) to c) display the magnitude of the magnetic field on the x=0-,y=0-, and z=0-cross-section. On the same cross-sections the cometary ion density is shown in the panels d) to f), whereas the solar wind density is shown in panels h) and i). The corresponding solar wind velocity on the same cross-sections is shown in g) and j). Finally, the cometary ion velocity is presented in the last two panels. The red and black circles in panels a) to c) show the projections to the cross-sections of *Point A* and *Point B*. More details are given in the text.

As discussed in the previous section, the solar wind is deflected towards the $+z$- hemisphere because of the presence of the cometary ions (Figure 3.8 g). Thus, downstream of the comet, a small density enhancement is formed on the $+z$-hemisphere and a depletion is present below it. This is the signature of the Mach cone, which is also visible in the magnetic field strength (Figure 3.8 b). Besides the Mach cone, the pick-up ion tail is identifiable in the magnetic field strength due to an increase in the field strength.

It is worthwhile to mention that the pick-up ion tail is fanned out, which is visible in the cometary ion density as well as in the magnetic field magnitude. Even in the $x < 0$ and $z < 0$ region a regular pattern in the cometary ion density and the magnetic field magnitude is present. As long as the nature of this pattern is unknown, the structures are referred to as phase fronts, since they appear as lines of the same phase in the perturbation. The amplitude of these variations is up to about $0.5\,\mathrm{nT}$ of the magnetic field in the region upstream of the main pick-up ion tail, whereas even larger variations are observed downstream. These phase fronts are also visible in the magnetic field on the z=0-cross-section within a band from $x = -200\,\mathrm{km}$ to $x = 200\,\mathrm{km}$.

Given by the fact that the phase fronts are visible in the magnetic field strength and in the cometary ion density, these variations are compressible. As one can easily see, the phase fronts are symmetric to the Sun-comet line, while the polarity of the magnetic field perturbation changes from the $-y$-hemisphere to the $+y$-hemisphere. In addition, the angles of the phase fronts to the Sun-comet line vary. Upstream of the nucleus an angle of about 60° can be found, whereas downstream the angle is about 20°, i.e. far away from the nucleus. The latter enhancement also has a signature in the solar wind density, whereas the solar wind density does not show any variations in the regions where the phase fronts in the magnetic field can be found. From Figures (3.8 a and d) one can obtain that the strength of the variation rises towards $-z$-direction. Given by the configuration of the simulation, a transition of refinement levels takes place at $z = -778\,\mathrm{km}$, where also the smoothing values change. This is why the amplitude of the variations is reduced on the coarser numerical mesh. In addition, the figures reveal that no phase fronts are present at the $+z$-hemisphere. This indicates that the wave which causes these phase fronts can only expand along the magnetic field and is triggered in the regions of higher cometary ion density.

Because the phase fronts are neither stationary in space nor in time, several quantities are recorded at two fixed points in the simulation box at every fourth time step. This corresponds to a sampling rate of $t_{\mathrm{sampling}} = 0.011\,\mathrm{s}$ or a frequency of $f_{\mathrm{sampling}} = 93.8\,\mathrm{Hz}$. The first position where the time series is recorded is at (-150,0,-300) km, which is called *Point A*, and the second point, *Point B*, is located at (0,-300,-200) km. Both points are located in the $-z$-hemisphere, where the strongest wave activity is present. Their positions are shown in Figures (3.8 a to c). While *Point A* is located in front of the main pick-up ion tail, at $y = 0\,\mathrm{km}$, *Point B* is placed aside the pick-up ion tail, where a lower cometary ion density can be found. In addition, the mean magnetic field has a negative B_x-component at *Point B* due to the draping of the magnetic field at the comet. It appears that *Point B* is located in a region of a regular pattern, i.e. where the phase fronts are more parallel to each other, while *Point A* is located where the phase fronts of the $+y$- and $-y$-hemisphere intersect each other (Figure 3.9). The time series at *Point A* has a length of about 1700 s and at *Point B* the values are recorded for about 1400 s. For the two points the resulting time series are shown for an interval of 100 s in Figures (3.11) and (3.10). This interval is

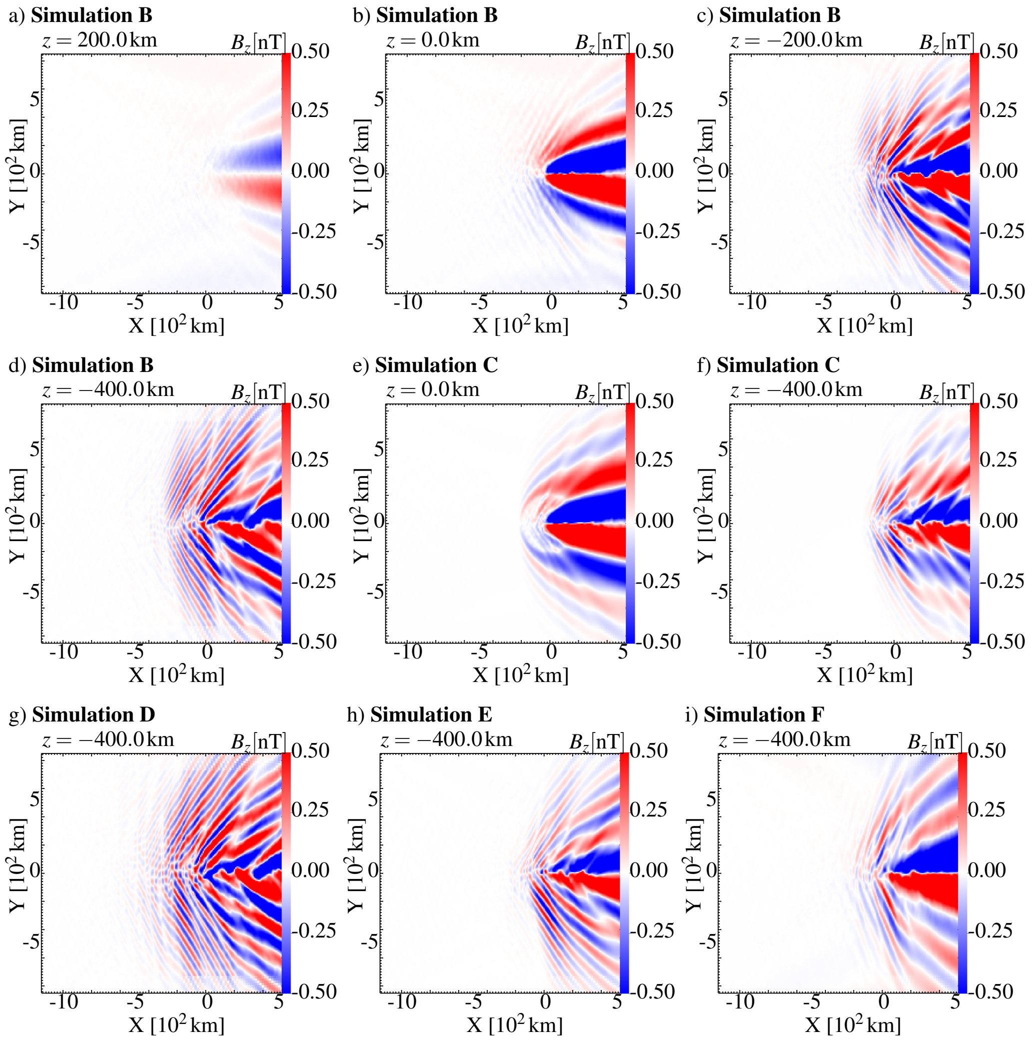

Figure 3.9: The variations of z-component of the magnetic field B_z. The panels a) to d) show the z-component of the magnetic field on the z-cross-sections with z=200 km, z=0 km, z=−200 km, and z=−400 km. While no phase fronts are visible on the z=200 km-cross-section, a parabolic shape is visible downstream of the comet on the z=0 km-cross-section. Upstream of this paraboloid the phase fronts are visible. In the cross-sections beneath, the clear paraboloid is not present, here some wake effects occur, but the phase fronts upstream increase in amplitude and remain in their regular pattern as on the z=0 km-cross-section. The panels e) and f) show the B_z-component obtained from *Simulation C*. In the region upstream of x=−200 km no variation of the magnetic field is present. In addition, no phase fronts can be found on the z=0-cross-section. On the cross-section beneath, phase fronts are present, but again, fluctuations in B_z are only present downstream of $x = -200\,\mathrm{km}$. The panels g), h), and i) show B_z on the z=−400 km-cross-section obtained from *Simulation D*, *E*, and *F*.

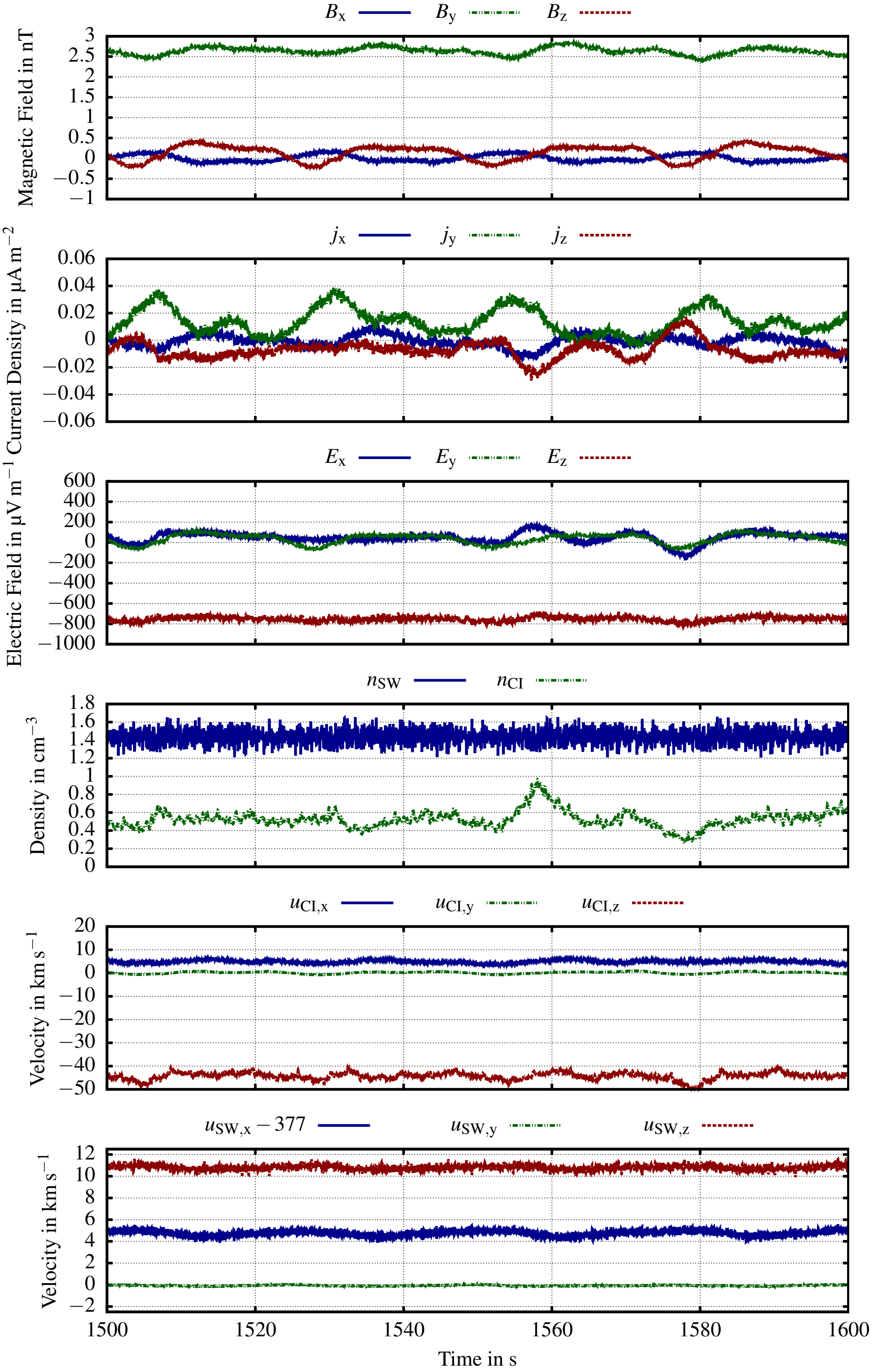

Figure 3.10: A time series obtained from *Simulation B* at *Point A* at (-150,0,-300) km.

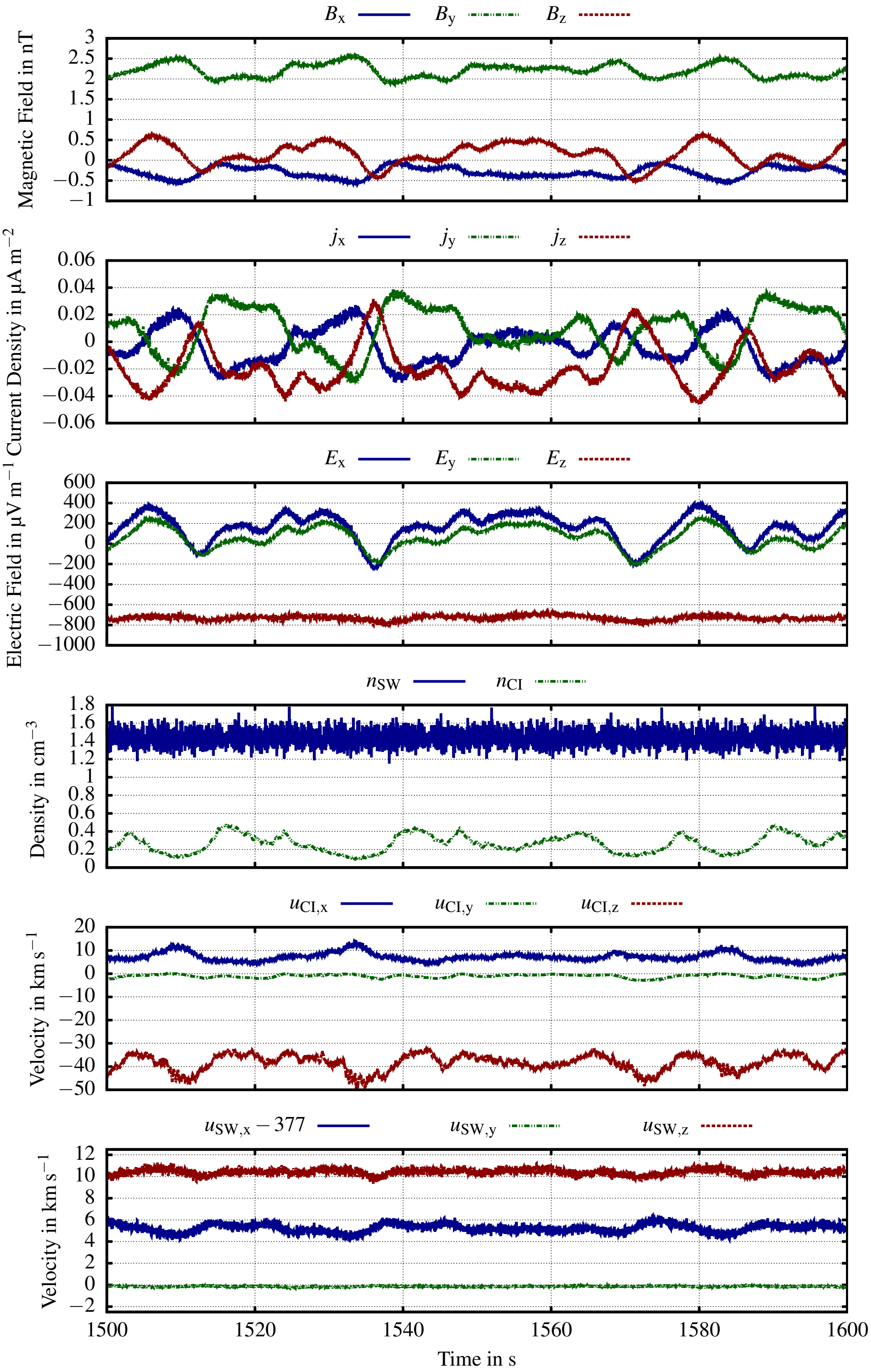

Figure 3.11: A time series obtained from *Simulation B* at *Point B* at (0,-300,-200) km.

Table 3.2: Mean values, indices m, and the results of a minimum variance analysis at *Point A* and *Point B*. $\vec{Sp}_{\mathrm{m}}$ and $\delta\vec{Sp}_{\mathrm{m}}$ denote the total Poynting flux and the Poynting flux caused by the waves. The angles are used as follows: $\theta_{\vec{k}_{\mathrm{min}},\vec{B}_{\mathrm{m}}} = \sphericalangle(\vec{k}_{\mathrm{min}},\vec{B}_{\mathrm{m}})$, $\theta_{\vec{k}_{\mathrm{min}},\vec{v}_{\mathrm{SW,m}}} = \sphericalangle(\vec{k}_{\mathrm{min}},\vec{v}_{\mathrm{SW,m}})$, $\theta_{\vec{k}_{\mathrm{min}},\delta\vec{Sp}_{\mathrm{m}}} = \sphericalangle(\vec{k}_{\mathrm{min}},\delta\vec{Sp}_{\mathrm{m}})$ and $\theta_{\vec{B}_{\mathrm{m}},\delta\vec{Sp}_{\mathrm{m}}} = \sphericalangle(\vec{B}_{\mathrm{m}},\delta\vec{Sp}_{\mathrm{m}})$.

Quantity	**Point A**	**Point B**	
$\vec{B}_{\mathrm{m}}$	(0.08,2.6,0.13)	(-0.296,2.2,0.14)	nT
$\mid \vec{B}_{\mathrm{m}} \mid$	2.6	2.2	nT
$\vec{E}_{\mathrm{m}}$	(47,35,-750)	(158,63,-731)	$\mu\mathrm{V\,m^{-1}}$
$\mid \vec{E}_{\mathrm{m}} \mid$	760	751	$\mu\mathrm{V\,m^{-1}}$
$\vec{j}_{\mathrm{m}}$	(-0.84,14,-7.3)	(-3.3,8.97,-19.3)	$\mathrm{nA\,m^{-2}}$
$\mid \vec{j}_{\mathrm{m}} \mid$	16	21.5	$\mathrm{nA\,m^{-2}}$
$n_{\mathrm{SW,m}}$	1.43	1.44	$\mathrm{cm^{-3}}$
$\vec{u}_{\mathrm{SW,m}}$	(380,-0.072,11)	(382,-0.144,10.4)	$\mathrm{km\,s^{-1}}$
$\mid \vec{u}_{\mathrm{SW,m}} \mid$	380	383	$\mathrm{km\,s^{-1}}$
$n_{\mathrm{CI,m}}$	0.52	0.27	$\mathrm{cm^{-3}}$
$\vec{u}_{\mathrm{CI,m}}$	(4.9,0.14,-44)	(7.24,-1.06,-38.3)	$\mathrm{km\,s^{-1}}$
$\mid \vec{u}_{\mathrm{CI,m}} \mid$	45	39	$\mathrm{km\,s^{-1}}$
$\vec{k}_{\mathrm{min}}$	(-0.893,-0.387,-0.231)	(-0.786,-0.618,0.005)	
$\lambda_1 : \lambda_2 : \lambda_3$	28:3:1	112:33:1	
$\theta_{\vec{k}_{\mathrm{min}},\vec{B}_{\mathrm{m}}}$	66°	60°	
$\theta_{\vec{k}_{\mathrm{min}},\vec{v}_{\mathrm{SW,m}}}$	26°	38°	
$\vec{Sp}_{\mathrm{m}}$	(1.58,-0.009,0.098)	(1.29,0.154,0.292)	$\mathrm{mW\,m^{-2}}$
$\mid \vec{Sp}_{\mathrm{m}} \mid$	1.59	1.33	$\mathrm{mW\,m^{-2}}$
$\delta\vec{Sp}_{\mathrm{m}}$	(6.06,-4.96,3.99)	(21.7,-28.2,-9.5)	$\mathrm{mW\,m^{-2}}$
$\mid \delta\vec{Sp}_{\mathrm{m}} \mid$	8.78	36.8	$\mathrm{mW\,m^{-2}}$
$\theta_{\vec{k}_{\mathrm{min}},\delta\vec{Sp}_{\mathrm{m}}}$	60°	89.3°	

randomly selected.

At *Point A* the mean magnetic field is about $\mid \vec{B}_{\mathrm{m}} \mid = 2.6\,\mathrm{nT}$, whereas the perturbations are in the order of $\mid \delta\vec{B}_{\mathrm{m}} \mid = 0.4\,\mathrm{nT}$. A minimum variance analysis (MVA, Sonnerup and Cahill,1967) is conducted with the magnetic field data at this point within the selected time interval. The quality of this analysis, which is given by the ratio of the intermediate to the minimum value, is 3. Thus, the direction of the wave propagation is parallel or anti-parallel to the direction of the minimum variation of the magnetic field. In this case, the direction of the minimum variance $\vec{k}_{\mathrm{min}}$ is mainly along the x-axis. The angle between $\vec{k}_{\mathrm{min}}$ and the mean magnetic field is about 66°, that is, a quasi-perpendicular propaga-

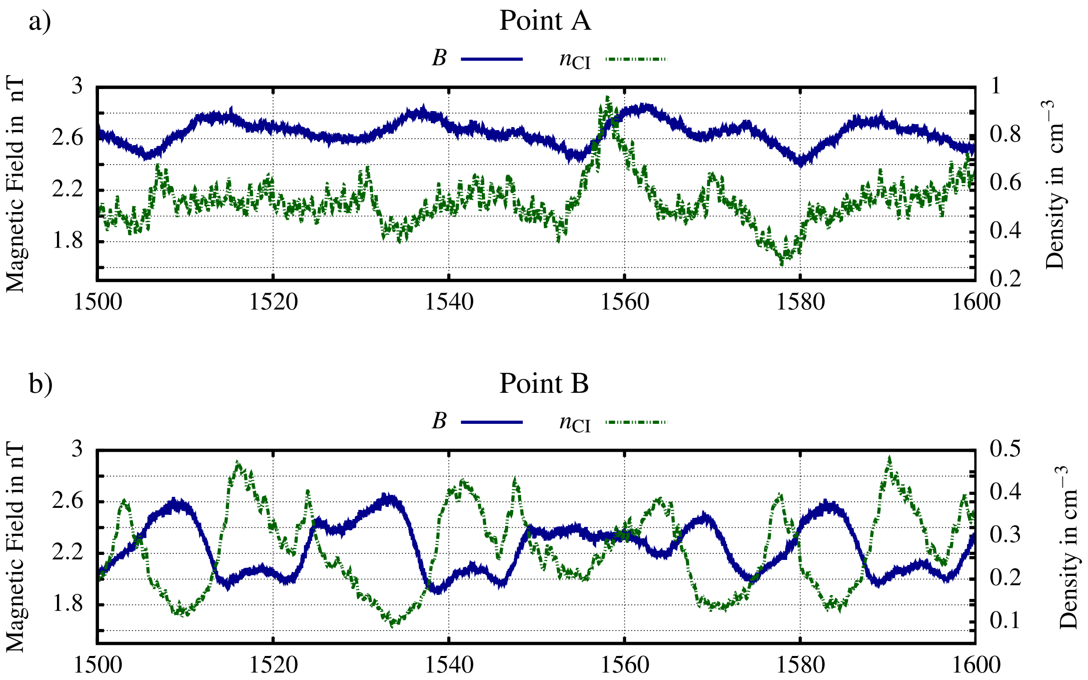

Figure 3.12: The magnetic field magnitude and the cometary ion density at *Point A* and *Point B*, which are measured in *Simulation B* for a randomly selected time interval. The dashed-dotted lines in the lower panel highlight the maxima of the cometary ion density at *Point B*.

tion. It is worthwhile to mention that the solar wind density remains constant when the quasi-stationary state is reached at about 40 s. The solar wind density is also constant at *Point B*, whereas the cometary ion densities vary with an amplitude of $\delta n_{\mathrm{CI,m}} = 0.2\,\mathrm{cm}^{-3}$. Thus, the perturbations are as big as or even bigger than the mean cometary ion density $n_{\mathrm{CI,m}}$, which is also true for the cometary ion density at *Point A*. In contrast to the small perturbations in the magnetic field at *Point A*, the perturbations are close to 1 nT, peak to peak, at *Point B*. The MVA of the magnetic field data from *Point B* reveals that the propagation of the wave has an orientation of (-0.786,-0.618,0.005). The angle between the mean magnetic field and the orientation of the minimum variance is about 60°. A list of mean values is given in Table (3.2).

The magnitudes of the magnetic field at both points as well as the cometary ion density are presented in Figure (3.12). For the selected time interval the phase shift between the cometary ion density and the magnetic field is between 180° and 90°.

In Figure (3.13) hodograms of the magnetic fields at *Point A* and *Point B* are shown. Therefore, the magnetic field is transformed into the mean-field-aligned coordinate system, where a low-pass filter for periods above 100 s is applied to the data to determine the mean magnetic field. The component of the magnetic field in direction of the mean magnetic field is given by $B_{\|}$. The perpendicular components are labelled $B_{\perp,1}$ and $B_{\perp,2}$. In the figure the magnetic field between 1500 s and 1600 s is shown. At both points the magnetic field is elliptically left-handed polarised.

The results of a spectral analysis of the time series at *Point A* and *Point B* are shown in Figure (3.14). In the first two rows the power spectral densities of the variation of the magnetic field magnitude and of the cometary ion density are presented. Both spectra at

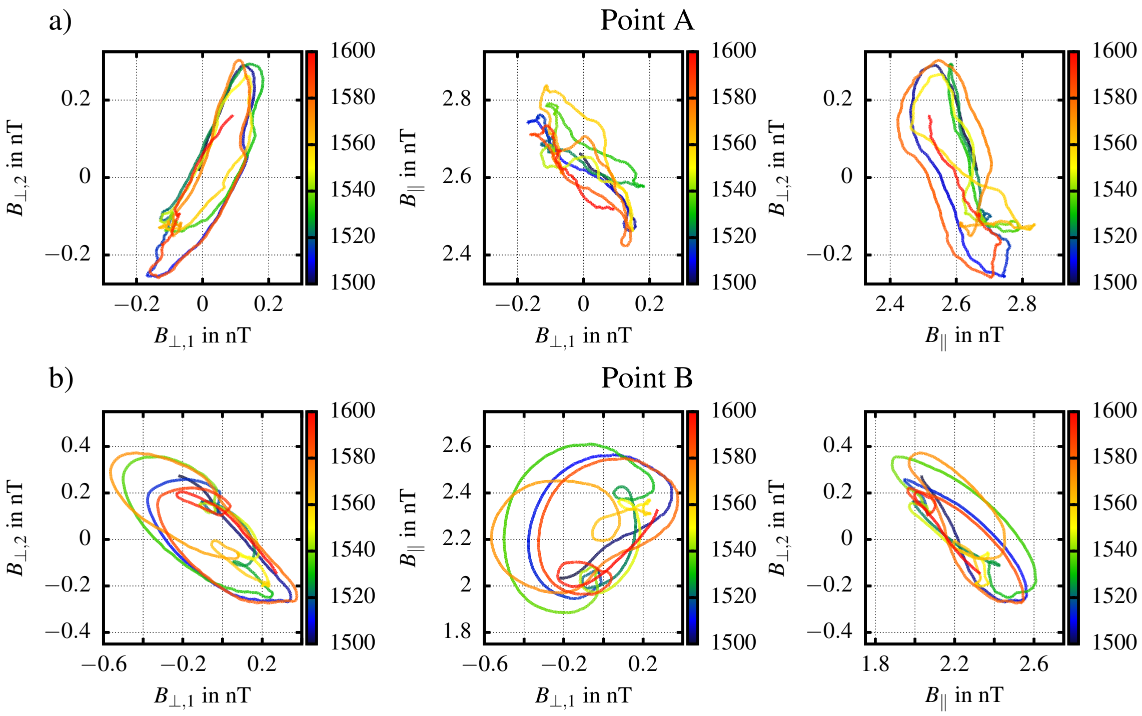

Figure 3.13: The hodograms of the magnetic field for an time interval of 100 s at *Point A*, in the upper row, and at *Point B*, in the lower row. The magnetic field is rotated into the mean-field-aligned coordinate system. $B_{\parallel}$ denotes the fluctuations parallel to the mean magnetic field and $B_{\perp,2}$ and $B_{\perp,1}$ are the perpendicular fluctuations, respectively. The magnetic field values are smoothed and plotted with a colour code, which represent the time in s.

Point A reveal sharp peaks at a frequency of $f_{\mathrm{p,A}} = 39\,\mathrm{mHz}$, which is close to the local solar wind proton gyrofrequency $f_{\mathrm{gyr,sw,A}} = 40.5\,\mathrm{mHz}$. Further peaks are present in the cometary ion power spectrum at 75 mHz, 117 mHz, 157 mHz, and 255 mHz. Except for the last frequency, the frequencies are very close (within 5 mHz) to the harmonics of $f_{\mathrm{p,A}}$. In the spectra of the magnetic field an additional peak is only visible at the second harmonic. Nevertheless, both spectra show a strong decay towards higher frequencies.

In comparison to the presented cometary simulations, a hybrid simulation without a comet, i.e. with a pure and constant solar wind flow, has only a constant magnetic field value. This is caused by the fact, that the solar wind is modelled as a constant flow in the hybrid simulation, without applying any special turbulence spectra. Hence, the expected Fourier analysis would yield a single peak at the frequency zero. Consequently, the frequencies observed in the spectrum at *Point A* as well as at *Point B* are only caused by the comet.

Similar to the spectra at *Point A*, both spectra at *Point B* (Figure 3.14) reveal a peak at $f_{\mathrm{p,B}} = 50\,\mathrm{mHz}$. But in contrast to *Point A*, this time the peak is much broader and not that prominent. In addition, this peak is not as close to the local proton gyrofrequency of $f_{\mathrm{gyr,sw,B}} = 35.3\,\mathrm{mHz}$ as the peak at *Point A* to $f_{\mathrm{gyr,sw,A}}$. Furthermore, no peaks at the harmonic frequencies can be identified.

In the third and fourth row of Figure (3.14) the coherence and the phase between the variations in the magnetic field magnitude and the variations in the cometary ion density

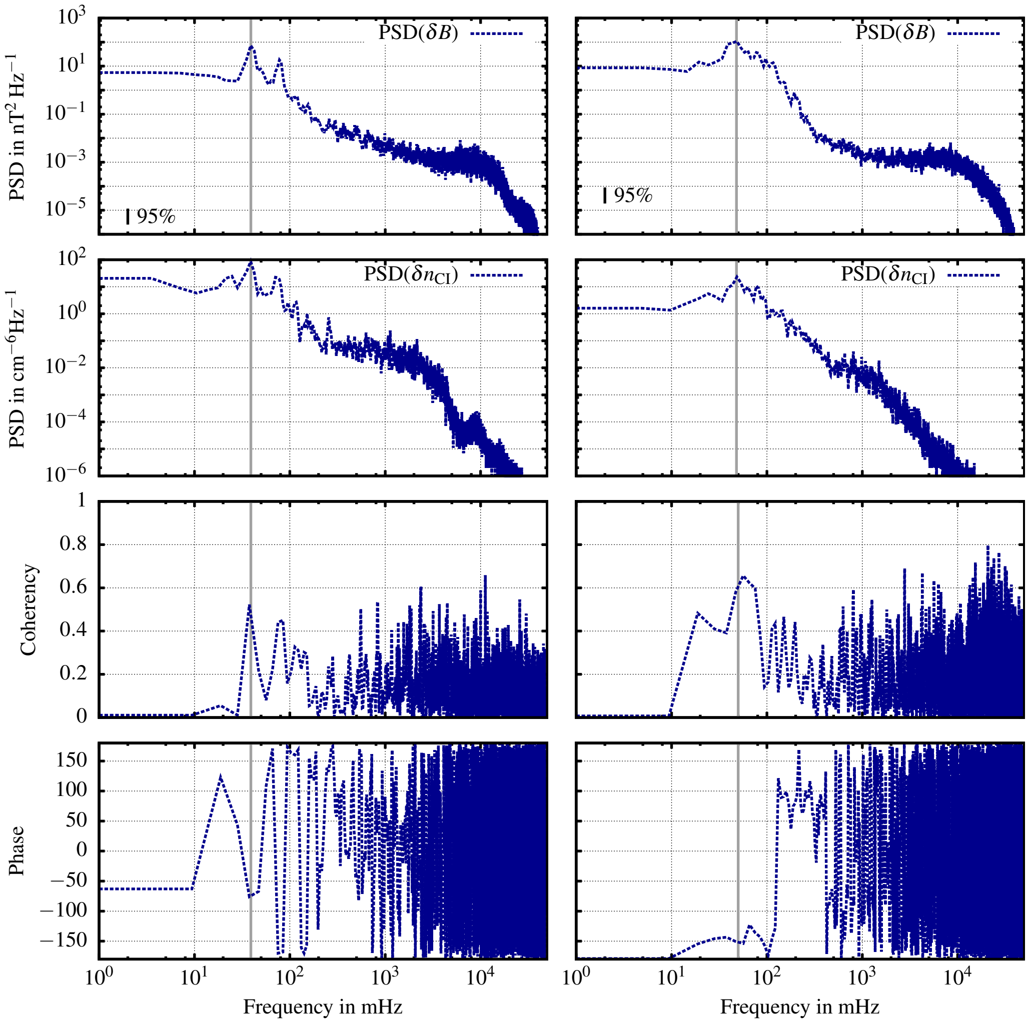

Figure 3.14: The results of a spectral analysis of the magnetic field magnitude and the cometary ion density at *Point A* and *Point B*. The panels on the left hand side present the results for *Point A*, and the panels on the right side show the results for *Point B*. In the first row the trace of the power spectral density of the magnetic field are plotted for both points. At *Point A* a clear peak is visible at a frequency of about 39 mHz. A broader peak is present in the spectrum at *Point B*, which has its maximum at about 50 mHz. Both frequencies are highlighted by a grey vertical line. The panels in the second row show the spectra of the cometary ion density. In both spectra a peak occurs at the same frequencies as in the magnetic field spectra. The coherencies between the magnetic field and the cometary ion density, which are obtained by a cross spectral analysis, peak at the frequencies 39 mHz and 50 mHz, respectively, which is shown in the third row. In the lowest row the phase between the magnetic field and the cometary ion density is shown. At *Point A* the phase is about $-80°$, whereas at *Point B* a phase of about $-150°$ is present. The spectral analyses have 34 degrees of freedom for *Point A* and 20 for *Point B* because of the different lengths of the time series.

are plotted. For this analysis a window width of about 106 s is used. Hence, about 17 independent time intervals can be used at *Point A* and about 14 at *Point B*, which corresponds to 34 and 20 degrees of freedom for the analysis. Although both coherence plots reveal a small enhancement at the peak frequencies $f_{\mathrm{p,A}}$ and $f_{\mathrm{p,B}}$ the coherence is only about 0.5 at *Point A* and about 0.6 at *Point B*. In addition, the maxima at the peak frequencies are as large as the enhancements at higher frequencies. Consequently, no linear dependency between the magnetic field magnitude and the cometary ion density is present.

Based on the fact that the wave mainly propagates in the xy-plane, the distance between the phase fronts was determined by a 2D Fourier-analysis. This analysis uses data from the $z = -300\,\mathrm{km}$-cross-section in the $-460\,\mathrm{km} < x < 140\,\mathrm{km}$ and $-620\,\mathrm{km} < y < 20\,\mathrm{km}$ sector from 60 time levels separated by 27 s. From this analysis a mean wavelength of $65(13)$ km was obtained.

In contrast to the frequency, the orientation of the wave propagation and the length of the wave vector, the direction of the wave is not known. In order to determine the direction, the wave telescope technique is applied to the data (Motschmann et al. 1996, Glassmeier et al. 2001). This technique has the advantage that only 4 time series at selected points are needed instead of all values in a specific volume in case of a spatial and temporal Fourier analysis, which saves memory. The time series are obtained at four different locations around *Point B* for about 400 s. The distance between the four different location is set to 15 km. Hence, the four locations create a tetrahedron. The version of the wave telescope which is used for this analysis assumes plane waves in the magnetic field, which should also be fulfilled due to the parallel character of the phase fronts at *Point B*. The results of this analysis are shown in Figure (3.15). In the left panel the frequency is plotted against the power spectral density. Here, several peaks are identified and highlighted by yellow horizontal lines. The panel in the middle shows the maximum value of the spatial spectrum for each frequency in arbitrary units. One can easily see that no clear peaks in the spatial spectrum are present at the frequencies with a high power spectral density, which are marked by yellow lines. This indicates that the energy of the identified wave vector is not different to the other wave vectors at the other frequencies. Consequently, the technique is not able to obtain spatial information from this dataset, although the magnitude of the wave vector, which is shown in the right panel, seems reasonable. A potential explanation could be that spatial and temporal variations of the phase fronts lead to a variation of the phase velocity. Although this variation seems to be small since parallel structures are clearly visible, it is not small enough compared to the mean phase velocity and, therefore, is not negligible. Consequently, each sensor records phase fronts which seem to be uncorrelated and, thus, the wave telescope analysis failed. Another explanation could be the presence of spherical waves, but the wave telescope assumes plane waves. These spherical waves, as for example discussed in the last section for the fast mode, interfere and create straight phase fronts, as in the case of the Mach cone.

Figure (3.16) shows the temporal evolution of the z-component of magnetic field B_z and the cometary ion density along two lines. The first line is in x-direction with $y = -250\,\mathrm{km}$ and $z = -200\,\mathrm{km}$. Along that line the z-component of the magnetic field and the cometary ion density are shown in a) and b). Both reveal that the phase fronts remain at their position at small x-positions, i.e. upstream of the pick-up ion tail, except for an oscillation of their positions of about 20 km. Downstream of the pick-up ion tail, i.e. at about x>0 km, the phase fronts move downstream towards larger x-values and the velocity increases.

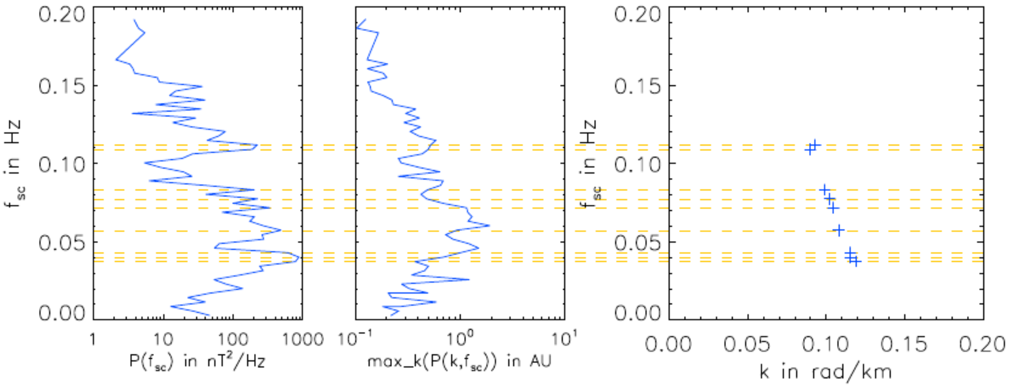

Figure 3.15: The results of the wave telescope applied to the magnetic field data obtained around *Point B*. For this method time series are recorded at four points close to *Point B*, which have a distance of 15 km to each other. The left panel shows the power spectral density versus the frequency. The peaks in this panel are highlighted by yellow horizontal lines. The panel in the middle shows the maximum value of the spatial spectrum for each frequency. On the right panel the magnitude of the wave vector against the frequency is shown.

At intermediate positions the phase fronts seem to split and become dispersive. This might be the reason why the wave telescope technique failed, since it assumes plane waves. In Figure (3.16 c) the temporal evolution along a second line in y-direction with $y = -28\,\mathrm{km}$ and $z = -200\,\mathrm{km}$ is shown. Here, the phase fronts in the magnetic field move towards $y = 0\,\mathrm{km}$. Based on this temporal evolution, the group velocity is directed towards negative x and towards the plasma tail.

The energy flow due to electromagnetic fields can be computed with the Poynting vector. The Poynting vector $\vec{Sp}_\mathrm{m}$ of the mean magnetic and electric field mainly points into x-direction for both cases. But the mean of the Poynting vector of the variations, which represents the energy transport of the wave, is calculated by

$$\delta\vec{Sp}_\mathrm{m} = \frac{1}{\mu_0 N}\sum_{\mathrm{t_n}}\left(\delta\vec{E}(t_\mathrm{n}) \times \delta\vec{B}(t_\mathrm{n})\right) , \tag{3.16}$$

where $\delta E(t_\mathrm{n})$ and $\delta\vec{B}(t_\mathrm{n})$ denote the variations of the electric and magnetic field and N is the number of vectors in the time series. It is remarkable that the angle between this Poynting vector $\delta\vec{Sp}_\mathrm{m}$ and $\vec{k}_\mathrm{min}$ is about 60° for *Point A* and about 89° for *Point B*. Thus, the directions of the wave propagation and the Poynting vector are quite different, especially for *Point B*.

Besides *Simulation B* some other simulations with similar parameters have been conducted.

- In *Simulation C* the ionisation profile is chopped at a radius of 200 km, i.e. cometary ions are only injected into the simulation box up to this radius. In addition, the extended upstream boundary model is not used in this simulation, in order to stabilise the simulation. The resulting z-component of the magnetic field on the z=0 km- and z=−400 km-cross-section are shown in Figure (3.9 e and f). It is worthwhile that in

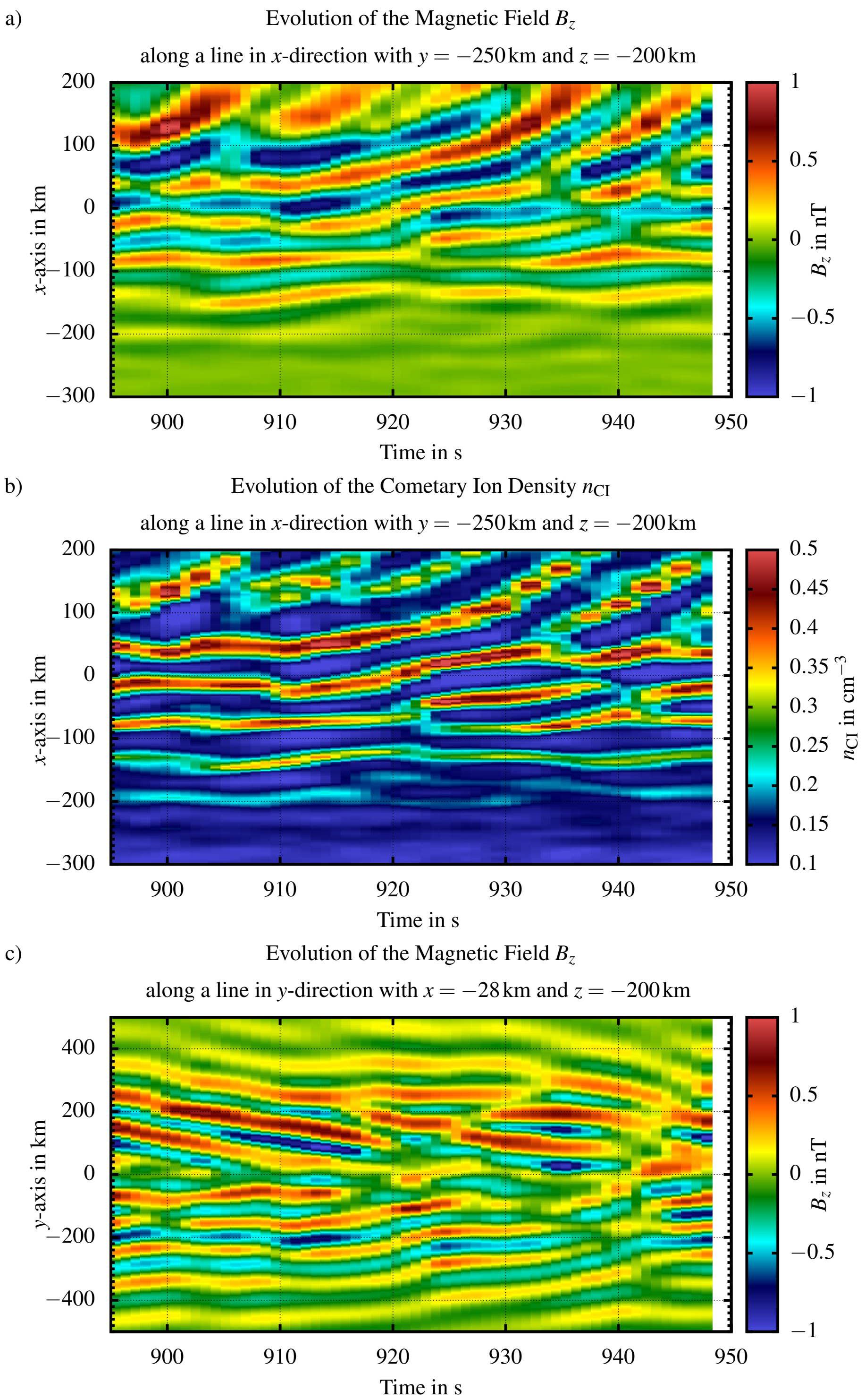

Figure 3.16: The temporal evolution of the z-component of the magnetic field and the cometary ion density along two lines across the simulation box. In a) and b) the magnetic field B_z and the cometary ion density are shown along a line in x-direction with $y = -250\,\mathrm{km}$ and $z = -200\,\mathrm{km}$. In c) the magnetic field B_z is presented along a line in y-direction with $y = -28\,\mathrm{km}$ and $z = -200\,\mathrm{km}$.

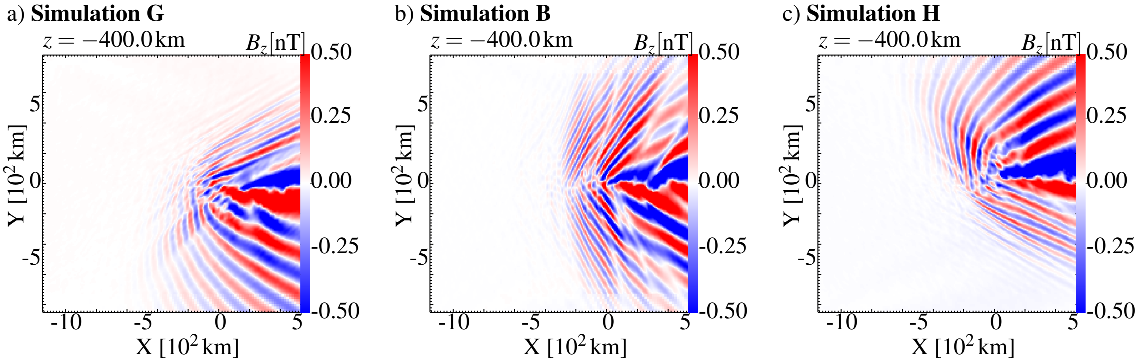

Figure 3.17: The z-component of the magnetic field on the z=-400 km-cross-section for three configurations of the orientation of the background magnetic field. In panel a) the magnetic field has an angle of 45° to the solar wind velocity. In panel b) and c) the angle increases to 90° and 135°. In the perpendicular case the phase fronts are symmetric, whereas in the oblique cases the phase fronts are tilted and depending on the orientation the phase fronts are compressed or stretched in the different hemispheres.

these figures no perturbations of the field are present upstream of $x = -200$ km and the striations are not as parallel as in *Simulation B*.

- In contrast to the *Simulation B*, the cometary ion mass is set to $m_{\mathrm{CI}} = 8$ amu in *Simulation D*. The resulting perturbations in B_z on the z=-400 km-cross-section are shown in Figure (3.9 g). In comparison with the perturbations in *Simulation B* (Figure 3.9 d) the perturbations appear stronger. This is why the intersection of the striations upstream are more prominent in the result of *Simulation D*.

- A cometary ion mass of $m_{\mathrm{CI}} = 34$ amu is used in *Simulation E* and the B_z structures on the z=-400 km-cross-section are presented in Figure (3.9 h). In comparison to *Simulation D* and *Simulation B*, the perturbations are weaker in this simulation.

- The strength of the background magnetic field is doubled in *Simulation F* in comparison to the *Simulation B*. The B_z-component on the z=-400 km-cross-section (Figure 3.9 i) reveals that the perturbations are weaker and the wavelength of the phase fronts are longer. Furthermore, the opening angle of the striations grow to about 80°.

- In *Simulation G* and *Simulation H* the orientation of the magnetic field is changed. While in *Simulation B* the angle between the magnetic field and the solar wind velocity is 90°, the angle is set to 45° in *Simulation G* and to 135° in *Simulation H*. The resulting structures in the z-component of the magnetic field are shown in Figure (3.17). In case of *Simulation G* phase fronts are compressed on the $+y$-hemisphere, whereas on the $-y$-cross-section the wavelength is larger and the structures are present in regions further upstream than in the perpendicular case. The latter fact is also true for *Simulation H*, but the compression and stretching of the phase fronts is opposed to *Simulation G*.

3.3.2 Discussion

The global structure of the interaction on the small scales can partially be deduced from structures also visible on the large scales. This means that the beginning of the cometary pick-up ion tail and the footpoint of the first Mach cone are present in the small scale simulations. Consequently, RPC confirmed that the cometary ions move perpendicularly to the Sun-comet line and observed a deflection of the solar wind into the Mach cone as long as the comet's gas production rate is low (Nilsson et al. 2015). The small anti-sunward plasma tail (Figure 3.8 f) was not visible in the simulation of the large scales. The reason for that is the coarse resolution of the numerical mesh in large scale simulations. As a consequence, the draping of the magnetic field is neglected in the large scale simulation in Section (3.2). However, this draping is responsible for the formation of the anti-sunward plasma tail (Alfven 1957). Another effect, which is not visible in the large scale simulation, are the phase fronts. These have never been predicted by a global simulation of the cometary plasma environment.

First of all, it is necessary to ensure that the waves are not a result of the numerical mesh. This means to exclude a common problem in the hybrid simulations and probably every simulation which uses a regular mesh. In hybrid simulations, waves are caused by the finite mesh size in the simulation box, which cannot describe all physical effects. The waves can be observed favourably at the edges of the simulation box or at transitions of refinement levels. But the main characteristic of these *mesh waves* are wavelengths in the order of the mesh size, i.e. alternating from cell to cell. The presented simulations have a mesh size of about 8.1 km in the inner region, whereas the waves have a wavelength of about 65 km. In addition by using various mesh configurations, i.e. with respect to the position of the refinement levels, no significant change in the wave pattern was observed. Thus, it is unlikely that the observed waves are generated by the numerical mesh.

There are basically two possibilities to explain the observed phase fronts. The first assumes that the phase fronts are excited in the solar wind. This is possible, for example, since due to the presence of the cometary ions the solar wind becomes unstable. The resulting phase fronts move towards the comet where, for example, the flow modifications yield to a bending of the phase fronts around the nucleus. The second possibility assumes that an obstacle in the flow continuously excites waves. These waves superimposed by the solar wind flow lead to the phase fronts, which rest in the comet frame, e.g. the fast-magnetosonic Mach cone. Based on a modification of the flow caused by these phase fronts, the phase fronts become unstable which leads to a tailward motion of the phase fronts. This is why various wave types and excitation types are discussed in this section.

The classical fast-magnetosonic wave has frequencies far below the ion cyclotron frequency. Thus, this wave type can be excluded, if the wave is embedded in the comet frame. However, if the wave is caused in the solar wind frame or in the cometary ion frame, the frequency observed in the comet frame has to be shifted to other frequency values. Nevertheless, the fast magnetosonic mode can be excluded by using a phasing argument. In general, a fast magnetosonic wave is characterised by a magnetic field which is in phase to the density. This is obviously not the case in our simulation. In addition, the fast-mode is not restricted to a propagation parallel to the magnetic field (Baumjohann and Treumann 1996). Hence, a restriction to the $-z$-hemisphere cannot be explained.

A type of waves, which are commonly present in the cometary environment, are mirror mode waves (Glassmeier et al. 1993). As discussed in general plasma textbooks (cf. Baumjohann and Treumann 1996) a mirror mode is excited if

$$\frac{\beta_\perp}{\beta_\parallel} > 1 + \frac{1}{\beta_\perp} \tag{3.17}$$

is satisfied. $\beta_\perp$ and $\beta_\parallel$ denote the ratio of kinetic to magnetic pressure. Hence, in case the perpendicular pressure exceeds the parallel pressure a mirror instability is excited. A strong magnetic field stabilises the mode. In the cometary interaction region the ring distribution of the picked up cometary ions leads to a large temperature anisotropy. By also considering an anisotropic electron pressure, Remya et al. (2013) showed that the ion cyclotron growth rate is suppressed and the mirror mode growth rate is increased and exceeds that of the ion cyclotron waves. The most recent study on mirror modes at comets was conducted by Volwerk et al. (2014). They studied the occurrences of mirror modes at comet 1P/Halley during the flybys of VEGA 1, VEGA 2, and Giotto, which visited the comet within 8 days. Volwerk et al. (2014) used only magnetic field data to search for mirror modes. Their algorithm identifies a wave structure as a mirror mode if the following criteria are satisfied: 1) The angle between the minimum variance direction and the background magnetic field is above 80°. 2) The angle between the maximum variance direction and the background magnetic field is below 20°. 3) The amplitude of the waves is $\delta B/B > 0.3$. In case of the wave in the simulation presented above and measured at *Point B*, the first and the third criterion are satisfied, but the angle between the direction of the maximum variance and the background magnetic field exceeds 20° by far. An even better argument against the presence of mirror mode waves in the simulation is presented in Figure (3.12). In general, a mirror mode is characterised by a magnetic pressure oscillation which is anticorrelated to the plasma pressure oscillation and the total pressure remains constant. In case the temperatures are more or less constant, even the magnetic field strength oscillation is anticorrelated to the total density. However, the waves in the simulation do not show this behaviour. Schmid et al. (2014) found that the mirror mode waves at 1P/Halley had a size of about $1-2$ cometary ion gyroradii and that they are triggered at the bow shock, therefore, Volwerk et al. (2014) conclude that mirror mode waves at 67P/Churyumov-Gerasimenko can be expected, when the stand-off distance of the bow shock is more than 2 cometary ion gyroradii. This is not fulfilled in the current scenario. In addition, the size of the simulation box is much smaller than one cometary ion gyroradius. Summarising one can say that these waves are no mirror modes waves.

As already briefly mentioned above, the dominant wave type which has been observed during the past cometary missions is the ion cyclotron wave (Tsurutani and Smith 1986, Tsurutani et al. 1989, Glassmeier et al. 1989). This wave is triggered by the instability of the ring-beam distribution of the cometary ions. In case the density of the cometary ions is much smaller than the solar wind density and in the case of an oblique magnetic field orientation, Wu and Davidson (1972) identified a resonant instability with a resonant condition of

$$\omega_{(\mathrm{sw})} = k u_\parallel \pm \Omega_\mathrm{i} \, , \tag{3.18}$$

where $\omega_{(\mathrm{sw})}$ is the wave frequency in the solar wind frame and $u_\parallel$ denotes the velocity of the ion beam parallel to the magnetic field. The gyrofrequency of the new ions is denoted by Ω_i and the $\pm$ sign refers to the polarisation. Thus, in case new ions with zero speed in the solar wind frame are injected, the plasma is resonant for frequencies $\omega_{(\mathrm{sw})}$ close to the gyrofrequencies of the new ions, and also at the gyrofrequencies of the other plasma components, i.e. protons or electrons. However, in the cometary interaction the new ions have a velocity of about 1 km s^{-1} in the comet frame, and a velocity $-u_\mathrm{SW}\cos\theta$ parallel to the magnetic field in the solar wind frame. Hence, $\omega_{(\mathrm{sw})}$ differs from Ω_i. But as demonstrated by Tsurutani and Smith (1986) the Doppler shift from the solar wind frame to the comet frame or spacecraft frame shifts the frequency of the ion cyclotron wave to the gyrofrequency Ω_i. Thus, in the scenario used for the hybrid simulation the ion cyclotron wave should have a frequency of about $f_\mathrm{gyr,CI} = 2\,\mathrm{mHz}$, which is about an order of magnitude smaller than that of the observed waves. In addition, the model by Wu and Davidson (1972) only requires a few newborn ions. However, close to the comet the number density of the cometary ions is as large as or even larger than the solar wind number density. At a real comet, cometary protons, which are produced due to the dissociation of water molecules, can cause waves at the frequencies which are observed in the hybrid simulation. However, in the hybrid simulation only heavy cometary ions are produced.

During the ICE flyby at comet 21P/Giacobini-Zinner, Smith et al. (1986b) and Tsurutani and Smith (1986) observed two different types of waves in the upstream region: long period oscillations with periods of about 100 s, which are the ion cyclotron waves, and short period waves. This second type has periods of about 3 s and Tsurutani et al. (1989) got the impression that the short period waves occur at the leading edge of the long period waves, which have a magnitude of 44 nT peak-to-peak. While Tsurutani and Smith (1986) and Brinca and Tsurutani (1988a) suggest that these waves are caused by hydrogen pick-up, as discussed above , Goldstein et al. (1987) propose that these waves are caused by another instability of the water-group ions, which was identified by Wu and Davidson (1972). Goldstein et al. (1987) studied this instability and found that right-handed whistler waves are triggered. The authors found that the phase velocity of these waves are smaller but comparable to the solar wind speed. Consequently, the right-handed wave changes its polarisation and the frequency is around a few seconds in the comet frame, which is about the solar wind proton gyrofrequency. In addition, Brinca and Tsurutani (1988b) showed that the frequency of this wave is between 0.5 to 1.8 of the proton gyrofrequency in the comet frame. But a comparison of the growth rates indicates that the growth rate of this whistler wave is smaller than the growth of the ion cyclotron wave due to hydrogen pick-up. An alternative explanation is suggested by Tsurutani et al. (1989). They propose that the waves are caused by the steepening of the long period waves. This would also be applicable to the scenario in the simulation, since the magnetic field increases from the undisturbed solar wind towards the nucleus or the cometary ion tail. However, due to the fact that the magnetic field and the cometary ion density perturbations reach background levels, a linear treatment of the instability analysis might not describe the situation correctly.

The aforementioned excitations take place in the solar wind. However, in this scenario the solar wind has a velocity of about 380 km s^{-1}. Hence, during the wave period of 25 s the solar wind moves about 13×10^3 km. A newborn cometary ion is accelerated to a speed of 110 km s^{-1}, mostly in $-z$-direction, and passed distances of 1386 km s^{-1} according to the single-particle-motion model presented in Section (3.1). In contrast to

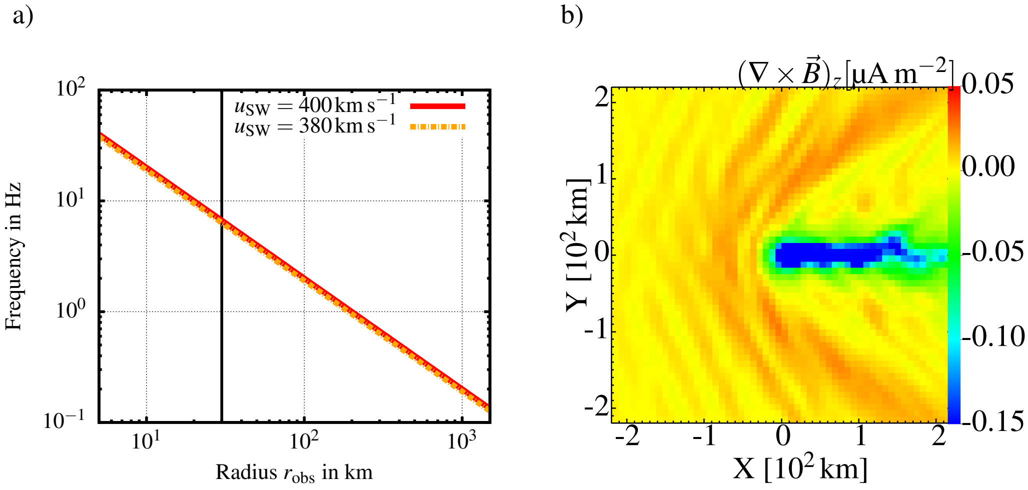

Figure 3.18: The left panel shows the frequencies excited by an obstacle with the radius r_{obs} embedded in a plasma flow with the velocity u_{sw}. The vertical black line highlights the radius of $r_{\mathrm{obs}} = 30\,\mathrm{km}$. The right panel shows the z-component of the current density, which is obtained from *Simulation B*. The most intense current is located in the direct vicinity of the centre of the ionisation cloud. Within a radius of about 30 km on the dayside the current density has a strong negative z-component, which dominates the current density vector. At larger distances, the direction of the current density oscillates in space as well as in time (Figure 3.11).

this high velocity, in the comet frame, the phase fronts upstream of the comet are nearly resting. The resulting wavelength of about 65 km is much smaller than the characteristic scales of the ion motion.

The simple presence of an obstacle like a planet, an asteroid or a comet within a flow can lead to an excitation of waves. The maximum frequency in the comet frame caused by the flow can be estimated by the Doppler shift

$$\omega_{(\mathrm{co})} = \omega_{(\mathrm{sw})} + k u_{\mathrm{sw}} \,, \tag{3.19}$$

where $\omega_{(\mathrm{co})}$ and $\omega_{(\mathrm{sw})}$ denote the frequency in the comet frame and in the solar wind frame, respectively. If the position of the obstacle is fixed, the latter frequency is zero. Hence, the only excitation is triggered by the flow passing the obstacle. Consequently, the wavenumber is expressed by

$$k = \frac{2\pi}{\lambda} = \frac{\pi}{r_{\mathrm{obs}}} \,. \tag{3.20}$$

λ is the wavelength and it is equal to the diameter of the obstacle. The radius is labelled r_{obs}. The frequency in the comet frame is given by (Thompson et al. 1996)

$$f_{(\mathrm{co})} = \frac{u_{\mathrm{sw}}}{2 r_{\mathrm{obs}}} \,. \tag{3.21}$$

Figure (3.18 a) shows this frequency versus the radius of the obstacle. It follows that an obstacle with a radius of about 5×10^3 km is required in order to excite waves with a frequency of about 35 mHz. Since the simulation box has only a length of about 1750 km, the waves observed in the simulation are not caused by an obstacle of that size.

Besides others, a current system can act as an obstacle for the flow (i.e. Thompson et al. 1996). The main current system in the presented hybrid simulation is located within a radius of 30 km to the comet (Figure 3.18 b). Thus, this effect cannot explain the presence of waves with a frequency of about 35 mHz in the simulation. Moveover, the current system can excite waves with a frequency of a about 6.7 Hz. Interestingly, the spectra of the magnetic field reveal a small and broad enhancement at this frequency. At higher frequencies the spectral power density drops sharply. However, this peak could also be caused by the smoothing of the electromagnetic fields in the simulations, which acts as a low-pass filter.

Triggered by the observed magnetic field fluctuations during the Galileo flyby at the asteroids Gaspra and Ida (Kivelson et al. 1993), the case of magnetised asteroids in the solar wind have been intensively discussed by various authors. Since the highest frequencies which can be excited by the asteroid are above the solar wind proton gyrofrequency, as discussed above, the various studies predicts the presence of whistler wings in the environment of an asteroid (Gurnett 1995b, Baumgártel et al. 1994, Baumgärtel et al. 1997, Omidi 2002, Blanco-Cano et al. 2003, Omidi et al. 2004). However, Blanco-Cano et al. (2003) conclude that the magnetic field fluctuations observed at the asteroids Gaspra and Ida were not caused by a magnetised asteroid. Moveover, the flybys at asteroids Braille (Richter et al. 2001), Steins (Auster et al. 2010) and Lutetia (Richter et al. 2012) do not reveal the presence of whistler waves. Thus, no observation at an asteroid can verify the presence of the predicted whistler wing.

Nevertheless, the structure of the whistler wings in previous studies have a similar appearance as those structures visible in the cometary simulations. The wavelengths of the observed structures are below an ion inertia length. In the presented scenario the ion inertia length in the undisturbed solar wind is about 194 km. Using a Hall-MHD model, Baumgärtel et al. (1997) found a regular pattern with wavelengths below one ion inertia length. Gurnett (1995b) estimated the wavelength in the whistler wing on the basis of the Cerenkov-condition to be

$$\lambda_\mathrm{c} = 2\pi \frac{\Omega_\mathrm{gyr,e} c^2}{\omega_\mathrm{p,e}^2 u_\mathrm{sw}} , \tag{3.22}$$

where $\Omega_\mathrm{gyr,e}$ and $\omega_\mathrm{p,e}$ denote the gyrofrequency and the plasma frequency of the electrons. c is the speed of light. $\omega_\mathrm{gyr,e}/\omega_\mathrm{p,e}^2$ is independent of the electron mass. And as shown by Simon (2004) and Müller et al. (2011), both versions, the A.I.K.E.F. code and its predecessor, are able to describe the propagation of whistler waves as long as electron damping is not important, i.e. $\omega < \Omega_\mathrm{gyr,e}$. Using Equation (3.22) for the parameters at *Point B*, the whistler wing wavelength is about 112 km. Thus, it is similar to the wavelength observed but not equal. However, in contrast to the asteroid scenario, the cometary plasma environment is inhomogeneous, which probably changes the properties of the wave. Another similarity of the observed structures to the whistler wings at asteroids is given by the accessible area, i.e. the area which can be influenced by the wave. Gurnett (1995b) showed that in case of a perpendicular orientation of the magnetic field to the flow velocity, the wing structure is confined to two wedge-shaped surfaces oriented along the magnetic field (see Figure 7 in Gurnett (1995b)). Furthermore, in the perpendicular case, the whistler wing can only access regions downstream of the comet. This changes in the case of an oblique configuration, as also predicted by Baumgärtel et al. (1997). The same behaviour can be found in the comet scenario. Firstly, the phase fronts can only spread out in the plane which contains the magnetic field since no phase fronts are present on the $+z$-hemisphere (Figure 3.8 a). The phase fronts on the $-z$-hemisphere are probably triggered by the presence of the cometary ion tail, since the phase fronts have the same opening angle to the x-axis on both y-hemispheres. Secondly, the accessible areas are comparable to each other: although the wave pattern starts upstream of the centre of the ion cloud in *Simulation B*, the waves do not propagate upstream. This is demonstrated by *Simulation C* in which the ionisation area is restricted to a sphere with a radius of 200 km. In this simulation no waves are upstream of this region (Figure 3.9 e and f). In addition, by changing the orientation of the magnetic field, the phase fronts react as shown in Figure (3.17). As a result, the wave pattern is present in regions further upstream than in the perpendicular case. Furthermore, due to this change the wavelength changes, as well, similar to the whistler wings in the simulations of Baumgärtel et al. (1997).

In contradiction to the asteroid simulations, the comet is not modelled with a magnetic moment. As shown by Thompson et al. (1996), a whistler wing can also be triggered by a current source. Consequently, the current system in the cometary scenario can also trigger a whistler wing. (Figure 3.18 b). But, neither Baumgärtel et al. (1997), Gurnett (1995a) nor Thompson et al. (1996) comment on time varying effects. However, in the cometary scenario these time varying effects are present since a frequency can be obtained. Thus, it remains unclear if the whistler wings in the asteroid scenario are time varying or if this is a feature of cometary interaction, which could be triggered by the moving cometary ions.

Although the solar wind density is constant, a large variation in the cometary ion density is present. This is remarkable since the solar wind protons are much lighter than the cometary ions. However, since the solar wind passes the distance between two phase fronts within about 0.13 s, it cannot react on the phase fronts. Whereas the cometary ions have only a speed of about $10\,\mathrm{km\,s^{-1}}$ to $50\,\mathrm{km\,s^{-1}}$ into $-z$-direction in the inner region. In addition, the ion motion is along the phase fronts in $-z$-direction. This is why, the cometary ion can react better on the electric field fluctuations.

Gary (1993) reported that whistler waves, which propagate oblique to the magnetic field, have a longitudinal electric field. The time series obtained at *Point B* (Figure 3.11) reveals that the electric field is linearly polarised (Ratio of Eigenvalues: 102:2:1) and the direction of the maximum variance is $\vec{k}_{\vec{E},\max} = (0.79, 0.61, -0.08)$. This vector deviates from the wave propagation direction by only 5°. Thus, a strong longitudinal electric field is present in the simulation. A longitudinal electric field can also affect the particle motions, which leads to density enhancements. In contrast to the electric field, the current density is circularly or elliptically polarised, since the ratios of the MVA of the current density at *Point B* are 95:39:1. This proves that the Hall conductivities are important.

In general, one finds a good agreement of the observed structures with the whistler wing observed at asteroids or the whistler wave. However, an oscillation or movement of the position of the phase fronts has never been observed so far. In contrast to the asteroid scenario, the cometary ions in the comet scenario will modify the plasma. For example, the density fluctuations of the cometary ions leads to different wave propagation properties. As a consequence, the whistler wing probably becomes unstable and phase fronts move towards the tail (Figure 3.16). This hypothesis has to be proved in further simulations.

3.4 Summary and Outlook

The aim of this chapter was the investigation of the weakly active cometary plasma interaction. This interaction regime is characterised by the small gas production rate, hence, the comet does not trigger the boundaries which have been found during the past cometary flybys.

In a first step a comparison of the hybrid model to a single-particle motion model and the new multifluid MHD model of Rubin et al. (2014a) was conducted. It was found that the motion of the cometary ions in the hybrid model is consistent with the single-particle model. Thus, the cometary ions are picked-up and perform a cycloidal motion with spatial dimensions according to their large gyroradius. This motion is responsible for the creation of the pick-up ion tail. Meanwhile, fast magnetosonic waves are excited in the solar wind by the presence of the cometary ions, which deflect the solar wind. These waves lead to the formation of standing phase fronts, so called Mach cones. For the first time, a repetitive Mach cone structure, a series of Mach cones along the pick-up ion tail, was found in the comparison to the multifluid MHD model. In the results of the latter model traces of these repetitive Mach cones can be found. Hence, the hybrid model is outstanding in describing the cometary plasma environment on these large scales.

The interaction region close to the comet, i.e. on relevant scales for the Rosetta mission, is dominated by cometary pick-up tail. Hence, close to the comet, the pick-up of newborn cometary ions leads to a perpendicular motion, as predicted by the hybrid simulation. In addition, the footpoint of the Mach cones, i.e. the deflection of the solar wind, is also a dominant structure in the vicinity of the comet. The hybrid simulations further suggest the formation of a small anti-sunward cometary ion tail, which is caused by the draping of the magnetic field. Furthermore, the hybrid simulations conducted for this thesis for the first time suggest the presence of waves with short wavelengths and frequencies in the order of the proton gyrofrequency. A first analysis leads to the conclusion that these waves are whistler waves, but a finial proof has to be made.

Although this work focusses on the predictions of the cometary plasma interaction, a first, coarse comparison to real data and the A.I.K.E.F. simulations has been done. In Figure (3.19) two spectra from RPC-MAG observations are shown. The first spectrum was obtained from data recorded on 13th June 2014 between 12:00 and 15:00 UTC. During this interval, Rosetta was in the approach phase to the comet but still 291×10^3 km away from the comet. Thus, the spacecraft was located in the undisturbed solar wind. The spectrum shows an exponential decay, which indicates a turbulent solar wind. The second spectrum is based on data from 15th August 2014 between 14:00 and 16:00 UTC, when the spacecraft was at a distance of about 90 km to the nucleus. In this spectrum, the exponential decay is interrupted by a clear spectral enhancement in the range from 20 mHz to 80 mHz. This is caused by a quasi-harmonic wave which RPC-MAG has continuously been observing since August.

Additionally, the figure shows a spectrum of the simulation presented in Section (3.3). In the simulation the comet has a gas production rate of $8 \times 10^{25}\,\mathrm{s}^{-1}$ and is about 2.7 AU away from the Sun. This, most likely, differs from the situation on 15th August 2014, when the comet was still 3.5 AU away from the Sun. However, the A.I.K.E.F. simulation spectrum also reveals an increase at a frequency of about 39 mHz, which is very close to the measured peak.

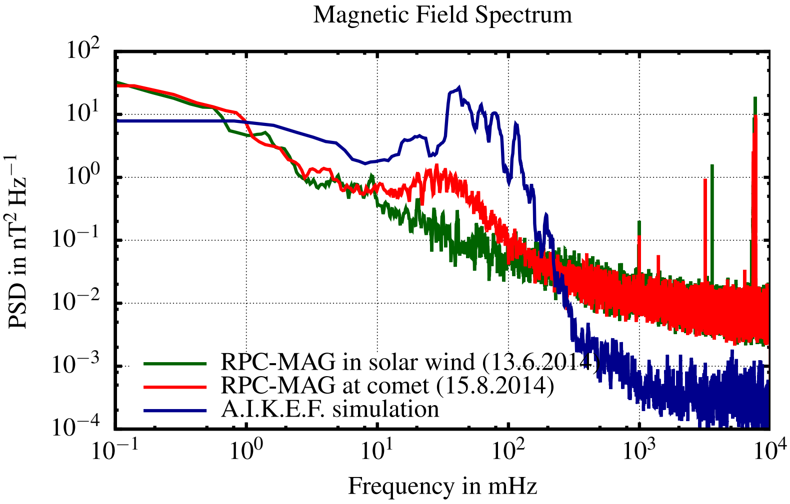

Figure 3.19: A comparison of the power spectral densities of data measured by RPC-MAG and the simulation presented above. The green line shows the power spectral density of data measured by the outboard magnetometer in burst mode on 13th June 2014 between 12:00 and 15:00 UTC. At this time, the spacecraft was located in the undisturbed solar wind, about 291×10^3 km away from the nucleus. The blue line shows the same for data gained on 15th August 2014 between 14:00 and 16:00 UTC, when the distance between Rosetta and the nucleus was below 100 km. The spikes in the spectra at frequencies of 1 Hz and greater are disturbances originated in the reaction wheels. In the spectra measured in August, a clear spectral enhancement is visible in the frequency range from 20 mHz to 80 mHz, with a broad peak around 30 mHz. As discussed above, the A.I.K.E.F. simulation reveals a peak at 39 mHz.

4 The Strongly Active Phase - Close to the Perihelion [1]

In the previous chapter the plasma environment of a weakly active comet was discussed in great detail. A key feature of the Rosetta mission is the escort of the comet along its journey around the Sun. By that, the distance to the central star is reduced steadily down to 1.24 AU and the insolation rises. As a consequence, the gas production rate increases and the character of the plasma interaction changes.

It was predicted by Hansen et al. (2007) that the interaction at 67P/Churyumov-Gerasimenko close to the perihelion will be similar to the interactions at the comets which have already been visited in the past. Thus, one expects structures like the bow shock, the diamagnetic cavity and an anti-sunward plasma tail, as described briefly in Section (1.2). In this case, the results of a single-fluid MHD simulation model are more trustworthy than MHD simulations at larger heliocentric distances with lower activity. However, previous hybrid simulations by Bagdonat (2004) and Gortsas (2010) were not able to verify the results of the MHD simulation qualitatively and quantitatively. For example, the single fluid simulations by Hansen et al. (2007) predict a stand-off distance of the diamagnetic cavity of about 40 km at 1.3 AU. Nonetheless, the former hybrid simulations had a mesh resolution of at least this size or even much larger. Hence, by construction those simulations were not able to study the physics in the innermost coma. In addition, the former hybrid simulations neglected the massloading of the solar wind upstream of the simulation box as described in Section (2.5.3.1). By that, a quantitative comparison of the bow shock stand-off position is inappropriate since numerical parameter have an non-negligible impact on the bow shock position. Moreover, the previous hybrid simulations only take photoionisation and a neutral drag force into account. But, as found by various authors (Cravens 1989, Gombosi et al. 1996), the recombination of ions plays an important role in the innermost cavity.

The focus of this chapter is to address the qualitative and quantitative comparison of the hybrid simulations and the MHD simulations and to discuss the differences physi-

---

[1] Major parts of the following chapter have been published before the submission of this thesis. The texts and figures are reprinted with permission from Elsevier. The publications can be found under the following references:

- **Koenders, C.**, Glassmeier, K.-H., Richter, I., Motschmann, U., Rubin, M., 2013, Revisiting cometary bow shock positions, Planetary and Space Science, 87, 85–95, ISSN 00320633
- **Koenders, C.**, Glassmeier, K.-H., Richter, I., Ranocha, H., Motschmann, U., 2015, Dynamical Features and Spatial Structures of the Plasma Interaction Region of 67P/Churyumov-Gerasimenko and the Solar Wind, Planetary and Space Science, 105, 101–116, ISSN 00320633

cally. This is possible since the important processes, like for example photo-ionisation, ion-neutral collisions, charge exchange and recombination have been newly implemented to the hybrid model or were reworked to a great extend. Furthermore, the use of the extended upstream boundary model and the extensive study of the influence of numerical parameters allows a quantitative comparison of all structures. Based on these features, the present work is able to resolve the innermost region of strongly active comets sufficiently in a hybrid model for the first time ever. Thus, in contrast to all previous models, kinetic effects on boundaries and structures and their position can be investigated. In addition, this study allows us to review the hybrid model and increase its validity for the planning of the Rosetta mission.

4.1 The Position of the Bow Shock

As discussed in great detail in the previous chapter, in case of perpendicular orientation of the IMF to the solar wind velocity vector, the newborn cometary ions are picked-up by the impinging solar wind and the interplanetary magnetic field. This process leads to the acceleration of the cometary ions and, by that, the solar wind has to be decelerated in order to fulfil momentum and energy conservation requirements.

At weak activity levels, the deceleration is only small and a Mach cone is imprinted to the solar wind. During the mission phase the activity of the comet will increase and, by that, the deceleration increases. At a certain point, the deceleration exceeds a critical value which manifested in the presence of the bow shock, where the solar wind reaches subsonic speeds.

The cometary bow shock has already been observed at different comets by previous spacecraft missions (cf. Neubauer et al., 1986, Neubauer et al., 1993, Richter et al., 2011 or Smith et al., 1986a), but predictions of the location differ depending on the model used. For example, the model by Biermann et al. (1967), hereafter also named the Biermann model, predicts a subsolar stand-off distance at comet 67P/Churyumov-Gerasimenko of about 5000 km at 1.3 AU (see Table 4.1). In contrast, the model by Gortsas (2010) only calculated a distance of 1610 km for the same comet while Hansen et al. (2007) reported a distance of about 3500 km in their 3D MHD simulations. The A.I.K.E.F. code predicts a bow shock stand-off distance of about 2000 km.

To understand the origin of these differences, it is necessary that the used models are revisited to provide a best-effort approach for the mission planning. Furthermore, a model which is able to describe the differences in the bow shock positions between the fluid approaches and the hybrid simulations is presented in this section. Firstly, an overview of some models which allow the calculations of the bow shock position will be given and revisited (Sections 4.1.1,4.1.2, 4.1.3 and 4.1.4). This is followed by Section (4.1.5), in which a comparison of the different model's results is drawn and their behaviour in case of the variation of important parameters will be shown. Additionally, the hybrid based model, which gives us a physical explanation of the behaviour of the bow shock position in the hybrid simulations, is also described in that section. Finally, an outlook on the bow shock position during the Rosetta mission will be presented.

4.1.1 The Biermann Model

The first model of the interaction between the solar wind and comets was proposed by Biermann et al. (1967). As already described in Section (2.4.2.1), it describes the interaction with a one-dimensional inviscid gas dynamic flow, which implies that no magnetic field effects are taken into account. The authors also assume a stationary situation in front of the bow shock and an ideal gas as a medium. Furthermore, the model treats newly ionised cometary ions in such a way that instantly after their ionisation the ions have the same bulk velocity as the ambient solar wind. The model by Biermann et al. (1967) describes the comet only as a source of mass M_{src} which adds mass to the solar wind flow and, thus, increases the mass density ρ of the flow whilst approaching the comet.

Based on the assumption of this model and every other single-fluid type model, a description of the pick-up process, as discussed in great detail in Chapter (3), is not possible. Thus, the fluid models assume that the newborn cometary ions have the same velocity as the ambient plasma immediately after the ionisation.

As discussed in Section (2.4.2.1) the following equation for the flow velocity can be deduced

$$u_x = \frac{1}{2\left(f+1\right)\left(\int_{-\infty}^{x} M_{\mathrm{src}} dx' + \rho_\infty u_\infty\right)} \cdot \Big[\left(f+2\right)\rho_\infty u_\infty^2 + \sqrt{\left(f+2\right)^2 \rho_\infty^2 u_\infty^4 - 4\left(f+1\right)\left(\int_{-\infty}^{x} M_{\mathrm{src}} dx' + \rho_\infty u_\infty\right)\rho_\infty u_\infty^3}\,\Big] \tag{4.1}$$

and has to be solved to obtain the deceleration of the plasma in front of the bow shock. In this way, the remaining quantities, such as the density or the pressure, can easily be computed (Section 2.4.2.1). In the equation f denotes the number of degrees of freedom of the ideal gas. This leads to $\gamma = \left(f+2\right)/f$, the ratio of specific heats. Initially, Biermann et al. (1967) chose a value of $\gamma = 2$ assuming only the motional degrees of freedom of a particle gyrating around the magnetic field.

In the model, the undisturbed solar wind approaches the comet. During the approach a small amount of mass is continuously added to the flow. Consequently, the mass density increases and the velocity decreases, as shown in Figure (2.6). In addition, the Mach number of the flow decreases as well.

In the discussed scenario the solution for the flow velocity becomes complex at a distance of about 3300 km upstream of the nucleus. By that also the expressions for the mass density and the pressure get an imaginary component. This is why the graphs stop at this distance. This position can be obtained by discussing the square root in Equation (4.1). If the radicand is positive, a real solution exists. In the opposite case, an imaginary part occurs. Hence, the case in which the radiand is zero is critical since it describes the maximum mass flux density of the flow:

$$\left(\rho u_{\mathrm{x}}\right)^{*}_{\mathrm{crit}} = \frac{\left(\int_{-\infty}^{x} M_{\mathrm{src}} dx' + \rho_\infty u_\infty\right)}{\rho_\infty u_\infty} = \frac{\left(f+2\right)^2}{4\left(f+1\right)} = \frac{\gamma^2}{\gamma^2 - 1}\,, \tag{4.2}$$

where $\left(\rho u_{\mathrm{x}}\right)^{*}_{\mathrm{crit}}$ denotes the normalised critical mass flux density.

Reaching this point, a stationary solution of the model does not exist anymore and the velocity of the flow becomes equal to the sonic speed. Biermann et al. (1967) reported that a shock will develop in a real flow in front of this point, which will generate a divergence of the flow and, thus, allows further mass loading. These effects cannot be described by the Biermann model, nevertheless, the model allows to calculate the position of the shock. This can be done for comet 67P/Churyumov-Gerasimenko using the mass continuity, Equation (2.54), and determining the position where the critical mass flux density is reached, which leads to the general equation:

$$(\rho u_{\mathrm{x}})^*_{\mathrm{crit}} = \frac{1}{\rho_\infty u_\infty} \int_{-\infty}^{R_{\mathrm{BS}}} M_{\mathrm{src}} dx' + 1 \; . \tag{4.3}$$

R_{BS} denotes the position of the cometary bow shock. In case of the weakly outgassing comet 67P/Churyumov-Gerasimenko, the mass source given in Equation (2.6) can be used. By that the position is determined by (cf. Galeev et al. 1985)

$$R_{\mathrm{BS,Biermann}} = \frac{\nu Q m_{\mathrm{i}}}{4\pi u_{\mathrm{ng}} n_\infty m_\infty u_\infty \left((\rho u_{\mathrm{x}})^*_{\mathrm{crit}} - 1\right)} \; . \tag{4.4}$$

$R_{\mathrm{BS,Biermann}}$ denotes the stand-off distance of the bow shock in the Biermann model.

It shall be noted that the total number of cometary ions, which are generated in the interaction region per second is Q. However, an integration from the nucleus to infinity over the $1/r^2$ ionisation profile violates this statement. Hence, the limits of the interaction region have to be determined by a given mass source profile. The lower limit is given by the radius of the nucleus R_{nucleus}. Due to this and the used mass source profile, the upper limit should be $R_{\mathrm{max}} = u_{\mathrm{ng}}/\nu + R_{\mathrm{nucleus}}$. This has an impact on the position of the bow shock :

$$R_{\mathrm{BS,Biermann,mod}} = \frac{\nu Q m_{\mathrm{i}}}{4\pi u_{\mathrm{ng}} n_\infty m_\infty u_\infty \left((\rho u_{\mathrm{x}})^*_{\mathrm{crit}} - 1 + A\right)} \; , \tag{4.5}$$

where $A = \nu Q m_{\mathrm{i}} / \left(4\pi u_{\mathrm{ng}} n_\infty m_\infty u_\infty \left(u_{\mathrm{ng}}/\nu + R_{\mathrm{nucleus}}\right)\right)$. Regarding 67P/Churyumov-Gerasimenko at 1.3 AU (Table 4.1), A would be in the order of 10^{-3} when using $\gamma = 2$. This means that the bow shock position would shift from 4972 km to 4957 km. This difference can be neglected due to uncertainties in other quantities, as for example the gas production rate. Hence, this work uses $R_{\mathrm{max}} = \infty$ for simplicity reasons as the upper limit of the integration, similar to Galeev et al. (1985).

4.1.2 Flammer's Magnetohydrodynamic Approach

Flammer and Mendis (1991) and Schmidt et al. (1993) extended the fluid model by Biermann et al. (1967) to a one-dimensional MHD model (hereafter named the Flammer model) by adding a thermal pressure in the undisturbed solar wind and a finite magnetic field to the flow. This is oriented perpendicular to the solar wind velocity. Similar to the last section, the basic set of equations of this model can be deduced from the generalised 1D single fluid model presented in Section (2.4.2.1). Based on the assumption, the following equation for the flow velocity has to be solved:

$$\begin{aligned}0 = &\frac{1}{2}(f+1)\left(\int_{-\infty}^{x} M_{\mathrm{src}}dx' + \rho_\infty u_\infty\right)u_x^3\\ &-\frac{1}{2}(f+2)P_\infty u_x^2\\ &+E_\infty u_\infty u_x\\ &+\frac{1}{2}(f-2)\,p_{\mathrm{m},\infty}u_\infty^2\,.\end{aligned} \tag{4.6}$$

In case of $f = 2$, the equation is reduced to a quadratic equation, which can be treated as in the model by Biermann et al. (1967). Similar to the Biermann model, one can identify a critical mass flux density at which the solution of the velocity becomes complex. In comparison to the Biermann model, the critical mass flux density does not only depend on the ratio of specific heats but also on the dynamic pressure, the magnetic pressure and the thermal pressure in the undisturbed solar wind. In case of $f > 2$, the cubic equation leads to three solutions. The important solution for this study is the one which has a normalised velocity $u_{\mathrm{x}}^* = 1$ in the undisturbed solar wind. The two others have different values and can be ignored. Again, a critical mass flux density can be identified, which depends on the ratio of specific heats, the dynamic pressure, the magnetic pressure and the thermal pressure in the undisturbed solar wind. Figure (4.1) shows the behaviour of the critical mass flux density for $f = 2$ and $f = 3$ cases when varying the magnetic field strength.

In case of a vanishing magnetic field and a vanishing thermal pressure in the undisturbed solar wind, the results of the Flammer model are in agreement with the critical mass flux density of the Biermann model. For a non-vanishing magnetic field in the solar wind, the critical mass flux density decreases. This implies that the flow can transport less cometary mass before the bow shock occurs. Hence, the distance between the bow shock and the cometary nucleus increases. This behaviour can be explained with the reaction of the pressures on the flow. The injection of mass into the flow decreases the velocity, which again increases the magnetic field strength due to the frozen-in assumption. The higher magnetic pressure acts on the incoming flow and further reduces the velocity. A similar behaviour can be observed in case of an increasing temperature.

In the same way as in the model by Biermann et al. (1967), the position of the bow shock can be obtained by using the mass continuity, Equation (2.54), and with the information that the mass flux density is critical at the bow shock position. Respectively, the position at weakly active comets can be described by

$$R_{BS,Flammer} = \frac{\nu Q m_{\mathrm{i}}}{4\pi u_{\mathrm{ng}} n_\infty m_\infty u_\infty \left((\rho u_{\mathrm{x}})^*_{\mathrm{crit,Flammer}} - 1\right)}\,. \tag{4.7}$$

However, as reported above, the critical mass flux density within the Flammer model is a function of $p_{\mathrm{r},\infty}$, $p_{\mathrm{t},\infty}$, $p_{\mathrm{m},\infty}$ and f. This leads to bow shock positions different to those obtained by the the Biermann model.

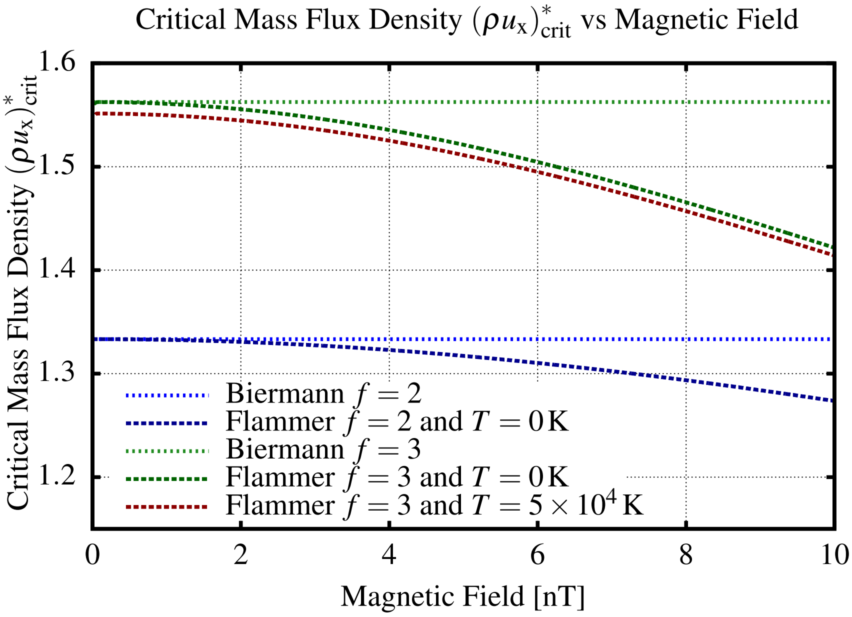

Figure 4.1: The critical mass flux density at different strengths of the interplanetary magnetic field. The blue and green dotted lines show the critical mass flux density based on the model by Biermann et al. (1967) with $f = 2$ and $f = 3$. In addition, the blue and green dashed lines show this entity based on the model by Flammer and Mendis (1991) with $f = 2$ and $f = 3$. Additionally, a case with $f = 3$ and a temperature of $T = 5 \times 10^4\,\mathrm{K}$ is plotted with a dark-red dashed line.

4.1.3 3D MHD Simulations

Besides these one-dimensional analytical models, this study also considers results of more complex 3D magnetohydrodynamic (MHD) numerical simulations by the BATS-R-US code. The BATS-R-US (Block Adaptive Tree Solarwind Roe-Type Upwind Scheme), which is part of the Space Weather Modeling Framework (Tóth et al. 2012). The basic equations are given in Section (2.4.2) but a detailed description of this model can be found in Gombosi et al. (1996) and Hansen et al. (2007). Based on the 3D simulation box, this model is able to describe the divergence of the flow and, therefore, allows the description of the bow shock wave and the region closer to the nucleus. This is beyond the models by Biermann et al. (1967) and Flammer and Mendis (1991). Additionally to the mass loading of the flow, the BATS-R-US code can describe several other effects such as recombination and charge exchange. Furthermore, the BATS-R-US code uses additional sources and sinks for the mass as well as momentum and energy equations. Consequently, this code uses a slightly different mass source than the other models in this study. But these differences in sources and sinks can be neglected at distances far away from the comet. Hansen et al. (2007) have applied the BATS-R-US code to 67P/-Churyumov-Gerasimenko and the simulation reveals a bow shock distance of 3500 km at 1.3 AU.

Quantity	**Value**
gas production rate Q	$5 \times 10^{27}\,\mathrm{s}^{-1}$
cometary ion mass m_i	$17\,\mathrm{amu}$
ionisation rate ν	$5.88\,\mathrm{s}^{-1}$
neutral gas velocity u_ng	$1\,\mathrm{km\,s}^{-1}$
solar wind number density n_{sw}	$6\,\mathrm{cm}^{-3}$
solar wind velocity u_{sw}	$400\,\mathrm{km\,s}^{-1}$
strength of interplanetary magnetic field B_{IMF}	$4.9\,\mathrm{nT}$
Parker angle θ	90°

Table 4.1: Characteristic parameters of the plasma interaction between comet 67P/Churyumov-Gerasimenko and the solar wind at 1.3 AU (Hansen et al. 2007). For a better comparability, the Parker angle is set to $\theta = 90^\circ$.

4.1.4 The Hybrid Model and the A.I.K.E.F. Code

The hybrid model and the A.I.K.E.F. code have already been described in great detail in Section (2.5.1). In this study, an adiabatic electron pressure is used. Furthermore, only photoionisation and an ion neutral drag are considered. However, the latter process has nearly no influence on the bow shock position since the neutral gas density is very small at large distances.

The results of a hybrid plasma simulation of comet 67P/Churyumov-Gerasimenko at 1.3 AU, simulated with the used code version, are presented in Figure (4.2). This simulation uses a hierarchical mesh with a minimum spatial resolution of $\Delta x_\mathrm{min} = 77\,\mathrm{km}$, which is doubled within a sphere with a radius of about 2500 km. Within a sphere with a radius of about 1000 km, the resolution increases to $\Delta x_\mathrm{max} = 19\,\mathrm{km}$. These mesh resolutions are chosen in order to save computational resources but, nevertheless, they resolve all major structures like the cometary bow shock, the magnetic pile-up and the diamagnetic cavity. The physical parameters for the scenario at 1.3 AU are the same as the ones used by Hansen et al. (2007). They are listed in Table (4.1), except for the Parker angle, which is 52° for this simulation. In the different panels one can identify the bow shock, the magnetic pile-up region, the diamagnetic cavity and the ion tail. A detailed discussion of the structures and boundaries in the innermost coma is given in Section (4.2). The focus of the current section is the bow shock position.

4.1.5 Discussion

As a basis of this study, a default parameter set is chosen which denotes the characteristic conditions at a heliocentric distance of about 1.3 AU. These parameters are similar to those used by Hansen et al. (2007), except for the Parker angle (Table 4.1). Since the Biermann model and the Flammer model are only valid for perpendicular magnetic fields, a Parker angle of 90° is chosen for reasons of comparability of the different models.

All hybrid simulations used for this comparison have a constant spatial mesh resolution of about $\Delta x = 77\,\mathrm{km}$ at the position of the bow shock and therefore can resolve the shock properly. In order to determine the subsolar stand-off position of the bow shock from

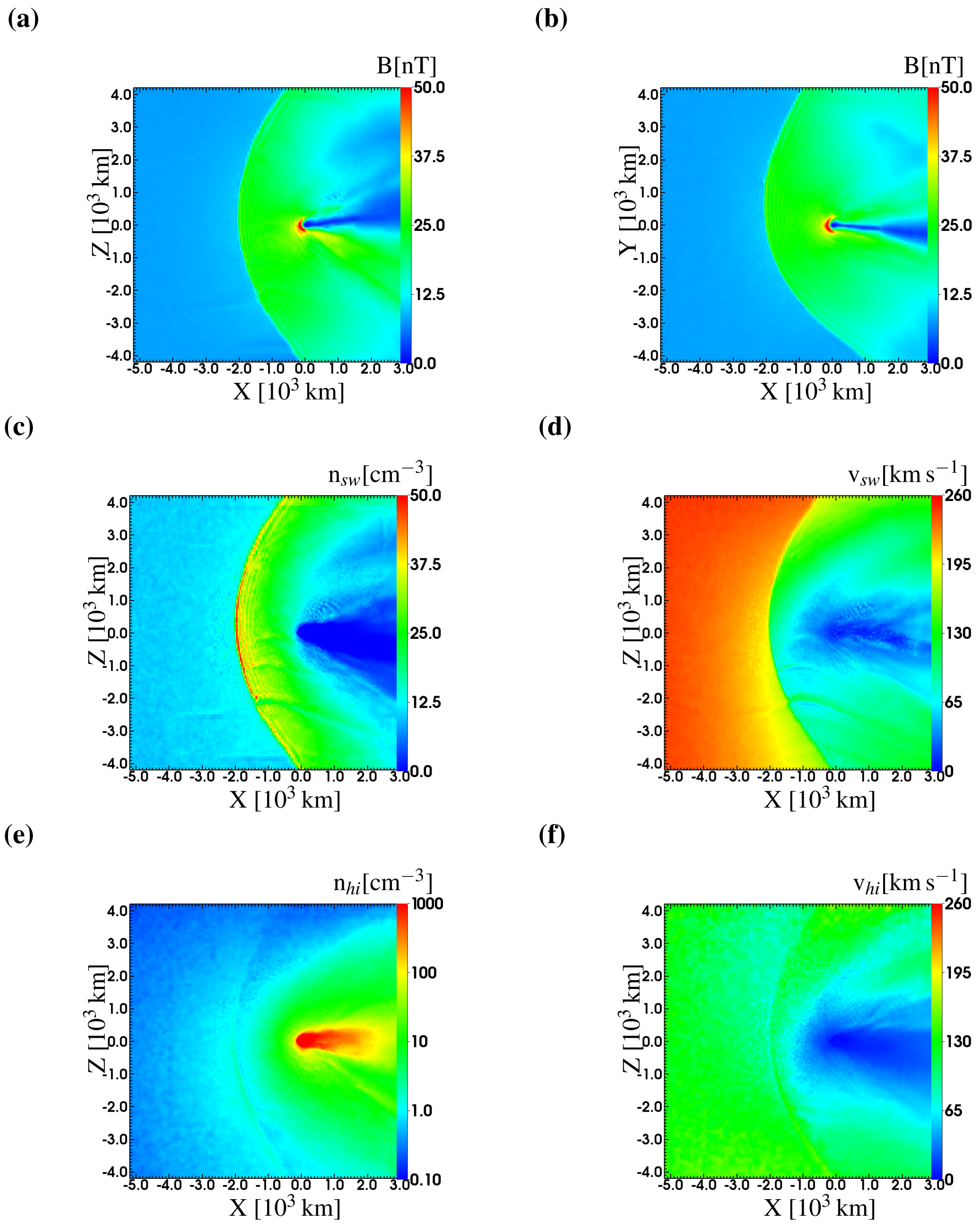

Figure 4.2: The figures show the result of a hybrid plasma simulation of the interaction of comet 67P/Churyumov-Gerasimenko at 1.3 AU. The parameters of the simulation are equal to the values used by Hansen et al. (2007) (see Table 4.1, the Parker angle is set to $\theta = 52°$). The solar wind approaches the comet from -x-direction and the IMF is in the (x,y) plane. In (a) and (b) the strength of the magnetic field in the (y=0)-cross section and in the (z=0)-cross section are shown, respectively. The plots (c) and (d) display the density and the velocity of the solar wind protons. The density and the velocity of the cometary ions are presented in (e) and (f). All main features of a the interaction, i.e. the bow shock, the magnetic pile-up region, the diamagnetic cavity and the cometary ion tail, can be observed. This study is focussing on the position of the bow shock at the sub-solar point.

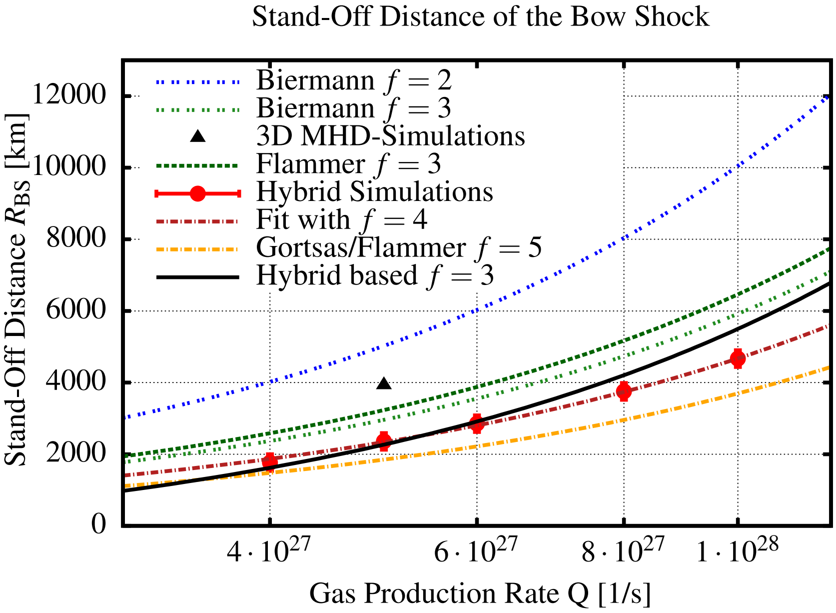

Figure 4.3: The bow shock distance as a function of the gas production rate for the different model approaches. The stand-off distances of the model by Biermann et al. (1967) with $f = 2$ and $f = 3$ are shown using the blue and the green dotted lines. The green dashed line presents the model by Flammer and Mendis (1991) with $f = 3$, where as the dark-red and the yellow dashed dotted lines represent the same model with $f = 4$ and $f = 5$. In addition, the stand-off distances of the bow shock in a 3D MHD simulation and in hybrid simulations are presented using a black triangle and red circles. The hybrid based model is represented by a solid black line.

the simulations, the characteristic jump of the magnetic field at the bow shock is used, which occurs at the same position as the jumps in density, velocity and temperature. This position can be obtained by fitting a $\tanh(x)$ to the magnetic field strength along the x-axis. To avoid errors in the position, an average of the position has been taken over several time steps. The standard deviation for each determined position is below the mesh resolution, since the simulations are quasi-stationary and the bow shock is not moving. However, the numerical mesh and the smoothing of the electric and magnetic fields lead to an uncertainty in the position which can only roughly be estimated by $\Delta R_{\mathrm{BS}} \approx 3\Delta x$ because the jump at the bow shock needs some mesh nodes to change the strengths of the fields.

The results of a first comparison of the different models against a changing of the gas production rate are presented in Figure (4.3). The model by Biermann et al. (1967) is plotted with $f = 2$ (blue dotted line) and $f = 3$ (green dotted line), which corresponds to the critical mass flux densities of $(\rho u_{\mathrm{x}})^{*}_{\mathrm{crit}} = 4/3$ and $(\rho u_{\mathrm{x}})^{*}_{\mathrm{crit}} = 1.56$. In addition the figure shows the model by Flammer and Mendis (1991) with $f = 3$, $f = 4$ and $f = 5$. For $f = 3$ and the chosen parameters the Flammer model, shown in the Figure by a green dashed line, has a constant critical mass flux density of $(\rho u_{\mathrm{x}})^{*}_{\mathrm{crit}} = 1.51$, in contrast to the gas dynamical value $(\rho u_{\mathrm{x}})^{*}_{\mathrm{crit}} = 1.56$, respectively. Thus, the stand-off distance of the bow shock in the Flammer model with $f = 3$ increases faster than that of the Biermann model with $f = 3$. Furthermore, in Figure (4.3) the red circles shows the results of a series of hybrid simulations for this comparison.

Gortsas (2010) reported that the bow shock position in their hybrid simulations fit to the model by Biermann et al. (1967) by using a critical mass flux density of $(\rho u_\mathrm{x})^*_\mathrm{crit} = 2.05$. Since the Flammer model is more suitable than the Biermann model, the result of Gortsas (2010) is applied to the Flammer model and the critical mass flux density of $(\rho u_\mathrm{x})^*_\mathrm{crit} = 2.05$ corresponds to $f = 5.03 \approx 5$ under the chosen parameters of this comparison. This is shown by a yellow dashed-dotted line in Figure (4.3). But Gortsas (2010) also varied the simulation box size in their simulations series close to the heliocentric distances but did neither use the extended upstream boundary conditions, which is explained in Section (2.5.3.1), nor similar modifications. Thus, the size of the simulation box most likely influences the stand-off distance of the bow shock and, therefore, the determined critical mass flux density, too. Based on that, the Flammer model is fitted to the hybrid simulation results presented in this comparison by using the number of degrees of freedom as a fit parameter. The Flammer model fits well to the simulation results if the number of degrees of freedom has a value of $f = 4.01 \approx 4$, which is shown by the dark-red dashed dotted line. This formally corresponds to a critical mass flux density of $(\rho u_\mathrm{x})^*_\mathrm{crit} = 1.71$.

Earlier studies, e.g. the 2D numerical simulations with $f = 2$ by Schmidt and Wegmann (1982), reported that the mass flux density at the bow shock is between 1.17 and 1.23 for different gas production rates. Huddleston et al. (1992a) calculated a critical mass flux density of $(\rho u_\mathrm{x})^*_\mathrm{crit} = 1.21$ for comet Giacobini-Zinner and a value of 1.22 for comet Grigg-Skjellerup, assuming that the solar wind flux is constant. Those results stay in agreement to the Biermann model, which predicts that the bow shock occurs before the critical mass flux density is reached. However, there has been no direct measurement of the subsolar bow shock position up to now. Gombosi et al. (1996) reported that their 3D MHD simulation of a Halley type comet reveals a bow shock position comparable to the measurement by Giotto (Neubauer et al. 1986). Thus, the 3D MHD model is able to describe the position of the bow shock of a comet, as long the kinetic behaviour of the ions is negligible. The bow shock position of the 3D MHD model in this study leads to a critical mass flux density of $(\rho u_\mathrm{x})^*_\mathrm{crit} \approx 1.42$ which corresponds to $f \approx 2.55$. In contrast to Biermann with $f = 2$, the Biermann model with $f = 3$ and the Flammer model with $f = 3$ predict bow shock positions more comparable to the 3D MHD simulation and the hybrid simulations.

The differences between the hybrid simulations and the 3D MHD model by Gombosi et al. (1996) should be mainly caused by the kinetic effects. The relative differences in the bow shock distances between those models decrease if the comet's gas production increases, since the stand-off distance of the bow shock will increase in this case and, as a result, the kinetic effects should become less important. The opposite occurs by using the Flammer model with $f = 4$ and $f = 5$, which results from fits of the model to hybrid simulation results at relatively low gas production rates. Hence, the fit of the Flammer model to the results of the hybrid simulations is inappropriate. A model which describes the bow shock position in the hybrid simulations in a correct way should have three degrees of freedom. Since the ions in hybrid simulations are described as particles without internal degrees of freedom, the number of degrees of freedom of $f = 4$ or $f = 5$ cannot be physically interpreted.

The results of a second comparison are shown in Figure (4.4) displaying changing IMF

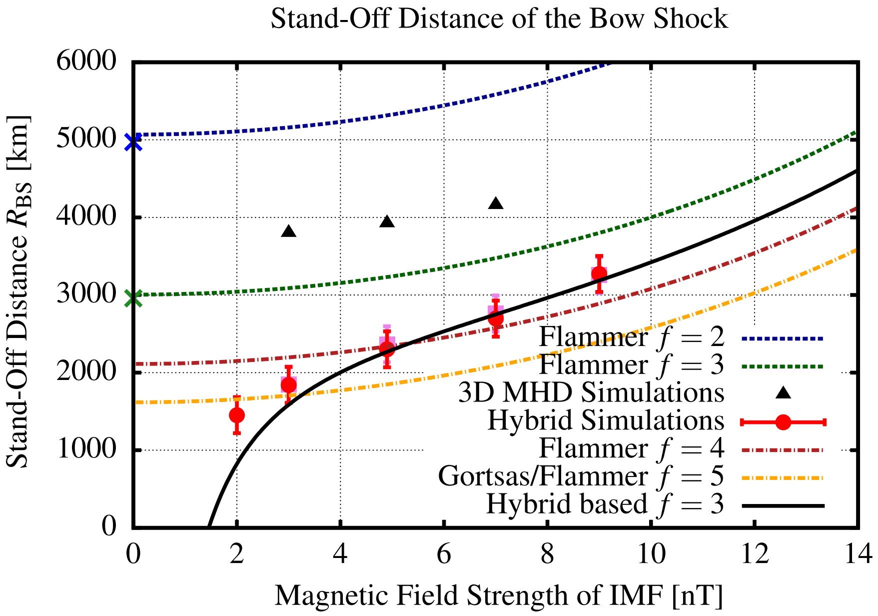

Figure 4.4: The figure shows the results of the comparison of the different models, versus varying IMF strengths. The blue and green crosses at 0 nT represent the results of the Biermann model with $f = 2$ and $f = 3$ and the blue and the green dashed lines the Flammer model with $f = 2$ and $f = 3$. The bow shock position of the Flammer model with $f = 4$ and $f = 5$ is represented by the dark-red and yellow dashed dotted line. The results of a series of 3D MHD simulations are shown with black triangles. The red circles and the purple squares represent the stand-off distances in hybrid simulations with different cut off radii, 8000 km and 11 900 km. The hybrid based model is drawn with a solid black line.

strength conditions. For low magnetic field strengths, the Flammer model transforms into the Biermann model because the critical mass flux density of the Flammer model becomes nearly equal to the Biermann value. Based on this, it is appropriate to put the Biermann model at 0 nT in this figure, marked by a blue and a green X. The small difference between the Biermann model and the Flammer model at 0 nT is based on the finite temperature of the solar wind used in the Flammer model (Figure 4.1). For increasing magnetic field strengths the critical mass flux density in the Flammer model decreases and the stand-off position increases. A similar behaviour can be observed in the results of the 3D MHD simulations, which are marked as black triangles. In contrast to the relatively small increases in the MHD models, the stand-off distances in the hybrid simulations vary to a great extent from 1500 km to 3300 km, which are indicated by red circles and purple boxes.

Although the Flammer model with $f = 4$ fits well to the results of the hybrid simulations with different gas production rates, it does not match the results of the simulations with different IMF strengths. Following Gortsas (2010) this leads to the conclusion that a selection of $f = 4$ or $f = 5$ seems to be arbitrary. This is why a slightly different default value of the magnetic field strength in this study will lead to a different critical mass flux density and a different number of degrees of freedom.

In order to find a model which is able to describe the stand-off distances of the hybrid simulations, an inspection of the assumptions by Biermann et al. (1967) is necessary. The supposition of a one-dimensional flow can be verified if the scales of the motion are compared to each other. The scales perpendicular to the flow direction are given by the cycloidal motion of cometary ions. However, this scale is much smaller than the length of the interaction region in x-direction. A justification for a one-dimensional approach can be seen in similar behaviours of the 3D MHD simulation and the model by Flammer and Mendis (1991). Both models only reveal a small increase in the stand-off distances. The assumption of a stationary flow in front of the bow shock is also fulfilled because strong fluctuations of the bow shock stand-off distance do not occur in the hybrid simulations.

As reported above, the model by Biermann et al. (1967) assumes that cometary ions have the same bulk velocity as the ambient solar wind immediately after their ionisation. This assumption is not justified because the new cometary ions have an initial speed of only $1\,\mathrm{km\,s^{-1}}$ and a finite mass. Thus, it needs a certain amount of time to accelerate the ions to a velocity which is comparable to the solar wind velocity. During this period of time, which is called pick-up time, the ions already move away from their initial position. For example, in a situation of constant background fields, i.e.a constant solar wind velocity and a perpendicular magnetic field, and under the assumption of the single particle motion model, a new cometary ion needs a time of about $\pi/\left(2\Omega_{ci}\right)$ to reach the solar wind speed u_{sw}, where Ω_{ci} is the gyrofrequency of the cometary ions. During this time the ion covers a distance of about $u_{sw}\left(\pi/2-1\right)/\Omega_{ci}$. For the solar wind conditions used in this comparison, this length is about 8000 km. Thus, in case of a weakly outgassing comet, this length is important since the distance of the bow shock to the nucleus is smaller than or comparable to this length. The same is even more true if the magnetic field is not perpendicularly oriented. In this case the time of the incorporation of the cometary ions into the flow is longer, and based on that the bow shock stand-off distance is smaller. Furthermore, the treatment of the flow as a fluid might be inappropriate during this pick-up time because the velocity of the new cometary ions is not comparable to the velocity of the ambient solar wind.

Based on these considerations a fluid approach only seems reasonable if a modified mass source is used: The new cometary ion, being ionised at a certain position r, is incorporated into the flow after the pick-up time when the velocities are comparable. But at this time the ion is at a position $r-R_{\mathrm{shift}}$, where R_{shift} is the distance which is caused by this pick-up time. Therefore, the modified mass source is

$$M_{\mathrm{s}}=\frac{\nu Q m_{\mathrm{i}}}{4\pi u_{\mathrm{ng}}}\frac{1}{\left(r+R_{\mathrm{shift}}\right)^{2}}\,. \tag{4.8}$$

This modification leads to a modified bow shock position

$$R_{BS,Hybrid}=\frac{\nu Q m_{\mathrm{i}}}{4\pi u_{\mathrm{ng}} n_{\infty} m_{\infty} u_{\infty}\left(\left(\rho u_{\mathrm{x}}\right)^{*}_{\mathrm{crit}}-1\right)}-R_{\mathrm{shift}}\,, \tag{4.9}$$

which is shifted towards the nucleus, by R_{shift}.

The shift R_{shift} can be determined by the comparison of the hybrid simulations and the corresponding values of the Flammer model (Equation 4.7). It has to be linked to the acceleration of an ion in order to determine the pick-up time, which should be constant in units of the gyrofrequency of the cometary ion. In order to get a rough estimation of this time, the single particle motion model is used. In this approach the acceleration depends on the local velocity of the solar wind and the strength of the IMF. However, these quantities again depend on the local mass flux density in the vicinity of the comet. Thus, the distance, which is caused by the pick-up time, changes while the solar wind approaches the comet. But in order to determine the local mass flux density, the shift has to be known because the mass source depends on it. Accordingly, a determination of the real acceleration time is hardly possible.

Nevertheless, a rough estimation of the acceleration time of a single ion can be calculated with constant background fields. Accordingly, the field strengths with the critical mass flux density are used. Although the fields are mostly varying in this region, these are the best guesses for the local fields next to the bow shock. In order to determine the pick-up time t_p, the shift should be equal to the distance which an ion travels during that time under the same conditions:

$$R_{\text{shift}} \overset{!}{=} x(t_p) = \frac{u_{sw}}{\Omega_{ci}} \left(\Omega_{ci} t_p - \sin\left(\Omega_{ci} t_p\right)\right) . \tag{4.10}$$

From the hybrid simulations with magnetic field strengths of $3, 4.9, 7$ and $9\,\text{nT}$, a mean value of $t_p \Omega_{ci}/2\pi = 0.216$ is determined. Equation (4.9) is visualised in Figure (4.4) where the mean value for the pick-up time is shown. This curve describes the hybrid simulation in an adequate manner. On the one hand, at high magnetic field strengths the hybrid based model with the shift approaches the Flammer model. It can be argued that the acceleration of the cometary ions needs less time under these conditions, which leads to a faster incorporation of the new ions into the flow. On the other hand, the acceleration of the ions needs more time at low magnetic field strengths. Consequently, the differences between the hybrid based and the Flammer model increase. Especially at a magnetic field strength of zero, no acceleration of the cometary ions should occur as long as no other effects are taken into account because the Lorentz force acting on the new cometary ions vanishes in this case. As a result, no mass loading of the solar wind happens and no bow shock can occur. The fluid and the MHD models, however, forecast a finite stand-off distance. In contrast to these models, the Flammer model with the shift hereafter named the hybrid based model does not predict a bow shock. At small stand-off distances the hybrid based model is not longer valid because the model only describes the comet as a source of mass. However, close to the comet the source of momentum and energy become important, too. Both sources are described by the hybrid simulations, which model the comet by inserting ions with a mass and a certain velocity into the simulation box. This is why the results of the hybrid based model and the results of the hybrid simulations differ from each other at small stand-off distances. This can be observed at $2\,\text{nT}$ for example: A closer look at this simulation (see Figure (4.5)) shows that the bow shock is asymmetric in the plane perpendicular to the undisturbed IMF (x-z plane). This indicates that the bow shock transforms into a Mach cone, which is caused by the kinetic behaviour of the solar wind ions. A detailed description of the Mach cone structure has already been discussed by Bagdonat and Motschmann (2002). The process of a finite pick-up time and the implications on the diamagnetic cavity were also studied by Kartalev (1998) and Kartalev et al. (2012) while using a modified current density.

The proposed hybrid based model is displayed by a black solid line in the comparison of the gas production rates (Figure 4.3). Although the model does neither perfectly fit

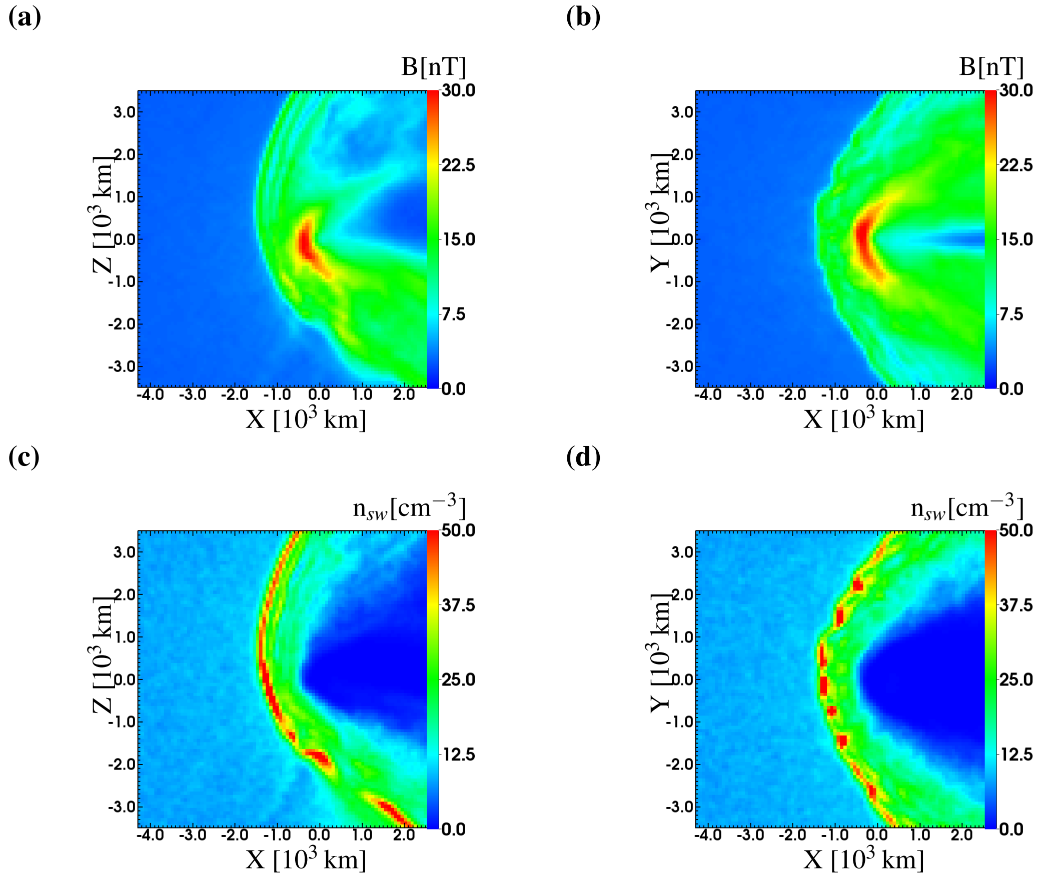

Figure 4.5: The figures show the magnetic field configuration of the hybrid plasma simulation for an IMF strength of 2 nT in the (y=0)-cross-section (a) and the (z=0)-cross-section (b). The spatial resolution in this simulation is about $\Delta x = 77\,\mathrm{km}$. Hence, the diamagnetic cavity can not be resolved in this simulation. However, the magnetic pile-up region can be identified in both cross-sections. Inside this structure, the magnetic field strength reaches about 30 nT. Further upstream, into -x-direction, a Mach cone structure occurs. Although the transition between a Mach cone into a bow shock is smooth, the comparison to the bow shock in Figure (4.2) reveals a much stronger asymmetry in the (y=0)-cross-section.

to the hybrid plasma simulation results nor the Flammer model with $f = 4$, the model reproduces the general behaviour. In case of a higher gas production rate the shift based on the pick-up time becomes less important.

Figure (4.6) shows the stand-off distances which have been forecast by the different models, in case the velocity of the undisturbed solar wind has been changed. All of these discussed models reveal that the stand-off distance increases if the solar wind velocity decreases. Nonetheless, the figure reveals differences between the models: Firstly, the Flammer model differs from the Biermann model at small velocities due to the critical mass flux density in the Flammer model, which depends on the velocity. Secondly, the figure also displays results of the hybrid based model, which has been determined in the comparison with different magnetic field strengths. Since the shift in this model also depends on the solar wind velocity, it increases to greater velocities. However, this model

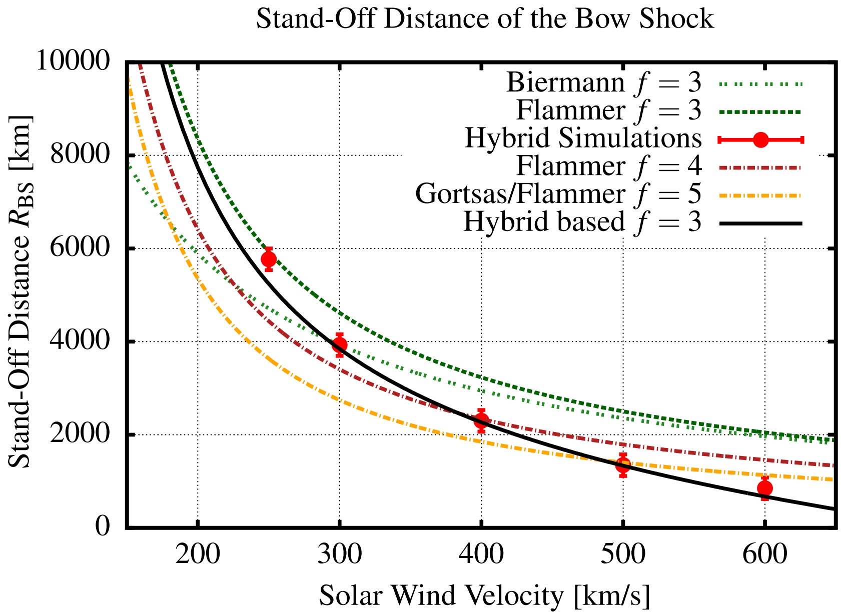

Figure 4.6: The bow shock stand-off distance as a function of the solar wind velocity. The green dotted line is based on the model by Biermann et al. (1967) with $f = 3$, whereas the green dashed as well as the red and yellow dashed dotted lines are based on the model by Flammer and Mendis (1991) with $f = 3$, $f = 4$ and $f = 5$. The red circles represent the distance of the bow shock in hybrid simulations with different solar wind velocities and the black solid line represents the hybrid based model.

is again able to reproduce the results of the hybrid simulations at different velocities of the solar wind very well. In contrast, the Flammer model with $f = 4$ differs from the hybrid simulation results even in the case of high velocities, for example at 1200 km at a solar wind speed of 600 km s^{-1}. The same applies even more to the Flammer model with $f = 5$, according to Gortsas (2010).

Figure (4.7) displays the variation of the stand-off distances at different solar wind densities. Unique for all models is a decrease in the stand-off distance with higher densities caused by a larger ram pressure and a nearly constant shift. The Flammer model with $f = 4$ as well as the hybrid based model with the shift are able to describe the positions of the bow shock obtained in the hybrid simulations, whereas the Flammer model with $f = 5$ only fits the hybrid simulation results if the density of the solar wind is high. The differences between the hybrid based model and the hybrid simulation at higher densities or higher gas production rates might be caused by the rough estimation of the acceleration time.

Up to this point, this comparison uses a Parker angle of 90°, but during the escort phase of the Rosetta mission the angle will be smaller most of the time. In order to investigate the impact of the Parker angle on the bow shock, this study performs a series of hybrid simulations using Parker angle variations between 90° and 45° (see Figure (4.8)). For comparison a dark-red dashed dotted curve of $A \sin(\theta)$ is plotted, too, where A is the stand-off distance at 90°. In case of $\vec{E} \times \vec{B}$-pick-up, the strength of the Lorentz force is determined by the Parker angle. However, the bow shock distances in the hybrid sim-

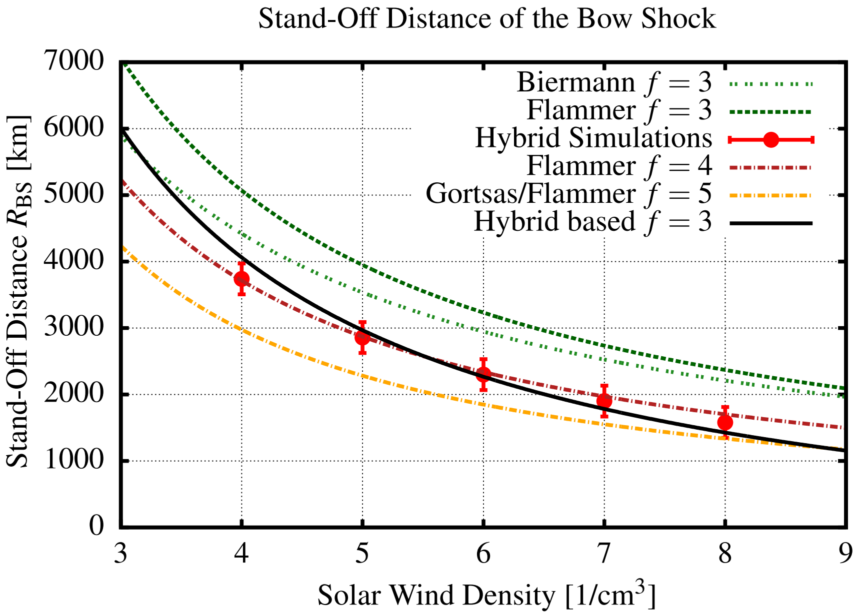

Figure 4.7: The impact of a varying solar wind density on the stand-off position of the bow shock. This distance in the model by Biermann et al. (1967) with $f = 3$ is represented by the green dotted line, whereas the green dashed line represents the model by Flammer and Mendis (1991) with $f = 3$. The red and yellow dashed lines show the distance of the model by Flammer and Mendis (1991) with $f = 4$ and $f = 5$. The red circles and the black solid line represent the stand-off distances in the hybrid simulations and the hybrid based model.

ulations are above the plotted sine values. A reason for this could be the quasi-parallel pick-up. To evaluate these higher values, an additional term to $A\sin(\theta)$ is introduced by $B\cos(\theta)$. Consequently, a curve with

$$R_{BS}(\theta) = A\sin(\theta) + B\cos(\theta) \tag{4.11}$$

is shown by a black solid line in the figure as well. The parameters A and B are used to fit this equation to the results of the hybrid simulations. It matches best if A is equal to the stand-off distance at 90° and B has a value of 163 km. Thus, A can again be interpreted as determined by the $\vec{E} \times \vec{B}$-pick-up whereas the fit parameter B is related to a pick-up which is possibly driven by some instabilities (Lee 1989).

Figure (4.9) reveals the stand-off distances of the bow shock at comet 67P/Churyumov-Gerasimenko using the models which have been discussed including the hybrid based model proposed as a function of the mission time of Rosetta, which implicitly is a measure for the comet-Sun distance. For this purpose the prediction of Lamy et al. (2007) for the gas production rate of 67P/Churyumov-Gerasimenko is used. The solar wind parameters are calculated with the model by Parker (1958) and Hansen et al. (2007). Except for the hybrid based model, all models predict a bow shock during the regarded mission time. But it should be clear that at a certain point the kinetic behaviour becomes more important and the fluid approach is not longer appropriately applicable. The hybrid simulations in this work show a Mach cone structure if the stand-off distance is below 1500 km. This

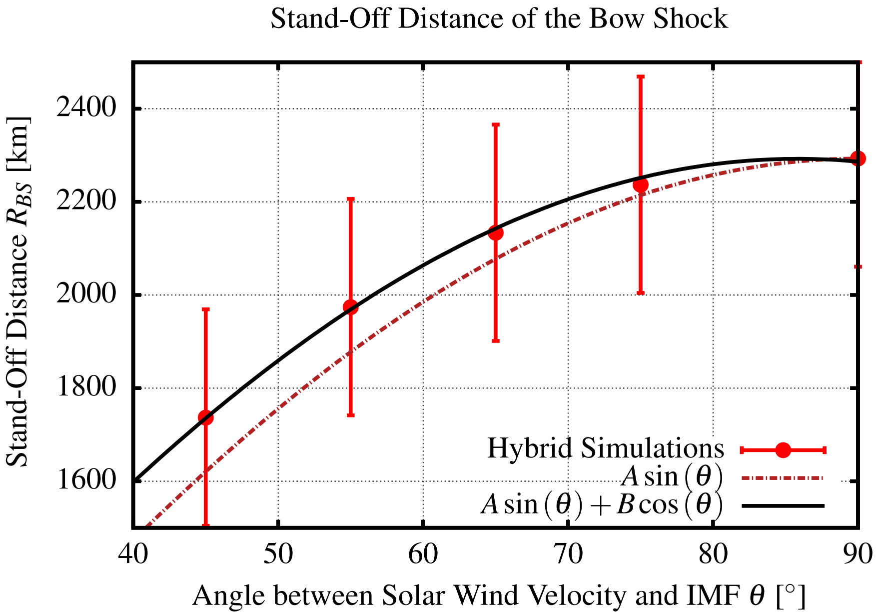

Figure 4.8: The bow shock distance in hybrid simulations as a function of the Parker angle θ. The dark-red dashed dotted line represents the function $A\sin(\theta)$, where A is the stand-off distance at 90°. The solid black line shows the function $A\sin(\theta)+B\cos(\theta)$. Hereby, A and B are obtained by a fit. It turns out that A is next to the stand-off distance at 90° and $B = 168(13)\,\text{km}$.

threshold is displayed by a red line in Figure (4.9). The details of the transition will be investigated in more detail in a future work.

The overall picture discussed in this work leads to the result that the cometary bow shock at 67P/Churyumov-Gerasimenko is only fully established in the hybrid based model using the chosen parameters as long as the heliocentric distance is below 1.35 AU.

4.1.6 Conclusion and Outlook

This section revisits different models which predict the position of the cometary bow shock at comet 67P/Churyumov-Gerasimenko, the target comet of ESA's Rosetta mission. A bow shock is expected close to the perihelion and predicted by all models. However, the position of the bow shock and the capabilities of the different models vary in a wide range. For example, the simple analytical one-dimensional fluid models by Biermann et al. (1967) and Flammer and Mendis (1991) both predict a bow shock at a position that can be calculated using the following formula:

$$R_{\text{BS,Biermann/Flammer}} = \frac{\nu Q m_{\text{i}}}{4\pi u_{\text{ng}} n_{\infty} m_{\infty} u_{\infty} \left((\rho u_{\text{x}})^{*}_{\text{crit}} - 1 \right)} .$$

The model by Biermann et al. (1967) uses a critical mass flux density $(\rho u_{\text{x}})^{*}_{\text{crit}}$ which is only determined by the number of degrees of freedom whereas the same entity in the model by Flammer and Mendis (1991) is additionally determined by upstream solar wind

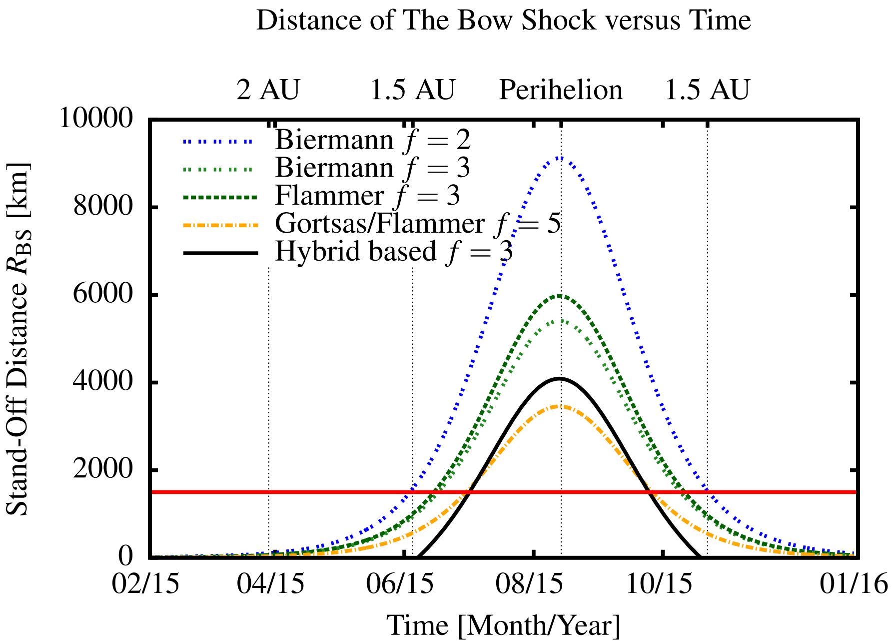

Figure 4.9: The predicted bow shock distances from the different model approaches during the Rosetta mission. The blue and green dotted lines represent the model by Biermann et al. (1967) and the dashed green line shows the bow shock distance based on the model by Flammer and Mendis (1991) with $f = 3$. The same model but with $f = 5$ is represented by the yellow dashed dotted line. In addition the hybrid based model is drawn with a solid black line and the lower limit of this model is expressed by the red line.

parameters. Moreover, this work also presents 3D MHD simulations and the state of the art hybrid plasma simulations, which use the A.I.K.E.F. code (Müller et al. 2011). By changing the important parameters of the interaction, this work investigates the behaviour of the subsolar cometary bow shock position in all presented models. It was found that the analytical models by Biermann et al. (1967) and Flammer and Mendis (1991) are not able to reproduce the bow shock positions in the hybrid simulations. Nevertheless, these analytical models are preferred for operational purposes, since they allow a fast computation of results. Another fact shown and discussed is that the differences between the model by Flammer and Mendis (1991) and the hybrid simulation results increase when the characteristic scales of the ion motion rise. To avoid the instant acceleration of the newborn cometary ions, this study suggests to introduce a pick-up time t_{p} into the magnetohydrodynamic approach by Flammer and Mendis (1991) with $f = 3$. This pick-up time is constant in terms of the cometary ion gyro-period and leads to a shift R_{shift} of the bow shock towards the nucleus:

$$R_{BS,Hybrid} = \frac{\nu Q m_{\mathrm{i}}}{4\pi u_{\mathrm{ng}} n_\infty m_\infty u_\infty \left((\rho u_{\mathrm{x}})^*_{\mathrm{crit}} - 1 \right)} - R_{\mathrm{shift}} \, .$$

In order to get a rough estimation of the pick-up time, this work uses a single particle motion model to describe the motion of a newborn cometary ion.

$$R_{\text{shift}} = \frac{u_{sw}}{\Omega_{ci}} \left(\Omega_{ci} t_p - \sin\left(\Omega_{ci} t_p\right)\right)$$

When using a pick-up time of $t_p = 0.216 \cdot 2\pi/\Omega_{ci}$, the hybrid based model fits well to all performed hybrid simulations. Furthermore, the hybrid based model allows a fast computation of the bow shock position and, therefore, can be used for operational planning, too. The hybrid based model, applied to the parameters of the interaction during the escort phase of the Rosetta mission with the gas production model of Lamy et al. (2007), shows that the bow shock is only fully established as long as the heliocentric distance is below 1.35 AU.

This study furthermore shows that small variations in the parameters can lead to huge shifts in the bow shock position. In the framework of the stationary hybrid based model, these variations have to persist at least for the time period in which the solar wind propagates from an undisturbed region to the point at which the critical mass flux density is reached. The propagation time is in order of a few hours and depends on the specific parameters. For example, the solar wind needs about 1.2 hours for the parameters shown in Table (4.1). Consequently, a non-stationary solar wind with enhancements over timescales in the orders of hours must lead to a different bow shock position. Due to this, the bow shock will move several times over the spacecraft if Rosetta is in an appropriate position and if enhancements in the solar wind will occur. This will allow the study of several bow shock crossings.

4.2 The Features in the Inner Coma

In 1986, the flyby of the European Space Agency's spacecraft Giotto at comet 1P/Halley revealed the presence of a region in the comet-solar wind interaction region without any magnetic field, the diamagnetic cavity (Neubauer et al. 1986), as briefly described in Section (1.2). This cavity is bounded by the cometary ionopause or cavity surface, which is characterised by a sharp decrease in the magnetic field strength.

At Halley, a decrease from 20 nT to zero within 25 km was observed by the magnetometer experiment at a distance of about 4500 km on the inbound and on the outbound path (Neubauer 1988). In parallel with the change in the magnetic field strength the Giotto ion mass spectrometer (IMS) observed a drop in the ion temperature and a change in the radial velocity. Within the diamagnetic cavity the plasma had a radial velocity of about 1 km s^{-1} (Balsiger et al. 1986), whereas the plasma radial velocity was close to zero over a distance of about 10 000 km before the passage of that boundary. In addition, Goldstein et al. (1989) found a sharp spike in the ion densities just at the inner edge of the cometary ionopause. The width of the spike was estimated to be about 47 km and the authors interpreted the enhancement as a boundary layer. The cometary plasma from the comet enters this region and piles up. Since the maximum density is limited by recombination, the authors called the region recombination layer.

These observations were expected and have been intensively studied by various authors (cf. Wallis and Dryer 1976, Cravens 1986, Ip and Axford 1987, Cravens 1989, Puhl-Quinn and Cravens 1995, Gombosi et al. 1996, Rubin et al. 2014a). The boundaries

Quantity	**Value**
gas production rate Q	$5 \times 10^{27}\,\mathrm{s}^{-1}$
cometary ion mass m_i	$19\,\mathrm{amu}$
ionisation rate ν	$5.88 \times 10^{-7}\,\mathrm{s}^{-1}$
neutral gas velocity u_NG	$1\,\mathrm{km\,s}^{-1}$
solar wind number density n_{SW}	$6\,\mathrm{cm}^{-3}$
solar wind velocity u_{SW}	$400\,\mathrm{km\,s}^{-1}$
strength of interplanetary magnetic field B_{IMF}	$4.9\,\mathrm{nT}$
Parker angle θ	52°

Table 4.2: Characteristic parameters of the plasma interaction between comet 67P/Churyumov-Gerasimenko and the solar wind at 1.3 AU (Hansen et al. 2007).

in the inner region occur because of the interplay of the impinging massloaded solar wind and a supersonic cometary plasma, which emanates radially from the inner region due to collisions between the ions and the neutral gas. As a consequence, the cometary ionopause can be found where the $\vec{j} \times \vec{B}$ force is balanced by the ion-neutral friction force. Since the massloaded flow is prevented to enter this region, the plasma stagnates and the magnetic field piles up.

In the advent of the Rosetta arrival at its target comet 67P/Churyumov-Gerasimenko (Glassmeier et al. 2007a) and the ongoing preparation of the measurements, the above mentioned results have to be revisited. Caused by the different gas production rates of the target comet, the interaction between the solar wind and a comet may differ from the situation observed at comet 1P/Halley. In the early phase of the escort phase of the Rosetta mission the relative motion between the cometary ions and the solar wind protons will lead to a Mach cone and a pick-up ion tail perpendicular to the solar wind velocity as discussed in great detail in Chapter (3). Those simulations do not show the presence of a diamagnetic cavity.

In addition, the previous hybrid plasma simulations of the plasma interaction at 67P/-Churyumov-Gerasimenko (cf. Bagdonat and Motschmann 2002, Motschmann and Kührt 2006, Gortsas et al. 2010) were neither able to resolve nor to describe all important processes in the innermost region at active comets, where the cometary ionopause and the cavity are anticipated by single-fluid MHD models (cf. Hansen et al. 2007, Rubin et al. 2012). But with the use of the A.I.K.E.F.-code and the work being described in Chapter (2) the situation changed.

This section investigates the plasma interaction in the innermost part of the coma of comet of 67P/Churyumov-Gerasimenko at 1.3 AU. The properties of the comet and the undisturbed solar wind are listed in Table (4.2). Not only macroscopic structures are discussed, rather the ion kinetics are described in great detail.

4.2.1 Simulation Setup

This study uses a version of the A.I.K.E.F. code which solves the electron pressure equation and models the collisions by a statistical process, as described in Chapter (2).

The simulation focusses on the structure of the plasma environment of comet 67P/-

Churyumov-Gerasimenko close to its perihelion, which will be passed at a heliocentric distance of 1.24 AU on 13th August 2015. For the purpose of comparability a setup similar to the configuration by Hansen et al. (2007) was chosen. They assumed typical solar wind conditions at a distance of 1.3 AU to the Sun and a comet gas production rate of $Q = 5 \times 10^{27}\,\mathrm{s}^{-1}$ for their simulations (cf. Table 4.2). The solar wind macro-particles enter the simulation box at the -x-boundary of the simulation box, i.e. the upstream boundary. They move into $+x$-direction, which is oriented anti-sunward. The interplanetary magnetic field lays the xy-plane with an angle of 52° to the solar wind velocity.

The simulation box is a cube with an edge length of 10 227 km. The upstream boundary is located at $x_{\mathrm{min}} = 6508\,\mathrm{km}$ and the nucleus centred with respect to the y- and z-direction. The boundary conditions at the upstream side, the $\pm y$- and $-z$-boundaries are inflow boundaries for particles and fields, whereas the $+x$- and $+z$-boundaries are outflow boundaries. This means that the macro-particles within these cells are removed at each time step and that the derivatives normal to the boundary of the fields are zero.

Due to the fact that the size of the massloading region at the comet (several million kilometre) exceeds the size of the simulation box to a large extend, the extended-upstream-boundary model, introduced by Koenders et al. (2013), is used to model the massloading of the solar wind upstream of the simulation box. Thereby, the position of the bow shock is fixed and does not depend on the size of the simulation box.

The simulation uses a hierarchical Cartesian mesh. In the outer regions of the simulation box only a coarse resolution is needed to resolve the interesting features, i.e. the mass loading or the cometary bow shock. Here, the numerical mesh has a coarse resolution of about 71 km. Within a cuboid of $-150\,\mathrm{km} < x < 80\,\mathrm{km}$, $-120\,\mathrm{km} < y < 120\,\mathrm{km}$ and $-120\,\mathrm{km} < z < 120\,\mathrm{km}$ the maximum resolution of $\Delta x_{\mathrm{max}} = 2.22\,\mathrm{km}$ is reached. Based on the requirements of the Hybrid-Block-AMR, the refinement takes place stepwise.

In order to reduce the numerical noise in the simulation caused by the limited amount of macro-particles within a numerical mesh cell, the macro-particles are split before they enter a region of higher spatial resolution. Opposed to this, the macro-particles are merged if their number per cell exceeds an optimal number. In case of the simulations presented in this study, this optimal number is 100 macro-particles per cell. In total, the simulation box is filled with about 6 billion macro-particles.

The Courant-Friedrichs-Levy condition forces us to half the size of a simulation time step when the resolution is doubled by an additional refinement level. Thus, the number of time steps of the simulation is at least doubled until a quasi-stationary state is reached. In order to save numerical resources, the following scheme is applied to gain the simulation results: At the beginning the simulation box with no refinement level is used. After reaching a quasi-stationary state, a new simulation is run with a halved time step and an additional refinement level is performed, which uses the pre-calculated state as the initial state. By repeating this procedure, the refinement increases over time. Since most of the structures are already quasi-stationary, these simulations reach their quasi-stationary state in a shorter time. Furthermore, this procedure allows us to use smaller smoothing values because strong gradients, such as the one at the cometary ionopause, can only be resolved if the plasma is already strongly decelerated and the spatial resolution is higher.

In its final configuration, the simulation has a numerical time step of $\Delta t = 1.78 \times 10^{-3}\,\mathrm{s}$. In this configuration the simulation runs about 75000 time steps, which corresponds to 133 s. During that time, the undisturbed solar wind would have passed the simulation box four times. During this time period, it should be possible for an ion to be ionised at the nucleus, to traverse the entire cavity (the radius is about 40 km) and to modify the flow. However, it does not seem possible for such an ion to leave the simulation box during this time. But most of the structures are already stationary after about 10000 time steps of the highest resolved simulation.

4.2.2 Results

4.2.2.1 Large Scale Structures

The movement of the new cometary ions, which are ionised close to the upstream boundary of the simulation box, is controlled by weakly disturbed interplanetary magnetic and electric fields. Close to the upstream boundary the magnetic field $\vec{B}_{\mathrm{IMF}}$ has an angle of 52° to the solar wind velocity vector and the electric field is dominated by the convective term $\vec{E}_{\mathrm{CONV}} = -\vec{u}_{\mathrm{SW}} \times \vec{B}_{\mathrm{IMF}}$, which points into $-z$-direction because the flow is still controlled by the solar wind. Thus, the resulting Lorentz force leads to a cycloidal motion of the cometary ions. This is a gyromotion around the magnetic field superimposed by an $\vec{E} \times \vec{B}$-drift. The gyroradius of a new cometary ion can be estimated by $r_{\mathrm{gyr}} = m_{\mathrm{CI}} v_{\perp} / (qB) \approx 4000\,\mathrm{km}$ in that region. And due to the orientation, the $\vec{E} \times \vec{B}$-drift leads to a movement into $+x$- and $-y$-direction. The resulting velocity distribution is shown in the upper part of Figure (4.10). In order to obtain these plots, the velocities of particles which are located in a specific volume at a time step are saved and visualised. For the purpose of better statistics, the data is collected over several time steps. Detector 1 is a cube with an edge length of 100 km and centred at $x = -5850\,\mathrm{km}$ on the Sun-comet line. The velocity distribution of the cometary ions at this detector shows a clear ring distribution in v_x and v_z, centred at the local solar wind speed of about $270\,\mathrm{km\,s^{-1}}$, and the drift in $+x$-, and $-y$-direction. The higher count rates for ions with negative v_z-component (small red sector) indicate the presence of relatively new cometary ions, which first move into $-z$-direction. Since the ion production, νn_{NG}, increases as the distance to the comet is reduced, higher count rates in the $-v_z$-component in contrast to the remaining ring are anticipated. This is why the distribution of the cometary ions is non-gyrotropic and triggers waves (Motschmann and Glassmeier 1993, 1998).

The mean velocity of the cometary ions is smaller than the solar wind speed and is oriented into $+x$-,$-y$-, and $-z$-direction due to the non-gyrotropic distribution. This can be seen in the orientation of the cometary ion velocity in Figure (4.11 g, and j), which also shows the bulk cometary ions on the x=0 and the y=0-cross-section.

On the way towards the comet more and more cometary ions are picked-up by the solar wind. This causes massloading and a deceleration of the solar wind (Figure 4.11 e, and f). In case a critical amount of cometary ions, i.e. mass, is injected into the solar wind, a transition from supersonic to subsonic speed, i.e. a bow shock, occurs (Biermann et al. 1967). For the given scenario, a bow shock is triggered (Figure 4.11). The mass flux density just upstream of the bow shock is $(\rho_{\mathrm{sw}} u_{\mathrm{sw}} + \rho_{\mathrm{ci}} u_{\mathrm{ci}}) \,/\, (\rho_0 u_0) \approx 1.49$, where ρ_0 and u_0 denote the density and the velocity of the undisturbed solar wind. This is below the critical value given by the model by Biermann et al. (1967) for a fluid with three degrees of freedom and just below the critical value of 1.51 obtained from the model by Flammer and Mendis (1991) for the given scenario. The magnetosonic Mach number of the flow

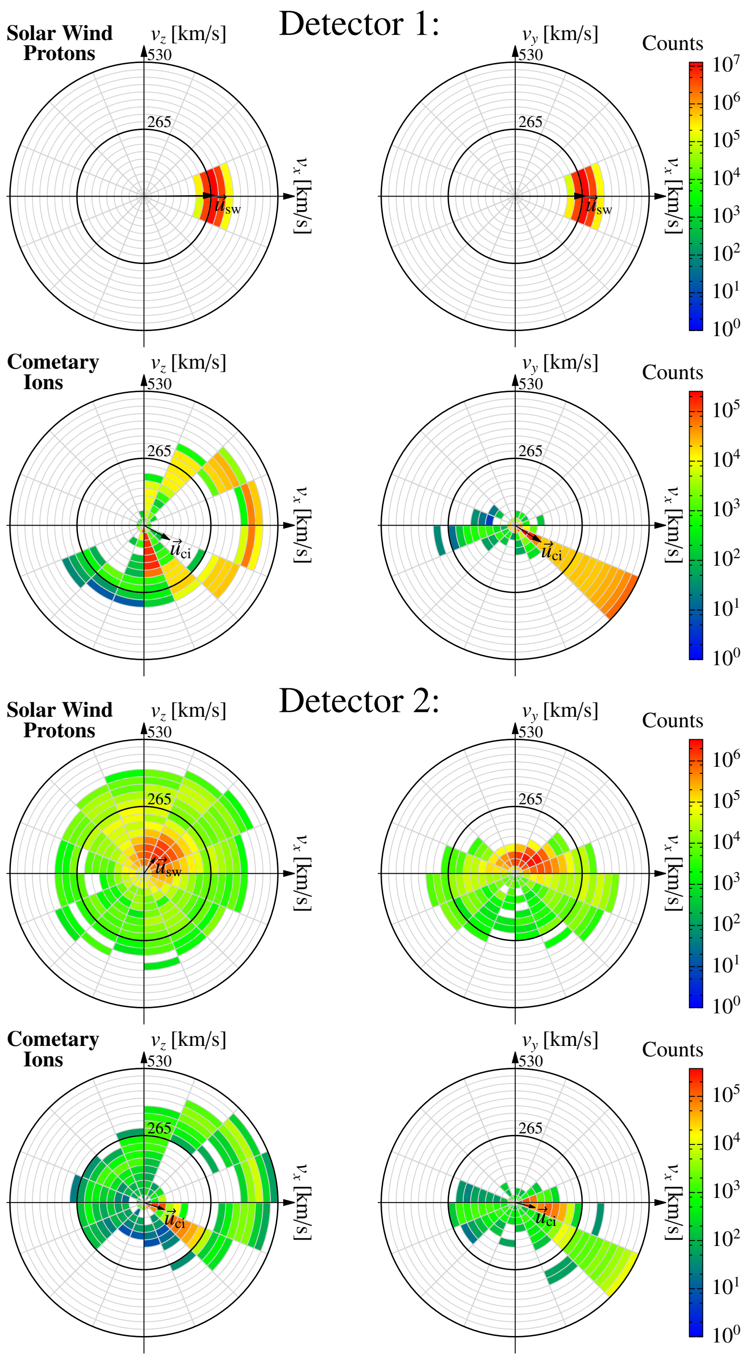

Figure 4.10: The particle distributions in velocity space in two different volumes of the simulation. The first detector is placed in the massloaded solar wind, about 4000 km upstream of the bow shock, whereas the second detector volume is located about 200 km behind the bow shock. For each detector, there are two plots per ion species in a row, which show different velocity components (v_x and v_z, respectively v_x and v_y). The counts are arbitrary units.

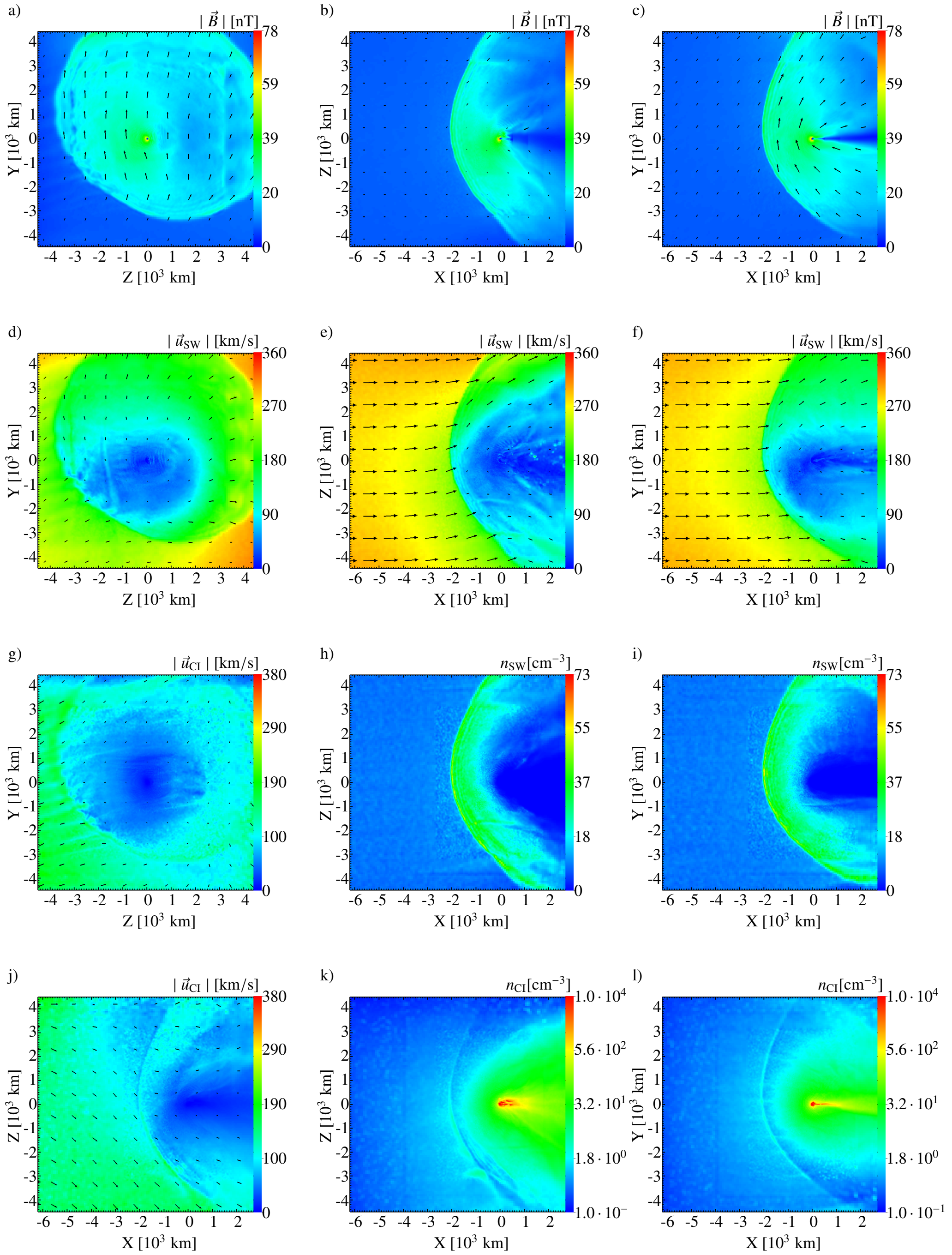

Figure 4.11: The results of the hybrid simulation of comet 67P/Churyumov-Gerasimenko at 1.3 AU on large scales. The first row shows the strength of the magnetic field, and the second row the solar wind density at the x=0-, y=0-, and z=0-cross-sections. The arrows indicate the orientation of the magnetic field or the solar wind velocity within the cross-section. The plots g) and j) show the speed of the cometary ions and the direction into yz respectively xz-direction. Plots h), i), k), and l) show the solar wind and the cometary ion density on the y=0-cross-section, and the z=0-cross-section.

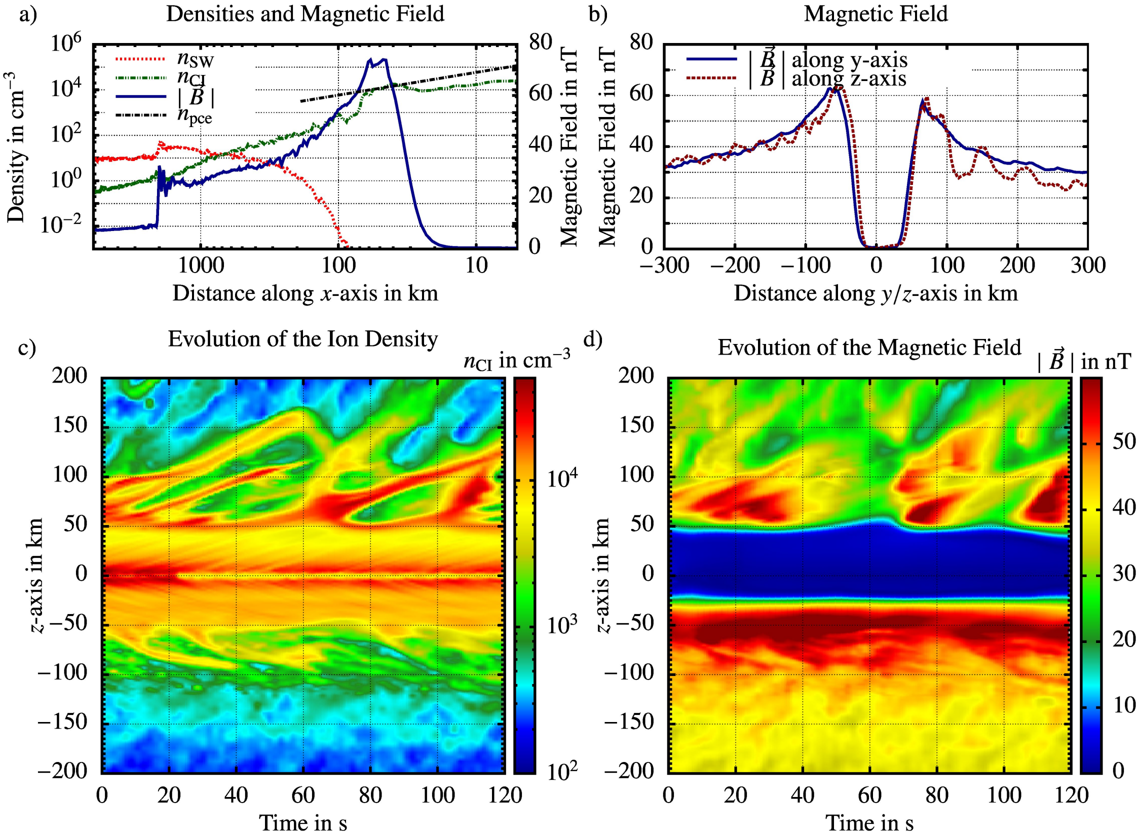

Figure 4.12: This figure shows various cuts through the simulation box. Panel a) shows the densities of the solar wind, the cometary ions and an assumed photochemical equilibrium n_{pce}. This equilibrium is obtained with an electron temperature of 250 K and a resting plasma. In addition, the magnetic field strength is shown. The values are obtained from the Sun-comet line on the dayside. The panel b) shows the values of the magnetic field strength along the y- and the z-axis. The panels c) and d) show the evolution of the ion density and the magnetic field strength along the z-axis.

just upstream of the bow shock is $M_{\mathrm{ms}} \approx 2$. The magnetic field, the solar wind density and the solar wind velocity jump by a factor of about 2.5 at the subsolar point (Figure 4.12). Thus, the bow shock in the simulation is only a weak shock, which is in agreement with the observations at the comets visited so far (Neubauer et al. 1986, Coates 1995, Richter et al. 2011) and other theoretical studies (cf. Wallis 1973, Gombosi et al. 1996). The stand-off distance of the bow shock in our simulation is about 2000 km, which is explained in the last Section (4.1).

Besides the deceleration of the solar wind, a change in its direction is also visible upstream of the bow shock (Figure 4.11 d, and f). This is caused by the pick-up of the cometary ions, which leads to a bulk velocity of the cometary ions into $+x$-,$-y$-, and $-z$-direction. The conservation of momentum and energy requires that the solar wind is slightly deflected towards $+y$- and $+z$-direction. Due to this modification of the flow pattern, the entire outer interaction region is shifted towards $+y$- and $+z$-direction. A similar shift is visible in the hybrid simulations by Motschmann and Kührt (2006) and Delamere (2006) and the multi-fluid MHD simulations by Rubin et al. (2014a).

The deflection into $+y$- and $+z$-direction is also visible in the velocity distribution function (Figure 4.10). Detector 1, 4000 km upstream of the bow shock, shows that the solar wind moves in $+x$-direction, and has a relatively small thermal velocity. At Detector 2, which is located on the Sun-comet line 200 km behind the bow shock, the solar wind particles are distributed over a wide range of velocities. The broadening of the distribution function is more prominent in the x- and z-velocity components. This indicates that the solar wind is already partially heated up by the bow shock structure. However, the velocity distribution of the solar wind protons in v_x and v_y still reveals an asymmetry.

In the solar wind velocity distribution one can identify ions which move into $-x$-direction. Due to the fact that the distance of the detector to the bow shock is below the gyroradius of the solar wind protons, one can assume that these particles are reflected by the enhanced magnetic field at the bow shock. A similar population is also visible in the cometary ion velocity distribution. These cometary ions are also observable at the first detector which is caused by the fact that the distance of this detector to the bow shock is smaller than the gyroradius of cometary ions. In addition, one can see that the ring distribution in the cometary ion velocity distribution at the second detector is broadened in comparison to the distribution at the first detector, which is caused by the shock.

The cometary ion velocity distribution at Detector 2 also reveals that the orientation of the electric and the magnetic field has changed (Figure 4.11). Here newborn cometary ions move more towards $+x$-direction and the velocity components in $-y$-, and $-z$-direction have nearly vanished. However, due to conservation of the magnetic moment, the cometary ions which are picked-up upstream of the bow shock remain in their motion. As discussed by Galeev et al. (1985), newborn cometary ions have a smaller magnetic moment the more the solar wind speed is reduced. Since the bow shock causes an abrupt decrease, a gap in the velocity distribution function may occur, as observed at comet 1P/Halley (Thomsen et al. 1987, Coates 1991). However, this gap is not visible in this detector as the time for the evolution of a new ring distribution is too short. But at a third detector, which is located at a distance of 90 km upstream of the comet, the cometary ion velocity distribution reveals a gap (Figure 4.13). Here we found a ringlike distribution with a mean velocity of about $150\,\mathrm{km\,s^{-1}}$, and a second ion population with much smaller velocities. Further features of the velocity distribution at Detector 3 will be discussed in Section (4.2.2.2).

By comparing the panels b) and c) of Figure (4.11), it becomes obvious that the magnetic field is more confined within the z=0-cross-section. This can be reinforced by the structure of the cometary ion density; see panels k) and l). In the z=0-cross-section the cometary ions are concentrated due to the magnetic field, whereas the cometary ion tail is spread out on the y=0-cross-section.

The solar wind density reveals that the solar wind is excluded from the inner region of the comet. The transition occurs steadily and a sharp transition along the Sun-comet line cannot be found. At about 100 km upstream of the nucleus the solar wind density is about $10^{-3}\,\mathrm{cm^{-3}}$ (Figure 4.12). Thus, only the heavy cometary ions, which are picked up by the solar wind, enter the innermost region.

4.2.2.2 Structures in the Inner Coma

In the inner part of the interaction region collisions between the ions and the neutral gas, escaping radially from the nucleus, play a dominant role and lead to structures already

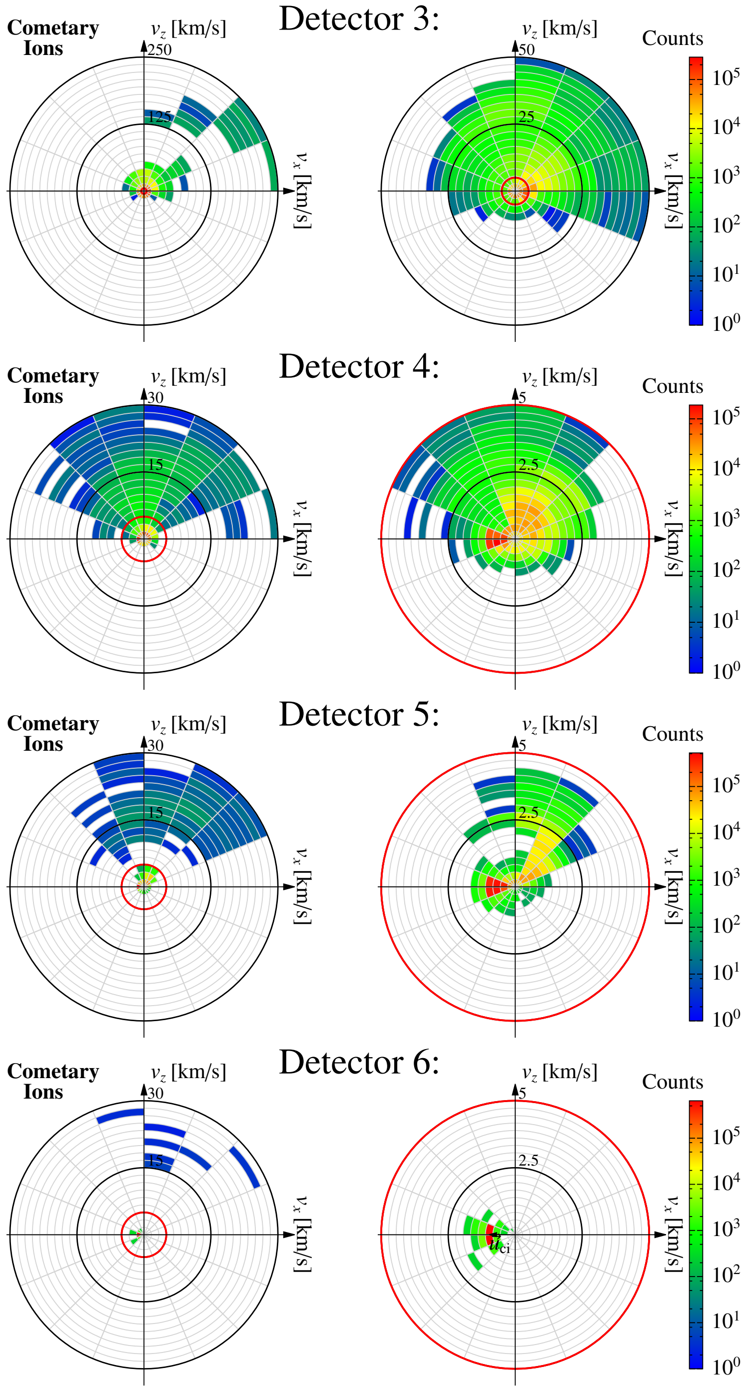

Figure 4.13: The velocity distribution in x- and z-direction at 4 different detector positions. All detectors are oriented along the Sun-comet line. Detector 3 is placed upstream of the magnetic barrier region at 90 km distance to the comet. The centres of the detectors 4, 5 and 6 are located at 47.5 km, 32.5 km and 16 km upstream of the nucleus. The plots on the right side are enlarged versions of the plots on the left side. All figures show the v_x and v_z velocity components.

observed at comet 1P/Halley. However, in order to do so, a sufficient gas production rate is required. Our hybrid simulation of the selected scenario reveals that the gas production rate is sufficient to form a diamagnetic cavity and to remove the impinging massloaded plasma from the innermost region almost completely.

The closer the flow approaches the nucleus, the more the plasma is decelerated. In this way the magnetic field strength increases as well and piles-up, which is visible in Figures (4.11 a, b, and c) and in an enlarged version in Figures (4.14 a, b, and c). These figures show the strength of the magnetic field in the x=0-, the y=0-, and the z=0-cross-sections. The orientation of the magnetic field in the cross-sections is shown as well. In Figure (4.14 c) one can see the strong draping of the magnetic field around the comet. The simulation reveals a maximum field strength of 78 nT at a distance of 45 km to the nucleus. At this location, the bulk velocity of the cometary ion reaches its minimum of about $0.16\,\mathrm{km\,s^{-1}}$ (Figure 4.14 g, h, and i). The magnetic field along the Sun-comet line is shown in Figure (4.12 a).

The exact conditions for the previous cometary flybys are unknown, however, the maximum magnetic field strength in our simulation is in the range as the observed maximum magnetic field strengths from the flybys at comets in the past decades (Richter et al. 2011). Hansen et al. (2007) reported a maximum value of 73.5 nT in a MHD simulation of 67P/-Churyumov-Gerasimenko with nearly the same parameters.

Beyond the stagnation point, the direction of the bulk velocity is outward, and the magnetic field strength drops rapidly. Within a distance of 25 km the magnetic field strength drops to values below 1 nT. The simulation reveals a minimum field strength of 28 pT in the diamagnetic cavity. Within the transition, the bulk velocity of the cometary ions steadily increases to $1\,\mathrm{km\,s^{-1}}$ radially away from the nucleus, which is the speed of the neutral gas. The velocity is constant within the diamagnetic cavity. In Figures (4.14 d, e, and f), which show the cometary ion density (The projection to the cross-section of a possible trajectory of the Rosetta spacecraft is shown in this row by a black line (Section 4.2.2.3).), one can see that the ion density is enhanced at the transition of the magnetic field. This is also presented in an enlarged version in Figure (4.14 l), which shows the cometary ion density and the flow of the cometary ions on the z=0-cross-section, as well. However, in this plot a black solid contour line indicates where the $\vec{j} \times \vec{B}$ force and the ion neutral drag force are balanced. In addition, the position of the inner shock are highlighted by a dotted black curve. In this transition region along the Sun-comet line, the cometary ion density reaches values equal to the density at a photochemical equilibrium n_{pce}, which is also shown in this figure by a black dashed line (Section 2.5.3.5). Here, an electron temperature of 250 K is used, which is present in the ion pile-up region. For this calculation a resting plasma is assumed. In addition, the figure shows the cometary ion density. At the ion pile-up region both are in agreement. Thus, this region between the cavity and the stagnation point is the recombination layer, which was observed at comet 1P/Halley by Goldstein et al. (1989).

In comparison to the cometary ionopause at 1P/Halley, the transition in our simulation is much narrower. While the magnetometer observed a change in the field strength of 20 nT within 25 km at 1P/Halley (Neubauer 1988) close to the terminator, we find a change of 78 nT within 25 km along the Sun-comet line in our simulation. However, close to the terminator plane, the change is less drastic. An example will be discussed in Section (4.2.2.3).

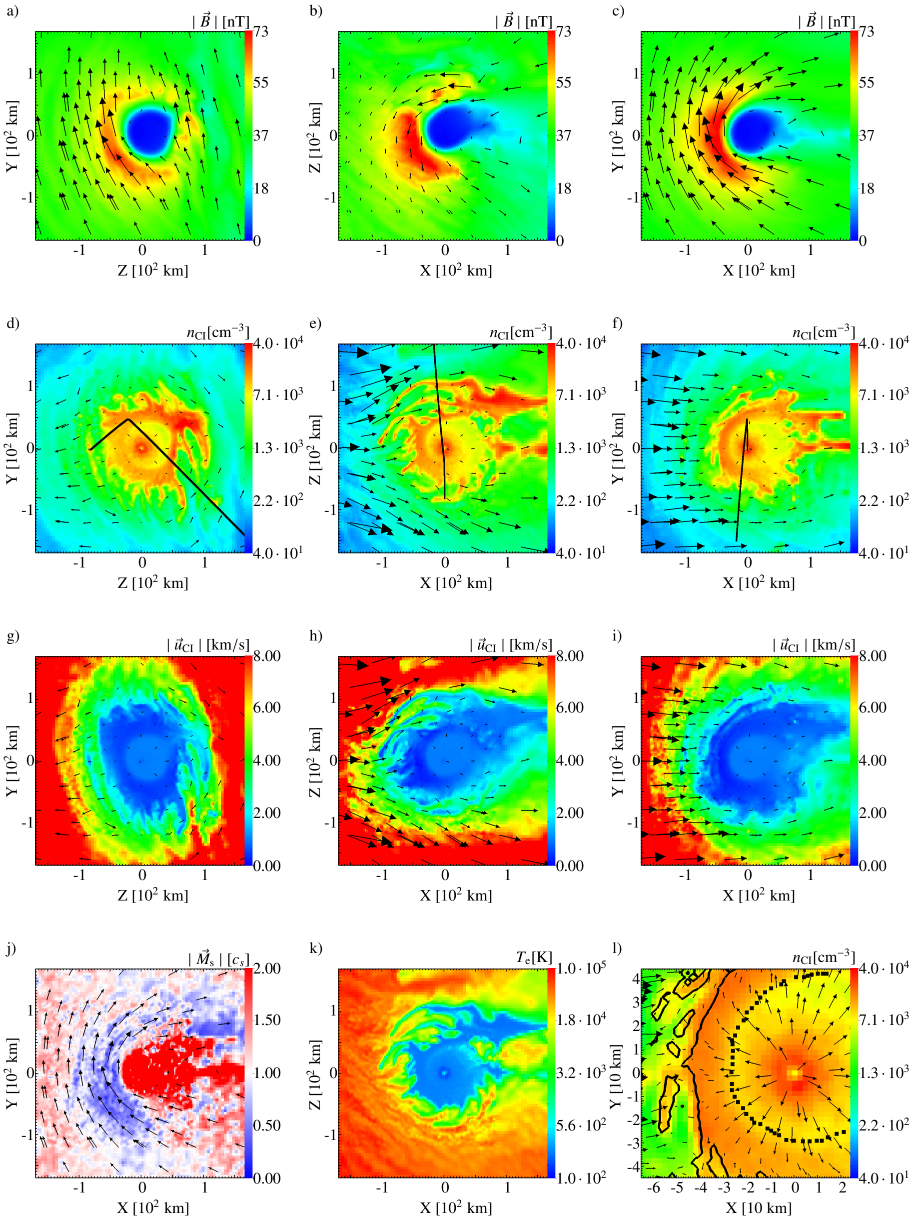

Figure 4.14: The plasma interaction in the inner coma of comet 67P/Churyumov-Gerasimenko. Plots a), b), and c) show the magnetic field strength and the orientation of the magnetic field on the x=0-, y=0-, and z=0-cross-section. The plots in the second row show the cometary ion density, i.e. the orientation of the velocity of the cometary ions in the same cross-sections. The plots g) to i) show the magnitude of the cometary ion velocity and its orientation. The magnetosonic Mach number at the z=0-cross-section, and the orientation of the magnetic field is shown in plot j). The electron temperature is shown in plot k). Plot l) shows the cometary ion density and the orientation of the velocity of the cometary ions in the z=0-cross-section in an enlarged version. Along the black solid contour-line the ion-neutral drag force and the $\vec{j} \times \vec{B}$-force are balanced and the black dotted line highlights the position of the inner shock.

Because of the fact that nearly no magnetic field penetrates the cavity and that the plasma is cooled by collisions, the plasma in the cavity is supersonic (Figure 4.14 j), and subsonic near the stagnation point. In between these regions an inner shock can be found, as predicted by Wallis and Dryer (1976). Figure (4.14 k) shows the electron temperature in the inner coma. It becomes clear that a sharp transition in the electron temperature occurs, where the cometary ions pile-up. In the diamagnetic cavity an electron temperature of about 200 K is predicted by the simulation. A similar sharp transition of the electron temperature was observed by Eberhardt and Krankowsky (1995) at 1P/Halley.

A different behaviour in the electron temperature can be observed in a simulation which uses an adiabatic state equation for the electron fluid, in the following named *adiabatic simulation*. In this simulation the temperature of the solar wind electrons is 5×10^4 K and that of the cometary electrons is 180 K. The global structure of this simulation is shown in Figure (4.2). A comparison between the *adiabatic simulation* and the *none-adiabatic simulation* discussed in this section, which solves the electron pressure equation directly, is shown in Figure (4.15). In both simulations the bow shock has a subsolar stand-off distance of 2000 km, but the position of the magnetic pile-up region and the cometary ionopause differ. In the *adiabatic simulation* both structures have a larger stand-off distance and the point with the maximum magnetic field strength is shifted from 50 km to 93 km. In addition, the maximum magnetic field strength is reduced in the *adiabatic simulation*. The larger stand-off distances in the *adiabatic simulation* are caused by the electron pressure term in Equation (2.74). Since the cometary ion density increases towards the nucleus, the electron pressure increases as well. The resulting electric field supports the neutral drag force. As a consequence, the size of the diamagnetic cavity in the *adiabatic simulation* strongly depends on the configured temperature of the cometary electrons. Another difference is the absence of the ion pile-up region in the cometary ion density in the *adiabatic simulation*. Since the electron temperature is obtained from the density ratios in the *adiabatic simulation*, the electron temperature profiles differ heavily. In addition, the adiabatic state equation for the electrons is not able to describe the heating of the plasma at the bow shock. In contrast, the *none-adiabatic simulation* predicts a large increase of the electron temperature up to about 3×10^5 K. Finally, only the *none-adiabatic simulation* developed as part of this work is able to reproduce a sharp temperature decrease towards the nucleus, which is similar to that observed at comet 1P/Halley.

Up to now, the observed structures in our hybrid simulation are in agreement with observations at 1P/Halley and other comets (cf. Balsiger et al. 1986, Neubauer et al. 1986, Neubauer 1988, Richter et al. 2011) and previous simulations (c.f. Cravens 1989, Gombosi et al. 1996, Benna and Mahaffy 2007, Rubin et al. 2014a). However, our new hybrid simulations reveal important features not yet described in the literature. Figure (4.13) displays the velocity distribution at four different positions along the Sun-comet line. Detector 3 counts all particles located in a cube which is centred at $x = -85$ km and has an edge length of 10 km. The centres of Detectors 4, 5, and 6 are located at $x = -47.5$ km, $x = -32.5$ km, and $x = -16$ km. The edge lengths are 5 km, 5 km, and 4 km. The count values in the figure are in arbitrary units. The figure shows the distribution in v_x- and v_z-direction with different scales on two separate panels. The red circle corresponds to $5\,\mathrm{km\,s^{-1}}$.

Detector 3 is located on the sunward side of the magnetic barrier. It is obvious that the

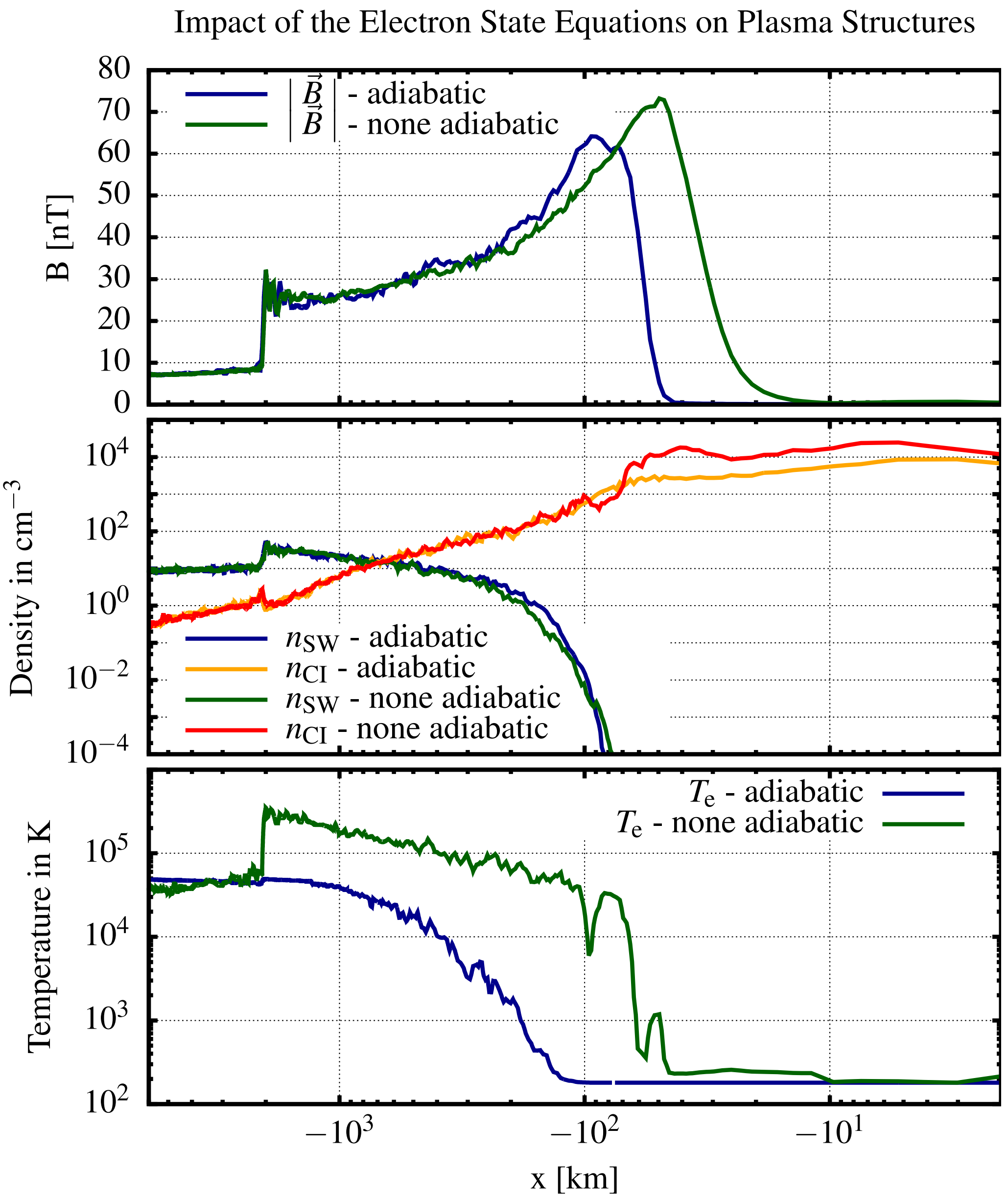

Figure 4.15: The results of two hybrid simulations. The curves labelled with *none adiabatic* are obtained from the simulation presented in this section, in which the pressure equation for the electron fluid is solved. The remaining curves, which are labelled with *adiabatic*, are from a simulation which uses an adiabatic state equation for the electron fluid. The results of the latter simulation are shown in Figure (4.2). In the upper panel the magnetic field along the x-axis is shown. The densities of the solar wind and the cometary ions are presented below. Finally, the lower panel shows the electron temperature from the two simulations.

bulk velocity has a positive z- and x-component. In addition, the two ion populations reveal two distinct velocity distributions. The faster particles with speeds above $125\,\mathrm{km\,s^{-1}}$ are picked-up upstream of the bow shock. In contrast, the slower population, with velocities up to $75\,\mathrm{km\,s^{-1}}$, is probably picked-up downstream of the bow shock. At the stagnation point, Detector 4, the population which originates from regions upstream of the bow shock, is not present anymore.

In the enlarged version of the figure (see right side of Figure 4.13) one can identify many ions moving in sunward direction with a speed of $1\,\mathrm{km\,s^{-1}}$. This population is caused by the ionisation of the neutral gas and by the collisions of ions with the neutral gas. Since we model the collisions on a statistical basis, this distinct population can be identified in detector 4, 5, and 6.

Besides the population caused by ionisation and collisions, a second population is present. This population is much hotter and has a small bulk velocity in $+x$- and $+z$-direction. Most of these particles have a velocity of about $1\,\mathrm{km\,s^{-1}}$. In the presence of a magnetic field of 78 nT, they have a gyroradius of about 2.5 km. This population is visible at detector 5, which is located in the cometary ionopause and in the recombination layer. Thus, at the recombination layer, our hybrid simulations reveal the presence of a mixture of the plasma which is picked-up upstream and plasma which originates from the cavity. A similar effect was observed by Puhl-Quinn and Cravens (1995) using 1D hybrid simulations of the cometary ionopause at 1P/Halley.

MHD simulations of comet 1P/Halley by Gombosi et al. (1996) reveal a current system at the cometary ionopause and a second one at the inner shock. In addition, a distinct region, i.e. the cavity transition layer between the cometary ionopause and the inner shock, can be observed in the simulations by Cravens (1989) and Gombosi et al. (1996). This separation is not visible in our hybrid simulation. But at 67P/Churyumov-Gerasimenko the situation differs from that at 1P/Halley: the interaction region is smaller than at 1P/Halley and the hybrid simulation shows a finite gyroradius of the ions at the stagnation point as well as the presence of different ion populations in the transition region. This will prevent a separation of the current system at 67P/Churyumov-Gerasimenko.

The velocity distributions at Detector 4,5, and 6 reveal a third ion population (Figure 4.13), which consists of ions with speeds in the range between 10 and $30\,\mathrm{km\,s^{-1}}$. This population is sparsely populated and has a velocity into $+x$-, $+y$-, and $+z$-direction, whereby the z-component clearly dominates. The more the distance to the nucleus is reduced, the more this population is thinned out because the probability for collisions increases and removes ions from this population. Nevertheless, a few ions are able to enter the cavity for about 5 km, where Detector 6 is placed. While this population is connected to the first two populations at the stagnation point, a clear separation is present at detectors 5 and 6. This separation is caused by the statistical description of the ion-neutral collisions. The faster particles can penetrate deeper into the cometary ionopause and into the cavity. Caused by the fact that these ions move into $+y$- and $+z$-direction, they should not be present at the $+y$- and $+z$-side of the cometary ionopause.

Not only the velocity distributions at the different detectors show an asymmetry with respect to the Sun-comet line, but also the structures shown in Figure (4.14) reveal a similar asymmetry in the inner coma. Due to the deflection of the solar wind flow in the outer coma, the plasma along the Sun-comet line arrives in the inner coma with a positive y- and z-velocity component. This can be emphasised by the location of the stagnation

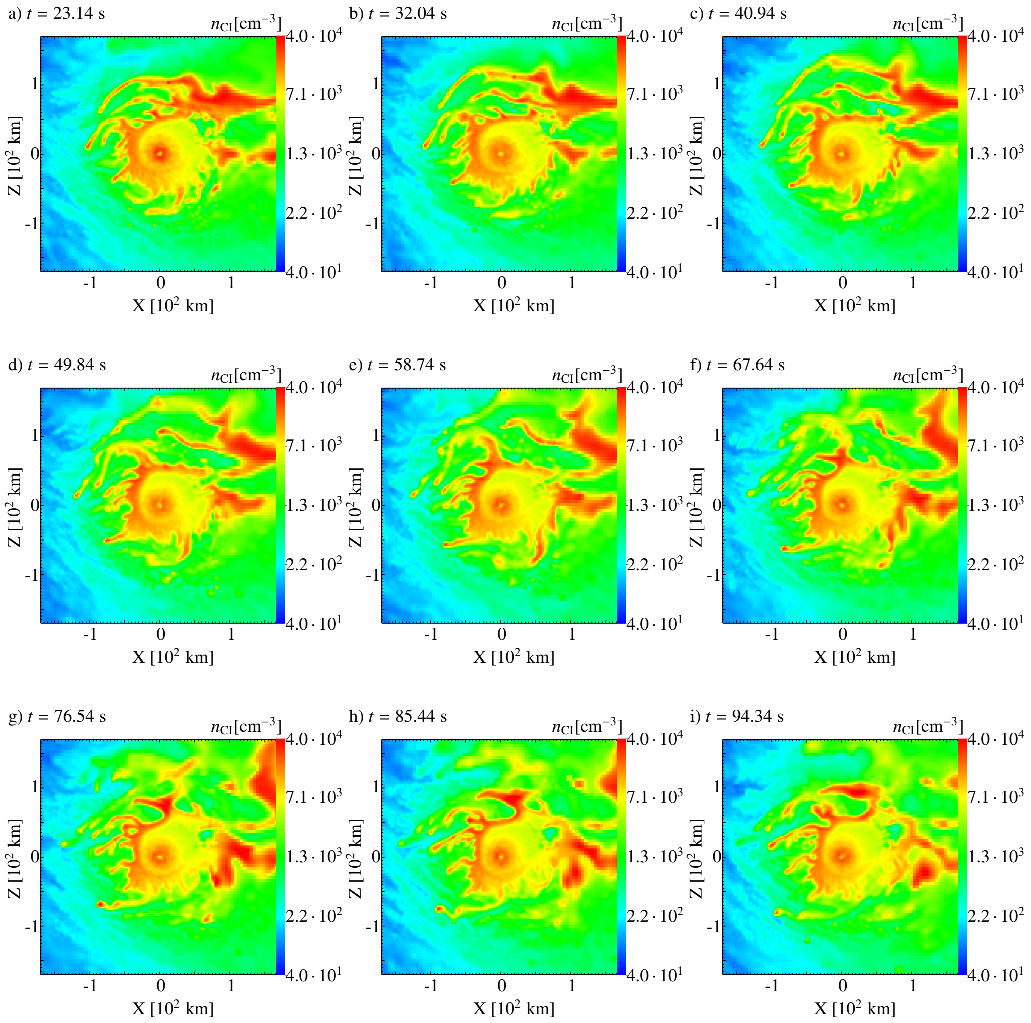

Figure 4.16: The cometary ion density on the y=0-cross-section is shown for different times during our simulation.

point, which is at (x=-44.6, y=-0.26, z=-7.49) km. Although the ions are not at rest at this point, as discussed above, the bulk velocity has at this point its minimum. Again, the shift of the stagnation point in the bulk velocity shows the deflection of the flow towards $+y$- and $+z$-direction. Based on that, the magnetic pile-up is more pronounced on the $-y$- and $-z$-side (Figure 4.14 a, and b), while the cometary ion tail is shifted towards $+y$- and $+z$-direction (Figure 4.14 d, and e).

In the same figure one can identify several thin density spikes outside the main ion pile-up region. At these thin spikes the bulk velocity of the cometary ions is reduced. Furthermore, because of the higher density therein, the electron temperature is strongly reduced in comparison to the direct vicinity of these spikes. During the simulation time, the density spikes leave the ion pile-up region on the dayside and move tailward along the boundary (Figure 4.16). During that phase the distance of the density spikes to the comet increases. The motion of the density spikes in z-direction is presented in Figure (4.12 c), which shows the density along the z-axis at various time steps. It becomes clear that the ion clouds, which are visible as as spikes, move in z-direction with a nearly constant velocity. As one can see from Figure (4.16), the density in these spikes decreases over the time, which is caused by an enhanced recombination rate in these regions due to the cold electrons. In addition, Figure (4.12 c) and Figure (4.16) show that the density spikes on the $+z$-hemisphere are much more pronounced. While the enhanced density region on the $-z$-hemisphere is limited to about 100 km, the ion density on the $+z$-hemisphere reaches higher values and the spikes can expand to about 150 km. Although the simulated time-period is limited to about 120 s, about three density enhancements can be identify.

Various authors studied the stability of the cometary ionopause and the inner shock (cf. Ershkovich and Flammer 1988, Thomas 1995) and found that the boundaries are unstable for Kelvin-Helmholtz instabilities and Rayleigh-Taylor instabilities. Recently, Rubin et al. (2012) studied the stability of the cometary ionopause in their MHD simulations of 67P/Churyumov-Gerasimenko. Their results show that a Kelvin-Helmholtz instability can be triggered either by a reduction of the spatial resolution or by the onset of a jet. In their simulation density enhancements similar to those in our simulations occurs in the case of the jet, whereas the instability in case of the enhanced spatial resolution behaves different. Although our simulation uses an isotropic neutral gas production rate, the ionisation is modelled via a statistical process, which can lead to small perturbations of the inner boundary.

Figure (4.12 d) shows the evolution of the magnetic field along the z-axis of the simulation. Here one can identify time varying structures and one can see that the size of the cavity is not constant in the $+z$-hemisphere. In the other directions the cavity surface has a nearly constant distance to the nucleus. Furthermore, the magnetic field strength reveals several enhancements, called magnetic bubbles, during the time of the simulation. Their evolution on the y=0-cross-section is shown in Figure (4.17). The magnetic bubbles leave the magnetic barrier on the dayside and move along the boundary into the direction of the tail. Thus, the magnetic field slips over the diamagnetic cavity into the tail to relax the magnetic tension, as reported by Gombosi et al. (1996). However, our simulation reveals that this process is pulsed. A comparison of the evolution of the ion density and the magnetic field shows that a magnetic bubble occurs directly after a density spike has passed the z-axis.

4.2.2.3 Outlook to Rosetta

The Rosetta spacecraft arrived at comet 67P/Churyumov-Gerasimenko in late Summer 2014 (Glassmeier et al. 2007a) and escorts the comet on its way through the inner solar system. Due to navigational constrains, the spacecraft has to increase the distance to the comet when the gas production rate of the comet increases. This is why only occasionally close flybys with closest approach distances of 8 to 20 km will be flown.

Since the gas production rate of the comet is not known yet, two scenarios are currently discussed. In the high activity case, the comet might have a gas production rate of $5 \times 10^{27}\,\mathrm{s}^{-1}$ in May 2015. At this time the comet is at 1.6 AU. Assuming that the gas production rate is equal and the solar wind values are comparable to the values used in our study, we use our simulation to obtain an outlook to the Rosetta measurements. It is planned to perform a close flyby trajectory as shown in Figure (4.14) in late May 2015. The spacecraft will fly close to the terminator and will start with a distance of about 100 km on the 21st May. The planned closest approach distance is reached on 23rd May with a minimum distance of 20 km (Figure 4.18). This figure shows the field strength of

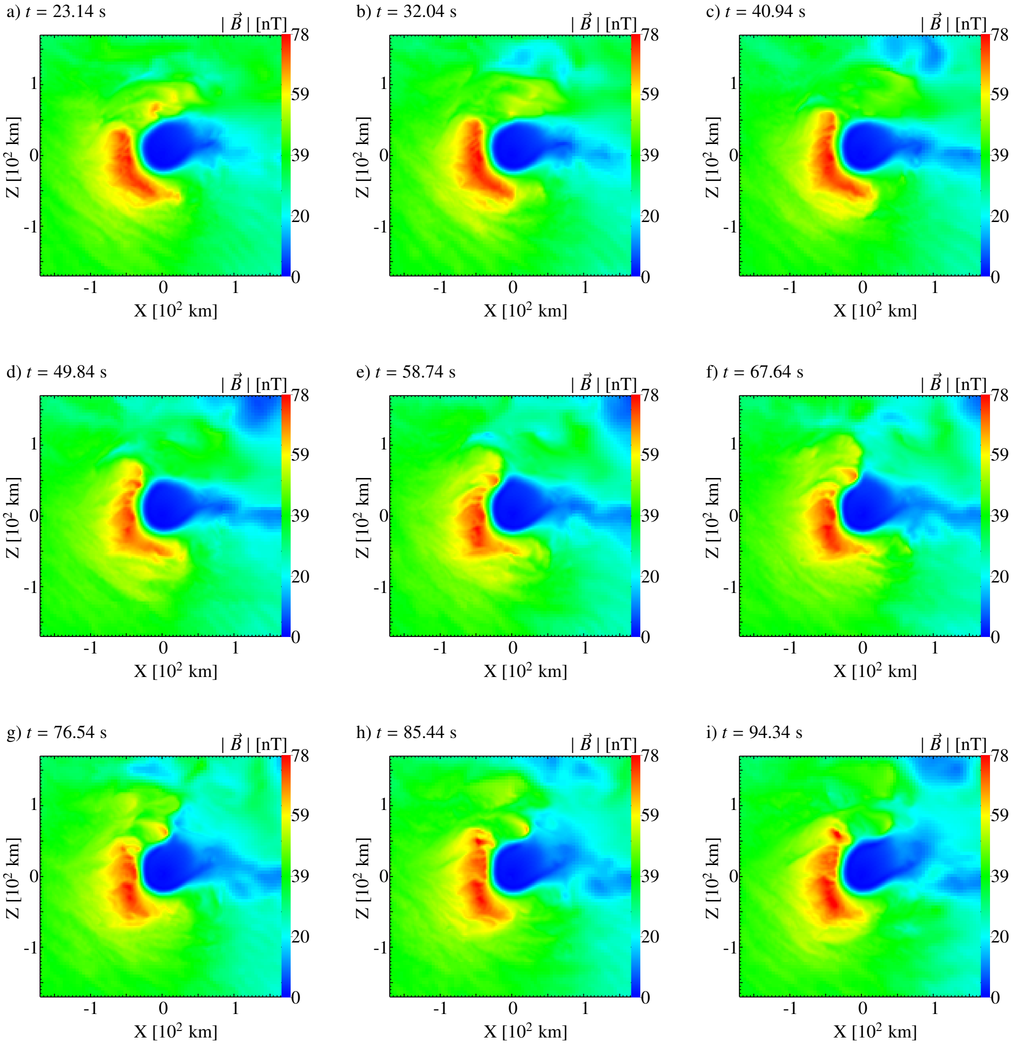

Figure 4.17: The magnetic field strength on the y=0-cross-section is shown for different times during our simulation.

the magnetic field, the cometary ions density, the electron temperature, the radial velocity, the velocity component in x-direction and the magnitude of the cometary ion velocity along the trajectory. Finally, the figure shows a simulated ion energy spectrum. This data was obtained from our simulation at a single time step, and it is assumed that the y-axis of our simulation and the ecliptic plane in real space are in coincidence.

As one can see in that figure, the spacecraft passes the pile-up region on the inbound path for about two days. In the early hours of 23$^{\text{rd}}$ May the spacecraft will enter the cavity, where it will stay for about six hours. Afterwards, it passes the pile-up region relatively quickly. The ion density will mainly be at about $10^3\,\text{cm}^{-3}$ on the first day, when the field strength of the magnetic field increases, and increases when the magnetic field will reach its maximum with about 62 nT. Here, the spacecraft will pass the ion pile-up region with densities up to $10^4\,\text{cm}^{-3}$. At about 70 km distance to the comet the x-component of the cometary ion velocity will dominate the flow, whereas the radial velocity will be comparable to the x-component at the pile-up of the ion density. In the diamagnetic cavity the radial velocity will dominate the flow, as discussed above. The energy spectra

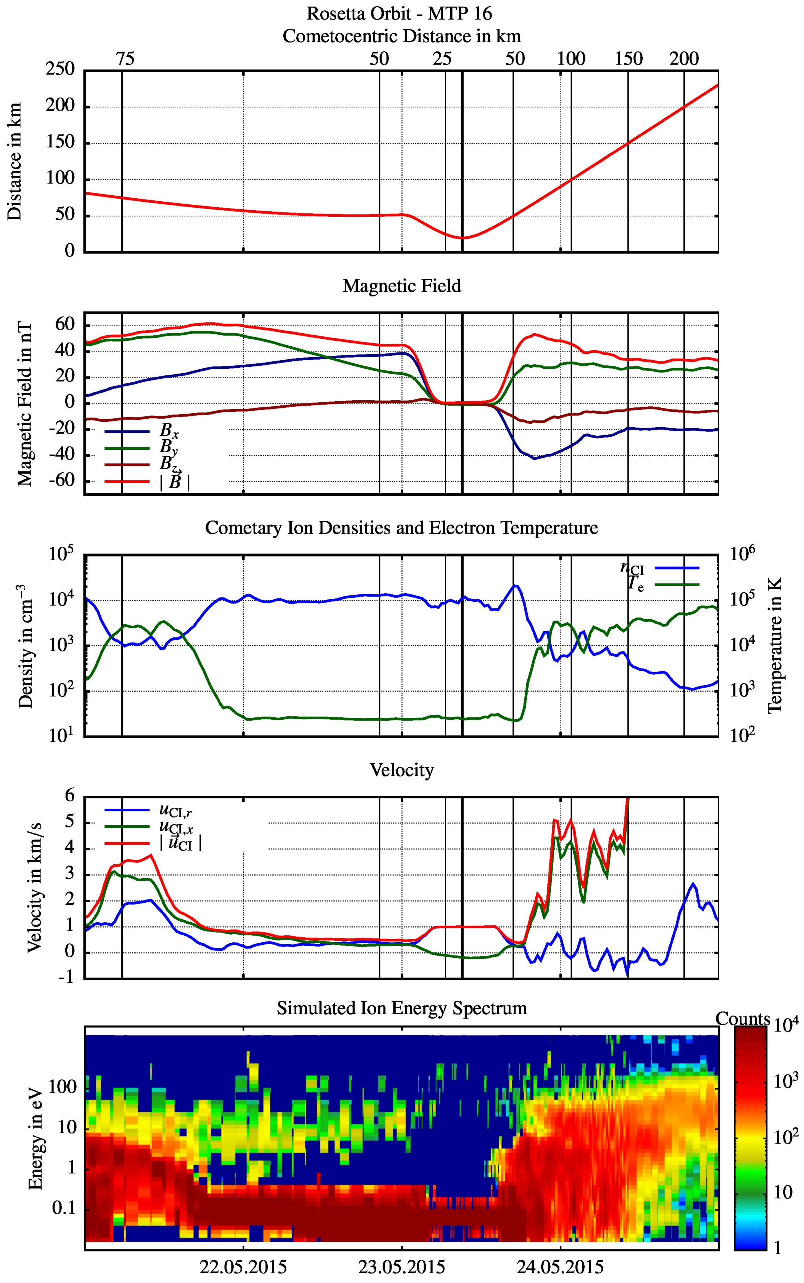

Figure 4.18: Values obtained from our simulation along a Rosetta trajectory. The first panel shows the distance of the spacecraft towards the comet over time. The second panel shows the magnetic field components and the magnitude, and the third one the cometary ion density and the electron temperature. The cometary ion velocity, its magnitude, the x-component u_{CI},x and the radial velocity u_{CI},r are shown in the fourth panel. The last panel shows an ion energy spectrum. The point of closed approach, passed on 23rd May 2015 on 9:07, is highlighted by a black line. The thinner black horizontal lines mark different cometocentric distances.

of the cometary ions along the path of the spacecraft will show a bifurcation at the ion pile-up region. The lower branch is populated with the ions from the ionisation, the ion-neutral collisions and the impinging ions. It is most dominant within a distance of about 70 km to the nucleus. Within the branch the magnetic field drops towards the nucleus. The upper branch is populated with the third ion population, which enters the transition region from $-y$-, and $-z$- direction. As the distance to the nucleus decreases, the upper branch is thinned out by ion-neutral collisions. Finally, as soon as the spacecraft enters the diamagnetic cavity, the lower branch is compressed to a thin line. This shows the presence of the inner shock, which thermalised the plasma emanating from the cavity.

Because of the fact that the ICA and IES experiments have an energy range starting at 1 eV they will not be able to detect this bifurcation (Nilsson et al. 2006, Burch et al. 2006). But the ROSINA experiments (Balsiger et al. 2007) might be able to observe this structure. We would like to point out that the real plasma conditions in May 2015 will probably be different from our parameters and, thus, Rosetta will detect a quantitatively different plasma environment. Qualitatively, however, Rosetta should observe the structures seen in our simulations and simulations as those presented here will prove a valuable tool for the interpretation of these measurements.

4.2.3 Summary

In the discussed simulation the innermost interaction region could spatially be resolved in a global hybrid plasma simulation for the first time ever. In this region our simulation predicts a magnetic barrier, a cometary ionopause, a recombination layer, an inner shock and a diamagnetic cavity. Those structures have also been identified in single-fluid MHD simulations and in observations at comet 1P/Halley. However, in contrast to the single-fluid MHD models, our simulation reveals a shift of the interaction region towards $+y$- and $+z$-direction, which is visible in all structures and boundaries, e.g. the diamagnetic cavity extends from $z = -25\,\mathrm{km}$ to about $z = 40\,\mathrm{km}$. This shift is caused by the pick-up of the cometary ions upstream of the bow shock, and leads to a deflection of the incoming flow towards that direction. Furthermore, our simulation tool self-consistently reproduces the cold electron in the innermost coma.

Caused by the fact that the ions are modelled as particles and processes, like ion-neutral collisions, are described on a statistical basis, we are able to study the phase space distribution of the ions. For example, a ring distribution of the cometary ions is identified upstream of and behind the bow shock. At the magnetic barrier the simulation reveals a separation between fast cometary pick-up ions, ionised upstream of the bow shock, and cometary ions which are ionised behind the bow shock. Closer to the nucleus three distinct ion populations are visible in the phase space:

- A population of cold ions is moving in radial direction from the nucleus with a speed of about 1 km. This population is created by ionisation and ion-neutral collision.
- The second population moves towards the nucleus, but with an additional component which allows the plasma to move around the diamagnetic cavity. This population is hotter than the first population but also moves with low speeds.
- The third population of cometary ions in the inner boundary are ions that have

> already been ionised outside of the inner region. They have a velocity of about 10 to 30 km s^{-1} and move towards the $+z$-hemisphere. This indicates that these ions are picked-up with a specific magnetic moment and hit the innermost region on their way along the cycloid. In contrast to the second population, the third population can penetrate into the diamagnetic cavity.

The simulation also reveals the presence of an instability at the inner shock, similar to the Kelvin-Helmholtz instability identified by Rubin et al. (2012), but confined to the plane perpendicular to the magnetic field. This instability leads to the formation of thin, about 5 km to 20 km wide, sharp density spikes, which move tailward. Those density spikes are closely followed by regions of an enhanced magnetic field.

Finally, a possible measurement of the instruments onboard the Rosetta spacecraft is presented for a scenario in May 2016, in case the solar wind and the interplanetary magnetic field remain stable for about four days and the comet has an isotropic outgassing. During the close flyby, the spacecraft will stay in the diamagnetic cavity for about 6 hours and in the inner boundaries for about a day. In contrast to the Giotto spacecraft, which passed the cometary ionopause at 1P/Halley within a second, the Rosetta measurements are a unique opportunity to understand the cometary plasma interaction and to identify more interesting features. However, in order to understand these measurements, global simulations of the plasma environment are required.

5 An Introduction to RPC Science Planning

The aim of the RPC science planning is the best possible preparation of the RPC measurements at the comet. In principle, the RPC instruments are monitoring instruments, which means that they should always operate to allow a continuous exploration of the cometary plasma environment. This makes it possible to study structures or events that are difficult to predict but might be passed unexpectedly. But, since RPC is in a competition with the other instruments onboard Rosetta, only a very limited data rate is available for this survey. In addition, an allocation of a more appropriate pointing for the ICA and the IES instruments is neither possible.

Besides continuous operations, the RPC team has defined a list of about 40 measurement objectives which intend to study various effects, such as the known boundaries and structures, in more detail. For these studies, specific measurements with more appropriate instrument parameters, higher data rates and acceptable pointing conditions are needed. However, the fundamental requirement for most of these measurement objectives is the spacecraft trajectory, which has to pass the region of interest. In order to check this, the positions of these regions have to be determined for any time during the mission. Based on that, Windows of Opportunities (WoO) have to be computed for each of the measurement objectives, since these WoO are required for the planning process by the Rosetta mission (RSGS-Team 2013).

In the last three chapters the remarkable capabilities of the A.I.K.E.F. code at very different stages of the mission have been presented. It was shown that the model is qualified to make predictions about the position of the interesting plasma structures and boundaries during the entire mission phase. This chapter gives a short description of how the WoO are determined on the basis of the A.I.K.E.F. simulations and how they are used in the RPC science planning.

5.1 Requirements and the Approach

As given by the mission planning process, which was briefly described in Section (1.3.3), the predictions have to be made very early in the planning process, namely during the skeleton planning stage. At this stage trajectory designs for the different cometary activity levels, i.e. HAC, LAC or Preferred Activity Case as given by the SWT, are discussed and a first attempt at scheduling the measurements of all instruments is made. This implies that it has to be clear which measurement objectives can be fulfilled. In case no objective fits the parameter, actions can be taken to improve the trajectory, pointing or data rate.

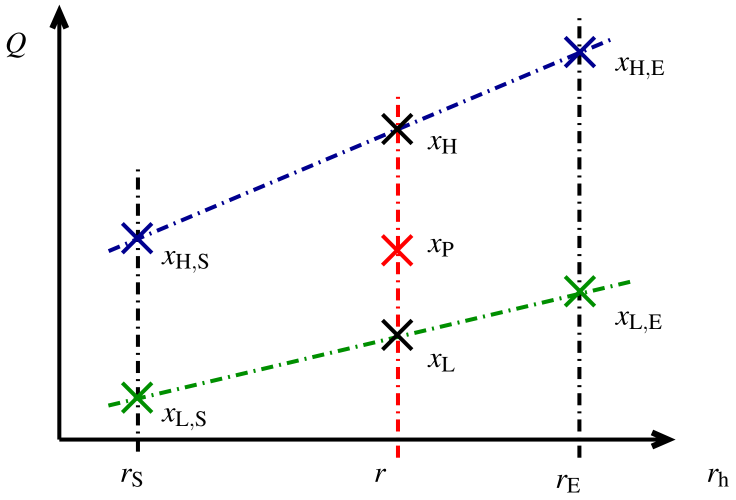

Figure 5.1: A sketch of the interpolation scheme for a parameter x_{p} from the parameters $x_{\mathrm{L,E}}$, $x_{\mathrm{H,S}}$ and $x_{\mathrm{H,E}}$. The horizontal axis indicates the heliocentric distance. The vertical axis represents the gas production rate Q. A description is given in the text.

Another requirement, which follows from this mission planning schedule, are appropriate turnaround times in the order of a few weeks or less for a recomputation of the WoO. Since it is intended to use A.I.K.E.F. simulations for the determination of the WoO, a problem arises from this constraint: the hybrid model is exceedingly demanding in terms of computational power and time and therefore it is not possible to rerun the simulations for new parameters within the required reaction times. In addition, it is not feasible to run simulation for all possible configurations which are expected during the mission time. Hence, only a limited number of hybrid simulations can be performed and the positions of structures and boundaries have to be interpolated from these results. For each planning segment at least four hybrid simulations are performed: two simulations with the solar wind conditions at the start of the segment, one with the gas production rate of the LAC and the other with the gas production rate of the HAC. The remaining two simulations study the plasma environment at the end of the segment, again one simulation with the LAC and one with the HAC gas production rate. Since a voxelwise[1] interpolation is not necessary, as will be discussed below, the various boundaries and structures are described by simple geometric shapes, like spherical shells, cylinders or hyperboloids. Thus, only the required parameters have to be interpolated in order to derive the positions of boundaries and structures at any given moment.

The interpolation works as follows: from each of the four simulations the parameters for geometric shapes are obtained, for example $x_{\mathrm{L,S}}$, $x_{\mathrm{L,E}}$, $x_{\mathrm{H,S}}$ and $x_{\mathrm{H,E}}$. The indices L,H,S and E denote LAC, HAC, start and end, respectively. This means that $x_{\mathrm{L,S}}$ is a parameter from the simulation with the LAC gas production rate at the start of the segment. In a first step the parameter x_{L} is determined by an interpolation between $x_{\mathrm{L,S}}$ and $x_{\mathrm{L,E}}$ which are parameters with different heliocentric distances and different gas productions rates. However, it can be assumed that for small intervals the parameters of the structures depend linearly on the gas production rate, which itself depends only on the heliocentric distance. The interpolation to a heliocentric distances r can be calculated in the same way

---

[1] A voxel represents the mean value of a numerical cell in the hybrid simulations.

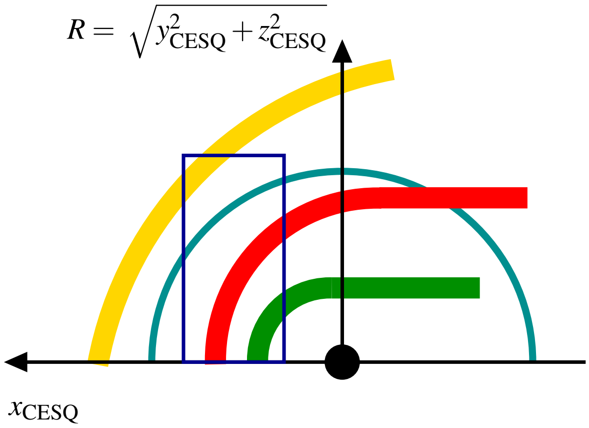

Figure 5.2: The cylindrical coordinate system used for the calculation of the WoO. The x-axis points towards the Sun and the distance to the Sun-comet line is given by R. The origin is in the centre of the nucleus. The coloured objects show the various boundaries and regions of interest in the environment of the comet schematically.

as the ESA flight dynamics team obtains the gas production rate between a pair of given values (Companys 2012). Hence, the parameter x_{L} is given by

$$x_{\mathrm{L}} = \exp\left(\frac{\log(x_{\mathrm{L,E}})\left(\log(r) - \log(r_{\mathrm{S}})\right) + \log(x_{\mathrm{L,S}})\left(\log(r_{\mathrm{E}}) - \log(r)\right)}{\left(\log(r_{\mathrm{E}}) - \log(r_{\mathrm{S}})\right)}\right), \tag{5.1}$$

where r_{S} and r_{E} denote the heliocentric distances at the start and the end. x_{H} is obtained by the same scheme. In order to obtain the value of interest x_{P}, between x_{L} and x_{H} a linear interpolation is done according to the gas production rates:

$$x_{\mathrm{P}} = \frac{x_{\mathrm{H}}(Q_{\mathrm{P}} - Q_{\mathrm{L}}) + x_{\mathrm{L}}(Q_{\mathrm{H}} - Q_{\mathrm{P}})}{Q_{\mathrm{H}} - Q_{\mathrm{L}}}, \tag{5.2}$$

where Q_{H}, Q_{L}, and Q_{P} are the gas production values from the HAC, LAC and the preferred case at the heliocentric distance r, respectively. By this interpolation scheme a fast recomputation of the WoO is possible, when a new gas production rate for the preferred case is suggested by the SWT.

Another problem for the RPC planning is the unknown state of the solar wind. Although solar wind predictions are possible, it is not feasible to use them in the mission planning because at the point in time when the prediction can be done, about a few days ahead of the actual execution onboard the spacecraft, the commands are already at MOC for a final check (Figure 1.7). Thus, only nominal solar wind parameters can be used for planning, as described in Section (2.1). Moreover, the orientation of the plasma interaction and all boundaries therein is controlled by the orientation of the interplanetary magnetic field in the undisturbed solar wind. However, this is also not predictable and, therefore, the position of the boundaries with respect to the CSEQ frame is not known[2]. If one assumes that the angle between the solar wind and the interplanetary magnetic field

---

[2] In the comet centered solar equatorial (CSEQ) frame the x-axis is pointing towards the Sun, the z-axis is the component of the rotation axis of the Sun, which is perpendicular to x, and the right handed system is completed by the y-axis, which is parallel to the Sun's equatorial plane.

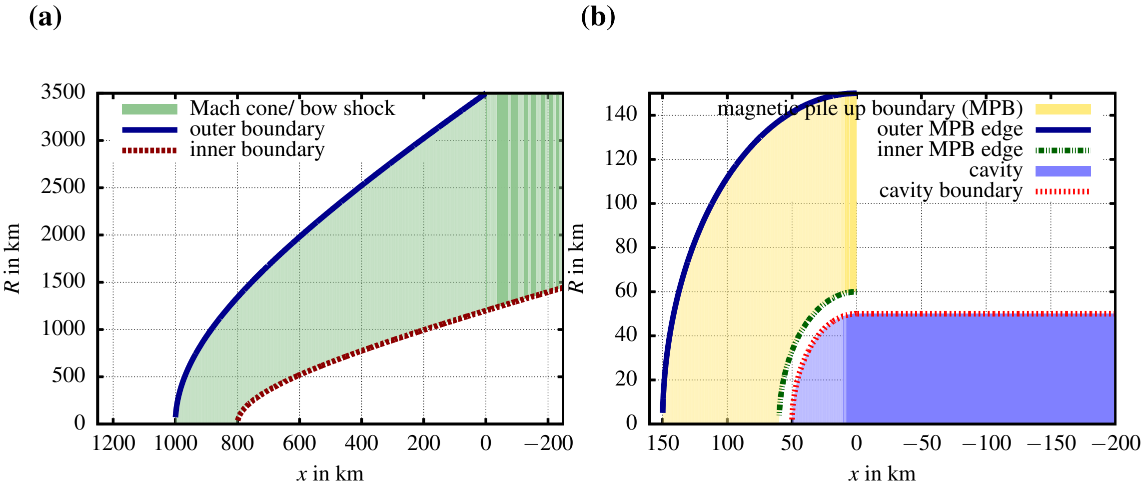

Figure 5.3: Models of some boundaries and structures in the cylindrical coordinate system. In panel a) a shape used for the bow shock and the Mach cone region is shown. In reality the bow shock or the Mach cone will be somewhere in this region. Consequently, the more sunward the more accurate is the prediction. In b) the shapes of the magnetic pile-up region and the diamagnetic cavity are presented.

is constant at a certain heliocentric distance and the nominal solar wind parameters are appropriate, only one degree of uncertainty remains: the orientation of the magnetic field in the yz-plane of the CSEQ coordinate system. Consequently, for the calculation of the WoO, a cylindrical coordinate system is used, which is given by the Sun-comet line as the cylinder axis and the radial distance to this line (Figure 5.2).

For each measurement objective that was agreed upon the RPC team, there are conditions that specify the WoO. Some definitions are rather simple, for example the measurement objective *PICKUPION* requests heliocentric distances smaller than 4 AU. Consequently, the WoO for this measurement objective opens on 22nd May 2014. Other simple definitions request specific time intervals, such as the first science sequence, which is the first interval of measurements conducted by the lander on the nucleus. But, most of the measurement objectives require the spacecraft to be in a specific region of the plasma environment. Here, only some examples are given:

- Bow shock and Mach cone:
  The measurement objectives *BOWSHOCKDYNAMICS* and *BOWSHOCKMONITORING* are intended to study the bow shock and the Mach cone. The first measurement objective focusses on the dynamics in the bow shock or the Mach cone, such as the heating and wave excitation and, therefore, requests the highest possible data rate. In contrast the second measurement objective monitors the properties of the Mach cone and the bow shock in a way that the evolution or its position can be studied on the basis of the measurements. Both measurement objectives require a spacecraft position in the bow shock or in the Mach cones. Although, both structures differ, the hybrid simulations suggest that the Mach cone transforms into a bow shock if the massloading of the plasma increases (Bagdonat and Motschmann 2002). Consequently, both structures are modelled with the same shape; a hyperboloid (Figure

5.3 a). The outer boundary is given by

$$r_{\mathrm{out}}(x) = \frac{R_{\mathrm{BS}} f_{\mathrm{max}}}{\sqrt{3}} \sqrt{\frac{(-x+2R_{\mathrm{BS}})^2}{R_{\mathrm{BS}}^2} - 1}\,, \tag{5.3}$$

and the inner edge by

$$r_{\mathrm{in}}(x) = \frac{(R_{\mathrm{BS}} - w)\, f_{\mathrm{min}}}{\sqrt{3}} \sqrt{\frac{(-x+2\,(R_{\mathrm{BS}} - w))^2}{(R_{\mathrm{BS}} - w)^2} - 1}\,. \tag{5.4}$$

R_{BS} denotes the subsolar stand-off position of the bow shock or the Mach cone and w represents the width of the shock, which is determined by the width of the current layer at the bow shock in the hybrid simulations. For example, the bow shock in the simulation discussed in Section (4.2) has a stand-off distance of $R_{\mathrm{BS}} = 2000\,\mathrm{km}$ and a width of $w = 200\,\mathrm{km}$. The asymmetry of the shape is considered in the flaring factors f_{max} and f_{min}. They are defined by the minimal and the maximal ratio of the bow shock distance at the terminator to the subsolar distance. For the simulation discussed in Section (4.2), the distance of the bow shock at the terminator to the nucleus varies between about 2800 km and 5000 km. Hence, f_{min} is 1.4 and f_{max} is 2.5.

In case of a Mach cone, no clear jumps in the field strengths occur and, this is why, the width w increases. In addition, since a Mach cone is more asymmetric than a bow shock, the minimum flaring factor is generally much smaller. Consequently, the predictions of the bow shock and the Mach cones are more precise far upstream of the comet.

- Magnetic pile-up boundary:
  In contrast to other boundaries and regions, the magnetic pile-up boundary could not be identfied in the hybrid simulations, yet. However, observations at other comets suggested that such a boundary might be a common feature and this is why RPC defines a measurement objective to search for this boundary. Consequently, the current knowledge has to be recaptured.

  The magnetic pile-up boundary was first discovered by the magnetometer onboard the Giotto spacecraft during the 1P/Halley flyby (Neubauer et al. 1986). The boundary is located between the bow shock and the cometary ionopause and is characterised by a sharp jump in the magnetic field strength. The magnetometer onboard Giotto observed a jump on the inbound leg from roughly 10 nT to 30 nT (Figure 1.2). The jump on the outbound path was not as well defined (Neubauer et al. 1986, Neubauer 1987).

  Other characteristics of the boundary are a decrease of the electron density and the electron perpendicular pressure (Mazelle et al. 1989). In addition, Fuselier et al. (1991) found an abrupt increase in the rate of charge exchange using the IMS instrument, which indicates a higher density. A decrease in the proton density was also found by the IMS and the JPA instruments (Goldstein et al. 1987). Mazelle et al. (1995) showed that the length scale of the boundary is smaller than the local heavy ion gyroradius.

Interestingly, the VEGA-1 and VEGA-2 missions to comet 1P/Halley found no evidence of such a boundary in the cometary environment (Neubauer 1987). However, during the flyby of the Giotto spacecraft at comet 26P/Grigg-Skjellerup, with the closest approach distance of 330 km, a region with an enhanced magnetic field was found that stretched over 2500 km along the trajectory (Neubauer et al. 1993). In the electron data set obtained by the RPA instrument, Mazelle et al. (1995) found a signature of the magnetic pile-up boundary at this comet.

By a minimum variance analysis of the magnetometer data Neubauer (1987) determined the positions of the magnetic pile-up boundary at 1P/Halley ($r_{\text{in}} = 136 \times 10^3$ km and $r_{\text{out}} = 262 \times 10^3$ km) and modelled the boundary with two models, as a half-sphere on the dayside with a cylinder on the nightside and as a paraboloid. The half-sphere has a radius of 2.19×10^5 km and its centre is located at $(-6.7,-8.7,1.3)\times 10^4$ km in CSE coordinates (cometocentered solar ecliptic coordinates), which differ from the nucleus position. The semi-latus rectum of the paraboloid is 202×10^3 km and the stand-off distance is 215×10^3 km. However, this paraboloid has an aberration from the solar wind direction of 6°. In order to explain the large discrepancy between the inbound and outbound position, Neubauer (1987) suggests a temporal variation of the incident solar wind. Another explanation of the huge discrepancy is a flaring of the boundary on the outbound side and a non-flaring inbound side.

As follows from the minimum variance analysis, the boundary is either a tangential discontinuity or a slowly propagated rotational discontinuity (Neubauer 1987). However, a stationary tangential discontinuity would prevent the transport of plasma and magnetic field into the magnetic pile-up region, which is required to create this region. The idea of a propagating rotational discontinuity is problematic because the boundary should not be present at other comets. Thus, the observation at 26P/Grigg-Skjellerup somewhat contradicts this idea.

The hybrid simulation which was presented in Section (4.2) reveals a clear magnetic pile-up region, but on the upstream side no jump in the magnetic field strength is present. The plasma interaction at Mars reveals a similar boundary, which is also named magnetic pile-up boundary and characterised by an increase in the magnetic field strength. Because of the larger amount of available data, Nagy et al. (2004) found that the increase is in coincident with a sharp drop in solar wind proton density and an increase in the heavy ion density, which indicates a region commonly called the ion composition boundary. Since it is present in the hybrid simulation, the position of this boundary is used for the magnetic pile-up boundary. Because this boundary reveals an asymmetry to the Sun-comet line, like all other boundaries in our study (Section 4.2), two half-circles are used to model the position for the WoO calculation (Figure 5.3 b).

- Diamagnetic cavity:
  About five measurement objectives of RPC intend to study the diamagnetic cavity and the cometary ionopause in detail. The diamagnetic cavity is modelled by a half-sphere and a cylinder on the night side (Figure 5.3 b). The cylinder on the nightside is motivated by the simulation in Section (4.2.2.2), where the asymmetry shifts the ion tail away from the Sun-comet line and modifies the cavity.

> Because the diamagnetic cavity is the innermost region in the plasma environment, it might be possible that the hybrid simulations cannot resolve the cavity. This is why the WoO is open whenever the spacecraft is closer to the nucleus than a size of three cells in the simulation.

5.2 The RPC WoO Tool

In order to satisfy all the needs arising from the planning and the limitations by the hybrid simulations, the *RPC WoO Tool* has been developed as part of this work. The program is written in C++, and it uses the Qt framework[3] to generate a graphical front-end and the SPICE tool kit[4] to obtain orbital information of the comet and the spacecraft.

Because some of the measurement objectives request the spacecraft to stay in the same region but might need different other parameters, such as instrument mode or pointing, the regions in the program are computed independently from the measurement objectives. Each region is modelled as an object of the *region* class, which stores information on the region, i.e. the parameters needed to compute the region position and the shape. Consequently, each object of this class can calculate the position or area where the structure, boundary or region of interest is located. A second class handles the RPC measurement objectives. An object of this class contains the information given by the RPC wiki and is requested by the Rosetta project:

- ID: a unique identification of the measurement objective
- Duration (min/pref): the minimum and the preferred duration of the measurements
- Frequency (min/pref): the minimum and the preferred repetition frequency of the measurement.
- PrefSchedulingCondition: the preferred scheduling condition defines additional conditions for the scheduling of a measurement, e.g. as close as possible to the nucleus or as most sunward as possible
- Pointing: the requested attitude of the spacecraft, either mandatory or optional
- ROMM (min/pref): a ROMM (RPC operation macro mode) defines the datarate produced by the instruments to perform the measurements
- JointOps: lists the instruments which have to operate in parallel during this measurement

In addition, each object has a link to the requested region and stores the times when the measurements are possible, i.e. the WoO. Other classes handle the orbital information on the comet and the spacecraft, such as the distance to the Sun and the position of the spacecraft at the comet, or the gas production rate.

The program works as follows: after the program start, some initial parameters are requested from the user which defines a scenario, such as the start and end time and the

---

[3] See https://qt-project.org

[4] See http://naif.jpl.nasa.gov/naif

information on a segment. For each hour in this segment, the heliocentric distance of the comet and the spacecraft position at the comet are calculated via the SPICE toolkit. Depending on this information, the gas production rate of the comet, based on a pre-set activity level, solar wind parameters, and the photoionisation rate at this point in time are computed. In the next step, the positions of the regions are recalculated on the basis of the gas production parameter via the interpolation scheme discussed above. Afterwards, it is checked for each measurement objective if the spacecraft position is within the requested region. In case the spacecraft enters or leaves the region, the time is recorded.

At the end, the program stores the time intervals when a measurement is feasible or not, which are the WoO. In order to deliver these WoO to the RPC team and the Rosetta project, the *RPC WoO Tool* generates a webpage for each segment. On this webpage one finds a table which on the one hand contains all information of a measurement objective in this segment, as listed above, plus a list of WoOs for this measurement objective. On the other hand, with a granularity of six hours the table highlights for each measurement objective, when a WoO is open during these six hours blocks. A granularity of six hours is used, since the measurements of all instruments onboard the spacecraft are also scheduled with a granularity of six hours in the skeleton planning stage. Hence, with the help of this table, the RPC planners[5] can schedule the measurement during the skeleton planning stage. Since, the information fields are copied into the spreadsheets of the skeleton planning by the RPC planners, as well, the ASPEN tool can perform a more detailed planning of the measurements in the LTP stage.

5.3 Mission Planning: Status Report

As mentioned above, the WoO have to be computed for each of the RPC measurement objectives for various cases almost continuously during the mission. In order to give an example of the calculated WoOs, Figure (5.4) presents the WoO for a few RPC measurement objectives in the segment MTP16b of the HAC. This segment starts on the 20th May 2015 and last until 2nd June 2015. At the time of writing, Rosetta is intended to perform a close flyby during this segment. The distance between Rosetta and the nucleus will vary between 19.9 km and 378.8 km. The gas production rate of the comet increases from $5 \times 10^{27}\,\mathrm{s}^{-1}$ to $6 \times 10^{27}\,\mathrm{s}^{-1}$. Despite the fact that the solar wind parameters and also the photoionisation are different from those used in Section (4.2), the comparable gas production rate indicates that the state of the plasma interaction is comparable to those discussed in Section (4.2). Hence, a fully developed bow shock and a diamagnetic cavity should be present.

As can be seen in Figure (5.4), the diamagnetic cavity will be crossed on the 23rd May. The WoO for the measurement objective *CAVITYINVESTIGATION* opens for 7 hours, from 06:00 to 13:00. Before and after this timeperiod, the WoO for the measurement objective *IPAUSESTABILITY* is open. Since the spacecraft approaches the point of closest approach from the nightside, i.e. between 18 o'clock and 6 o'clock local time, the spacecraft will cross the ionopause on the nightside as well. In this region, the measurement

---

[5] A team of RPC team members which schedules the measurements within a segment in the skeleton planning stage and is responsible for a segment from the skeleton planning stage to the MTP planning stage.

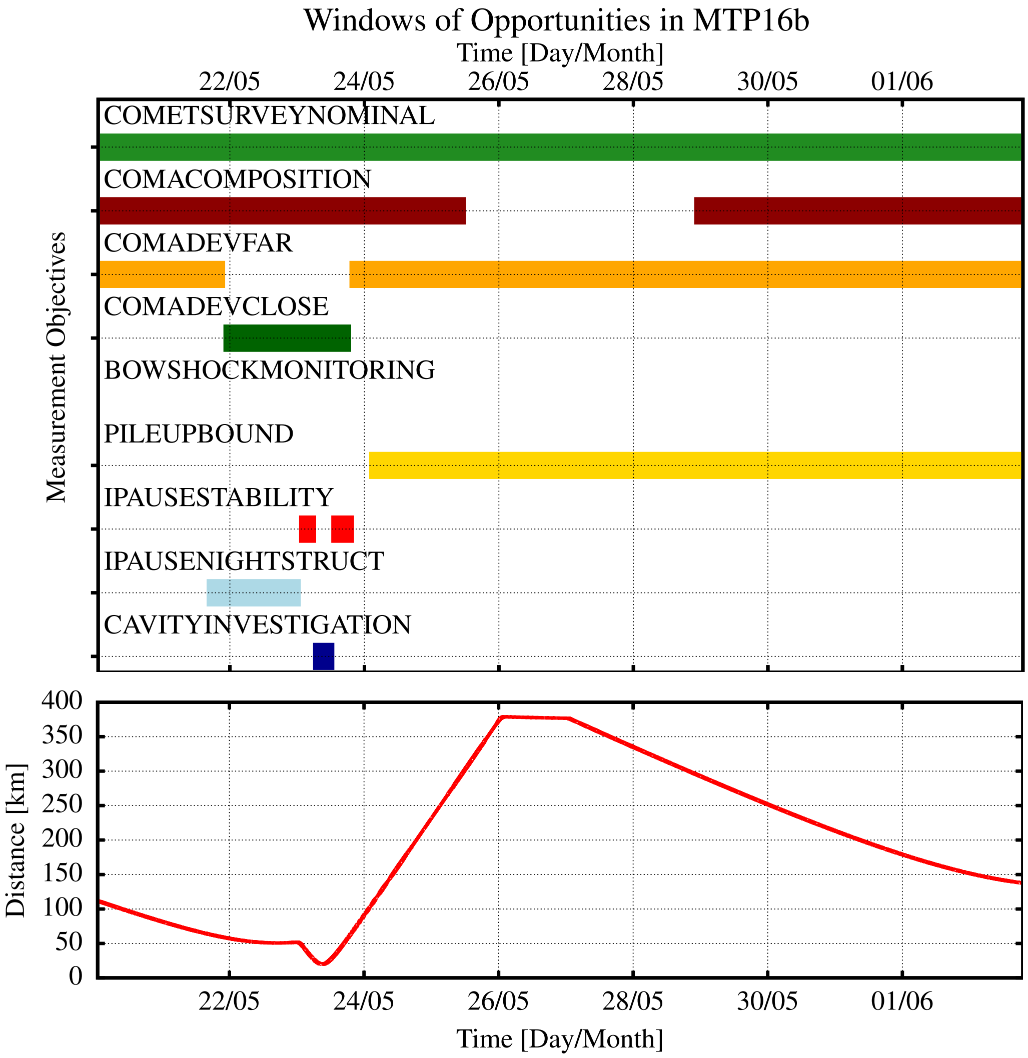

Figure 5.4: An overview of the WoO for a few measurement objectives during the MTP16b, which starts on 20th May 2015 and ends on 2nd June 2015, in the HAC. At the time of writing, a close flyby was planned during this interval. The bottom panel shows the cometocentric distance of the spacecraft versus the time by a red solid line. The closest approach distance of about 19.9 km will be reached on 23rd May 2015 at 09:07. During this segment, the maximum distance will be about 378.8 km. Coloured intervals in the upper panel indicate when the required location is met and the measurement objective could be scheduled. For the sake of simplicity, only nine of 40 measurement objectives are presented here.

objective *IPAUSENIGHTSTRUCT* can be scheduled. Since the flow of the plasma in this region is radial, the WoO for the measurement objective *COMADEVCLOSE* opens. During the remaining time the spacecraft is in a plasma where the flow does not move radially from the nucleus and the measurements for *COMADEVFAR* can be performed, therefore the IES instrument requests solar wind pointing. On the outbound path, the spacecraft is located on the dayside and close to the ion composition boundary. Thus, the WoO for the measurement objective *PILEUPBOUND* opens. In addition, the figure indicates that

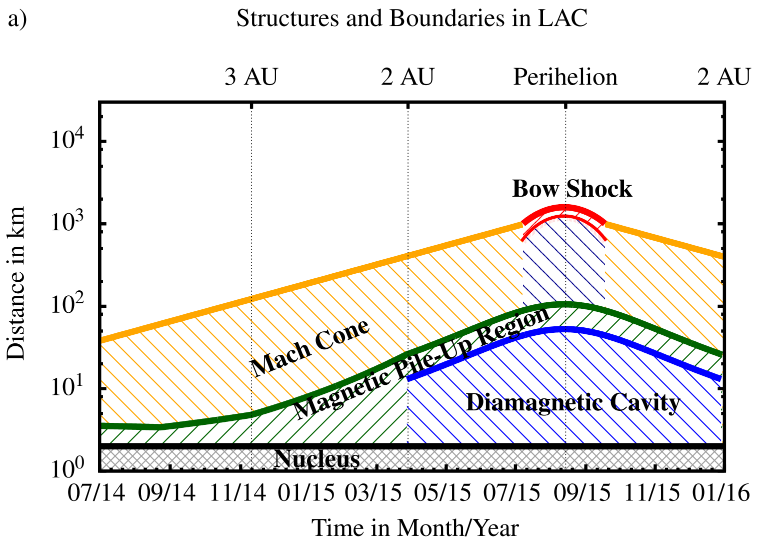

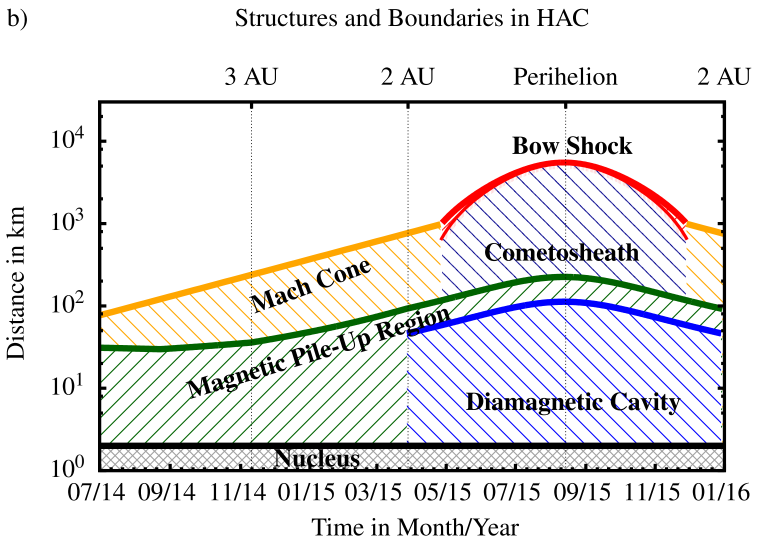

Figure 5.5: An overview of the major plasma structures and boundaries at comet 67P/Churyumov-Gerasimenko during the comet phase of the Rosetta mission for the LAC (a) and the HAC (b). In both plots, the subsolar distances are shown. More details are given in the text.

the measurement objective *COMACOMPOSITION* can be scheduled within two timeperiods. This measurement objective requests a spacecraft distance closer than 300 km to the nucleus. In order to guarantee measurements at least in a monitoring mode, with all RPC instruments in normal mode, the WoO for the measurement objective *COMETSURVEYNOMINAL* is open at any time. As mentioned above, in this example only a very limited number of measurement objectives are presented as an example.

Because the mission planning is still ongoing at the time of writing, a complete picture of the predicted plasma interaction on the basis of these new interpolation scheme and the simulation cannot be given, yet. Instead, an estimated overview based on lessons learned from this thesis and a simple analytical model is presented. Such an overview was also presented by Koenders et al. (2013), which is, however, based on the old gas production model by Lamy et al. (2007).

In a current version, which is shown in Figure (5.5), some improvements have been made. The figure shows the distances of plasma structures along the Sun-comet line over the time during the escort phase for both activity cases. At large heliocentric distances the gas production rate is low. Thus, only a Mach cone is triggered. In the beginning, the Mach cone is mostly present downstream and only a small footpoint is present on the dayside. Hence, the subsolar stand-off distance is small. However with an increasing gas production rate, the stand-off distance increases (Bagdonat and Motschmann 2002). This increase is only estimated by a logarithmic fit, since the gas production rate of the comet grows exponentially. At a distance of about 1000 km, the Mach cone transfers into a bow shock, as discussed in Section (4.1). In the case of the HAC, this occurs at the end of April 2015, while in the LAC the bow shock is only fully established in mid-June. In order to calculate the stand-off positions of the bow shock during the perihelion passage, Equation (4.9) is used. While the bow shock will reach a maximum distance of about 5400 km in the HAC, it will only reach 1500 km in the LAC.

The latter distance is reasonable to be reached by the Rosetta spacecraft with a limited amount of time and fuel. Hence, RPC requests a dayside excursion to study the dayside of the cometary plasma environment and a fully developed bow shock. Currently it is planned that this excursion will reach distances of 1500 km with an angle of about 55° to the Sun-comet line. Because of limitations in the planning process, the excursion can only be placed in the same segment for the two cases, i.e. HAC and Preferred Activity Case. Hence, on the basis of hybrid simulations the segment MTP21b, in October 2015, has been selected. For the HAC a crossing of the bow shock is not likely with this trajectory, but, as demonstrated in Section (4.1), the stand-off distance strongly depends on the solar wind parameters. For example, some small fluctuations of the interplanetary magnetic field lead to large variations in the stand-off position and the bow shock might pass the spacecraft during this excursion. However, the more likely scenario is the preferred activity case, which currently predicts a gas production rate of 125 % of the LAC. In this scenario, the hybrid simulation reveals that the bow shock will be crossed by the spacecraft trajectory. Consequently, RPC will gather data of the evolution of a Mach cone to a bow shock during the mission.

Closer to the nucleus, one finds the magnetic pile-up region. Since no analytical model is available to describe the position of this region, it is assumed that maximum distance of this region is about twice the size of the diamagnetic cavity. The size of the diamagnetic cavity is obtained from the model by Cravens (1986). In this model, it is assumed that the magnetic pressure and the ion-neutral friction force balance each other at the cometary ionopause. Furthermore, it assumes a stagnant plasma flow and discusses only radial changes:

$$\frac{1}{2\mu_0}\partial_x B^2 = k_{\mathrm{n}}^{\mathrm{coll}} n_{\mathrm{CI}} m_{\mathrm{CI}} n_{\mathrm{CN}} u_{\mathrm{CN}} \, . \tag{5.5}$$

The plasma density at the cometary ionopause can be estimated by the photochemical equilibrium (Equation 2.101) and the neutral gas density close to the nucleus is given by

Equation (2.7). Hence, the equation can be converted to

$$\partial_x B^2 = 2\mu_0 k_{\mathrm{n}}^{\mathrm{coll}} \sqrt{\frac{\nu Q}{4\pi u_{\mathrm{CN}} \alpha(T_{\mathrm{e}}) r^2}} m_{\mathrm{i}} \frac{Q}{4\pi u_{\mathrm{CN}} r^2} u_{\mathrm{CN}} \,. \tag{5.6}$$

After an integration from $r = \infty$, which is in the magnetic pile-up region, to r and the use of $B = 0\,\mathrm{nT}$ at the cometary ionopause, this equation yields

$$r_{\mathrm{cs}} = \sqrt{\mu_0 k_{\mathrm{n}}^{\mathrm{coll}} m_{\mathrm{CI}}} \left(\frac{\nu}{u_{\mathrm{CN}} \alpha(T_{\mathrm{e}})}\right)^{1/4} \left(\frac{Q}{4\pi}\right)^{3/4} \frac{1}{B_{pile-up}} \tag{5.7}$$

as the distance of the cometary ionopause to the nucleus.[6]

$B_{\mathrm{pile-up}}$ denotes the magnetic field strength in the magnetic pile-up region at $r = \infty$. This field strength can be estimated by assuming that the entire solar wind ram pressure is equal to the magnetic pressure in the pile-up region (Huddleston et al. 1992b)

$$B_{\mathrm{pile-up}} = \sqrt{2\mu_0 m_{\mathrm{SW}} n_{\mathrm{SW}} v_{\mathrm{SW}}^2} \,. \tag{5.8}$$

However, if one applies this to the scenario discussed in Section (4.2), one gets a maximum magnetic field strength of $B_{\mathrm{pile-up}} = 63.3\,\mathrm{nT}$, which is below the maximal magnetic field strength observed in the simulation of $B = 78\,\mathrm{nT}$. An evaluation of Equation (5.7) leads to a radius of the diamagnetic cavity of about 30 km, in case the maximum magnetic field is 63.3 nT, and about 24 km, in case of $B = 78\,\mathrm{nT}$. This is comparable to the result of the hybrid simulation. However, at larger heliocentric distances the kinetic effects become more important and the fluid approach collapses. This is why the diamagnetic cavity is not shown at larger heliocentric distances.

As already mentioned above, Rosetta will perform a number of close flybys during the mission. These close flybys will have closest approaches of 8 km to 20 km. Hence, a detection of the diamagnetic cavity by the RPC instruments seems to be reasonable, but the time in the cavity will be very limited. Because of navigational constraints, the spacecraft moves to large distances from the nucleus, for example about 400 km in MTP16b in HAC. Consequently, these close flybys can be used by RPC to observe all major structures in a very limited amount of time. However, in order to prepare those few close flybys the hybrid simulations and the resulting WoO are absolutely necessary. Only by doing so, a success of the RPC measurements can be achieved.

---

[6] The deduced equation seems reasonable and has the same functional dependency to Q and $B_{\mathrm{pile-up}}$ as the Equation (20) given in Cravens (1986). However, both equations produce different distances for the same parameters. This might be caused by a different expression for the photochemical equilibrium used by Cravens (1986). However, in contrast to the equation by Cravens (1986), the equation which is deduced here is not able to reproduce the observed ionopause distance at comet 1P/Halley.

6 Summary and Outlook

6.1 Summary

In this thesis the plasma interaction between comet 67P/Churyumov-Gerasimenko and the solar wind has been studied using numerical simulations. This interaction is caused by several processes taking place in the neutral cometary atmosphere, such as photo-ionisation or recombination. Depending on the gas production rate of the comet, the formation of various plasma structures and boundaries, e.g. the anti-sunward plasma tail or the diamagnetic cavity, is triggered.

With the arrival of the Rosetta spacecraft and the start of the measurements at comet 67P/Churyumov-Gerasimenko, a unique opportunity for the cometary science community has started. However, the measurements of the cometary physics have to be prepared and planned beforehand. This is especially true for the plasma measurements conducted by the experiments of the Rosetta Plasma Consortium (RPC), which can only be successful if the spacecraft is in the right place at the right time and if the instruments are in an appropriate mode. Hence, the best possible predictions on the positions and the physics of the various structures and boundaries in the cometary environment have to be made prior to the measurements and considered in the mission planning. Consequently, the aim of this thesis is to make these predictions, to support the mission and to ensure the scientific success.

In order to achieve this aim, the processes that eventually lead to the plasma structures, i.e. photo-ionisation, charge exchange, recombination, and electron excitation processes and cooling mechanisms have been reviewed and their impact on the cometary plasma environment has been studied. The formation and evolution of the plasma structures has been analysed by means of various plasma models. Especially, the promising A.I.K.E.F. (Adaptive Ion Kinetic Electron Fluid) code, which considers the kinetic motion of the ions, has carefully been reviewed. The implementations of the important processes were newly developed or at least optimised and revised in such a way that they can make use of the hierarchical mesh of the A.I.K.E.F. code. This hierarchical mesh is of particular importance since the cometary plasma interaction triggers structures on very different spatial scales. For example, 67P/Churyumov-Gerasimenko will have a bow shock stand-off distance of about 2000 km at about 1.3 AU distance from the Sun, whereas the smallest structures only have a width of about 25 km, as predicted by this thesis. Furthermore, this work suggested and used a new model for the boundary conditions at the upstream boundary of the simulation box. The extended upstream boundary conditions describe the physics upstream of the hybrid simulation box, e.g. the pick-up of the cometary ions and the reduction of the solar wind velocity, with a one-dimensional semi-kinetic approach.

This boundary condition saves computational resources since a smaller simulation box is required and, by that, quantitative and reliable estimations of the position of boundaries were obtained by global 3D hybrid simulations for the first time ever. In addition, it was shown that due to the implementation of the improvements of the A.I.K.E.F. code by Ranocha (2013), i.e. a solver for the pressure equation of the electron fluid, and the adaptation to the cometary environment, the temperature of the electrons in the innermost coma can be modelled self-consistently. The advanced A.I.K.E.F. code is well suited to describe complex atmospheric processes, e.g. the photochemical equilibrium or the cooling of the electrons by water excitation, but is also able to gain a remarkable resolution with very low numerical smoothing values, which made the discovery of new effects possible.

By means of the improved A.I.K.E.F. code various simulations of the cometary plasma environment have been conducted to explore the plasma environment of comet 67P/Churyumov-Gerasimenko during the Rosetta mission. In the first months of the escort phase of Rosetta the gas production of the comet is small, about two orders of magnitude below the expected maximum value. Consequently, the interaction between the comet and the solar wind will be only very weak. The simulations predict that Rosetta will explore an uncharted type of plasma interaction, which has never been observed so far. It was found that the interaction on large scales, i.e. large in comparison to the ion inertia length, is dominated by the cometary pick-up ion tail. This cycloidal ion tail, which has also been observed in previous studies, continuously triggers fast magnetosonic waves in the solar wind, which have not been predicted by previous studies so far. Especially at the cusps and the long edges of the pick-up ion tail, those waves form Mach cones. Hence, along the pick-up ion tail a regular pattern of Mach cones are formed. Since the multifluid MHD code was only partially able to reproduce the effects due to limitations in this model, this work emphasises the worth of the hybrid simulation for the Rosetta mission planning.

However, in comparison to the effects on large spatial scales, the direct environment of the nucleus is much more important for the mission as a consequence of the trajectory design of the spacecraft. The hybrid simulations predict that the RPC instruments will be able to observe the beginning of the pick-up ion tail. In contrast to the anti-sunward ion tail at strongly active comets, the pick-up ion tail is orientated perpendicular to the solar wind flow. Furthermore, RPC will observe the footpoint of the Mach cone, which is detectable by the solar wind deflection and an enhanced magnetic field strength. In addition, the hybrid simulations presented in this thesis predict the presence of a wave pattern in direct vicinity of the nucleus. The waves propagate close to the plane containing the magnetic field. In case of a perpendicular orientation of the magnetic field, the corresponding phase fronts with a wavelength far below the ion inertia length are parallel to each other in a hemisphere and are placed next to the nucleus and the pick-up ion tail. Upstream of the nucleus and the pick-up ion tail these phase fronts intersect. In general, the observed structures are comparable to whistler waves observed at magnetised asteroids. In this thesis it was found that the waves at the comet reveal a frequency close to the proton gyrofrequency in the comet frame and that the oscillations are present among others in the magnetic field and the cometary ion density, but the solar wind ion density remains constant. Although a final conclusion could not be drawn yet, the study indicates that the observed waves are whistler waves, which are triggered by the presence of cometary ions in the solar wind flow.

In a first preliminary comparison to the magnetometer data from RPC measured at the comet, a similarity to the waves in hybrid simulations was found. This indicates even more strongly that the hybrid code A.I.K.E.F. is not only very valuable for the mission planning, but also for data analysis afterwards, since the simulations presented in this thesis are the first simulations which predict such a wave activity.

As the comet approaches the Sun, the gas production rate increases and the Mach cone will transfer into a bow shock. In their pioneering work, Biermann et al. (1967) found that the cometary bow shock is triggered when the mass density in the solar wind flow exceeds a critical value. Hence, the position of the bow shock strongly depends on solar wind parameters but also on the ionisation profile, i.e. the mass source. Since the predictions of the bow shock position in the various existing models differ to a large extent, i.e. several thousand kilometres, these models have been revisited in this work. Therefore, a large number of hybrid simulations were run in order to determine the positions of the bow shock and its behaviour if different parameters are changed. These positions are compared to the other models afterwards and a similar behaviour was found to the fluid model by Biermann et al. (1967) and magnetohydrodynamic models in case of a variation of the gas production rate and the solar wind density. However, as a major result of this study, a completely divergent behaviour was found in case of a variation of the magnetic field strength and the solar wind velocity. The hybrid simulations, for example, predict that the bow shock stand-off distance varies by about 3000 km if the magnetic field strength changes by only 7 nT. Since the magnetic field strength and the solar wind velocity determine the characteristic scales of the ion motion, a modified mass source for fluid models is proposed. In contrast to the classical mass source, the new mass source considers a finite pick-up time, which is required by the ions to accelerate to speeds comparable to the solar wind speed. Using this modified mass source in the magnetohydrodynamic model by Flammer and Mendis (1991), the bow shock positions obtained with the hybrid model can be reproduced and the differences between the various models are now comprehensible. Another lesson learned from this study is that the bow shock is much closer to the comet than predicted by the other models. Hence, a crossing of the fully developed bow shock by the Rosetta spacecraft is more likely. Furthermore, this study showed that small variations of the solar wind parameters can shift the bow shock to a large extent, which makes a detection of the bow shock by RPC even more likely. Based on this the decision was made to perform a special dayside excursion with the Rosetta spacecraft. During this trajectory segment Rosetta will be able to study the fully developed cometary bow shock. Hence, RPC is able to study the evolution from the onset of activity to the Mach cones, and their transition to a fully developed cometary bow shock.

In a next step, the innermost coma and the interaction region of comet 67P/Churyumov-Gerasimenko in the active phase were studied in this thesis. For the first time ever, a global hybrid simulation was able to resolve the innermost interaction region sufficiently to allow for an investigation of the plasma boundaries in that region (Figure 6.1). The simulation predicts the presence of a magnetic barrier, a cometary ionopause, a recombination layer, an inner shock, and a diamagnetic cavity. So far, those structures have also been identified in single-fluid MHD simulations and in observations at comet 1P/Halley. However, the hybrid simulation also reveals a shift of the entire interaction region, and all related structures and boundaries therein, away from the Sun-comet line. It was found

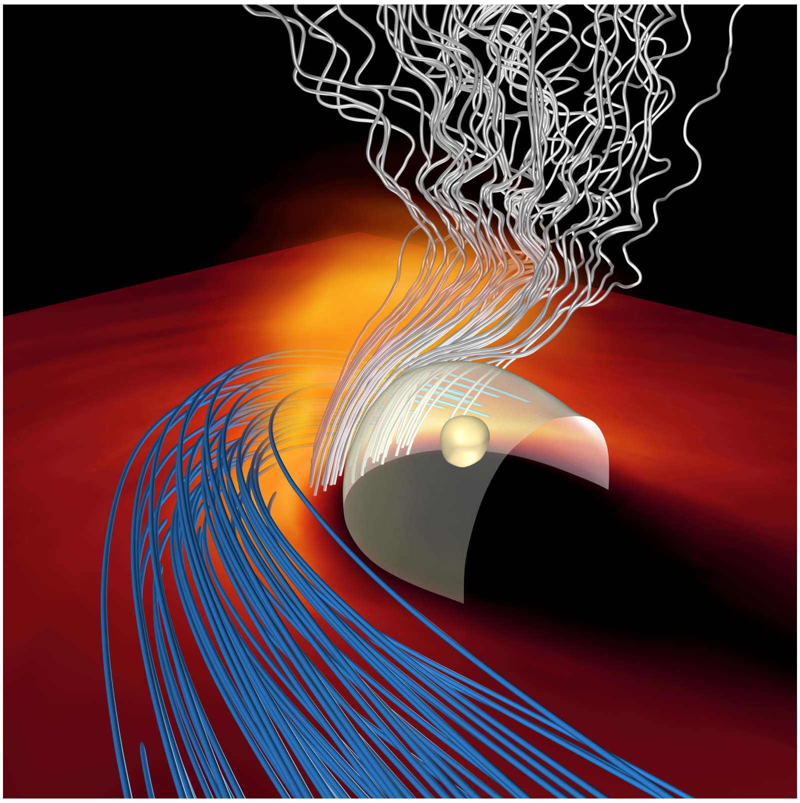

Figure 6.1: A three dimensional picture of the structures in the innermost coma of an active comet. The figure is based on the simulation result presented in Section (4.2) and was created in cooperation with the ZIB (Zuse Institut Berlin and the DLR (Deutsches Zentrum für Luft- und Raumfahrt). The blue lines represent magnetic field lines in the magnetic pile up region. This region is highlighted by an orange volume rendering of the magnetic pressure, which is also presented by a cross-section. Parts of the current density are shown as grey lines separating the magnetic pile-up region and the diamagnetic cavity. The transparent isosurface shows the position of the inner shock, where the Mach number is equal to one.

that this shift is caused by the pick-up of the cometary ions upstream, which then leads to the deflection of the incoming flow.

In addition, this simulation is the first hybrid simulation which is able to reproduce the cold electrons in the innermost coma self-consistently. Further ion kinetic effects were found by the analysis of individual ion velocities at different places in the innermost coma. The simulation showed that the cometary ions reveal a ring-beam distribution upstream of the bow shock. This distribution suddenly broadens after the bow shock crossing. The solar wind is also broadened, but it cannot reach the innermost region. There, the hybrid simulation predicts three distinct cometary ion populations, which are visible in the phase space. In the first population one finds cold ions created by ionisation and ion-neutral collisions, moving in radial direction away from the nucleus with the same speed as the neutral gas. A second population of slow cometary ions moves towards the nucleus, but they move around the diamagnetic cavity and cannot enter this magnetic-field free region. In contrast to this, the third ion population has a higher speed and can penetrate into the cometary ionopause and the diamagnetic cavity. Hence, this study predicts an energy bifurcation at the inner most boundaries, which might be observed by the experiments on Rosetta. These results show that a hybrid model is needed in order to study the global plasma interaction of comet 67P/Churyumov-Gerasimenko during the active phase.

This thesis showed that the kinetic effects are a key part in the description of the cometary plasma interaction region of weakly active as well as of strongly active comets. In addition, the presented studies in this thesis reveal that the A.I.K.E.F. code is a valuable tool for the prediction of the plasma environment of comet 67P/Churyumov-Gerasimenko. It is the only model that is able to describe the weakly active phase of the cometary plasma interaction as well as that of the strongly active phase precisely. Consequently, the hybrid code A.I.K.E.F. is the best available plasma model to prepare the measurements of RPC.

In order to satisfy the needs and requirements of the mission planning, a software tool, the RPC WoO Tool, has been developed as part of this work. The RPC WoO Tool calculates the Windows of Opportunities, which indicate time segments when the spacecraft is in an appropriate position to perform measurements of an interesting plasma structure or boundary, on the basis of pre-calculated A.I.K.E.F. simulations. These Windows of Opportunity are the basis for the subsequent and ongoing RPC science planning and guarantee that the consideration of the best possible predictions in the mission planning of RPC.

6.2 Outlook

In the upcoming two years, including a mission extension, the Rosetta spacecraft and the RPC instruments will perform unique measurements. In order to collect the best possible data, the predictions of this thesis about the location of plasma boundaries and structures are currently used and will be used during the mission.

However, as Rosetta stays close to the comet for an extended period of time, new findings will occur and the understanding of physical processes, such as the electron cooling, have to be revised. Consequently, the A.I.K.E.F. code has to be improved to refine the predictions. The neutral gas profiles have to be improved and adapted to the measurements, i.e. the nucleus' shape, immediately. The required routines are already included in the A.I.K.E.F. code. They have been newly developed or optimised and revised during this thesis.

In addition to the questions related to the Rosetta mission, improvements of the hybrid code A.I.K.E.F. should be considered, as well. Among those, an update and improvement of the solver for the electric field and for the magnetic field should be on the agenda. This update will allow for a further reduction of the numerical smoothing as well as for enabling an improved description of boundaries. Only by doing so, the A.I.K.E.F. code will still be groundbreaking, as shown in this thesis, and will also be able to produce results in the future.

Besides the predictions and the evolution of the A.I.K.E.F. code, the analysis of the measurements by Rosetta will reveal new findings. However, in order to understand these measurements, global simulations of the plasma environment are required. This has briefly been demonstrated in the case of the weakly active phase (Section 3.3), where the simulations of this thesis reveal the real character of the waves and the interaction pattern. A possible topic to be considered in the plasma environment will be dust grains. As reported, on board the spacecraft there are three instruments dedicated to the study of dust particles. The RPC instruments will observe effects which are caused by charged dust, as well. Numerical simulations, such as those performed with the A.I.K.E.F. code, will allow to link the different observations and gain knowledge on the dust properties and their distribution in the coma and, thereby, also on the comet.

Bibliography

Acton, C. H., 1996, Ancillary data services of NASA's Navigation and Ancillary Information Facility, Planetary and Space Science, 44, 65–70, ISSN 00320633

A'Hearn, M. F., Belton, M. J. S., Delamere, W. A., Feaga, L. M., Hampton, D., Kissel, J., Klaasen, K. P., McFadden, L. A., Meech, K. J., Melosh, H. J., Schultz, P. H., Sunshine, J. M., Thomas, P. C., Veverka, J., Wellnitz, D. D., Yeomans, D. K., Besse, S., Bodewits, D., Bowling, T. J., Carcich, B. T., Collins, S. M., Farnham, T. L., Groussin, O., Hermalyn, B., Kelley, M. S., Li, J.-Y., Lindler, D. J., Lisse, C. M., McLaughlin, S. A., Merlin, F., Protopapa, S., Richardson, J. E., Williams, J. L., 2011, EPOXI at comet Hartley 2., Science, 332, 1396–400, ISSN 1095-9203

Alfven, H., 1957, On the theory of comet tails, Tellus, pp. 92–96

Almeida, M., 2013, RO-SGS-PR-1005: RSGS-PI Interactions Document, Tech. rep., ESA, Villa Franca, Madrid

Auster, H. U., Apathy, I., Berghofer, G., Remizov, A., Roll, R., Fornacon, K. H., Glassmeier, K.-H., Haerendel, G., Hejja, I., Kührt, E., Magnes, W., Moehlmann, D., Motschmann, U., Richter, I., Rosenbauer, H., Russell, C. T., Rustenbach, J., Sauer, K., Schwingenschuh, K., Szemerey, I., Waesch, R., 2007, ROMAP: Rosetta Magnetometer and Plasma Monitor, Space Science Reviews, 128, 221–240, ISSN 0038-6308

Auster, H. U., Richter, I., Glassmeier, K.-H., Berghofer, G., Carr, C. M., Motschmann, U., 2010, Magnetic field investigations during ROSETTA's 2867 Šteins flyby, Planetary and Space Science, 58, 1124–1128, ISSN 00320633

Bagdonat, T. B., 2004, Hybrid simulation of weak comets, Dissertation, Technische Universität Braunschweig, Braunschweig

Bagdonat, T. B., Motschmann, U., 2002, From a weak to a strong comet - 3d global hybrid simulation studies, Earth, Moon, and Planets, 90, 305–321

Balsiger, H., Altwegg, K., Bühler, F., Geiss, J., Ghielmetti, A. G., Goldstein, B. E., Goldstein, R., Huntress, W. T., Ip, W.-H., Lazarus, A. J., Meier, A., Neugebauer, M. ., Rettenmund, U., Rosenbauer, H., Schwenn, R., Sharp, R. D., Shelley, E. G., Ungstrup, E., Young, D. T., 1986, Ion composition and dynamics at comet Halley, Nature, 321, 330–334, ISSN 0028-0836

Balsiger, H., Altwegg, K., Bochsler, P., Eberhardt, P., Fischer, J., Graf, S., Jäckel, A., Kopp, E., Langer, U., Mildner, M., Müller, J., Riesen, T., Rubin, M., Scherer, S., Wurz, P., Wüthrich, S., Arijs, E., Delanoye, S., Keyser, J. D., Neefs, E., Nevejans, D., Rème, H., Aoustin, C., Mazelle, C., Médale, J.-L., Sauvaud, J. A., Berthelier, J.-J., Bertaux, J.-L., Duvet, L., Illiano, J.-M., Fuselier, S. A., Ghielmetti, A. G., Magoncelli, T., Shelley, E. G., Korth, A., Heerlein, K., Lauche, H., Livi, S., Loose, A., Mall, U., Wilken, B., Gliem, F., Fiethe, B., Gombosi, T. I., Block, B., Carignan, G. R., Fisk, L. A., Waite, J. H., Young, D. T., Wollnik, H., 2007, Rosina – Rosetta Orbiter Spectrometer for Ion and Neutral Analysis, Space Science Reviews, 128, 745–801, ISSN 0038-6308

Baumgártel, K., Sauer, K., Bogdanov, A., 1994, A magnetohydrodynamic model of solar wind interaction with asteroid gaspra., Science, 263, 653–5, ISSN 0036-8075

Baumgärtel, K., Sauer, K., Story, T. R., 1997, Solar Wind Response to a Magnetized Asteroid: Linear Theory, Icarus, 129, 94–105, ISSN 00191035

Baumjohann, W., Treumann, R. A., 1996, Basic Space Plasma Physics, Imperial College Press, London, Edition 2004, ISBN 1-86094-079-X

Benna, M., Mahaffy, P., 2007, Multi-fluid model of comet 1P/Halley, Planetary and Space Science, 55, 1031–1043, ISSN 00320633

Bhardwaj, A., Haider, S., 2002, Chemistry of O(1D) atoms in the coma: implications for cometary missions, Advances in Space Research, 29, 745–750, ISSN 02731177

Bhardwaj, A., Raghuram, S., 2012, A COUPLED CHEMISTRY-EMISSION MODEL FOR ATOMIC OXYGEN GREEN AND RED-DOUBLET EMISSIONS IN THE COMET C/1996 B2 HYAKUTAKE, The Astrophysical Journal, 748, 13, ISSN 0004-637X

Biele, J., Herfort, U., 2012, RO-ESC-TN-5566: Rosetta Project Comet Reference Models, Tech. rep., ESA, Darmstadt

Biele, J., Ulamec, S., 2013, Preparing for Landing on a Comet — The Rosetta Lander Philae, 44th Lunar and Planetary Science Conference (2013), pp. 4–5

Biermann, L., Brosowski, B., Schmidt, H. U., 1967, The interaction of the solar wind with a comet, Solar Physics, 1, 254–284, ISSN 0038-0938

Blanco-Cano, X., Omidi, N., Russell, C. T., 2003, Hybrid simulations of solar wind interaction with magnetized asteroids: Comparison with Galileo observations near Gaspra and Ida, Journal of Geophysical Research, 108, 1216, ISSN 0148-0227

Blum, J., Gundlach, B., Mühle, S., Trigo-Rodriguez, J. M., 2014, Comets formed in solar-nebula instabilities! - An experimental and modeling attempt to relate the activity of comets to their formation process, Icarus, 235, 156–169, ISSN 00191035

Boesswetter, A., Auster, U., Richter, I., Fränz, M., Langlais, B., McKenna-Lawlor, S., Simon, S., Motschmann, U., Glassmeier, K.-H., Edberg, N. J. T., Lundin, R., 2009, Rosetta swing-by at Mars – an analysis of the ROMAP measurements in comparison with results of 3-D multi-ion hybrid simulations and MEX/ASPERA-3 data, Annales Geophysicae, 27, 2383–2398, ISSN 1432-0576

Brinca, A. L., Tsurutani, B. T., 1988a, Survey of low-frequency electromagnetic waves stimulated by two coexisting newborn ion species, Journal of Geophysical Research, 93, 48, ISSN 0148-0227

Brinca, A. L., Tsurutani, B. T., 1988b, Temperature effects on the pickup process of water group and hydrogen ions: Extensions of "A theory for low-frequency waves observed at comet Giacobini-Zinner" by M. L. Goldstein and H. K. Wong, Journal of Geophysical Research, 93, 243, ISSN 0148-0227

Burch, J. L., Goldstein, R., Cravens, T. E., Gibson, W. C., Lundin, R. N., Pollock, C. J., Winningham, J. D., Young, D. T., 2006, RPC-IES: The Ion and Electron Sensor of the Rosetta Plasma Consortium, Space Science Reviews, 128, 697–712, ISSN 0038-6308

Carr, C., Cupido, E., Lee, C. G. Y., Balogh, A., Beek, T., Burch, J. L., Dunford, C. N., Eriksson, A. I., Gill, R., Glassmeier, K.-H., Goldstein, R., Lagoutte, D., Lundin, R., Lundin, K., Lybekk, B., Michau, J. L., Musmann, G., Nilsson, H., Pollock, C., Richter, I., Trotignon, J. G., 2007, RPC: The Rosetta Plasma Consortium, Space Science Reviews, 128, 629–647, ISSN 0038-6308

Coates, A. J., 1991, Cometary plasma energisation, in European Geophysical Society, Symposium on Acceleration and Heating Processes in Solar System Plasmas, vol. 9, pp. 158–169, Annales Geophysicae, Copenhagen

Coates, A. J., 1995, Heavy ion effects on cometary shocks, Advances in Space Research, 15, 403–413, ISSN 02731177

Coates, A. J., 1997, Ionospheres and magnetospheres of comets, Advances in Space Research, 20, 255–266, ISSN 02731177

Coates, A. J., 2010, Ion Pickup at Comets: Comparison with Other Unmagnetized Objects, in Pickup Ions throughout the Heliosphere and Beyond: Proceedings of the 9th Annual International Astrophysics Conference, (Eds.) J. A. le Roux, V. Florinski, G. P. Zank, A. J. Coates, pp. 213–224, American Institute of Physics, ISBN 9780735408579

Coates, A. J., Jones, G. H., 2009, Plasma environment of Jupiter family comets, Planetary and Space Science, 57, 1175–1191, ISSN 00320633

Coates, A. J., Johnstone, A. D., Wilken, B., Neubauer, F. M., 1993, Velocity Space Diffusion and Nongyrotropy of Pickup Water Group Ions at Comet Grigg-Skjellerup, Journal of Geophysical Research, 98, 20 985–20 994, ISSN 0148-0227

Colangeli, L., Lopez-Moreno, J. J., Palumbo, P., Rodriguez, J., Cosi, M., Corte, V. D., Esposito, F., Fulle, M., Herranz, M., Jeronimo, J. M., Lopez-Jimenez, A., Epifani, E. M., Morales, R., Moreno, F., Palomba, E., Rotundi, A., 2007, The Grain Impact Analyser and Dust Accumulator (GIADA) Experiment for the Rosetta Mission: Design, Performances and First Results, Space Science Reviews, 128, 803–821, ISSN 0038-6308

Companys, V., 2012, RO-ESC-TN-5569: Rosetta: Trajectory planning constraints for the extended monitoring phase, Tech. rep., ESA, Darmstadt

Constantinescu, O., Glassmeier, K.-H., Auster, U., Richter, I., Fornaçon, K.-H., Carr, C., 2012, On the possibility to determine the electrical conductivity of 67P/CG from ROSETTA magnetic field observations, Planetary and Space Science, 65, 1–9, ISSN 00320633

Coradini, A., Capaccioni, F., Drossart, P., Arnold, G., Ammannito, E., Angrilli, F., Barucci, A., Bellucci, G., Benkhoff, J., Bianchini, G., Bibring, J. P., Blecka, M., Bockelee-Morvan, D., Capria, M. T., Carlson, R., Carsenty, U., Cerroni, P., Colangeli, L., Combes, M., Combi, M., Crovisier, J., Desanctis, M. C., Encrenaz, E. T., Erard, S., Federico, C., Filacchione, G., Fink, U., Fonti, S., Formisano, V., Ip, W. H., Jaumann, R., Kuehrt, E., Langevin, Y., Magni, G., Mccord, T., Mennella, V., Mottola, S., Neukum, G., Palumbo, P., Piccioni, G., Rauer, H., Saggin, B., Schmitt, B., Tiphene, D., Tozzi, G., 2007, Virtis: An Imaging Spectrometer for the Rosetta Mission, Space Science Reviews, 128, 529–559, ISSN 0038-6308

Cravens, T. E., 1986, The physics of the cometary contact surface, in Proceedings 20th ESLAB Symposium on the Exploration of Halley's Comet, vol. 20, pp. 241–246, ESA SP-250, Heidelberg

Cravens, T. E., 1989, A magnetohydrodynamical model of the inner coma of comet Halley, Journal of Geophysical Research, 94, 15 025–15 040, ISSN 0148-0227

Cravens, T. E., Gombosi, T. I., 2004, Cometary magnetospheres: a tutorial, Advances in Space Research, 33, 1968–1976, ISSN 02731177

Cravens, T. E., Kozyra, J. U., Nagy, A. F., Gombosi, T. I., Kurtz, M., 1987, Electron impact ionization in the vicinity of comets, Journal of Geophysical Research, 92, 7341, ISSN 0148-0227

Crifo, J., 2002, Comparison between Navier–Stokes and Direct Monte–Carlo Simulations of the Circumnuclear Coma I. Homogeneous, Spherical Source, Icarus, 156, 249–268, ISSN 00191035

Crifo, J., Loukianov, G., Rodionov, A., Zakharov, V., 2003, Navier–Stokes and direct Monte Carlo simulations of the circumnuclear coma II. Homogeneous, aspherical sources, Icarus, 163, 479–503, ISSN 00191035

Curdt, W., Wilhelm, K., Craubner, A., Krahn, E., Keller, H., 1988, Position of comet P/Halley at the Giotto encounter, Astronomy and Astrophysics, 191, L1–L3

Davidsson, B. J. R., 2008, Comet Knudsen Layers, Space Science Reviews, 138, 207–223, ISSN 0038-6308

Delamere, P. A., 2006, Hybrid code simulations of the solar wind interaction with Comet 19P/Borrelly, Journal of Geophysical Research, 111, A12 217, ISSN 0148-0227

Dones, L., Boyce, D. C., Levison, H. F., Duncan, M. J., 2005, Dynamical and Physical Models of Ecliptic Comets, in DPS meeting #37, vol. 37, p. 736, American Astronomical Society

Eastwood, J. P., Schwartz, S. J., Horbury, T. S., Carr, C. M., Glassmeier, K.-H., Richter, I., Koenders, C., Plaschke, F., Wild, J. A., 2011, Transient Pc3 wave activity generated by a hot flow anomaly: Cluster, Rosetta, and ground-based observations, Journal of Geophysical Research, 116, A08 224, ISSN 0148-0227

Eberhardt, P., Krankowsky, D., 1995, The electron temperature in the inner coma of comet P/Halley, Astronomy and Astrophysics, 295, 795–806

Edberg, N., Eriksson, A., Auster, U., Barabash, S., Böß wetter, A., Carr, C., Cowley, S., Cupido, E., Fränz, M., Glassmeier, K.-H., Goldstein, R., Lester, M., Lundin, R., Modolo, R., Nilsson, H., Richter, I., Samara, M., Trotignon, J., 2009, Simultaneous measurements of Martian plasma boundaries by Rosetta and Mars Express, Planetary and Space Science, 57, 1085–1096, ISSN 00320633

Eriksson, A. I., Boström, R., Gill, R., Å hlén, L., Jansson, S.-E., Wahlund, J.-E., André, M., Mälkki, A., Holtet, J. a., Lybekk, B., Pedersen, A., Blomberg, L. G., 2006, RPC-LAP: The Rosetta Langmuir Probe Instrument, Space Science Reviews, 128, 729–744, ISSN 0038-6308

Ershkovich, A. I., Flammer, K. R., 1988, Nonlinear stability of the dayside cometary ionopause, The Astrophysical Journal, 328, 967, ISSN 0004-637X

Festou, M., Keller, H., Weaver, H. A., 2004, Comets II, The University of Arizona Press, Tucson, ISBN 0816524505

Finklenburg, S., Thomas, N., 2014, Relating in situ gas measurements to the surface outgassing properties of cometary nuclei, Planetary and Space Science, ISSN 00320633

Flammer, K. R., Mendis, D. A., 1991, A note on the mass-loaded MHD flow of the solar wind towards a cometary nucleus, Astrophysics and Space Science, 182, 155–162, ISSN 0004-640X

Fu, R. R., Weiss, B. P., 2012, Detrital remanent magnetization in the solar nebula, Journal of Geophysical Research, 117, E02 003, ISSN 0148-0227

Fuselier, S. A., Shelley, E. G., Goldstein, B. E., Goldstein, R., Neugebauer, M. ., Ip, W.-H., Balsiger, H., Reme, H., 1991, Observations of solar wind ion charge exchange in the Comet Halley coma, The Astrophysical Journal, 379, 734, ISSN 0004-637X

Galeev, A. A., Cravens, T. E., Gombosi, T. I., 1985, Solar wind stagnation near comets, The Astrophysical Journal, 289, 807–819, ISSN 0004-637X

Gan, L., Cravens, T. E., 1990, Electron energetics in the inner coma of comet Halley, Journal of Geophysical Research, 95, 6285, ISSN 0148-0227

Gary, S., 1991, Electromagnetic ion/ion instabilities and their consequences in space plasmas: A review, Space Science Reviews, 56, 373–415, ISSN 0038-6308

Gary, S. P., 1993, Theory of Space Plasma Microinstabilities, Cambridge University Press, Cambridge, ISBN 0 521 43167 0

Glassmeier, K.-H., Coates, A. J., Acuña, M. H., Goldstein, M. L., Johnstone, A. D., Neubauer, F. M., Rème, H., 1989, Spectral characteristics of low-frequency plasma turbulence upstream of comet P/Halley, Journal of Geophysical Research, 94, 37, ISSN 0148-0227

Glassmeier, K.-H., Motschmann, U., Mazelle, C., Neubauer, F. M., Sauer, K., Fuselier, S. A., Acuña, M. H., 1993, Mirror Modes and Fast Magnetoacoustic Waves Near the Magnetic Pileup Boundary of Comet P/Halley, Journal of Geophysical Research, 98, 20 955–20 964, ISSN 0148-0227

Glassmeier, K.-H., Motschmann, U., Dunlop, M., Balogh, A., Acuña, M. H., Carr, C., Musmann, G., Fornaçon, K.-H., Schweda, K., Vogt, J., Georgescu, E., Buchert, S., Group, A. P., Kingdom, U., Space, G., 2001, Cluster as a wave telescope – first results from the fluxgate magnetometer, Annales Geophysicae, 19, 1439–1447, ISSN 1432-0576

Glassmeier, K.-H., Boehnhardt, H., Koschny, D., Kührt, E., Richter, I., 2007a, The Rosetta Mission: Flying Towards the Origin of the Solar System, Space Science Reviews, 128, 1–21, ISSN 0038-6308

Glassmeier, K.-H., Richter, I., Diedrich, A., Musmann, G., Auster, U., Motschmann, U., Balogh, A., Carr, C., Cupido, E., Coates, A., Rother, M., Schwingenschuh, K., Szegö, K., Tsurutani, B. T., 2007b, RPC-MAG The Fluxgate Magnetometer in the ROSETTA Plasma Consortium, Space Science Reviews, 128, 649–670, ISSN 0038-6308

Goldstein, B. E., Altwegg, K., Balsiger, H., Fuselier, S. A., Ip, W., Meier, A., Neugebauer, M. ., Rosenbauer, H., Schwenn, R., 1989, Observations of a shock and a recombination layer at the contact surface of comet Halley, Journal of Geophysical Research, 94, 17 251–17 257

Goldstein, M. L., Roberts, D. A., Matthaeus, W. H., 1987, Numerical simulation of the generation of turbulence from cometary ion pick-up, Geophysical Research Letters, 14, 860–863, ISSN 00948276

Gombosi, T. I., De Zeeuw, D. L., Häberli, R. M., Powell, K. G., 1996, Three-dimensional multiscale MHD model of cometary plasma environments, Journal of Geophysical Research, 101, 15 233–15 253, ISSN 0148-0227

Gortsas, N., 2010, Thermal and Plasma Simulations of Comet C, 1995 O1 (Hale-Bopp) and the Rosetta Target Comet 67P, Churyumov-Gerasimenko, Dissertation, TU Braunschweig

Gortsas, N., Motschmann, U., Kührt, E., Glassmeier, K.-H., Hansen, K. C., Müller, J., Schmidt, A., 2010, Global plasma-parameter simulation of Comet 67P/Churyumov-Gerasimenko approaching the Sun, Astronomy and Astrophysics, 520, A92, ISSN 0004-6361

Götz, C., 2014, Hybrid Simulations of Cometary Tail Disconnection Events, Master Thesis, Technische Universität Braunschweig

Gulkis, S., Frerking, M., Crovisier, J., Beaudin, G., Hartogh, P., Encrenaz, P., Koch, T., Kahn, C., Salinas, Y., Nowicki, R., Irigoyen, R., Janssen, M., Stek, P., Hofstadter, M., Allen, M., Backus, C., Kamp, L., Jarchow, C., Steinmetz, E., Deschamps, A., Krieg, J., Gheudin, M., Bockelée-Morvan, D., Biver, N., Encrenaz, T., Despois, D., Ip, W., Lellouch, E., Mann, I., Muhleman, D., Rauer, H., Schloerb, P., Spilker, T., 2006, MIRO: Microwave Instrument for Rosetta Orbiter, Space Science Reviews, 128, 561–597, ISSN 0038-6308

Gundlach, B., 2013, Surface Processes of Small Solar System Bodies, Dissertation, TU Braunschweig

Gurnett, D. A., 1995a, On a remarkable similarity between the propagation of whistlers and the bow wave of a ship, Geophysical Research Letters, 22, 1865–1868, ISSN 00948276

Gurnett, D. A., 1995b, The whistler-mode bow wave of an asteroid, Journal of Geophysical Research, 100, 21 623, ISSN 0148-0227

Güttler, C., Blum, J., Zsom, A., Ormel, C. W., Dullemond, C. P., 2010, The outcome of protoplanetary dust growth: pebbles, boulders, or planetesimals?, Astronomy and Astrophysics, 513, A56, ISSN 0004-6361

Haeberli, R. M., Altwegg, K., Balsiger, H., Geiss, J., 1995, Physics and chemistry of ions in the pile-up region of comet P/Halley., Astronomy and Astrophysics

Hanner, M., Tedesco, E., Tokunaga, A. T., Veeder, G. J., Lester, D. F., Witteborn, F. C., Bregman, J. D., Gradie, J., Lebofsky, L., 1985, The dust coma of periodic comet Churyumov-Gerasimenko (1982 VIII), Icarus, 64, 11–19, ISSN 00191035

Hansen, K. C., Bagdonat, T. B., Motschmann, U., Alexander, C., Combi, M. R., Cravens, T. E., Gombosi, T. I., Jia, Y.-D., Robertson, I. P., 2007, The Plasma Environment of Comet 67P/Churyumov-Gerasimenko Throughout the Rosetta Main Mission, Space Science Reviews, 128, 133–166, ISSN 0038-6308

Haser, L., 1957, Distribution d'intensite dans la tete d'une comete, Bulletin de la Societe Royale des Sciences de Liege, 43, 740–750

Huddleston, D. E., Coates, A. J., Johnstone, A. D., 1992a, Correction to "Predictions of the solar wind interaction with comet Grigg-Skjellerup" by D. E. Huddleston, A. J. Coates, and A. D. Johnstone, Geophysical Research Letters, 19, 1319–1319, ISSN 00948276

Huddleston, D. E., Coates, A. J., Johnstone, A. D., 1992b, Predictions of the solar wind interaction with Comet Grigg-Skjellerup, Geophysical Research Letters, 19, 837–840, ISSN 00948276

Huebner, W. F., Keady, J. J., Lyon, S. P., 1992, Solar photo rates for planetary atmospheres and atmospheric pollutants, Astrophysics and Space Science, 195, 1–294, ISSN 0004-640X

Ip, W.-H., Axford, W. I., 1987, The formation of a magnetic-field-free cavity at comet Halley, Nature, 325, 418–419, ISSN 0028-0836

Itikawa, Y., 2005, Cross Sections for Electron Collisions with Water Molecules, Journal of Physical and Chemical Reference Data, 34, 1, ISSN 00472689

Jia, Y.-D., Combi, M. R., Hansen, K. C., Gombosi, T. I., 2007, A global model of cometary tail disconnection events triggered by solar wind magnetic variations, Journal of Geophysical Research, 112, A05 223, ISSN 0148-0227

Johansen, A., Youdin, A., 2007, Protoplanetary Disk Turbulence Driven by the Streaming Instability: Nonlinear Saturation and Particle Concentration, The Astrophysical Journal, 662, 627–641, ISSN 0004-637X

Johnstone, A., Coates, A., Kellock, S., Wilken, B., Jockers, K., Rosenbauer, H., Studemann, W., Weiss, W., Formisano, V., Amata, E., Cerulli-Irelli, R., Dobrowolny, M., Terenzi, R., Egidi, A., Borg, H., Hultquist, B., Winningham, J., Gurgiolo, C., Bryant, D., Edwards, T., Feldman, W., Thomsen, M., Wallis, M. K., Biermann, L., Schmidt, H., Lust, R., Haerendel, G., Paschmann, G., 1986, Ion flow at comet Halley, Nature, 321, 344–347, ISSN 0028-0836

Kartalev, M., Dobreva, P., Keremidarska, V., Dryer, M., 2012, Solar Wind-Comet Exosphere Interaction. 2. Could the Single-Fluid Gas-Dynamic Model be Applicable to the Rosetta Mission, Journal of Theoretical and Applied Mechanics, 42, 71–90, ISSN 0861-6663

Kartalev, M. D., 1998, On the single-fluid modeling of mass-loaded plasma, Geophysical & Astrophysical Fluid Dynamics, 88, 131–164, ISSN 0309-1929

Keller, H. U., Arpigny, C., Barbieri, C., Bonnet, R. M., Cazes, S., Coradini, M., Cosmovici, C. B., Delamere, W. A., Huebner, W. F., Hughes, D. W., Jamar, C., Malaise, D., Reitsema, H. J., Schmidt, H. U., Schmidt, W. K. H., Seige, P., Whipple, F. L., Wilhelm, K., 1986, First Halley Multicolour Camera imaging results from Giotto, Nature, 321, 320–326, ISSN 0028-0836

Keller, H. U., Barbieri, C., Lamy, P. L., Rickman, H., Rodrigo, R., Wenzel, K.-P., Sierks, H., A'Hearn, M. F., Angrilli, F., Angulo, M., Bailey, M. E., Barthol, P., Barucci, M. A., Bertaux, J.-L., Bianchini, G., Boit, J.-L., Brown, V., Burns, J. A., Büttner, I., Castro, J. M., Cremonese, G., Curdt, W., Deppo, V. D., Debei, S., Cecco, M. D., Dohlen, K., Fornasier, S., Fulle, M., Germerott, D., Gliem, F., Guizzo, G. P., Hviid, S. F., Ip, W.-H., Jorda, L., Koschny, D., Kramm, J. R., Kührt, E., Küppers, M., Lara, L. M., Llebaria, A., López, A., López-Jimenez, A., López-Moreno, J., Meller, R., Michalik, H., Michelena, M. D., Müller, R., Naletto, G., Origné, A., Parzianello, G., Pertile, M., Quintana, C., Ragazzoni, R., Ramous, P., Reiche, K.-U., Reina, M., Rodríguez, J., Rousset, G., Sabau, L., Sanz, A., Sivan, J.-P., Stöckner, K., Tabero, J., Telljohann, U., Thomas, N., Timon, V., Tomasch, G., Wittrock, T., Zaccariotto, M., 2007, OSIRIS – The Scientific Camera System Onboard Rosetta, Space Science Reviews, 128, 433–506, ISSN 0038-6308

Kissel, J., Altwegg, K., Clark, B. C., Colangeli, L., Cottin, H., Czempiel, S., Eibl, J., Engrand, C., Fehringer, H. M., Feuerbacher, B., Fomenkova, M., Glasmachers, a., Greenberg, J. M., Grün, E., Haerendel, G., Henkel, H., Hilchenbach, M., Hoerner, H., Höfner, H., Hornung, K., Jessberger, E. K., Koch, a., Krüger, H., Langevin, Y., Parigger, P., Raulin, F., Rüdenauer, F., Rynö, J., Schmid, E. R., Schulz, R., Silén, J., Steiger, W., Stephan, T., Thirkell, L., Thomas, R., Torkar, K., Utterback, N. G., Varmuza, K., Wanczek, K. P., Werther, W., Zscheeg, H., 2007, Cosima – High Resolution Time-of-Flight Secondary Ion Mass Spectrometer for the Analysis of Cometary Dust Particles onboard Rosetta, Space Science Reviews, 128, 823–867, ISSN 0038-6308

Kivelson, M. G., Russell, C. T., 1995, Introduction to Space Physics, Cambridge University Press, Cambridge, ISBN 0521457149

Kivelson, M. G., Bargatze, L. F., Khurana, K. K., Southwood, D. J., Walker, R. J., Coleman, P. J., 1993, Magnetic Field Signatures Near Galileo's Closest Approach to Gaspra., Science, 261, 331–4, ISSN 0036-8075

Koenders, C., Glassmeier, K.-H., Richter, I., Motschmann, U., Rubin, M., 2013, Revisiting cometary bow shock positions, Planetary and Space Science, 87, 85–95, ISSN 00320633

Koenders, C., Glassmeier, K.-H., Richter, I., Ranocha, H., Motschmann, U., 2015, Dynamical features and spatial structures of the plasma interaction region of 67P/Churyumov–Gerasimenko and the solar wind, Planetary and Space Science, 105, 101–116, ISSN 00320633

Kofman, W., Herique, a., Goutail, J.-P., Hagfors, T., Williams, I. P., Nielsen, E., Barriot, J.-P., Barbin, Y., Elachi, C., Edenhofer, P., Levasseur-Regourd, A.-C., Plettemeier, D., Picardi, G., Seu, R., Svedhem, V., 2007, The Comet Nucleus Sounding Experiment by Radiowave Transmission (CONSERT): A Short Description of the Instrument and of the Commissioning Stages, Space Science Reviews, 128, 413–432, ISSN 0038-6308

Kriegel, H., 2013, The Plasma Environments of Saturn's Moons Enceladus and Rhea: Modeling of Cassini Magnetic Field Data, Dissertation, TU Braunschweig

Krolikowska, M., 2003, 67P/Churyumov-Gerasimenko - Potential Target for the Rosetta Mission, Acta Astronomica, 53, 195–208

Kührt, E., 1999, H2O-Activity of Comet Hale-Bopp, Space Science Reviews, 90, 75–82

Küppers, M., Bertini, I., Fornasier, S., Gutierrez, P. J., Hviid, S. F., Jorda, L., Keller, H. U., Knollenberg, J., Koschny, D., Kramm, R., Lara, L.-M., Sierks, H., Thomas, N., Barbieri, C., Lamy, P., Rickman, H., Rodrigo, R., 2005, A large dust/ice ratio in the nucleus of comet 9P/Tempel 1., Nature, 437, 987–90, ISSN 1476-4687

Lamy, P. L., Toth, I., Davidsson, B. J. R., Groussin, O., Gutiérrez, P., Jorda, L., Kaasalainen, M., Lowry, S. C., 2007, A Portrait of the Nucleus of Comet 67P/Churyumov-Gerasimenko, Space Science Reviews, 128, 23–66, ISSN 0038-6308

Lamy, P. L., Toth, I., Groussin, O., Jorda, L., Kelley, M. S., Stansberry, J. A., 2008, Spitzer Space Telescope observations of the nucleus of comet 67P/Churyumov-Gerasimenko, Astronomy and Astrophysics, 489, 777–785, ISSN 0004-6361

Lamy, P. L., Toth, I., Fernandez, Y., Weaver, H. A., 2014, The Sizes, Shapes, Albedos, and Colors of Cometary Nuclei, in Comets II, (Eds.) M. C. Festou, H. U. Keller, H. A. Weaver, p. 223, University of Arizona Press, ISBN 978-0816524501

Lecar, M., Podolak, M., Sasselov, D., Chiang, E., 2006, On the Location of the Snow Line in a Protoplanetary Disk, The Astrophysical Journal, 640, 1115–1118, ISSN 0004-637X

Lee, M. A., 1989, Plasma Waves and Instabilities at Comets and in Magnetospheres, vol. 53 of Geophysical Monograph Series, American Geophysical Union, Washington, D. C., ISBN 0-87590-073-9

Lowry, S., Duddy, S. R., Rozitis, B., Green, S. F., Fitzsimmons, A., Snodgrass, C., Hsieh, H. H., Hainaut, O., 2012, The nucleus of Comet 67P/Churyumov-Gerasimenko, Astronomy and Astrophysics, 548, A12, ISSN 0004-6361

Matthews, A. P., 1994, Current Advance Method and Cyclic Leapfrog for 2D Multispecies Hybrid Plasma Simulations, Journal of Computational Physics, 112, 102–116, ISSN 00219991

Mazelle, C., Rème, H., Sauvaud, J. A., D'Uston, C., Carlson, C. W., Anderson, K. A., Curtis, D. W., Lin, R. P., Korth, A., Mendis, D. A., Neubauer, F. M., Glassmeier, K. H., Raeder, J., 1989, Analysis of suprathermal electron properties at the magnetic pile-up boundary of comet P/Halley, Geophysical Research Letters, 16, 1035–1038, ISSN 00948276

Mazelle, C., Reme, H., Neubauer, F. M., 1995, Comparison of the Main Magnetic and Plasma Features in the Environments of Comets Grigg-Skjellerup and Halley, Advances in Space Research, 16, 41–45

McKenna-Lawlor, S., Kirsch, E., O'Sullivan, D., Thompson, A., Wenzel, K.-P., 1986, Energetic ions in the environment of comet Halley, Nature, 321, 347–349, ISSN 0028-0836

Morbidelli, A., Lunine, J. I., O'Brien, D. P., Raymond, S. N., Walsh, K. J., 2012, Building Terrestrial Planets, Annual Review of Earth and Planetary Sciences, 40, 251–275, ISSN 0084-6597

Motschmann, U., 2009, Plasmaphysik - Vorlesungsmanuskript, Braunschweig

Motschmann, U., Glassmeier, K.-H., 1993, Nongyrotropic Distribution of Pickup Ions at Comet P/Grigg-Skjellerup: A Possible Source of Wave Activity, Journal of Geophysical Research, 98, 20 977–20 983, ISSN 0148-0227

Motschmann, U., Glassmeier, K.-H., 1998, Dispersion and wave excitation in nongyrotropic plasmas, Journal of Plasma Physics, 60, 111–132, ISSN 00223778

Motschmann, U., Kührt, E., 2006, Interaction of the Solar Wind with Weak Obstacles: Hybrid Simulations for Weakly Active Comets and for Mars, Space Science Reviews, 122, 197–208, ISSN 0038-6308

Motschmann, U., Sauer, K., Roatsch, T., 1992, Simulation of Ion Acceleration in a Charged Dust Cloud, Geophysical Research Letters, 19, 225–228, ISSN 00948276

Motschmann, U., Woodward, T. I., Glassmeier, K. H., Southwood, D. J., Pinçon, J. L., 1996, Wavelength and direction filtering by magnetic measurements at satellite arrays: Generalized minimum variance analysis, Journal of Geophysical Research, 101, 4961, ISSN 0148-0227

Mottola, S., Lowry, S., Snodgrass, C., Lamy, P. L., Toth, I., Sierks, H., Angrilli, F., Barbieri, C., Barucci, M. A., Cremonese, G., Davidsson, B., Cecco, M. D., Debei, S., Fornasier, S., Fulle, M., Groussin, O., Hviid, S. F., Ip, W., Jorda, L., Keller, H. U., Knollenberg, J., Koschny, D., Kramm, R., Lara, L., Lazzarin, M., Moreno, J. J. L., Marzari, F., Michalik, H., Naletto, G., Rickman, H., Rodrigo, R., Sabau, L., Thomas, N., Agarwal, J., Bertini, I., Ferri, F., Magrin, S., Oklay, N., Tubiana, C., Rożek, A., A'Hearn, M. F., Bertaux, J.-L., Da Deppo, V., De Cecco, M., Gutiérrez, P., Kührt, E., Küppers, M., Lopez Moreno, J. J., Wenzel, K.-P., Güttler, C., Vincent, J.-B., 2014, The rotation state of 67P/Churyumov-Gerasimenko from approach observations with the OSIRIS cameras on Rosetta, Astronomy and Astrophysics, 569, L2, ISSN 0004-6361

Müller, J., 2007, Entwicklung eines numerischen Modells zur Untersuchung der Wechselwirkung leitfähiger Objekte mit dem Sonnenwind, Diplomarbeit, Technische Universität Braunschweig

Müller, J., 2012, A.I.K.E.F.: An Adaptive Hybrid Model with Application to Fossil Fields at Titan and Mercury's Double Magnetopause, Dissertation, Technische Universität Braunschweig

Müller, J., Simon, S., Motschmann, U., Glassmeier, K.-H., Saur, J., Schüle, J., Pringle, G. J., 2010, Magnetic field fossilization and tail reconfiguration in Titan's plasma environment during a magnetopause passage: 3D adaptive hybrid code simulations, Planetary and Space Science, 58, 1526–1546, ISSN 00320633

Müller, J., Simon, S., Motschmann, U., Schüle, J., Glassmeier, K.-H., Pringle, G. J., 2011, A.I.K.E.F.: Adaptive hybrid model for space plasma simulations, Computer Physics Communications, 182, 946–966, ISSN 00104655

Musmann, G., Neubauer, F. M., Lammers, E., 1977, Radial variation of the interplanetary magnetic field between 0.3 AU and 1.0 AU, Journal of Geophysics - Zeitschrift für Geophysik, 42, 591–598

Nagy, A., Winterhalter, D., Sauer, K., Cravens, T., Brecht, S., Mazelle, C., Crider, D., Kallio, E., Zakharov, A., Dubinin, E., Verigin, M., Kotova, G., Axford, W., Bertucci, C., Trotignon, J., 2004, The Plasma Environment of Mars, Space Science Reviews, 111, 33–114, ISSN 0038-6308

Nakai, Y., Shirai, T., Tabata, T., Ito, R., 1987, Cross sections for charge transfer of hydrogen atoms and ions colliding with gaseous atoms and molecules, Atomic Data and Nuclear Data Tables, 37, 69–101

Neubauer, F. M., 1987, Giotto magnetic-field results on the boundaries of the pile-up region and the magnetic cavity, Astronomy and Astrophysics, 187, 73–79

Neubauer, F. M., 1988, The ionopause transition and boundary layers at comet Halley from Giotto magnetic field observations, Journal of Geophysical Research, 93, 7272, ISSN 0148-0227

Neubauer, F. M., Glassmeier, K.-H., Pohl, M., Raeder, J., Acuna, M. H., Burlaga, L. F., Ness, N. F., Musmann, G., Mariani, F., Wallis, M. K., Ungstrup, E., Schmidt, H. U., 1986, First results from the Giotto magnetometer experiment at comet Halley, Nature, 321, 352–355, ISSN 0028-0836

Neubauer, F. M., Marschall, H., Pohl, M., Glassmeier, K.-H., Musmann, G., Mariani, F., Acuña, M. H., Burlaga, L. F., Ness, N. F., Wallis, M. K., Schmidt, H. U., Ungstrup, E., 1993, First results from the Giotto magnetometer experiment during the P/Grigg-Skjellerup encounter, Astronomy and Astrophysics, 268, L5–L8

Nilsson, H., Lundin, R., Lundin, K., Barabash, S., Borg, H., Norberg, O., Fedorov, a., Sauvaud, J.-a., Koskinen, H., Kallio, E., Riihelä, P., Burch, J. L., 2006, RPC-ICA: The Ion Composition Analyzer of the Rosetta Plasma Consortium, Space Science Reviews, 128, 671–695, ISSN 0038-6308

Nilsson, H., Stenberg Wieser, G., Behar, E., Wedlund, C. S., Gunell, H., Yamauchi, M., Lundin, R., Barabash, S., Wieser, M., Carr, C., Cupido, E., Burch, J. L., Fedorov, A., Sauvaud, J.-A., Koskinen, H., Kallio, E., Lebreton, J.-P., Eriksson, A., Edberg, N., Goldstein, R., Henri, P., Koenders, C., Mokashi, P., Nemeth, Z., Richter, I., Szego, K., Volwerk, M., Vallat, C., Rubin, M., 2015, Birth of a comet magnetosphere: A spring of water ions, Science, 347, ISSN 0036-8075

Nübold, H., 2000, Accretional Remanence of Magnetized Dust in the Solar Nebula, Icarus, 144, 149–159, ISSN 00191035

Nübold, H., Poppe, T., Rost, M., Dominik, C., Glassmeier, K.-H., 2003, Magnetic aggregation, Icarus, 165, 195–214, ISSN 00191035

Ogilvie, K. W., Coplan, M. A., Bochsler, P., Geiss, J., 1986, Ion composition results during the international cometary explorer encounter with giacobini-zinner., Science, 232, 374–7, ISSN 0036-8075

Omidi, N., 2002, Hybrid simulations of solar wind interaction with magnetized asteroids: General characteristics, Journal of Geophysical Research, 107, 1487, ISSN 0148-0227

Omidi, N., Winske, D., 1987, A kinetic study of solar wind mass loading and cometary bow shocks, Journal of Geophysical Research, 92, 13 409, ISSN 0148-0227

Omidi, N., Blanco-Cano, X., Russell, C. T., Karimabadi, H., 2004, Dipolar magnetospheres and their characterization as a function of magnetic moment, Advances in Space Research, 33, 1996–2003, ISSN 02731177

Oort, J. H., 1950, The structure of the cloud of comets surrounding the Solar System and a hypothesis concerning its origin, Bulletin of the Astronomical Institutes of the Netherlands, 11, 91–110

Parker, E. N., 1958, Dynamics of the Interplanetary Gas and Magnetic Fields., The Astrophysical Journal, 128, 664–676

Pätzold, M., Häusler, B., Aksnes, K., Anderson, J. D., Asmar, S. W., Barriot, J.-P., Bird, M. K., Boehnhardt, H., Eidel, W., Grün, E., Ip, W. H., Marouf, E., Morley, T., Neubauer, F. M., Rickman, H., Thomas, N., Tsurutani, B. T., Wallis, M. K., Wickramasinghe, N. C., Mysen, E., Olson, O., Remus, S., Tellmann, S., Andert, T., Carone, L., Fels, M., Stanzel, C., Audenrieth-Kersten, I., Gahr, A., Müller, A.-L., Stupar, D., Walter, C., 2007, Rosetta Radio Science Investigations (RSI), Space Science Reviews, 128, 599–627, ISSN 0038-6308

Powell, K. G., Roe, P. L., Linde, T. J., Gombosi, T. I., De Zeeuw, D. L., 1999, A Solution-Adaptive Upwind Scheme for Ideal Magnetohydrodynamics, Journal of Computational Physics, 154, 284–309, ISSN 00219991

Prialnik, D., Sarid, G., Rosenberg, E. D., Merk, R., 2008, Thermal and Chemical Evolution of Comet Nuclei and Kuiper Belt Objects, Space Science Reviews, 138, 147–164, ISSN 0038-6308

Puhl-Quinn, P., Cravens, T. E., 1995, One-dimensional hybrid simulations of the diamagnetic cavity boundary region of comet Halley, Journal of Geophysical Research, 100, 21 631, ISSN 0148-0227

Raith, W. (Ed.), 1997, Erde und Planeten, De Gruyter, Berlin, ISBN 3-11-012985-X

Ranocha, H., 2013, Erweiterung des Hybrid-Codes A.I.K.E.F. um eine Energiegleichung für das Elektronenfluid, Bachelor Thesis, Technische Universität Braunschweig

Reinhard, R., 1986, The Giotto encounter with comet Halley, Nature, 321, 313–318, ISSN 0028-0836

Rème, H., Sauvaud, J. A., D'Uston, C., Cotin, F., Cros, A., Anderson, K. A., Carlson, C. W., Curtis, D. W., Lin, R. P., Mendis, D. A., Korth, A., Richter, A. K., 1986, Comet Halley–solar wind interaction from electron measurements aboard Giotto, Nature, 321, 349–352, ISSN 0028-0836

Remya, B., Reddy, R. V., Tsurutani, B. T., Lakhina, G. S., Echer, E., 2013, Ion temperature anisotropy instabilities in planetary magnetosheaths, Journal of Geophysical Research: Space Physics, 118, 785–793, ISSN 21699380

Richardson, J. D., Paularena, K. I., Lazarus, A. J., Belcher, J. W., 1995, Radial evolution of the solar wind from IMP 8 to Voyager 2, Geophysical Research Letters, 22, 325–328, ISSN 00948276

Richter, I., Brinza, D. E., Cassel, M., Glassmeier, K.-H., Kuhnke, F., Musmann, G., Othmer, C., Schwingenschuh, K., Tsurutani, B. T., 2001, First direct magnetic field measurements of an asteroidal magnetic field: DS1 at Braille, Geophysical Research Letters, 28, 1913–1916, ISSN 00948276

Richter, I., Koenders, C., Glassmeier, K.-H., Tsurutani, B. T., Goldstein, R., 2011, Deep Space 1 at comet 19P/Borrelly: Magnetic field and plasma observations, Planetary and Space Science, 59, 691–698, ISSN 00320633

Richter, I., Auster, H. U., Glassmeier, K.-H., Koenders, C., Carr, C., Motschmann, U., Müller, J., McKenna-Lawlor, S., 2012, Magnetic field measurements during the ROSETTA flyby at asteroid (21)Lutetia, Planetary and Space Science, 66, 155–164, ISSN 00320633

Riedler, W., Torkar, K., Jeszenszky, H., Romstedt, J., Alleyne, H. S. C., Arends, H., Barth, W., Biezen, J. V. D., Butler, B., Ehrenfreund, P., Fehringer, M., Fremuth, G., Gavira, J., Havnes, O., Jessberger, E. K., Kassing, R., Klöck, W., Koeberl, C., Levasseur-Regourd, A.-C., Maurette, M., Rüdenauer, F., Schmidt, R., Stangl, G., Steller, M., Weber, I., 2006, MIDAS – The Micro-Imaging Dust Analysis System for the Rosetta Mission, Space Science Reviews, 128, 869–904, ISSN 0038-6308

RSGS-Team, 2013, RO-SGS-IF-1001: RSGS-PI Interface Control Document, Tech. rep., ESA, Villa Franca, Madrid

Rubin, M., Hansen, K. C., Combi, M. R., Daldorff, L. K. S., Gombosi, T. I., Tenishev, V. M., 2012, Kelvin-Helmholtz instabilities at the magnetic cavity boundary of comet 67P/Churyumov-Gerasimenko, Journal of Geophysical Research, 117, A06 227, ISSN 0148-0227

Rubin, M., Combi, M. R., Daldorff, L. K. S., Gombosi, T. I., Hansen, K. C., Shou, Y., Tenishev, V. M., Tóth, G., van der Holst, B., Altwegg, K., 2014a, Comet 1P/Halley Multifluid Mhd Model for the Giotto Fly-By, The Astrophysical Journal, 781, 86, ISSN 0004-637X

Rubin, M., Koenders, C., Altwegg, K., Combi, M., Glassmeier, K.-H., Gombosi, T., Hansen, K., Motschmann, U., Richter, I., Tenishev, V., Tóth, G., 2014b, Plasma environment of a weak comet – Predictions for Comet 67P/Churyumov–Gerasimenko from multifluid-MHD and Hybrid models, Icarus, 242, 38–49, ISSN 00191035

Russell, C. T., Snare, R. C., Means, J. D., Elphic, R. C., 1980, Pioneer Venus Orbiter Fluxgate Magnetometer, IEEE Transactions on Geoscience and Remote Sensing, GE-18, 32–35, ISSN 0196-2892

Schleicher, D. G., 2006, Compositional and physical results for Rosetta's new target Comet 67P/Churyumov–Gerasimenko from narrowband photometry and imaging, Icarus, 181, 442–457, ISSN 00191035

Schmid, D., Volwerk, M., Plaschke, F., Vörös, Z., Zhang, T. L., Baumjohann, W., Narita, Y., 2014, Mirror mode structures near Venus and Comet P/Halley, Annales Geophysicae, 32, 651–657, ISSN 1432-0576

Schmidt, H. U., Wegmann, R., 1982, Plasma Flow and Magnetic Fields in Comets, in Comets, (Ed.) L. L. Wilkening, pp. 538–560, University of Arizona Press, Tucson, ISBN 0816507694

Schmidt, H. U., Wegmann, R., Neubauer, F. M., 1993, MHD Modeling Applied to Giotto Encounter with Comet P/Grigg-Skjellerup, Journal of Geophysical Research, 98, 21 009–21 016, ISSN 0148-0227

Schulz, R., Stüwe, J. A., Boehnhardt, H., 2004, Rosetta target comet 67P/Churyumov-Gerasimenko, Astronomy and Astrophysics, 422, L19–L21, ISSN 0004-6361

Schunk, R., Nagy, A. F., 2009, Ionospheres: Physics, Plasma Physics, and Chemistry, Cambridge University Press, Cambridge, ISBN 0521877067

Shi, M., Baragiola, R. A., Grosjean, D. E., Johnson, R. E., Jurac, S., Schou, J., 1995, Sputtering of water ice surfaces and the production of extended neutral atmospheres, Journal of Geophysical Research, 100, 26 387, ISSN 0148-0227

Simon, S., 2004, Zur Interaktion leitfähiger und magnetisierter Objekte mit dem Sonnenwind, Diplomarbeit, TU Braunschweig

Simon, S., 2007, Titan’s highly variable plasma environment: A 3D hybrid simulation study, Dissertation, Technische Universität Braunschweig

Simon, S., Bagdonat, T. B., Motschmann, U., Glassmeier, K.-H., 2006, Plasma environment of magnetized asteroids: a 3-D hybrid simulation study, Annales Geophysicae, 24, 407–414, ISSN 1432-0576

Skorov, Y., Blum, J., 2012, Dust release and tensile strength of the non-volatile layer of cometary nuclei, Icarus, 221, 1–11, ISSN 00191035

Smith, E. J., Tsurutani, B. T., Salvin, J. A., Jones, D. E., Siscoe, G. L., Mendis, D. A., 1986a, International cometary explorer encounter with giacobini-zinner: magnetic field observations., Science, 232, 382–5, ISSN 0036-8075

Smith, E. J., Tsurutani, B. T., Slvain, J. A., Jones, D. E., Siscoe, G. L., Mendis, D. A., 1986b, International cometary explorer encounter with giacobini-zinner: magnetic field observations., Science, 232, 382–5, ISSN 0036-8075

Snodgrass, C., Tubiana, C., Bramich, D. M., Meech, K., Boehnhardt, H., Barrera, L., 2013, Beginning of activity in 67P/Churyumov-Gerasimenko and predictions for 2014-2015, Astronomy and Astrophysics, 557, A33, ISSN 0004-6361

Sonnerup, B. U. O., Cahill, L. J., 1967, Magnetopause structure and attitude from Explorer 12 observations, Journal of Geophysical Research, 72, 171, ISSN 0148-0227

Stern, S. A., 2003, The evolution of comets in the Oort cloud and Kuiper belt., Nature, 424, 639–42, ISSN 1476-4687

Stern, S. A., Slater, D. C., Scherrer, J., Stone, J., Versteeg, M., A'hearn, M. F., Bertaux, J. L., Feldman, P. D., Festou, M. C., Parker, J. W., Siegmund, O. H. W., 2006, Alice: The rosetta Ultraviolet Imaging Spectrograph, Space Science Reviews, 128, 507–527, ISSN 0038-6308

Szego, K., Juhasz, A., Bebesi, Z., 2014, Possible observation of charged nanodust from comet 67P/Churyumov-Gerasimenko: An analysis for the ROSETTA mission, Planetary and Space Science, ISSN 00320633

Tenishev, V., Combi, M., Davidsson, B., 2008, A Global Kinetic Model for Cometary Comae: The Evolution of the Coma of the Rosetta Target Comet Churyumov-Gerasimenko throughout the Mission, The Astrophysical Journal, 685, 659–677, ISSN 0004-637X

Thomas, V. A., 1995, Kinetic Kelvin-Helmholtz instability at a finite sized object, Journal of Geophysical Research, 100, 12 017, ISSN 0148-0227

Thompson, P., Southwood, D. J., Goodman, S., 1996, Plasma waves radiated by a moving conducting body between successive gyrofrequencies, Journal of Geophysical Research, 101, 19 849, ISSN 0148-0227

Thomsen, M. F., Feldman, W. C., Wilken, B., Jockers, K., Stuedemann, W., 1987, In-situ observations of a bi-modal ion distribution in the outer coma of comet P/Halley, Astronomy and Astrophysics (ISSN 0004-6361), 187, 141–148

Tóth, G., van der Holst, B., Sokolov, I. V., De Zeeuw, D. L., Gombosi, T. I., Fang, F., Manchester, W. B., Meng, X., Najib, D., Powell, K. G., Stout, Q. F., Glocer, A., Ma, Y.-J., Opher, M., 2012, Adaptive numerical algorithms in space weather modeling, Journal of Computational Physics, 231, 870–903, ISSN 00219991

Trávníček, P., 2005, Structure of the lunar wake: Two-dimensional global hybrid simulations, Geophysical Research Letters, 32, L06 102, ISSN 0094-8276

Trotignon, J. G., Michau, J. L., Lagoutte, D., Chabassière, M., Chalumeau, G., Colin, F., Décréau, P. M. E., Geiswiller, J., Gille, P., Grard, R., Hachemi, T., Hamelin, M., Eriksson, A., Laakso, H., Lebreton, J. P., Mazelle, C., Randriamboarison, O., Schmidt, W., Smit, A., Telljohann, U., Zamora, P., 2006, RPC-MIP: the Mutual Impedance Probe of the Rosetta Plasma Consortium, Space Science Reviews, 128, 713–728, ISSN 0038-6308

Tsurutani, B. T., Smith, E. J., 1986, Hydromagnetic waves and instabilities associated with cometary ion pickup: ICE observations, Geophysical Research Letters, 13, 263–266, ISSN 00948276

Tsurutani, B. T., Smith, E. J., Brinca, A. L., Thorne, R. M., Matsumoto, H., 1989, Properties of whistler mode wave packets at the leading edge of steepened magnetosonic waves: Comet Giacobini-Zinner, Planetary and Space Science, 37, 167–182, ISSN 00320633

Tsurutani, B. T., Echer, E., Richter, I., Koenders, C., Glassmeier, K.-H., 2013, SLAMS at comet 19P/Borrelly: DS1 observations, Planetary and Space Science, 75, 17–27, ISSN 00320633

Verdant, M., Schwehm, G. H., 1998, The International Rosetta Mission, ESA Bulletin, 93

Vigren, E., Galand, M., 2013, Predictions of Ion Production Rates and Ion Number Densities Within the Diamagnetic Cavity of Comet 67P/Churyumov-Gerasimenko At Perihelion, The Astrophysical Journal, 772, 33, ISSN 0004-637X

Vincent, J.-B., Lara, L. M., Tozzi, G. P., Lin, Z.-Y., Sierks, H., 2013a, Spin and activity of comet 67P/Churyumov-Gerasimenko, Astronomy and Astrophysics, 549, A121, ISSN 0004-6361

Vincent, J.-B., Sierks, H., Rose, M., 2013b, Jet Activity on the Cliffs of Comet 9P/Tempel 1, 44th Lunar and Planetary Science Conference

Volwerk, M., Koenders, C., Delva, M., Richter, I., Schwingenschuh, K., Bentley, M. S., Glassmeier, K.-H., 2013, Ion cyclotron waves during the Rosetta approach phase: a magnetic estimate of cometary outgassing, Annales Geophysicae, 31, 2201–2206, ISSN 1432-0576

Volwerk, M., Glassmeier, K.-H., Delva, M., Schmid, D., Koenders, C., Richter, I., Szegö, K., 2014, A comparison between VEGA 1, 2 and Giotto flybys of comet 1P/Halley: implications for Rosetta, Annales Geophysicae, 32, 1441–1453, ISSN 1432-0576

von Oertzen, J., 2003, Global modeling of comets: Nucleus, neutral and ionized coma of comets 67P/Churyumov-Gerasimenko and 46P/Wirtanen. Preparations for the Rosetta Radio Science Investigations., Dissertation, Universität Köln

Wallis, M. K., 1973, Weakly-shocked flows of the solar wind plasma through atmospheres of comets and planets, Planetary and Space Science, 21, 1647–1660, ISSN 00320633

Wallis, M. K., Dryer, M., 1976, Sun and comets as sources in an external flow, The Astrophysical Journal, 205, 895, ISSN 0004-637X

Walsh, K. J., Morbidelli, A., Raymond, S. N., O'Brien, D. P., Mandell, A. M., 2011, A low mass for Mars from Jupiter's early gas-driven migration., Nature, 475, 206–9, ISSN 1476-4687

Whipple, F. L., 1950, A comet model. I. The acceleration of Comet Encke, The Astrophysical Journal, 111, 375, ISSN 0004-637X

Wiehle, S., Motschmann, U., Gortsas, N., Glassmeier, K.-H., Müller, J., Koenders, C., 2011a, Simulation of cometary jets in interaction with the solar wind, Advances in Space Research, 48, 1108–1113, ISSN 02731177

Wiehle, S., Plaschke, F., Motschmann, U., Glassmeier, K.-H., Auster, H., Angelopoulos, V., Mueller, J., Kriegel, H., Georgescu, E., Halekas, J., Sibeck, D., McFadden, J., 2011b, First lunar wake passage of ARTEMIS: Discrimination of wake effects and solar wind fluctuations by 3D hybrid simulations, Planetary and Space Science, 59, 661–671, ISSN 00320633

Wu, C. S., Davidson, R. C., 1972, Electromagnetic instabilities produced by neutral-particle ionization in interplanetary space, Journal of Geophysical Research, 77, 5399–5406, ISSN 01480227

Youdin, A. N., Goodman, J., 2005, Streaming Instabilities in Protoplanetary Disks, The Astrophysical Journal, 620, 459–469, ISSN 0004-637X

Young, D. T., Crary, F. J., Nordholt, J. E., Bagenal, F., Boice, D., Burch, J. L., Eviatar, A., Goldstein, R., Hanley, J. J., Lawrence, D. J., McComas, D. J., Meier, R., Reisenfeld, D., Sauer, K., Wiens, R. C., 2004, Solar wind interactions with Comet 19P/Borrelly, Icarus, 167, 80–88, ISSN 00191035

Zieger, B., Hansen, K. C., 2008, Statistical validation of a solar wind propagation model from 1 to 10 AU, Journal of Geophysical Research, 113, A08 107, ISSN 0148-0227

Zimmerman, M., Farrell, W., a.R. Poppe, 2014, Grid-free 2D plasma simulations of the complex interaction between the solar wind and small, near-Earth asteroids, Icarus, 238, 77–85, ISSN 00191035

Zsom, A., Ormel, C. W., Güttler, C., Blum, J., Dullemond, C. P., 2010, The outcome of protoplanetary dust growth: pebbles, boulders, or planetesimals? II. Introducing the bouncing barrier, Astronomy and Astrophysics, 513, 1–22

Danksagung

Hiermit möchte ich all denen danken, die mich beim Erstellen dieser Arbeit in direkter oder indirekter Weise unterstützt haben.

In besonderer Weise möchte ich mich bei Herrn Prof. Dr. Karl-Heinz Glaßmeier für die Betreuung und die gute Zusammenarbeit danken. Als Mentor dieser Arbeit war er stets der erste Ansprechpartner bei wissenschaftlichen Fragen. Die vielen produktiven wissenschaftlichen Diskussionen haben mein Verständnis von physikalischen Prozessen erweitert. Er eröffnete mir auch unzählige Möglichkeiten meine Arbeit auf Konferenzen oder Meetings vorzustellen. Insbesondere möchte ich mich für die Aufgaben bedanken, die ich am Institut übernehmen durfte. Neben Tätigkeiten in der Lehre und der Betreuung des Plasmakristallversuchs hat mich besonders die Teilnahme am Rosetta Projekt immer wieder gefordert, aber auch stets motiviert.

Ich danke Herrn Prof. Dr. Uwe Motschmann für die Übernahme des Koreferats und die fachliche Unterstützung der Arbeit. Auch die gute Zusammenarbeit bereits während meiner Studien- und Diplomarbeitszeit werden mir in Erinnerung bleiben. Dazu zählen unter anderem die guten Vorlesungen und exzellenten Skripte, aus denen ich mehr gelernt habe als aus so manchem Lehrbuch.

Ich bedanke mich des Weiteren beim gesamtem RPC Team und dem SGS Team bei der ESA für die freundliche Zusammenarbeit im Rahmen der „sexiest mission in space“. Bei den unzähligen Telefonkonferenzen (grob geschätzt 300 in den letzten Jahren), aber vor allem bei den vielen Meetings zum Beispiel in Darmstadt, Noordwijk und Madrid habe ich viel über den Kometen und die Rosetta Mission gelernt. Speziell möchte ich mich auch bei Anders Eriksson für meinen produktiven Aufenthalt am IRF in Uppsala bedanken.

Martin Rubin und dem ISSI Team „Modelling cometary environments in the context of the heritage of the Giotto mission to comet Halley and the forthcoming new observations at comet 67P/Churyumov-Gerasimenko“ von Prof. Dr. Monio Kartalev möchte ich für die gute Zusammenarbeit und die wertvollen Diskussionen über die Modellierung der kometaren Wechselwirkung danken.

Die in dieser Arbeit gezeigten Simulationen wurden auf den Computern des Norddeutschen Verbundes für Hoch- und Höchstleistungsrechnen (HLRN) und dem JUROPA Cluster des Forschungszentrums Jülich berechnet. Für die erhaltende Rechenzeit und den Support möchte ich mich an dieser Stelle bedanken.

Für die unzähligen Schokokekse, aber vor allem für die vielen tiefgründigen Diskussionen, sowohl über wissenschaftlicher Probleme als auch über Implementierungen in A.I.K.E.F., möchte ich Hendrik Kriegel danken. Er hatte immer ein offenes Ohr, auch wenn spät abends eine wichtige Simulation mit einem Speicherleck oder einem MPI-Fehler abgestürzt ist.

Weiterhin bin ich auch allen Mitgliedern der Arbeitsgruppe *Weltraumphysik und Weltraumsensorik* zu Dank verpflichtet. Mit ihnen konnte ich über die großen und kleinen

Probleme der Arbeit sprechen. Insbesondere möchte ich mich bei Christopher Perschke bedanken, der unter anderem das Wellenteleskop auf meine Daten angewendet hat. Ich möchte auch allen anderen Kolleginnen und Kollegen im Institut danken. Unter anderem die hervorragende Arbeitsatmosphäre, die Kickerpausen, die Grillabende und der kürzlich eingeführte *Mettwoch* haben die Arbeit im Institut sehr angenehm und kurzweilig gestaltet. Mein Dank gilt auch allen, die diese Arbeit auf grammatikalische Ungereimtheiten und Rechtschreibfehler durchgelesen haben.

Meinen Freunden danke ich für die schönen Abende beim Kochen und im Garten, die Feiern und die erholsamen Pausen. Für die stete Unterstützung auf meinem Lebensweg möchte ich mich bei meinen Eltern und meiner ganzen Familie bedanken. Zum Schluss möchte ich mich ganz herzlich bei meiner Frau Joana für ihr Verständnis, wenn es mal wieder später geworden ist, und ihren Beistand in schwierigen Zeiten bedanken.